Advanced Structured Materials

Alexander L. Yarin
Min Wook Lee
Seongpil An
Sam S. Yoon

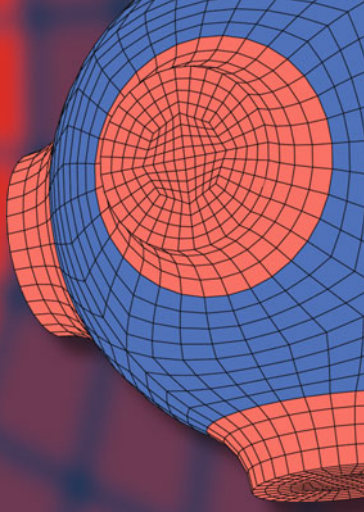

Self-Healing Nanotextured Vascular Engineering Materials

Springer

Advanced Structured Materials

Volume 105

Common engineering materials reach in many applications their limits and new developments are required to fulfil increasing demands on engineering materials. The performance of materials can be increased by combining different materials to achieve better properties than a single constituent or by shaping the material or constituents in a specific structure. The interaction between material and structure may arise on different length scales, such as micro-, meso- or macroscale, and offers possible applications in quite diverse fields.

This book series addresses the fundamental relationship between materials and their structure on the overall properties (e.g. mechanical, thermal, chemical or magnetic etc) and applications.

The topics of *Advanced Structured Materials* include but are not limited to

- classical fibre-reinforced composites (e.g. glass, carbon or Aramid reinforced plastics)
- metal matrix composites (MMCs)
- micro porous composites
- micro channel materials
- multilayered materials
- cellular materials (e.g., metallic or polymer foams, sponges, hollow sphere structures)
- porous materials
- truss structures
- nanocomposite materials
- biomaterials
- nanoporous metals
- concrete
- coated materials
- smart materials

Advanced Structured Materials is indexed in Google Scholar and Scopus.

More information about this series at http://www.springer.com/series/8611

Alexander L. Yarin · Min Wook Lee ·
Seongpil An · Sam S. Yoon

Self-Healing Nanotextured Vascular Engineering Materials

Springer

Alexander L. Yarin
Department of Mechanical and Industrial Engineering
University of Illinois at Chicago
Chicago, IL, USA

Seongpil An
Department of Mechanical and Industrial Engineering
University of Illinois at Chicago
Chicago, IL, USA

Min Wook Lee
Institute of Advanced Composite Materials
Korea Institute of Science and Technology
Jeollabuk-do, Korea (Republic of)

Sam S. Yoon
School of Mechanical Engineering
Korea University
Seoul, Korea (Republic of)

ISSN 1869-8433 ISSN 1869-8441 (electronic)
Advanced Structured Materials
ISBN 978-3-030-05266-9 ISBN 978-3-030-05267-6 (eBook)
https://doi.org/10.1007/978-3-030-05267-6

Library of Congress Control Number: 2018966402

This Springer imprint is published by the registered company Springer Nature Switzerland AG
The registered company address is: Gewerbestrasse 11, 6330 Cham, Switzerland

Preface

Nature-inspired self-healing strategies have been explored in biomimetic engineering designs with the goal of repairing structural damage or facilitating corrosion protection by the systematic transport of healing agents, which can be cured and polymerized at damage sites. Microscopic capsules filled with healing agents, the proposed strategy, are certainly viable and require no external energy to trigger the healing process. However, a material layer with such capsules is inherently thick because of the bulky microcapsules. Moreover, the capsule-based approach is inappropriate for repeatable healing, since capsules can be used only once. Accordingly, a different approach with much smaller confined containers for healing agents and the capacity for multiple healing was desired. Recent years have included success in the development and characterization of nanotextured vascular self-healing materials, which are the focus of the present book. Here, we discuss the state of the art in the field of such materials, which emerged to mimic multiple natural materials, for example, those characteristics of the human body (e.g., skin and bones healed by the vascular system).

The book describes relevant healing agents and the basic physicochemical phenomena characteristic of the self-healing materials and composites based on them. The book also details fabrication methods used for the key elements of vascular systems in modern nanotextured engineering self-healing materials, such as electrospinning (including co-electrospinning and emulsion spinning) and solution blowing (including coaxial solution blowing and emulsion blowing). It also outlines other approaches based on hollow fibers, tubes, etc.

Self-healing materials should be capable of self-restoring their mechanical properties, e.g., stiffness, toughness, adhesion, and cohesion. It is necessary to heal the invisible and practically undetectable fatigue cracks, which endanger airplanes and multiple other vehicles and structures using composite components. Nanotextured vascular self-healing can also prevent or delay delamination in composites on ply surfaces. Therefore, the book details certain fundamental mechanical tests (e.g., tensile, fatigue, blister, and impact tests) and the performance of nanotextured vascular self-healing materials in these tests. It demonstrates the

degree to which such materials can restore their stiffness, toughness, adhesion, and cohesion.

Another field where nanotextured vascular self-healing materials are extremely desirable is in corrosion protection. The corrosion of metals is recognized as one of the major problems in various metal-framed structures. As an introduction to corrosion phenomena, the book discusses the electrochemical fundamentals of corrosion crack growth. Numerous corrosion protection approaches have been suggested, including the cathodic protection method, the anti-corrosion paint coating method, and others. However, the toxicity of the chemical paints used and other problems relating to the cost and to the environment remain as serious concerns with these methods. Accordingly, the book describes the bio-inspired vascular self-healing techniques recently explored as alternative approaches for corrosion prevention. In particular, it discusses in detail the extrinsic self-healing based on nanotextured vascular nanofiber networks and demonstrates the successful performance of such materials in crack healing in corrosion protection layers. The results reveal that this approach to anti-corrosion protection holds great promise because of its economic and industrial feasibility.

Our personal research experience in this field covers and spans nearly all topics covered in this book. This monograph is based significantly on our own results published in peer-reviewed journals over the last 8 years.

The book begins with the Introduction, which provides an overview of the existing self-healing approaches and traces them back to naturally healing tissues of human tissue and bone. Thus, the idea of biomimetic approach for the development of self-healing engineering materials is introduced. The first biomimetically derived approach to composite engineering materials was based on microcapsules that contained healing agents, which were released by propagating cracks, thus healing the cracks. The benefits and drawbacks of the microcapsule-based approach are discussed, namely, the relatively large scale of such microcapsules and the difficulties in their manufacturing, which drove the development of nanotextured vascular composites. These composites are based on core-shell nanofiber networks filled with healing agents, which can be released by the propagation of cracks to heal these cracks. These nanotextured vascular self-healing materials are the main focus of the present book.

The Introduction is followed by four parts, each comprising several chapters. Part I begins with a description of the healing agents used in engineering self-healing materials (Chap. 2). This chapter of Part I is mostly chemical in nature. Chapter 3 is devoted to the fundamental physicochemical phenomena accompanying self-healing, namely, the spreading of the released drops of healing agents, their mixing, and the stitching of the cracks. This chapter involves some theory regarding drop spreading and imbibition in porous nanofiber mats, as well as experimental observations employing macroscopic models of self-healing materials.

Part II of the book addresses the fabrication methods used to form core-shell nanofiber mats, with the cores containing healing agents. These methods are, namely, electrospinning and co-electrospinning, emulsion spinning, solution

blowing, etc. (Chap. 4). In Chap. 5, the characterization methods used to detect the presence, release, polymerization, and solidification of the encaged healing agents on the nanometer scale are described.

The following Part III begins with Chap. 6, where the fundamental theoretical aspects of fracture mechanics are outlined. Namely, a brief theoretical description of cracks in brittle elastic materials is given and the fundamentals of the Griffith approach based on the surface energy are introduced. The fracture toughness of Mode I, II, and III cracks is described, including viscoelastic effects. Critical (catastrophic) and subcritical (fatigue) cracks and their growth are also described theoretically. The adhesion and cohesion energies are introduced as well, and the theory of the blister test for the two limiting cases of stiff and soft materials is developed. In addition, the effect of non-self-healing nanofiber mats on the toughening of ply surfaces in composites is discussed. Then, in Chap. 7 in Part III, the experimental data acquired with self-healing nanotextured vascular materials in tensile tests are discussed. Blister and impact tests, as well as the results on the interfacial toughening associated with nanofibers are the focus of Chap. 8. The interpretation of the results of blister tests is based on the previously introduced theory and allows the elucidation of the extent to which such mechanical properties as stiffness and the adhesion/cohesion energy are restored in self-healing nanotextured vascular materials. Double-cantilever beam and bending tests are also discussed in this chapter.

Part IV begins with Chap. 9, which contains a brief description of the electrochemical theory of corrosion crack growth. Then, the discussion turns to representative extrinsic self-healing techniques developed in the last decade, with the capsule-based (Chap. 9) and nanofiber-based self-healing approaches (Chap. 10) being in focus. Such physicochemical approaches are expected to effectively replace or supplement existing corrosion protection methods. An overview of the corrosion protection in the self-healing extrinsic nanotextured vascular engineering materials formed using the capsule-based and nanofiber-based self-healing approaches is given.

The final Chap. 11 of the book is devoted to future perspectives, with the current limitations being highlighted and attractive directions for future research discussed. These directions hold great promise for the further improvement of extrinsic self-healing techniques for the recovery of mechanical properties and corrosion protection, and their industrial scalability.

Each chapter in the book can be read by itself. A wide range of relevant references to existing literature are included at the end of each chapter. This does not preclude the discussion of all topics in the book in a sufficiently self-contained, detailed, and in-depth manner.

This book is intended as a comprehensive guide in the field of self-healing nanotextured vascular materials for senior-year undergraduate students, graduate students, researchers, engineers, and practitioners in industry. The reader can benefit from previous exposure to the fundamentals of chemistry, fluid and solid mechanics, and electrochemistry. However, if the reader has not been introduced to these topics, all necessary concepts are briefly but thoroughly introduced in the

appropriate chapters. Investigators from the following different fields are addressed: materials science, aerospace engineering, automotive and chemical engineering, production, as well as polymer science, and fluid and solid mechanics. The book may be of special importance to researchers and engineers interested in the development of novel self-healing engineering materials, because they can benefit from its in-depth and comprehensive exposition of physicochemical and mechanical fundamentals relevant to materials development.

We are indebted to our parents and families whose permanent support has been tremendously beneficial to our research. We are thankful to our students and colleagues who directly or indirectly, via fruitful discussions contributed to the results explained in this book. Many of their names are listed as our coauthors in the references included in each chapter. ALY is extremely grateful to Emmanuel Y, for his special contribution to this work. In addition, we acknowledge the generous support of our joint work by the Agency for Defense Development of the Republic of Korea through its International Collaboration Program.

Chicago, USA — Alexander L. Yarin
Jeollabuk-do, Korea (Republic of) — Min Wook Lee
Chicago, USA — Seongpil An
Seoul, Korea (Republic of) — Sam S. Yoon

Contents

About the Authors

Alexander L. Yarin works on nano-textured self-healing materials, electrospinning, solution blowing, drop impacts, and collision phenomena, generally in the field of materials science, applied physics, fluid, and solid mechanics. He completed M.Sc. in 1977 (in Applied Physics), Ph.D. (in Physics and Mathematics) in 1980, and D.Sc. (Habilitation in Physics and Mathematics) in 1989. His affiliations include Junior & Senior Research Associate at The Institute for Problems in Mechanics of the Academy of Sciences of the USSR, Moscow (1977–1990) and concurrently Professor at the Department of Molecular and Chemical Physics of The Moscow Physico-Technical Institute (1985–1989) and The Aviation Technology Institute, Moscow, USSR (1988–1990); Professor at The Technion-Israel Institute of Technology (1990–2006; Eduard Pestel Chair Professor in Mechanical Engineering at The Technion in 1999–2006); Professor at The University of Illinois at Chicago, USA (2006–present; Distinguished Professor in 2014–present); Fellow of the Center for Smart Interfaces at the Technical University Darmstadt, Germany (2008–2012); and Visiting Professor at Korea University (Seoul, Republic of Korea, 2013–2017). He was a Visiting Professor on sabbatical at the University of Wisconsin-Madison (Chemical Engineering Department) in 1996–1997, and at The University of Illinois at Chicago in 2003–2004. He is the author of 4 books, 12 book chapters, 344 research papers in leading peer-reviewed journals, 60 conference papers, 7 miscellaneous publications, and 10 patents. His present h-index (Google Scholar, 1/2019) is 61.

He is one of the three co-editors of *Springer Handbook of Experimental Fluid Mechanics*, 2007, and the Associate Editor of the journal *Experiments in Fluids*. He is also the member of the International Editorial Advisory Board of the Bulletin of the Polish Academy of Sciences, and of the journal *Archives of Mechanics*, as well as the member of the Editorial Advisory Board of the journal *Electrospinning*. He is the Fellow of the American Physical Society. He was also the Fellow of the Rashi Foundation, The Israel Academy of Sciences and Humanities in 1992–1995. He was awarded Gutwirth Award, Hershel Rich Prize, and Prize for Technological Development for Defense against Terror of the American-Technion Society.

Min Wook Lee completed his BS and MS in Mechanical Engineering at Korea University in 2008 and 2010, respectively. He pursued his Ph.D. studies at Korea University at the School of Mechanical Engineering (2014), followed by post-doctoral studies at the University of Illinois at Chicago at the Department of Mechanical and Industrial Engineering (in 2014–2017). In 2017, he has been appointed as a Senior Researcher in Institute of Advanced Composite Materials at KIST (Korea Institute of Science and Technology). His research interests include electrospinning, solution blowing, self-healing composites, and fracture mechanics. His present h-index (Scopus, 8/2018) is 17. He is the author of 40 research papers and 24 domestic/PCT patents.

Seongpil An received his BS and Ph.D. degrees at the School of Mechanical Engineering from Korea University (Seoul, Republic of Korea) in 2012 and 2017, respectively. He is a Postdoctoral Research Associate at the Department of Mechanical and Industrial Engineering at the University of Illinois at Chicago from 2017. His current research interests include various mechanical, chemical, and electrical engineering applications of nano- and micro-scale electrospun polymer fibers, as well as nanotextured self-healing materials. He has hitherto published 64 research papers in peer-reviewed international journals and has registered 11 patents in Republic of Korea. His present h-index (Google Scholar, 01/2019) is 19.

Sam S. Yoon is a Professor of the School of Mechanical Engineering at Korea University since 2005. He received a BS degree from Colorado School of Mines in 1997, MS and Ph.D. degrees in Aeronautics and Astronautics from Purdue University in 1999 and 2002, respectively. He was a Postdoctoral Fellow at the Department of Fire Science and Technology (9132) at Sandia National Laboratory from 2002 to 2005. He was a Visiting Professor at the NREL (National Renewable Energy Laboratory) in 2011. He has so far published over 210 peer-reviewed journal papers in the areas of electronics thermal management, heaters, thermal barrier coatings, supersonic cold spraying, inkjet printing, electrospraying, electrospinning, aerosol deposition, surface modification (superhydrophobic and superhydrophilic), self-cleaning, and self-healing composite materials with focus on energy and environmental applications. His present h-index (Google Scholar, 01/2019) is 32.

Chapter 1
Introduction

In this introductory chapter, the fundamental concepts related to self-healing in nature are introduced and the applications of this phenomenon in engineering materials are outlined. Although natural self-healing is predominantly based on vascular systems, self-healing engineering materials initially used another path. Therefore, the observation of self-healing related to microcapsules and other non-vascular systems are also considered in this section as an introduction to self-healing vascular networks, which are the main focus of this monograph.

The importance of corrosion protection is also highlighted, and a survey of the existing non-vascular methods used to protect metal-framed structures from corrosion is given, as an introduction to the nanotextured vascular self-healing technique, which may overcome several problems characteristic of the existing methods. Intrinsic and extrinsic self-healing techniques are also delineated.

Section 1.1 introduces the first ideas of nature-inspired biomimetic self-healing of the vascular type intended to achieve self-sustained mechanical properties. It also discusses the potentially disastrous consequences of cracking of engineering materials without a self-healing backup. Then, Sect. 1.2 extends the conceptual applicability of self-healing materials into the realm of the corrosion protection. In addition, it introduces the idea of self-healing engineering materials based on vascular macro-, micro- and nanoscale networks containing healing agents. Several specific approaches to self-healing materials of non-vascular, and thus, 'unnatural' type are considered next to illustrate the background on which the nanotextured vascular technique had appeared. Namely, Sect. 1.3 addresses self-healing materials based on microcapsules used for the recovery of mechanical properties or for the maintenance of corrosion protection. It also discusses carbon nanotubes (CNTs) filled with healing agents, which are essentially healing nano-capsules. Vascular networks based on glass pipes and tubing, which are already a step in the biomimetic direction, are outlined in Sect. 1.4. Several additional approaches used to form self-healing engineering materials, in particular, sacrificial materials used to form channels for healing agents and shape-memory polymers, are discussed in brief in Sect. 1.5.

A. L. Yarin et al., *Self-Healing Nanotextured Vascular Engineering Materials*, Advanced Structured Materials 105, https://doi.org/10.1007/978-3-030-05267-6_1

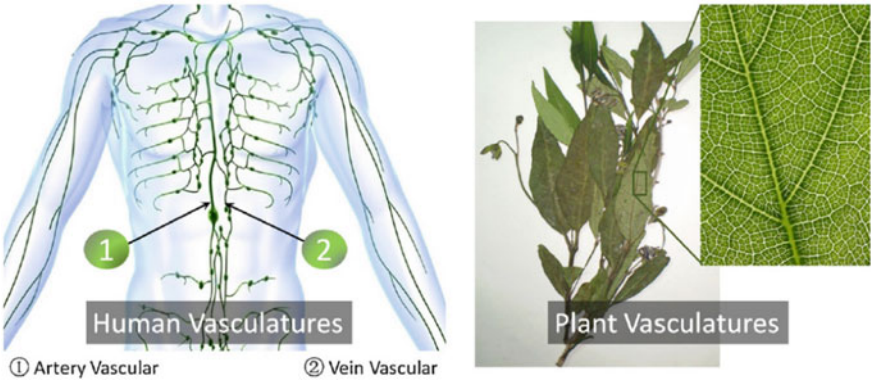

Fig. 1.1 Branching vasculature networks in the human body and plant leaves. Reprinted with permission from Zhang and Li (2016)

1.1 Nature-Inspired Biomimetic Self-Healing for Self-sustained Mechanical Properties

Natural self-healing is a fascinating autonomous phenomenon characteristic of most living organisms. For instance, scratched skin and fractured bones are readily healed because of the activation of the human vascular system. The survival of plants, animals, and human beings is facilitated by their ability to recover from injury. However, this characteristic, though a highly desirable phenomenon, is normally absent in engineering materials. The search for bioinspired self-healing materials that can self-recover their mechanical properties from internal or external damage is illustrated by the work of White et al. (2001). In the case of engineering materials, it is desirable for certain embedded healing agents to be released at the damaged location (e.g., within internal or external microcracks) and solidified there to stitch or conglutinate the ruptured surfaces, in a manner similar to that of blood delivery by capillaries to a wound that triggers the healing process. Nature demonstrates that the key element for self-healing is a vascular capillary network that can carry the healing agent to the damaged location or wound. Thus, nature-inspired self-healing strategies have been explored in biomimetic engineering designs with the goal of repairing structural damage through the systematic transport of healing agents that can be cured and polymerized at the site of damage.

In mammals as well as in the leaves of plants, vascular networks enable the rapid and continuous transport of healing agents to the damaged location (see Fig. 1.1). These effective microvascular systems have network-like structures that cover the entire volume or surface of the body.

Crack-induced accident can cause great damage to engineering materials, which do not possess self-healing features. Very small cracks can experience rapid growth, causing failure of the entire structure. The application of engineering materials in high-risk and high-value structures, e.g., spacecraft, power plants, etc., requires

secondary or tertiary support to preserve the safety of human life and prevent of massive economic losses.

On March 4, 1965, a 32-inch gas transmission pipeline north of Natchitoches, Louisiana, exploded and burned from stress-corrosion cracking (SCC). Seventeen people were killed, including nine children, with at least nine others were injured; seven homes within 450 feet of the explosion were destroyed. State police estimated the damages from the blast and the accompanying fire at ≥$1 M. The same pipeline suffered another explosion only 280 m far from the location of the 1965 one (The Washington Observer 1965).

In 2006 and 2010, NASA inspectors found more than four cracks on the external fuel tank of the space shuttle Discovery, which was covered by insulation foam. Some of the cracks were located on the bracket connecting a liquid oxygen feedline to the fuel tank. Fortunately, the flaw was discovered before the shuttle was launched, and its repair caused a delay of only several weeks (CNN 2010).

Another example is quite peculiar. A football-size hole opened suddenly in the fuselage of Boeing 737 (Southwest Airlines) during a flight from Nashville, Tennessee, to Baltimore, Maryland, forcing an emergency landing in Charleston, West Virginia. Very fortunately, none of the 131 people onboard were injured, but one photograph taken by a passenger vividly illustrates the fear of that moment. Southwest Airlines was ordered to pay $7.5 M for the jets flying with undiagnosed fatigue cracks. However, even with best practices used in pre-flight inspections, miniscule fatigue cracks can remain undetected and cause tremendous damage (Goldsmith 2009).

An alarm bell rang because multiple cracks were present in the core of a nuclear reactor of the Hunterston B plant located in Scotland, UK, in May 2018. The defects were probably irreversible and could not be repaired after their detection. Most ageing plants of 20–40 years in age shall suffer increasing risks of such emergency breakdowns. It should be emphasized that the cracks inherently develop faster than expected, especially under extreme conditions, such as in super-heated reactors or under the effects of earthquakes (Chestney 2018).

The four examples from engineering practice given above demonstrate the necessity of a nature-inspired backup for engineering materials in the form of embedded vascular self-healing elements. A vascular self-repairing system based on hollow tubes was first demonstrated in Dry (1992, 1996). This system was originally proposed for repairing cracks in concrete and restoring its mechanical properties. Subsequently, this approach was expanded to incorporate composite polymeric materials. Healing agents were initially encapsulated within capillaries (e.g., hollow tubes, channels, or electrospun/solution-blown nanofibers). Because the capillaries formed a connected network-like structure, the healing agent could be delivered through this network for multiple localized healing events (Fig. 1.2). The core-shell vascular system containing self-healing agents was advantageous in many respects, with a high healing agent content, outstanding healing agent distribution, and controllable transparency (Kousourakis and Mouritz 2010; Norris et al. 2011; Patrick et al. 2012, 2014; Lee et al. 2014a; An et al. 2015). Electrospun core-shell beads-on-the-string nanofibers (NFs) were first introduced as a vascular system containing self-healing

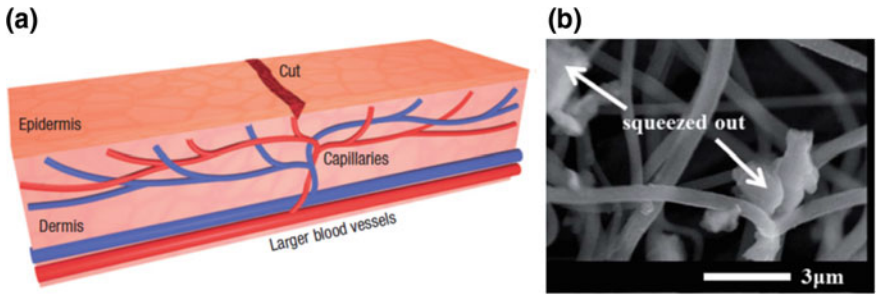

Fig. 1.2 **a** Schematic of capillary network in dermis layer of skin with a cut in the epidermis layer. Reprinted with permission from Toohey et al. (2007). **b** Scanning electron microscopy (SEM) image of self-healing NFs and squeezed-out core (healing) agent. Reprinted with permission from Lee et al. (2014a)

agents by Park and Braun (2010). Then, both the co-electrospinning and the solution blowing of uniform NFs containing self-healing agents were demonstrated by Sinha-Ray et al. (2012), Wu et al. (2013), Wu and Yarin (2013), Lee et al. (2014a, b), An et al. (2015), Lee et al. (2015a, b, 2016a, b, c, 2017). This approach, especially its nanotextured realization, is a focus of this book.

In the framework of this approach, vascular channels with healing agents in their core are embedded in the surrounding matrix, forming self-healing durable composites (Wu et al. 2008; Ghosh 2009; Samadzadeh et al. 2010; Blaiszik et al. 2010; Hager et al. 2010; Binder 2013; Yang and Urban 2013; Wei et al. 2014, 2015; Aissa et al. 2014; Yang et al. 2015; Hillewaere and Du Prez 2015; Thakur and Kessler 2015; Diesendruck et al. 2015; Behzadnasab et al. 2017). The structure of the vascular system and the diameter of the embedded fibers can be controlled using various fabrication methods and manufacturing conditions (Stratmann et al. 1996; Bleay et al. 2001; Pang and Bond 2005a, b; Toohey et al. 2007; Park and Braun 2010; Patrick et al. 2012; Sinha-Ray et al. 2012; White et al. 2014; Lee et al. 2014a, b; An et al. 2015; Doan et al. 2016) . To improve the healing performance in the framework of the vascular self-healing approach, the diameter of the embedded core-shell fibers must be reduced, because the composite strength and resilience against delamination are increased as the cross-sectional diameter decreases (Kousourakis and Mouritz 2010; Sinha-Ray et al. 2013).

1.2 Self-Healing: Extension to Corrosion Protection

Metals, which are strong, shiny, and superior in both electrical and thermal conductivities, have been crucial materials throughout human history. In particular, since the Industrial Revolution in the 18th century, the global demand for metals as raw materials for various products and structures, including buildings, vehicles, electronic devices, pipes, and home appliances, has increased continuously. Nevertheless, the

corrosion of metals, which is a characteristic adverse phenomenon accompanying metal usage in oxygen-containing environments, remains a permanent problem for engineers. Metal-framed products undergo significant degradation because of natural corrosion, which produces metal oxides, which are more chemically stable than the metal itself but highly undesirable from both mechanical and safety-related perspectives.

For example, although modern water supply facilities could meet the increasing demand for clean drinking water in recent decades, rusty metal pipelines have presented a continuous threat to public health (Silva et al. 2017). In addition, corrosion in buildings and bridges can cause significant strength deterioration and severe cracking, which may cause catastrophic failure. A report by the US government estimates the annual expense related to corrosion at $276 billion (Koch et al. 2002). To protect metal-framed structures from corrosion, the cathodic protection method and several types of coatings are commonly used. In the cathodic protection method, a sacrificial metal is corroded instead of the protected one, while with coatings, a multilayered chemical barrier protects the underlying metal (Wei et al. 2015). However, it is necessary to develop alternative protection methods because the galvanic anode (or sacrificial metal) must be replaced regularly, while commonly used coatings rely on toxic chemical barriers that endanger human health and the environment.

Accordingly, several self-healing techniques have been studied actively in recent years as alternative approaches for corrosion prevention, because they can promote the self-recovery of the damaged area without using either a galvanic anode or toxic chemical coatings. The phenomenon of self-healing can occur in two modes: intrinsic and extrinsic (Hager et al. 2010). Intrinsic self-healing is based on the inherent reversibility of materials composed of chemical bonds that can be rearranged by external stimuli (Binder 2013), whereas extrinsic self-healing is activated by the release of intentionally embedded self-healing agents from an encapsulating container after damage. In recent decades, the extrinsic self-healing technique has developed significantly owing to advances in both fabrication and measurement techniques. Specifically, capsules and hollow fibers have been used to form the containers needed to encapsulate the self-healing agents, as is discussed in detail in Chaps. 9 and 10.

1.3 Capsule-Based Approach to Self-Healing

Although nature suggests vascular self-healing systems (Sect. 1.1), one of the first approaches to self-healing engineering composite materials was far from a natural one, because it involved the use of discrete embedded microcapsules instead of a vascular capillary network (White et al. 2001; van der Zwaag 2007; Ghosh 2009). Figure 1.3 illustrates that such capsules are certainly a viable solution; they do not require external energy to trigger the healing process. The capsule size could obstruct their use for interfacial toughening and the prevention of delamination at ply surfaces; miniaturization would be required for these applications. As a first step in

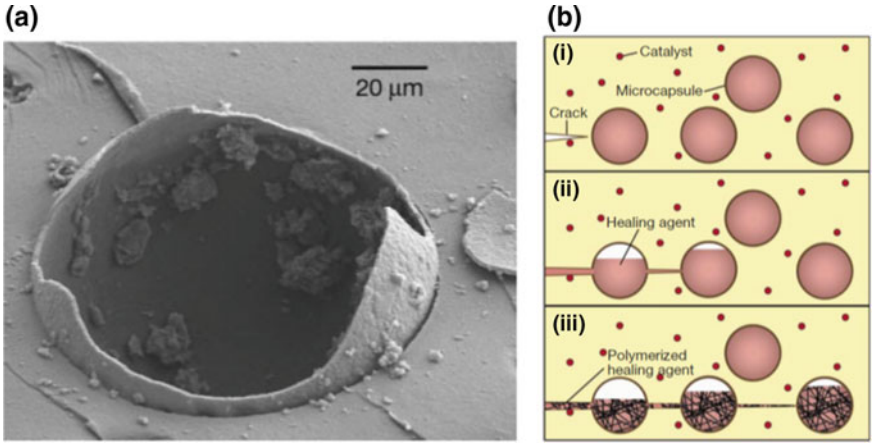

Fig. 1.3 **a** Scanning electron microscopy (SEM) image showing the fracture plane of a self-healing material in which a ruptured urea-formaldehyde microcapsule is embedded in the thermosetting matrix. **b** Concept of autonomic healing: healing agent is encased within the microcapsules, which are embedded in the structural composite matrix containing a catalyst capable of polymerizing the healing agent. In panel **b**: (i) Cracks form in the matrix wherever damage occurs. (ii) Sketch of the crack, which ruptures the microcapsules, releasing healing agent into the crack plane. (iii) Healing agent makes contact with the catalyst dispersed within matrix, triggering polymerization and causing the closure of crack faces. Reprinted with permission from White et al. (2001)

that direction, nanocapsules, namely, carbon nanotubes (CNTs) filled with healing agents, are also considered in this chapter.

1.3.1 Microcapsules Filled with Healing Agents

After White et al. (2001) first introduced a capsule-based self-healing approach, many studies have used the framework of this approach in the past two decades (Ullah et al. 2016). White et al. (2001) reported a process for fabricating microcapsules and examined the self-healing effects resulting from the use of these microcapsules. Subsequently, a similar urea-formaldehyde (UF) polycondensation method (Brown et al. 2003) was used to form microcapsules with an outer diameter of 220 µm (cf. Table 1.1).

In the work of White et al. (2001), microcapsules containing liquid dicyclopentadiene (DCPD; cf. Sect. 2.1) were dispersed in the epoxy matrix, in which Grubbs' catalyst was also embedded [Fig. 1.3b(i)]. When a microcrack had been formed and began propagating in this composite, it also penetrated through the microcapsules. This caused the release of liquid DCPD, which subsequently wetted and infiltrated the crack [Fig. 1.3b(ii)]. As a result, DCPD made contact with the Grubbs' catalyst embedded in the crack banks, triggering a ring-opening metathesis polymerization

Table 1.1 Self-healing based on healing agent-containing capsules

Fabrication method	Shell material	Composite structure	Capsule diameter (μm)	Healing agent	References
UF polycondensation	UF	Epoxy matrix	220 (OD)	DCPD-based, Grubbs' catalyst	White et al. (2001)
UF polycondensation	UF	Epoxy matrix	5–100 (OD)	LO	Suryanarayana et al. (2008)
UF polycondensation	UF	Epoxy matrix	0.75–6 (OD)	LO	Boura et al. (2012)
UF polycondensation with stabilizer	UF	Epoxy matrix	48–138 (OD)	LO	Lang and Zhou (2017)
UF polycondensation/Interfacial polymerization	UF/PU	Epoxy matrix	60 (OD, UF)/90 (OD, PU)	Siloxane-based	Cho et al. (2009)
UF polycondensation	UF	Epoxy matrix	100 (OD)	Silyl ester-based	García et al. (2011)
Interfacial polymerization/In situ sol-gel process	Polyurea/silica	Epoxy matrix	57–328 (OD)	Isocyanate-based	Wu et al. (2014)
Interfacial polymerization	Polyurea	Epoxy matrix	88 (OD)	Isocyanate-based	Sun et al. (2015)
Pickering emulsion polymerization	UF/TiO_2	Epoxy matrix	87–520 (OD)	Epoxy-based	Gao et al. (2015)
Interfacial polymerization	Polyurea/PVA	Epoxy matrix	96 (OD)	Isocyanate-based	He et al. (2017)

UF—urea-formaldehyde, OD—outer diameter, DCPD—dicyclopentadiene, LO—linseed oil, PU—polyurethane, PVA—polyvinyl alcohol

(ROMP) process, which, in turn, caused the formation of a cross-linked network [Fig. 1.3b(iii)]. As a result, the damaged area was stitched.

Corrosion inhibitors, instead of healing agents, can also be encased within microcapsules in order to prevent corrosion (Hager et al. 2016). When the encapsulated corrosion inhibitor is released from the capsules, it makes contact with the surrounding metal and suppresses the electrochemical corrosion reactions that can occur, thereby decreasing the corrosion rate (see Sect. 9.4).

1.3.2 Nanoscale Capsules Filled with Healing Agents

Sinha-Ray et al. (2012) encapsulated healing agents in commercial, as-grown, highly graphitic turbostratic CNTs (PR-24, Pyrograph III). The CNTs contained some iron (<14,000 ppm) and less than 5% moisture, and had inner diameters of 50–100 nm and lengths in the 10–100 μm range. To encapsulate healing agents within CNTs, they used the method of self-sustained diffusion introduced by Bazilevsky et al. (2007, 2008) and Sinha-Ray et al. (2011) for intercalating CNTs at ambient pressure and temperature. In this method empty CNTs were blended with a dilute or semi-dilute solute solution for intercalation [polymers, surfactants, nanoparticles, triglycerides, and wax in Bazilevsky et al. (2007, 2008) and Sinha-Ray et al. (2011), or such healing agents as DCPD and isophorone diisocyanate in the present chapter; cf. Sects. 2.1 and 2.3]. The Fickian diffusion of the solute paired with convection achieve rapid equilibration (within milliseconds) of the solute concentration inside the CNTs with that in the bulk. At this relatively low solute concentration inside the CNTs, the intercalation process would have stopped. However, when a solution with suspended CNTs is left to evaporate (a process requiring minutes to hours), the bulk concentration of the solute gradually increases, because the solvent is lost. The increased solute concentration in the bulk permanently sustains the Fickian diffusion of the solute into the CNTs, which allows their almost complete intercalation, sometimes practically filling nearly the entire CNT bore. The self-sustained diffusion process implemented by Sinha-Ray et al. (2012) to intercalate CNTs with healing agents is discussed below.

CNTs in powder form with a mass of 0.018–0.024 g were added to each of the solutions of DCPD or isophorone diisocyanate in benzene. Then, each solution was sonicated for 30 min and the vials were left open inside a chemical hood to allow all the benzene to evaporate. The benzene evaporation drove the self-sustained diffusion of the solutes (DCPD or isophorone diisocyanate) into the CNTs. After the benzene was completely evaporated, the solute intercalation into the CNTs complete. Then, fresh benzene was added to the vials and sonicated for 3–4 min to clean the outside of the CNTs. Afterward, the content was filtered immediately to isolate the intercalated CNTs with clean outside surfaces.

It should be emphasized that when fresh benzene was added to fully dissolve and clean the solutes deposited outside the CNTs, almost no solute was lost from the inside. Indeed, similarly to Dror et al. (2007), the solute from the interior could be dissolved in this added benzene only through an open CNT cross-section normal to the tube axis. Then, the solute molecules were removed from the dissolution front by Fickian diffusion. As the dissolution front moved into the CNT, the solute gradient in the benzene was decreased as the length from the opening increased. As a result, the solute concentration level near the dissolution front was sustained longer, which, in turn, decelerated the dissolution process. Therefore, with relatively long solute slugs inside relatively long CNTs, the frontal dissolution of solute from the CNT interior quickly became very slow, whereas the dissolution of the solute layer deposited outside the CNT proceeded at a much higher rate and from a much larger area. As a

result, the solute deposited outside the CNTs dissolved much faster than that inside, and the losses of healing agents from the CNTs in the rinsing stage were negligibly small.

The CNT samples intercalated with the healing agents were inspected using transmission electron microscopy (TEM) (see Fig. 1.4), and compared to the CNT image before intercalation, used as the control (Fig. 1.5). Figure 1.4a and b show DCPD intercalated into the CNTs, and Fig. 1.4c and d show isophorone diisocyanate intercalated into the CNTs. Both figures demonstrate that the CNT bores are filled with the healing agents. Furthermore, the exteriors of the CNTs are clean of any deposits, demonstrating that the rinsing process was sufficiently effective. In Fig. 1.4b, the CNT wall is observed to be partially broken by the sonication; the broken location is marked by an arrow. This observation shows that the intercalated amorphous turbostratic CNTs can be easily broken, which facilitates the release of the healing agents. It should be emphasized that all TEM images in Fig. 1.4 were captured over the holes in the holey carbon grid, allowing avoidance of the contrast associated with the carbon film used for support.

1.4 Tube and Channel Networks and Microfibers

Studies on microscopic fiber encapsulation for self-healing have introduced vascular self-healing structures, given the similarity between the hollow fibers and blood vessels (Wang et al. 2015). Before discussing self-healing systems based on micrometer-scale hollow fibers, it should be noted that such fibers were reported before the more recently developed nanometer-scale ones (NFs), which are a focus in this book. Accordingly, most studies on self-healing hollow microfibers (MFs) were reported in the early 2000s, whereas those on hollow NFs (as discussed in detail in Sects. 4.1–4.6) have only appeared in the recent years, mostly since 2012.

Dry (1996) introduced a microscopic hollow-tube-based self-healing technique. He fabricated a thin-pipette-embedded polymeric matrix, wherein the two components of a cyanoacrylate-based adhesive had already been injected into two distinct pipettes (cf. Table 1.2). Cracks were formed artificially in the polymeric matrix either by impact or bending. These cracks were self-repaired by the adhesives released from the pipettes. Then, the two mutually jointed components of the adhesive were solidified by crosslinking, thus preventing both crack formation and growth in the damaged polymeric matrix.

Motuku et al. (1999) developed a vacuum-assisted resin transfer molding process for fabricating microtube-embedded composites (or laminates). They also parametrically investigated the self-healing performance of these composites as functions of the type of tube used, number of tubes embedded in the composite, spatial distribution of the tubes, type of the healing agent injected in the tubes, and composite thickness. Among the various types of tubes and healing agents investigated, 1.15-mm glass micropipettes containing the vinyl ester (VE) resin C50 as the curing agent (cf. Table 1.2) showed the best performance during impact tests.

Table 1.2 Self-healing materials based on micrometer-scale hollow fibers (self-healing efficiency was evaluated through mechanical tests)

Fiber type	Composite structure	Fiber diameter (μm)	Healing agent	Self-healing efficiency (%)	Cycles	References
Thin pipette	Polymeric matrix	Hundreds	Cyanoacrylate-based	Healed	–	Dry (1996)
Glass tube	Laminate	1150 (ID)	Vinyl ester-based	Healed	–	Motuku et al. (1999)
Glass fiber	Polymeric matrix	5 (ID)	Cyanoacrylate-based	Healed	–	Bleay et al. (2001)
Glass fiber	Polymeric matrix	60 (OD)	Amine-epoxy-based	97	–	Pang and Bond (2005a, b)
Microchannel	Polymeric matrix	330 (ID)	Acylhydrazine/methacrylate-based	Healed	–	White et al. (2014)
Microchannel	Epoxy matrix	200 (OD)	DCPD-based, Grubbs' catalyst	70 (at 2nd cycle)	7	Toohey et al. (2007, 2009)
Microchannel	Epoxy matrix	230 (ID)	Amine-epoxy-based	100 (at 5th cycle)	15	Hamilton et al. (2011, 2012)
Microchannel	Epoxy matrix	300 (ID)	Amine-epoxy-based	>100 (at 3rd cycle)	3	Patrick et al. (2014)
PVC tube	Sandwich structure	1500 (ID)	Amine-epoxy-based	Healed	–	Williams et al. (2007, 2008a, b)
Glass fiber	Carbon epoxy matrix	170–680 (ID)	–	Healed	–	Kousourakis and Mouritz (2010)
Microchannel	PU foam	970 (ID)	Isocyanate-based	>100	4	Patrick et al. (2012)
Microchannel	FRP laminate	250, 500 (ID)	Amine-epoxy-based	99	–	Norris et al. (2011, 2012, 2013)

ID—inner diameter, OD—outer diameter, DCPD—dicyclopentadiene, PVC—polyvinyl chloride, PU—polyurethane, FRP—fiber-reinforced polymer

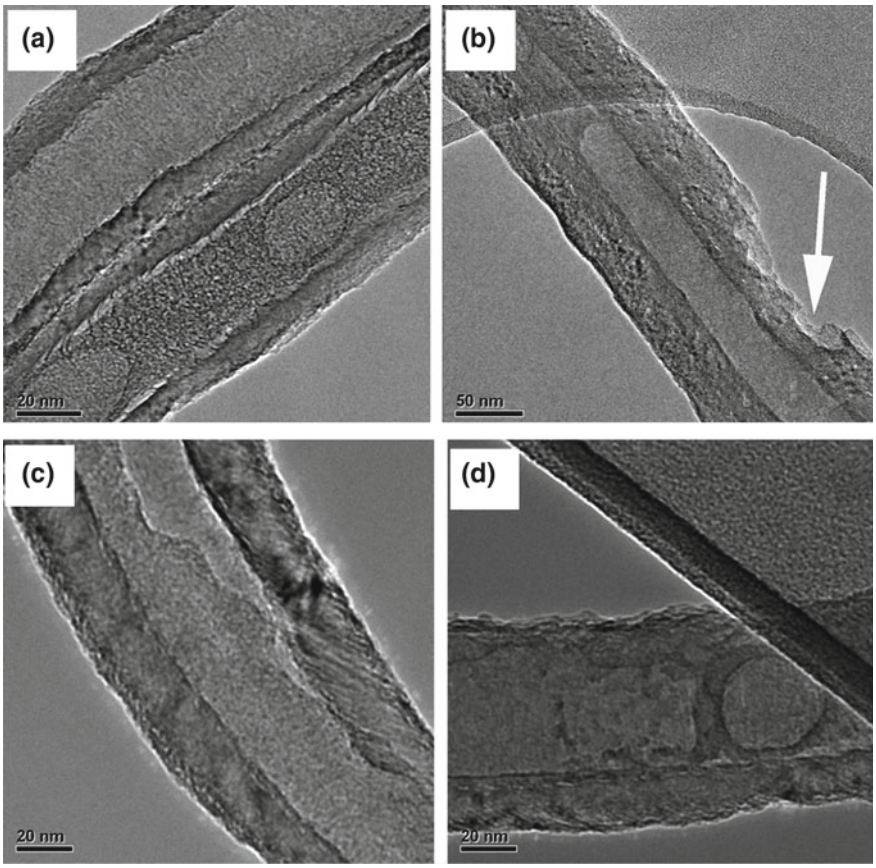

Fig. 1.4 TEM images of intercalated self-healing materials inside CNTs. Panels **a** and **b** show DCPD inside CNTs, while panels **c** and **d** show isophorone diisocyanate inside CNTs. In panel **b**, the arrow indicates the partially broken CNT wall. Reprinted with permission from Sinha-Ray et al. (2012)

Fiber-reinforced composites (FRCs) consist of hollow fibers embedded in a surrounding matrix. The first microscopic vascular-type composites were fabricated by Bleay et al. (2001). They used hollow MFs not only as healing-agent containers but also as structural reinforcements for the fiber-embedding polymeric matrix composite. Hollow glass fibers were incorporated within the composite panels and then impregnated with an epoxy by a vacuum-assisted capillary-action-based filling technique. Based on the assumption that fibers with larger diameters could inadvertently cause the failure of the composite, Bleay et al. (2001) used thinner hollow fibers with inner and outer diameters of 5 and 15 μm, respectively (cf. Table 1.2). In addition, they employed solvent-mixed epoxy resins to reduce the viscosity; this facilitated the rapid release of the resin into the dam-

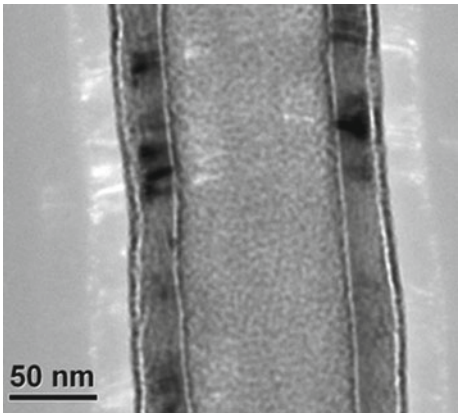

Fig. 1.5 TEM image of an empty CNT before the intercalation of self-healing materials. Reprinted with permission from Sinha-Ray et al. (2012)

aged regions. They also used heating to accelerate the solidification of the released resin. These measures dramatically enhanced the self-healing effect and have been explored extensively by other researchers as well. Bleay et al. (2001) also proposed a method involving the use of both hollow fibers and microcapsules in the polymeric matrix. This method was demonstrated later by Lee et al. (2014b), who used NFs formed by emulsion spinning and capsuleless microdroplets (cf. Sect. 4.3).

Hollow glass fibers, which had diameters in the $10–10^2$ μm range, were used as empty channels in composite laminates and subsequently filled with a healing agent (see Fig. 1.6) (Trask and Bond 2006; Fifo et al. 2014; Yerro et al. 2016). On a larger scale, polyvinylchloride (PVC) tubing (inner/outer diameters of 1.5/2.5 mm) was incorporated in sandwich panels by Williams et al. (2007). Furthermore, empty channels to be filled with resin and hardener were prepared by manually pulling out embedded wires (d = 0.9 mm) from a sandwich composite after an epoxy layer had been cured in mold (Hansen et al. 2009).

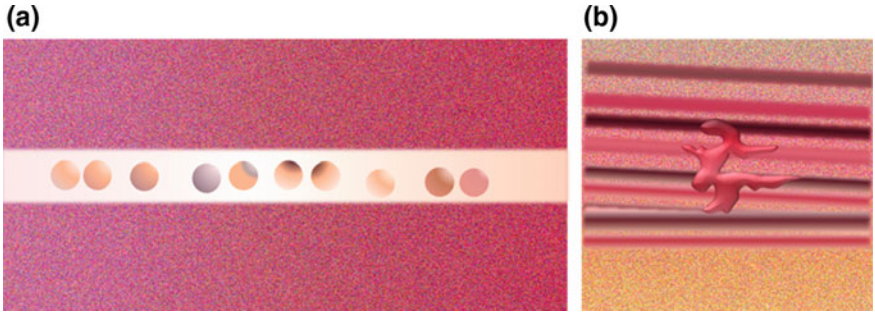

Fig. 1.6 **a** Cross-section of a sample containing empty glass tubes. **b** Sample immediately after impact test; liquid self-healing agent released on the surface can be seen

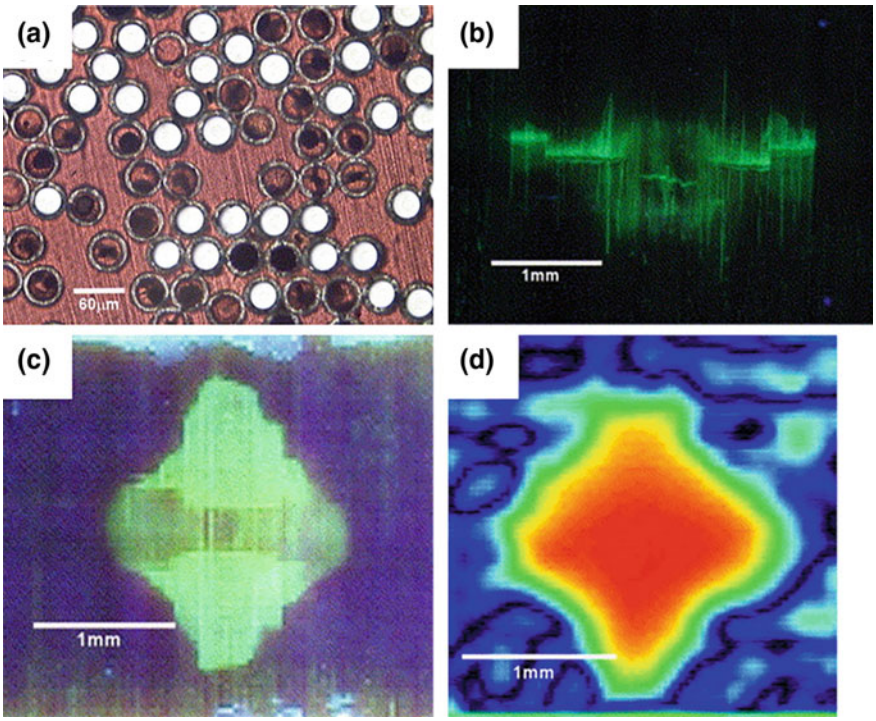

Fig. 1.7 **a** Optical microscopy image of hollow-fiber-embedded composite containing hollow MFs at the volume fraction of 50%. Epoxy-based healing agent is encased within 60-μm MFs. **b** Front and **c** rear images of composite obtained using UVMT. **d** C-scan image of composite. Reprinted with permission from Pang and Bond (2005b)

Fiber-embedded epoxy composites with encased 60-μm hollow glass fibers as 50% of the total volume were fabricated by Pang and Bond (2005a, b), as shown in Fig. 1.7 and Table 1.2. The hollow MFs were filled with an uncured amine-based epoxy resin and a hardener, as well as a UV- fluorescent dye. The dye improved the detection of "bleeding" from the broken hollow MFs into the polymeric composite. They also employed ultrasonic C-scanning and the UV mapping technique (UVMT) to observe otherwise barely visible impact damage, as shown in Fig. 1.7. These techniques are efficient for determining the scope of microscopic damage within fiber-embedded composites.

For large-scale macrocracks, a sufficiently long period is required for the healing agents to harden once they have fully filled the damaged spaces. Otherwise, unhealed microscopic gaps can remain, permitting continuous crack propagation. Large-scale macrocrack healing was investigated by White et al. (2014) using a two-stage polymer chemistry approach. The gelation stage entailed the sufficient filling of the macrocracks. This was followed by the polymerization stage, which was necessary for the solidification of the polymer-filled crack. White et al. (2014)

carefully adjusted the component proportions in the self-healing agent used to ensure that the macrocracks were filled by the agent to a sufficiently high degree, permitting subsequent complete solidification. They found that a macrocrack of 35 mm in diameter could be recovered completely by these two steps of filling and solidification, whose durations were several minutes and a few hours, respectively (cf. Table 1.2; for additional details, see Sect. 8.4).

Multi-cycle healing was investigated by Toohey et al. (2007), who also evaluated the healing efficiency. They fabricated 200-μm 3D polymeric microchannels in a rectangular epoxy matrix. The microchannels were infiltrated with DCPD monomer (cf. Sect. 2.1) and Grubb's catalyst particles were embedded in the surrounding epoxy matrix (cf. Table 1.2). The self-healing process was attributed to the release of the DCPD monomer from the microchannels once they were damaged by a propagating crack and its subsequent contact with the Grubbs' catalyst in the matrix. A continuous release of the self-healing agent from the 3D vascular microstructure and the subsequent ring-opening metathesis polymerization (ROMP) reaction enabled repeatable self-healing, with the healing efficiency of each cycle being 30–70%. This repeatable self-healing process could be repeated for up to seven cycles; in contrast, microcapsule-based self-healing is a single-event process, Toohey et al. (2009). Hamilton et al. (2011, 2012) reported that, when a vascular system consisting of 230-μm microchannels embedded in an epoxy matrix was subjected to active pressurization using external pumps, it exhibited satisfactory healing efficiency for up to 15 cycles (cf. Table 1.2).

Multi-cycle self-healing was also studied by Hansen et al. (2009) and Patrick et al. (2014), who evaluated the self-healing efficiency of 300-μm stitch-like and parallel microchannels (Fig. 1.8 and Table 1.2). The self-healing efficiency of the herring-bone-like stitch-patterned microchannels increased to >100% as the number of cycles was increased, whereas that of the parallel microchannels remained at 35–85%.

Based on the use of different types of structural elements, self-healing materials can be employed in various industrial fields, ranging from vehicles, which have scales of a few meters, to buildings, which have characteristic scales of a few hundred meters. Williams et al. (2007, 2008a, b) studied the effects of a vascular self-healing system on sandwich-structured composites using 1.5-mm PVC tubes (cf. Table 1.2). They showed that, when embedded in composites, this vascular network, comprising tubes filled with either a premixed amine-epoxy resin or an unmixed amine-epoxy resin and a hardener in separate tubes, showed complete healing after flexural failure tests.

Kousourakis and Mouritz (2010) evaluated the vascular self-healing efficiency of carbon-epoxy-based composite panels. They explored the effects of changing the direction of the hollow fibers, which had outer diameters of 170, 320, 430, and 680 μm, from parallel to perpendicular to the direction of loading (cf. Table 1.2). They also conducted mechanical tests in the absence of self-healing agents, in order to examine the changes induced in the mechanical properties solely by the presence of the hollow MFs for reference. While the overall mechanical durability was not affected adversely when the hollow MFs were aligned parallel to the external load, it was reduced significantly when the MFs were oriented normal to the external load.

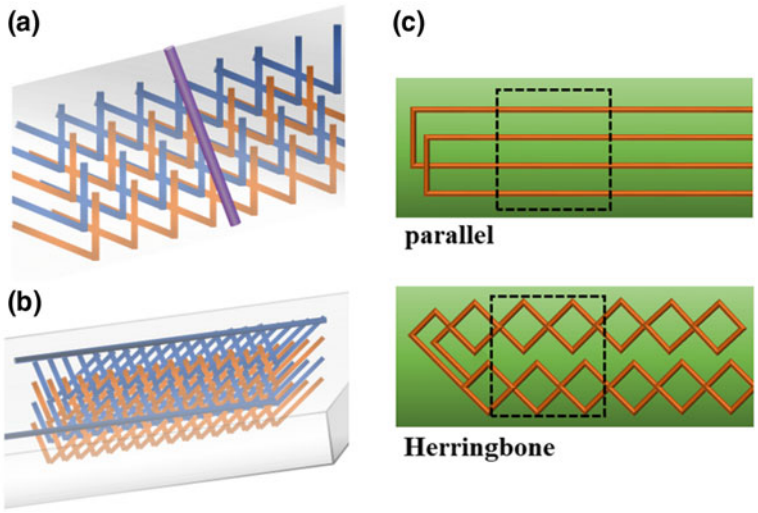

Fig. 1.8 **a** Schematic view of interpenetrating microvascular network supplying two fluids (red and blue) to crack plane, where mixing occurs (purple, at lower borderline). **b** Interpenetrating microvascular network fabricated by direct-write assembly of wax (orange)- and pluronic (blue)-based fugitive inks. **c** Pre-vascularized, fiber-reinforced composite (FRC) laminate samples with sacrificial poly(lactic acid) (PLA) stitching patterns and post-vascularized, X-ray computed micro-tomographic reconstructions of vascular networks filled with eutectic gallium–indium alloy for radiocontrast

Patrick et al. (2012) used polyurethane foam as an encasing composite material to encapsulate isocyanate-based healing agents (cf. Table 1.2). During mechanical tests performed to evaluate the self-healing efficiency of the material, they observed that it allowed for a complete recovery of the mechanical properties in the healed material and could be used for four cycles of self-healing. The microscale porosity of the foam allowed the rapid dispersion of the healing agents because of their good pore wettability and their ready solidification (healing). The microchannels were large in this case (970 μm in diameter). The microchannels were filled with the healing agents using an external pumping system (Fig. 1.9).

Fiber-reinforced polymer (FRP) composites have attracted attention because of their outstanding mechanical strength and stiffness. Such composites also show good durability against mechanical cracking and chemical corrosion (Ku et al. 2011). Accordingly, FRP composites are widely used in the aerospace industry. Norris et al. (2011, 2012, 2013) studied a vascular self-healing system based on aerospace-grade carbon-based FRP laminates, wherein a steel wire with the outer diameter of 500 μm was used to form microchannels in the laminated composite. The microchannels were filled with thiol-epoxy-based healing agents (cf. Table 1.2). They investigated the ability of the system to heal using microchannels with different sizes and placed at different locations. When delamination occurred in the laminated composite under

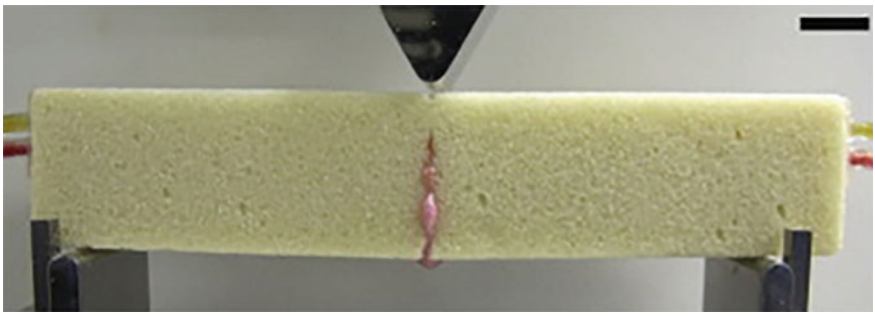

Fig. 1.9 Photograph of vascular self-healing systems in the foam-structured composites after impact damage. It can be seen that the two healing agents (pink color) are released at the damage sites. Reprinted with permission from Patrick et al. (2012)

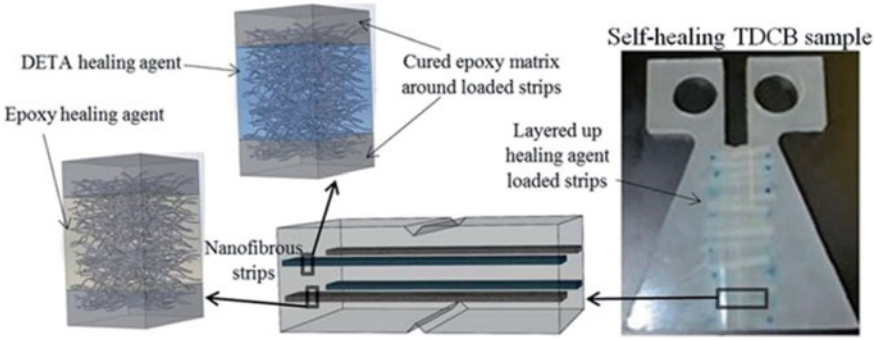

Fig. 1.10 Schematic of preparation method and resulting structure of self-healing specimen produced via impregnation of the inter-fiber pores in electrospun membrane. Reprinted with permission from Vahedi et al. (2015)

external impact, the self-healing agents were released into the delaminated area, allowing self-healing, with an efficiency of >96% for all the tests conducted.

Healing agents have also been encapsulated in the inter-fiber pores (~10 μm in scale) of electrospun fiber mats by immersing the fibers in a liquid epoxy solution (Vahedi et al. 2015). The fiber mats, in turn, were encapsulated within a composite, as shown in Fig. 1.10.

1.5 Sacrificial Materials and Shape-Memory Polymers

Three-dimensional vascular networks can be formed in composites by removing a sacrificial material. A pattern of filaments was formed using fugitive ink, which was subsequently melted and removed from the matrix material (cf. Fig. 1.8a and b) (Hansen et al. 2009). Similarly, poly(lactic acid) (PLA) monofilaments (300 μm in

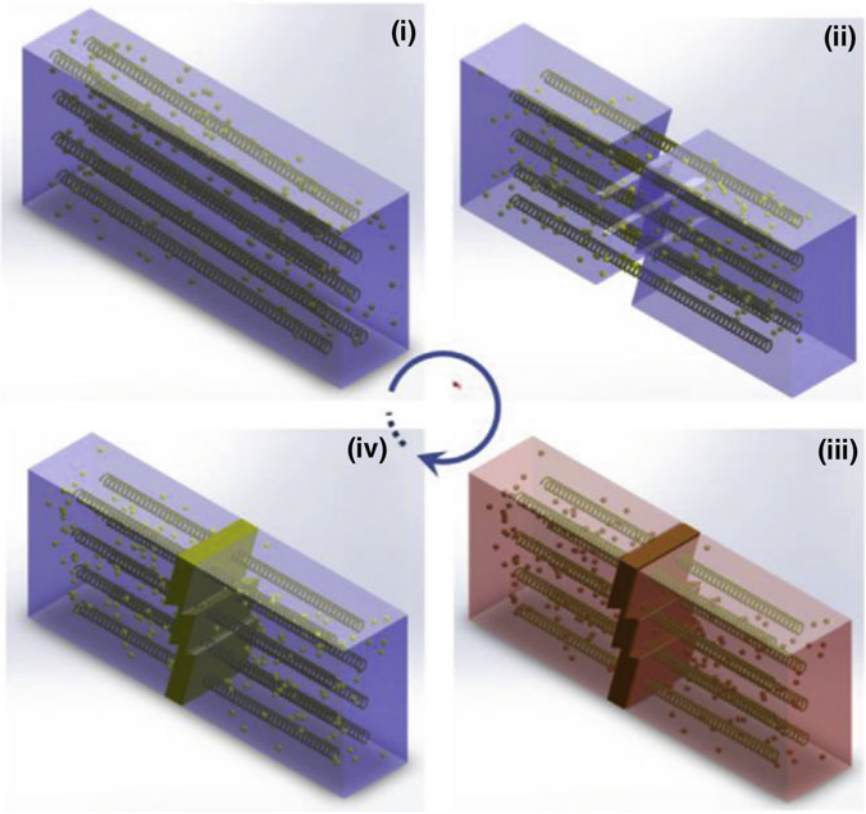

Fig. 1.11 Schematic of the on-demand healing process. Reprinted with permission from Zhang and Li (2015)

diameter) were used as a sacrificial material in Patrick et al. (2014) (see Fig. 1.8c). In these cases, as the sacrificial filaments were removed from the composite by evaporation or after melting, the empty channels were infiltrated by the healing material.

Shape-memory polymer (SMP)-based materials can also be used for the self-healing of emerging macrocracks (Li and John 2008; Li and Uppu 2010; Li and Nettles 2010; Nosonovsky and Rohatgi 2012; Li 2015; Zhang et al. 2016; Champagne et al. 2016). An artificial polymer muscle based on a healing-on-demand composite comprising a thermoset host, commercial fishing line, and thermoplastic particles has been demonstrated by Zhang and Li (2015). This artificial muscle is thermally sensitive and contracts when heated, which allows it to pull portions of a cracked material together. The crack-healing process proceeds via the following stages (see Fig. 1.11): (i) the polymer composite sample to be healed is reinforced by the polymer artificial muscle and the thermoplastic particles (melting temperature of 58–60 °C) in the matrix; (ii) a crack is initiated by an external load during use; (iii) the crack

is closed by the thermal contraction of the artificial muscle (fishing line coil) and healed by the melted particles, which fill the crack under external heating at T = 79 °C; and (iv) after cooling, the crack is filled and cured by the thermoplastic particles, resulting in the re-establishment of continuity between the healing agent and the matrix.

References

Aissa B, Haddad EI, Jamroz W (2014) Self-healing materials: innovative materials for terrestrial & space applications. Smithers Rapra Technologies, Shawbury, Shrewsbury

An S, Liou M, Song KY, Jo HS, Lee MW, Al-Deyab SS, Yarin AL, Yoon SS (2015) Highly flexible transparent self-healing composite based on electrospun core–shell nanofibers produced by coaxial electrospinning for anti-corrosion and electrical insulation. Nanoscale 7:17778–17785

Bazilevsky AV, Sun K, Yarin AL, Megaridis CM (2007) Selective intercalation of polymers in carbon nanotubes. Langmuir 23:7451–7455

Bazilevsky AV, Sun K, Yarin AL, Megaridis CM (2008) Room-temperature, open-air, wet intercalation of liquids, surfactants, polymers and nanoparticles within nanotubes and microchannels. J Mater Chem 18:696–702

Behzadnasab M, Mirabedini S, Esfandeh M, Farnood R (2017) Evaluation of corrosion performance of a self-healing epoxy-based coating containing linseed oil-filled microcapsules via electrochemical impedance spectroscopy. Prog Org Coat 105:212–224

Binder WH (ed) (2013) Self-healing polymers: from principles to applications. Wiley-VCH, Weinheim

Blaiszik B, Kramer S, Olugebefola S, Moore JS, Sottos NR, White SR (2010) Self-healing polymers and composites. Annu Rev Mater Res 40:179–211

Bleay SM, Loader CB, Hawyes VJ, Humberstone L, Curtis PT (2001) A smart repair system for polymer matrix composites. Compos A 32:1767–1776

Boura SH, Peikari M, Ashrafi A, Samadzadeh M (2012) Self-healing ability and adhesion strength of capsule embedded coatings—Micro and nano sized capsules containing linseed oil. Prog Org Coat 75:292–300

Brown EN, Kessler MR, Sottos NR, White SR (2003) In situ poly (urea-formaldehyde) microencapsulation of dicyclopentadiene. J Microencapsul 20:719–730

Champagne J, Pang SS, Li G (2016) Effect of confinement level and local heating on healing efficiency of self-healing particulate composites. Compos B 97:344–352

Chestney N (2018) Cracks in Scottish nuclear reactor core prompt safety checks. Reuters

Cho SH, White SR, Braun PV (2009) Self-healing polymer coatings. Adv Mater 21:645–649

CNN (2010) NASA finds more cracks on Discovery's fuel tank

Diesendruck CE, Sottos NR, Moore JS, White SR (2015) Biomimetic self-healing. Angew Chem Int Ed 54:10428–10447

Doan TQ, Leslie LS, Kim SY, Bhargava R, White SR, Sottos NR (2016) Characterization of core-shell microstructure and self-healing performance of electrospun fiber coatings. Polymer 107:263–272

Dror Y, Salalha W, Avrahami R, Zussman E, Yarin AL, Dersch R, Greiner A, Wendorff JH (2007) One-step production of polymeric micro-tubes via co-electrospinning. Small 3:1064–1073

Dry C (1992) Passive tunable fibers and matrices. Int J Mod Phys B 6:2763–2771

Dry C (1996) Procedures developed for self-repair of polymer matrix composite materials. Compos Struct 35:263–269

Fifo O, Ryan K, Basu B (2014) Glass fibre polyester composite with in vivo vascular channel for use in self-healing. Smart Mater Struct 23:095017

Gao L, He J, Hu J, Wang C (2015) Photoresponsive self-healing polymer composite with photoabsorbing hybrid microcapsules. ACS Appl Mater Interfaces 7:25546–25552
García SJ, Fischer HR, White PA, Mardel J, González-García Y, Mol AJMC, Hughes AE (2011) Self-healing anticorrosive organic coating based on an encapsulated water reactive silyl ester: synthesis and proof of concept. Prog Org Coat 70:142–149
Ghosh SK (ed) (2009) Self-healing materials: fundamentals, design strategies, and applications. Wiley-VCH, Weinheim
Goldsmith S (2009) Southwest Airlines Flight 2294 lands in West Virginia with football-sized hole in fuselage. Daily News; Southwest Airlines Information Regarding Flight 2284. http://www.blogsouthwest.com/news/southwest-airlines-information-regarding-flight-2294/Aviation Safety Network http://aviation-safety.net/database/record.php?id=20110401-0
Hager MD, Greil P, Leyens C, van der Zwaag S, Schubert US (2010) Self-healing materials. Adv Mater 22:5424–5430
Hager MD, van der Zwaag S, Schubert US (eds) (2016) Self-healing materials. Springer, Heidelberg
Hamilton AR, Sottos NR, White SR (2011) Pressurized vascular systems for self-healing materials. J R Soc Interface 2011:1–9
Hamilton AR, Sottos NR, White SR (2012) Mitigation of fatigue damage in self-healing vascular materials. Polymer 53:5575–5581
Hansen CJ, Wu W, Toohey KS, Sottos NR, White SR, Lewis JA (2009) Self-healing materials with interpenetrating microvascular networks. Adv Mater 21:4143–4147
He Z, Jiang S, Li Q, Wang J, Zhao Y, Kang M (2017) Facile and cost-effective synthesis of isocyanate microcapsules via polyvinyl alcohol-mediated interfacial polymerization and their application in self-healing materials. Compos Sci Technol 138:15–23
Hillewaere XK, Du Prez FE (2015) Fifteen chemistries for autonomous external self-healing polymers and composites. Prog Polym Sci 49:121–153
Koch GH, Brongers MPH, Thompson NG, Virmani YP, Payer JH (2002) Corrosion cost and preventive strategies in the United States. NACE International. https://www.nace.org/uploadedFiles/Publications/ccsupp.pdf. Accessed 11 June 2018
Kousourakis A, Mouritz A (2010) The effect of self-healing hollow fibres on the mechanical properties of polymer composites. Smart Mater Struct 19:085021
Ku H, Wang H, Pattarachaiyakoop N, Trada M (2011) A review on the tensile properties of natural fiber reinforced polymer composites. Compos B Eng 42:856–873
Lang S, Zhou Q (2017) Synthesis and characterization of poly (urea-formaldehyde) microcapsules containing linseed oil for self-healing coating development. Prog Org Coat 105:99–110
Lee MW, An S, Jo HS, Yoon SS, Yarin AL (2015a) Self-healing nanofiber-reinforced polymer composites: 1. Tensile testing and recovery of mechanical properties. ACS Appl Mater Interfaces 7:19546–19554
Lee MW, An S, Jo HS, Yoon SS, Yarin AL (2015b) Self-healing nanofiber-reinforced polymer composites: 2. Delamination/debonding, and adhesive and cohesive properties. ACS Appl Mater Interfaces 7:19555–19561
Lee MW, An S, Lee C, Liou M, Yarin AL, Yoon SS (2014a) Self-healing transparent core–shell nanofiber coatings for anti-corrosive protection. J Mater Chem A 2:7045–7053
Lee MW, An S, Lee C, Liou M, Yarin AL, Yoon SS (2014b) Hybrid self-healing matrix using core–shell nanofibers and capsuleless microdroplets. ACS Appl Mater Interfaces 6:10461–10468
Lee MW, Sett S, Yoon SS, Yarin AL (2016a) Fatigue of self-healing nanofiber-based composites: static test and subcritical crack propagation. ACS Appl Mater Interfaces 8:18462–18470
Lee MW, Sett S, Yoon SS, Yarin AL (2016b) Self-healing of nanofiber-based composites in the course of stretching. Polymer 103:180–188
Lee MW, Yoon SS, Yarin AL (2016c) Solution-blown core–shell self-healing nano- and microfibers. ACS Appl Mater Interfaces 8:4955–4962
Lee MW, Yoon SS, Yarin AL (2017) Self-healing nano-textured vascular-like materials: Mode I crack propagation. ACS Appl Mater Interfaces 9:27223–27231
Li G (2015) Self-healing composites: shape memory polymer based structures. Wiley, New York

Li G, John M (2008) A self-healing smart syntactic foam under multiple impacts. Compos Sci Technol 68:3337–3343
Li G, Nettles D (2010) Thermomechanical characterization of a shape memory polymer based self-repairing syntactic foam. Polymer 51:755–762
Li G, Uppu N (2010) Shape memory polymer based self-healing syntactic foam: 3-D confined thermomechanical characterization. Compos Sci Technol 70:1419–1427
Motuku M, Vaidya U, Janowski GM (1999) Parametric studies on self-repairing approaches for resin infused composites subjected to low velocity impact. Smart Mater Struct 8:623–638
Norris CJ, Bond IP, Trask RS (2013) Healing of low-velocity impact damage in vascularised composites. Compos A 44:78–85
Norris CJ, Meadway GJ, O'Sullivan MJ, Bond IP, Trask RS (2011) Self-healing fibre reinforced composites via a bioinspired vasculature. Adv Funct Mater 21:3624–3633
Norris CJ, White JAP, McCombe G, Chatterjee P, Bond IP, Trask RS (2012) Autonomous stimulus triggered self-healing in smart structural composites. Smart Mater Struct 21:094027
Nosonovsky M, Rohatgi PK (2012) Biomimetics in materials science: self-healing, self-lubricating, and self-cleaning materials. Springer, Heidelberg
Pang JWC, Bond IP (2005a) 'Bleeding composites'—damage detection and self-repair using a biomimetic approach. Compos A 36:183–188
Pang JWC, Bond IP (2005b) A hollow fibre reinforced polymer composite encompassing self-healing and enhanced damage visibility. Compos Sci Technol 65:1791–1799
Park JH, Braun PV (2010) Coaxial electrospinning of self-healing coatings. Adv Mater 22:496–499
Patrick JF, Hart KR, Krull BP, Diesendruck CE, Moore JS, White SR, Sottos NR (2014) Continuous self-healing life cycle in vascularized structural composites. Adv Mater 26:4302–4308
Patrick JF, Sottos NR, White SR (2012) Microvascular based self-healing polymeric foam. Polymer 53:4231–4240
Samadzadeh M, Boura SH, Peikari M, Kasiriha S, Ashrafi A (2010) A review on self-healing coatings based on micro/nanocapsules. Prog Org Coat 68:159–164
Silva ACM, Moghadam AD, Singh P, Rohatgi PK (2017) Self-healing composite coatings based on in situ micro–nanoencapsulation process for corrosion protection. J Coat Technol Res 14:1–29
Sinha-Ray S, Lee MW, Sinha-Ray S, An S, Pourdeyhimi B, Yoon SS, Yarin AL (2013) Supersonic nanoblowing: a new ultra-stiff phase of nylon 6 in 20–50 nm confinement. J Mater Chem C 1:3491–3498
Sinha-Ray S, Pelot DD, Zhou ZP, Rahman A, Wu X-F, Yarin AL (2012) Encapsulation of self-healing materials by coelectrospinning, emulsion electrospinning, solution blowing and intercalation. J Mater Chem 22:9138–9146
Sinha-Ray S, Sahu RP, Yarin AL (2011) Nanoencapsulated smart tunable phase change materials. Soft Matter 7:8823–8827
Stratmann M, Leng A, Fürbeth W, Streckel H, Gehmecker H, Groβe-Brinkhaus KH (1996) The scanning Kelvin probe; a new technique for the in situ analysis of the delamination of organic coatings. Prog Org Coat 27:261–267
Sun D, An J, Wu G, Yang J (2015) Double-layered reactive microcapsules with excellent thermal and non-polar solvent resistance for self-healing coatings. J Mater Chem A 3:4435–4444
Suryanarayana CV, Rao KC, Kumar D (2008) Preparation and characterization of microcapsules containing linseed oil and its use in self-healing coatings. Prog Org Coat 63:72–78
Thakur VK, Kessler MR (2015) Self-healing polymer nanocomposite materials: a review. Polym 69:369–383
The Washington Observer (1965) 17 killed as gas line explodes
Toohey KS, Sottos NR, Lewis JA, Moore JS, White SR (2007) Self-healing materials with microvascular networks. Nat Mater 6:581–585
Toohey KS, Sottos NR, White SR (2009) Characterization of microvascular-based self-healing coatings. Exp Mech 49:707–717
Trask RS, Bond IP (2006) Biomimetic self-healing of advanced composite structures using hollow glass fibres. Smart Mater Struct 15:704–710

Ullah H, Azizli KAM, Man ZB, Ismail MBC, Khan MI (2016) The potential of microencapsulated self-healing materials for microcracks recovery in self-healing composite systems: a review. Polym Rev 56:429–485

Vahedi V, Pasbakhsh P, Piao CS, Seng CE (2015) A facile method for preparation of self-healing epoxy composites: using electrospun nanofibers as microchannels. J Mater Chem A 3:16005–16012

van der Zwaag S (ed) (2007) Self healing materials: an alternative approach to 20 centuries of materials science. Springer, Heidelberg

Wang Y, Pham DT, Ji C (2015) Self-healing composites: a review. Cogent Eng 2:1075686

Wei H, Wang Y, Guo J, Shen NZ, Jiang D, Zhang X, Yan J, Zhu J, Wang Q, Shao L (2015) Advanced micro/nanocapsules for self-healing smart anticorrosion coatings. J Mater Chem A 3:469–480

Wei Z, Yang JH, Zhou J, Xu F, Zrínyi M, Dussault PH, Osada Y, Chen YM (2014) Self-healing gels based on constitutional dynamic chemistry and their potential applications. Chem Soc Rev 43:8114–8131

White SR, Moore JS, Sottos NR, Krull BP, Santa Cruz WA, Gergely RCE (2014) Restoration of large damage volumes in polymers. Science 344:620–623

White SR, Sottos NR, Geubelle PH, Moore JS, Kessler MR, Sriram SR, Brown EN, Viswanathan S (2001) Autonomic healing of polymer composites. Nature 409:794–797

Williams HR, Trask RS, Bond IP (2007) Self-healing composite sandwich structures. Smart Mater Struct 16:1198–1207

Williams HR, Trask RS, Weaver PM, Bond IP (2008a) Minimum mass vascular networks in multifunctional materials. J R Soc Interface 5:55–65

Williams HR, Trask RS, Bond IP (2008b) Self-healing sandwich panels: restoration of compressive strength after impact. Compos Sci Technol 68:3171–3177

Wu DY, Meure S, Solomon D (2008) Self-healing polymeric materials: a review of recent developments. Prog Polym Sci 33:479–522

Wu G, An J, Sun D, Tang X, Xiang Y, Yang J (2014) Robust microcapsules with polyurea/silica hybrid shell for one-part self-healing anticorrosion coatings. J Mater Chem A 2:11614–11620

Wu X-F, Rahman A, Zhou Z, Pelot DD, Sinha-Ray S, Chen B, Payne S, Yarin AL (2013) Electrospinning core-shell nanofibers for interfacial toughening and self-healing of carbon-fiber/epoxy composites. J Appl Polym Sci 129:1383–1393

Wu X-F, Yarin AL (2013) Recent progress in interfacial toughening and damage self-healing of polymer composites based on electrospun and solution-blown nanofibers: an overview. J Appl Polym Sci 129:2225–2237

Yang Y, Ding X, Urban MW (2015) Chemical and physical aspects of self-healing materials. Prog Polym Sci 49:34–59

Yang Y, Urban MW (2013) Self-healing polymeric materials. Chem Soc Rev 42:7446–7467

Yerro O, Radojevic V, Radovic I, Petrovic M, Uskokovic PS, Stojanovic DB, Aleksic R (2016) Thermoplastic acrylic resin with self-healing properties. Polym Eng Sci 56:251–257

Zhang P, Li G (2015) Healing-on-demand composites based on polymer artificial muscle. Polymer 64:29–38

Zhang P, Li G (2016) Advances in healing-on-demand polymers and polymer composites. Prog Polym Sci 57:32–63

Zhang P, Ogunmekan B, Ibekwe S, Jerro D, Pang SS, Li G (2016) Healing of shape memory polyurethane fiber-reinforced syntactic foam subjected to tensile stress. J Intell Mater Syst Struct 27:1792–1801

Part I
Materials and Fundamental Physicochemical Phenomena

Chapter 2
Healing Agents Used for Mechanical Recovery in Nanotextured Systems

Several main healing agents currently used in self-healing nanotextured materials are discussed in this section. These include dicyclopentadiene (DCPD) and Grubbs' catalyst (Sect. 2.1) and dimethyl siloxane (DMS, a resin monomer) and dimethyl-methyl hydrogen-siloxane (curing agent) polymerized as poly(dimethyl siloxane) (PDMS, Sect. 2.2). Several other elastomers used for self-healing are discussed in Sect. 2.3. Self-healing agents can also comprise epoxy-hardener systems (Sect. 2.4), and gels (Sect. 2.5). Multiple other materials used in self-healing systems based on different physicochemical principles are omitted here, and the reader is directed to the more comprehensive list compiled in Wypych (2017) and the references therein.

2.1 Dicyclopentadiene (DCPD) and Grubbs' Catalyst

The dicyclopentadiene (DCPD, $C_{10}H_{12}$) monomer has been used in several studies on self-healing, beginning with the original system reported by White et al. (2001), Brown et al. (2004), Mauldin et al. (2007) and Yerro et al. (2016). In self-healing nanotextured materials based on electrospun and solution-blown nanofiber mats, DCPD was used by Sinha-Ray et al. (2012) and Wu et al. (2013). Ring-opening metathesis polymerization (ROMP) is activated as the DCPD monomer makes contact with the solid-state Grubbs' catalyst ($C_{43}H_{72}Cl_2P_2Ru$) dispersed within the epoxy matrix (see Fig. 2.1). The DCPD monomer is highly stable, low in viscosity, and is insensitive to the presence of oxygen and water/humidity under the polymerization conditions (cf. van der Zwaag 2007). In addition, poly(dicyclopentadiene) (PDCPD) is available as a highly crosslinkable polymer with desirable mechanical properties, namely, high toughness and strength (Perring et al. 2010; Lenhardt et al. 2013). It should be emphasized that the need to disperse the solid-state Grubbs' catalyst within the composite matrix introduces an extra technological step in the use of DCPD monomer as a healing agent. This step can be avoided when using other healing agents, such as those discussed below.

A. L. Yarin et al., *Self-Healing Nanotextured Vascular Engineering Materials*, Advanced Structured Materials 105, https://doi.org/10.1007/978-3-030-05267-6_2

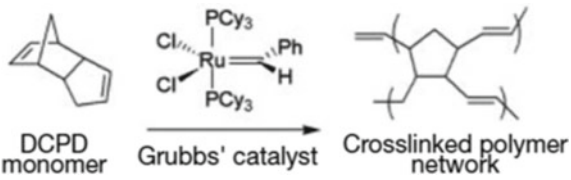

Fig. 2.1 Polymerization of DCPD activated by Grubbs' catalyst. Reprinted with permission from White et al. (2001)

2.2 Poly(Dimethyl Siloxane) (PDMS)

PDMS is the crosslinked product of DMS (the resin monomer) and dimethyl-methyl hydrogen-siloxane (the curing agent). The chemical structure and curing process of PDMS are briefly explained in Fig. 2.2. The resin consists of dimethylvinyl-terminated dimethyl siloxane (CAS: 68083-19-2), while the curing agent consists of dimethyl-methyl hydrogen-siloxane (CAS: 68037-59-2). The resulting silicone elastomer reveals superior mechanical strength and elasticity, outstanding chemical properties, and good biocompatibility; it is used widely in microfluidic devices, medical applications, cosmetics, and food items (as an antifoaming agent). The PDMS elastomer was first used for self-healing in Cho et al. (2006) and Keller et al. (2007), where the two components of PDMS, namely, the resin monomer and the crosslinker (curing agent), were encapsulated within urethane microcapsules. Then, PDMS has also been employed in self-healing nanotextured materials. For example, the encapsulation of PDMS within co-electrospun beaded fibers was reported in Park and Braun (2010) (see Sect. 4.2). Furthermore, PDMS has been also employed in self-healing composites reinforced with nano- and microfibers in Lee et al. (2014a, b, 2015a, b, 2017b, 2018) and An et al. (2015). In the latter series of works, the two components of PDMS were encased separately within the cores of the core-shell [polyacrylonitrile (PAN) shell] fibers by co-electrospinning or emulsion spinning (cf. Sects. 4.2 and 4.3, respectively). This dual self-healing system comprising DMS resin monomer and curing-agent encapsulated in nanofibers was also subsequently used as a healing agent in Neisiany et al. (2016).

2.3 Other Elastomers

Rubber elastomers are also excellent candidates for use in self-healing materials because they offer bonding sites for functional groups on their backbone chains (Rahman et al. 2013). Bromobutyl rubber (BIIR), synthetic material mostly used for automobile tires, also showed the reversible healing of cracks or cut pieces (Das et al. 2015; Lee et al. 2017a). The recovering mechanism is similar to the supramolecular one. Namely, the cut ends of rubber segments are rearranged by dynamic ionic association and thus physically crosslinked to each other. BIIR can be formed as a

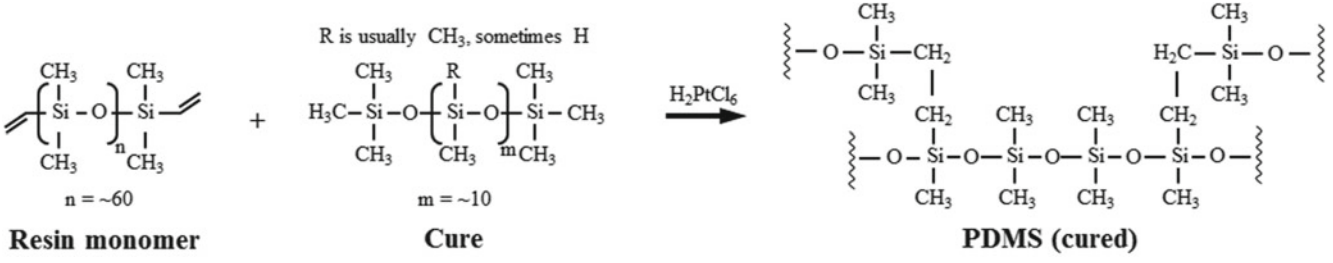

Fig. 2.2 Chemical structure and curing process of PDMS. Reprinted with permission from Campbell et al. (1999)

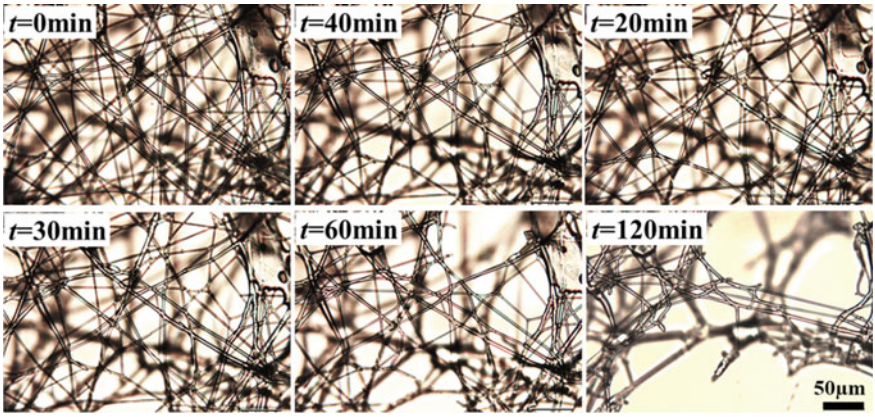

Fig. 2.3 BIIR fibers spun by solution blowing

thin film (Lee et al. 2017a) or a fiber (Fig. 2.3) by solution casting or solution blowing (Sect. 4.4), respectively.

Poly(butyl acrylate) films showed self-healing adhesion as the material coalesced and adhered to the contact interface (Faghihnejad et al. 2014). A low-melting-point polyimide ($T_m < 200$ °C) has been developed for the applications in wire insulation, coatings, and adhesives with self-healing properties (Jolley et al. 2012). Poly(methyl methacrylate) (PMMA) is another thermoplastic material that mechanically heals by the dynamic hydrogen bonding of the polyacrylate-amide (PAA) matrix without external stimuli (Chen and Guan 2015). Hydrogels composed of cellulose nanofibrils, poly(vinyl alcohol) (PVA) and borax have shown autonomous self-repairing abilities by the reformation of mobile hydrogen bonds (Spoljaric et al. 2014).

Polyurethane (PU) is one of the most popular mass-produced plastics. It can be formed as rigid panels or flexible foams for many applications including freezer insulation, mattresses, adhesives, and sports gear, etc. Traditionally PU is obtained by reacting isocyanate with polyol. Isocyanate is another extrinsic self-healing material that recovers broken bonds facilitated by water molecules (Sinha-Ray et al. 2012; Wang et al. 2014). Isophorone diisocyanate (IPDI) and hexamethylene diisocyanate (HDI) encapsulated in PU microcapsules have also been used in protective coatings (Yang et al. 2008; Huang and Yang 2011; Wang et al. 2014; Xiao et al. 2017). These compounds react with water vapor in the atmosphere, and thus show great potential as catalyst-free healing agents. The healing chemistry of diisocyanate monomers in contact with atmospheric moisture as the crosslinking agent is illustrated in Fig. 2.4.

The Diels–Alder reaction was used for heat-stimulated PUs in self-healing polymeric materials (Turkenburg et al. 2015). Acrylated polycaprolactone PUs were used in UV-cured self-healing coatings (Lutz et al. 2015). Zwitterionic multi-shape-memory PUs showed suitable shape-recovery properties (Chen et al. 2015b; cf. Fig. 2.5).

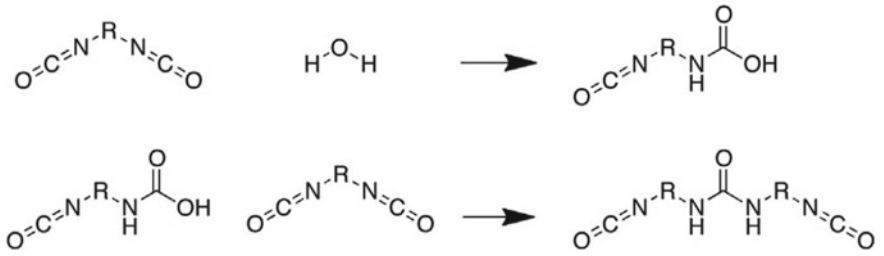

Fig. 2.4 Basic mechanism of moisture-assisted curing of diisocyanate monomers. Reprinted with permission from Keller et al. (2013)

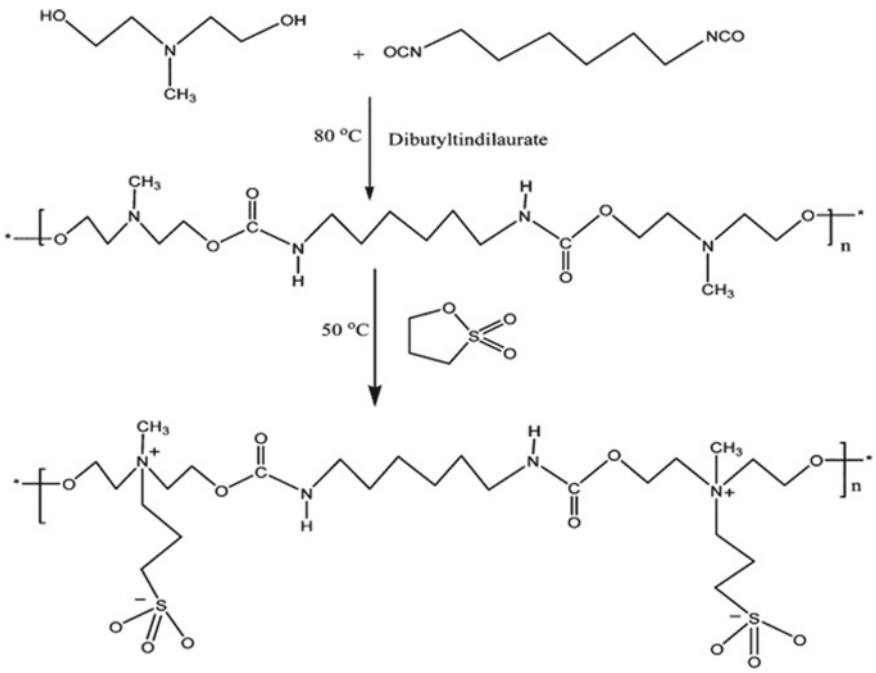

Fig. 2.5 Synthetic route toward zwitterionic shape-memory PUs (Chen et al. 2015b)

Thermoplastic PU containing carbon nanotubes showed autonomous healing requiring no intervention, i.e., an intrinsic healing process without the addition of any healing agents to the composite matrix, and a reversible healing that permits multiple healing events (Harmon and Bass 2014). Commercial polybutadiene can be modified to provide healing ability by the chemical Diels–Alder reaction (Bai et al. 2018; cf. Fig. 2.6), dual crosslinking with a transient network (Gold et al. 2016), and blending with a ring-opening agent (Jasra et al. 2015), among other mechanisms. Poly(ε-caprolactone) functionalized by the Diels–Alder reactions also shows thermo-reversible self-healing. The temperature increase induced by Joule heating

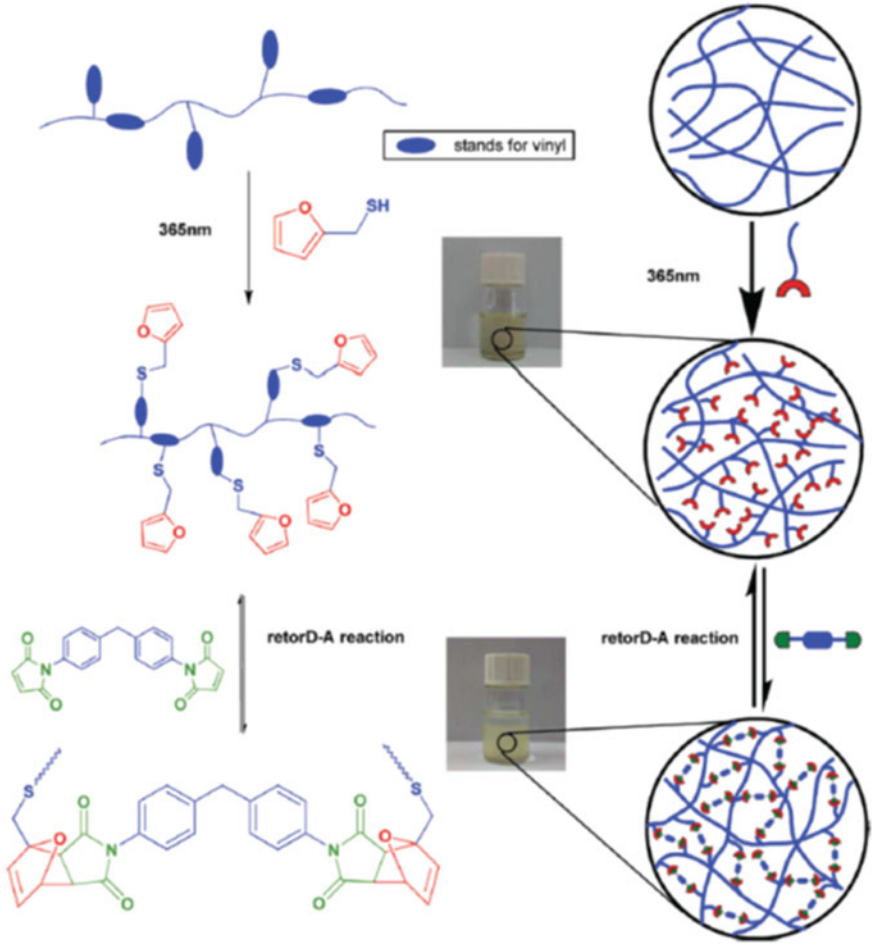

Fig. 2.6 UV reaction process used to prepare recyclable polybutadiene systems (Bai et al. 2018)

promotes chain mobility and heals cracks in the material within 3 min (Willocq et al. 2016).

Shape memory polymers (SMPs) can contract in response to localized heating. Accordingly, SMP fibers embedded in a matrix can span cracks that form in the matrix, essentially acting as springs (Li et al. 2013); see Sect. 1.5. Commercial fishing line and thermoplastic particles have been used to mimic muscles, with the line and particles spanning cracks as springs (Zhang and Li 2015); cf. Sect. 1.5.

2.4 Bisphenol-A-Based Epoxy and Other Types of Epoxy

From the perspective of materials properties, PDMS is among the most attractive self-healing agents owing to its aforementioned advantages. However, it normally requires a period of 24–48 h for full curing at room temperature. Furthermore, cured PDMS is soft and flexible. Accordingly, PDMS is not suitable for many applications, and other self-healing materials with a shorter curing times and higher strengths or greater stiffness are desirable. For this reason, the diglycidyl ether of bisphenol A (DGEBA, $C_{21}H_{24}O_4$), which comprises epichlorohydrin and bisphenol A (BPA, $C_{15}H_{16}O_2$) (Goosey 1985) and constitutes almost 90% of the global epoxy resin market (Raquez et al. 2010), has been used as a healing agent in several studies, mostly using microcapsules (Denq et al. 1999; Garcia et al. 2007; Blaiszik et al. 2009; Chen et al. 2013; Patrick et al. 2014; Jones et al. 2015; Vahedi et al. 2015). The likely reaction mechanism of DGEBA and diethylenetriamine (DETA) is illustrated in Fig. 2.7 (Farquharson et al. 2002). In addition, BPA epoxy resin diluted with neopentyl glycol diglycidyl ether (NGDGE) was used as a healing agent in Vahedi et al. (2015). However, BPA is also being gradually replaced with environmentally friendly materials because of its toxicity and related public health concerns (Flint 2012).

Ultimately, a BPA-based commercial epoxy was also employed as a healing agent embedded within solution-blown nanofibers and self-healing nanotextured materials based on them (Lee et al. 2016a, b, c; Neisiany et al. 2016). The epoxy used in the latter group of works set in 5 min and cures fully within 1 h. Note also that Zhang et al. (2014) and Zhang and Yang (2014) used DETA as an amine curing agent for cure the base epoxy.

Epoxy resins have experienced great development beginning in the early 20th century. Adhesives using epoxy are applied in almost every area of industry and daily life, because they offer reliable chemical and mechanical properties. Moreover, commercial epoxies are excellent candidate healing agents because they have wide ranges of physicochemical properties, such as adhesion strength, set and curing time, working temperature, and shelf-lifetime. The two-component epoxy system comprising a resin and curing agent (hardener) is in common use. Both components are stable and kept separately until they are mixed. Such dual components can be encapsulated in separate capsules, and are cured as the capsules rupture and their contents are mixed together. The healing chemistry and the release and curing process of such healing agents can be controlled by choosing different epoxies. For self-healing applications, the dual components of such epoxies can be stored in hollow tubes (Saeed et al. 2016), nano- or microfibers (Lee et al. 2016a, b) or microcapsules (Zhang et al. 2014) embedded in composite materials. In addition, the acrylic resin elastomer possesses autonomic self-healing ability based on hydrogen bonding entanglement and chain diffusion (Fan and Szpunar 2015). A palm oil-based alkyd was also used as a healing agent for epoxy resin (Shahabudin et al. 2016).

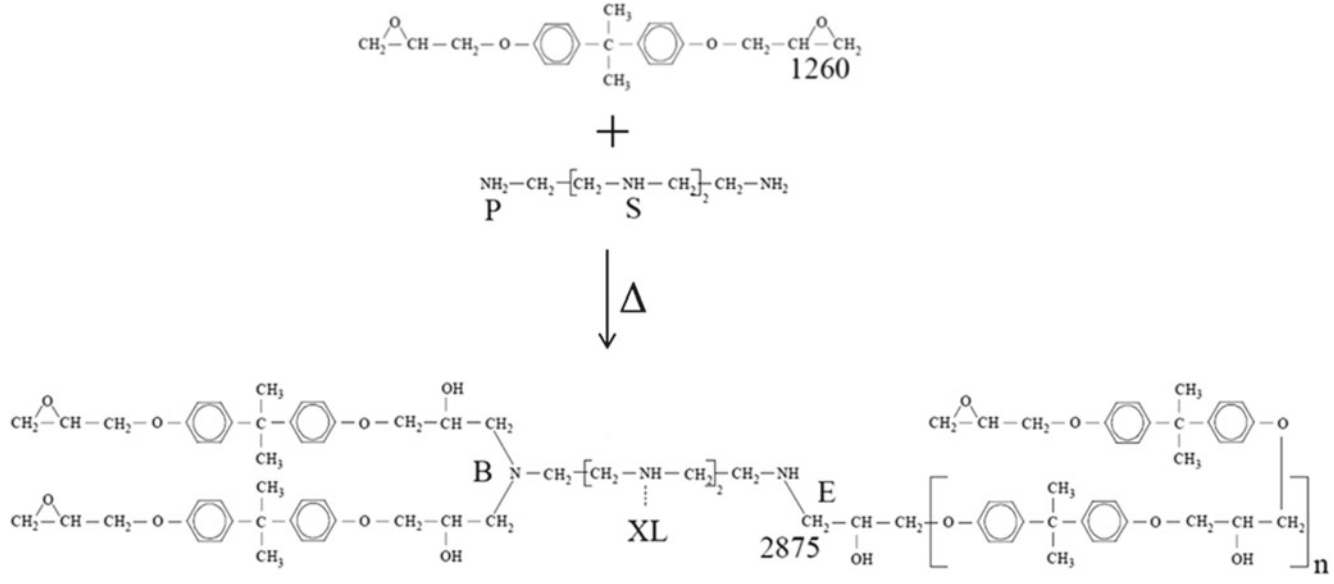

Fig. 2.7 Chemical structures of DGEBA and DETA and the corresponding curing reaction. P is the primary amine, E indicates chain extension, B indicates branching, and XL indicates crosslinking

2.5 Gels

Cellulose, which is suitable for grafting and blending with other materials, can be combined with chitosan to show gel-healing characteristics (Abdul Khalil et al. 2016). As a green material, chitosan is an especially promising candidate for self-healing under UV radiation or changes in pH (Urban and Ghosh 2015; Ou et al. 2015). Supramolecular polymeric hydrogels possess intrinsic self-healing characteristics based on the host–guest interactions, i.e., cyclodextrin and α-bromonaphthalene can act as the host and guest, respectively (Chen et al. 2015a).

White et al. (2014) demonstrated a regenerative-like approach that restored large-scale damage using shape-conforming dynamic gel components (gelator A/B, catalyst, initiator, promoter, and monomer), which are polymerized upon release into a crack.

References

Abdul Khalil HPS, Saurabh CK, Adnan AS, Nurul Fazita MR, Syakir MI, Davoudpour Y, Rafatullah M, Abdullah CK, Haafiz MKM, Dungani R (2016) A review on chitosan-cellulose blends and nanocellulose reinforced chitosan biocomposites: properties and their applications. Carbohydr Polym 150:216–226

An S, Liou M, Song KY, Jo HS, Lee MW, Al-Deyab SS, Yarin AL, Yoon SS (2015) Highly flexible transparent self-healing composite based on electrospun core–shell nanofibers produced by coaxial electrospinning for anti-corrosion and electrical insulation. Nanoscale 7:17778–17785

Bai J, Li H, Shi Z, Yin J (2018) An eco-friendly scheme for the cross-linked polybutadiene elastomer via thiolene and Diels-Alder click chemistry. Macromolecules 48:3539–3549

Blaiszik BJ, Caruso MM, McIlroy DA, Moore JS, White SR, Sottos NR (2009) Microcapsules filled with reactive solutions for self-healing materials. Polymer 50:990–997

Brown EN, White SR, Sottos NR (2004) Microcapsule induced toughening in a self-healing polymer composite. J Mater Sci 39:1703–1710

Campbell DJ, Beckman KJ, Calderon CE, Doolan PW, Ottosen RM, Ellis AB, Lisensky GC (1999) Replication and compression of bulk and surface structures with polydimethylsiloxane elastomer. J Chem Educ 75:537–541

Chen C, Peters K, Li Y (2013) Self-healing sandwich structures incorporating an interfacial layer with vascular network. Smart Mater Struct 22:025031

Chen L, Chen H, Yao X, Ma X, Tian H (2015a) A hybrid supramolecular polymeric hydrogel with rapid self-healing property. Chem Asian J 10:2352–2355

Chen S, Mo F, Yang Y, Stadler FJ, Chen S, Yang H, Ge Z, Zhuo H (2015b) Development of zwitterionic polyurethanes with multi-shape memory effects and self-healing properties. J Mater Chem A 3:2924–2933

Chen Y, Guan Z (2015) Self-healing thermoplastic elastomer brush copolymers having a glassy polymethylmethacrylate backbone and rubbery polyacrylate-amide brushes. Polymer 69:249–254

Cho SH, Andersson HM, White SR, Sottos NR, Braun PV (2006) Polydimethylsiloxane-based self-healing materials. Adv Mater 18:997–1000

Das A, Sallat A, Bohme F, Suckow M, Basu D, Wießner S, Stöckelhuber KW, Voit B, Heinrich G (2015) Ionic modification turns commercial rubber into a self-healing material. ACS Appl Mater Interfaces 7:20623–20630

Denq BL, Hu YS, Chen LW, Chiu WY, Wu TR (1999) The curing reaction and physical properties of DGEBA/DETA epoxy resin blended with propyl ester phosphazene. J Appl Polym Sci 74:229–237

Faghihnejad A, Feldman KE, Yu J, Tirrell MV, Israelachvili JN, Hawker CJ, Kramer EJ, Zeng HB (2014) Adhesion and surface interactions of a self-healing polymer with multiple hydrogen-bonding groups. Adv Funct Mater 24:2322–2333

Fan F, Szpunar J (2015) The self-healing mechanism of an industrial acrylic elastomer. J Appl Polym Sci 132:42135

Farquharson S, Smith W, Rose J, Shaw M (2002) Correlations between molecular (Raman) and macroscopic (rheology) data for process monitoring of thermoset composite. J Process Anal Chem 7:45–53

Flint S, Markle T, Thompson S, Wallace E (2012) Bisphenol A exposure, effects, and policy: a wildlife perspective. J Environ Manage 104:19–34

Garcia FG, Soares BG, Pita VJRR, Sanchez R, Rieumont J (2007) Mechanical properties of epoxy networks based on DGEBA and aliphatic amines. J Appl Polym Sci 106:2047–2055

Gold BJ, Hovelmann CH, Weiss C, Radulescu A, Allgaier J, Pyckhout-Hintzen W, Wischnewski A, Richter D (2016) Sacrificial bonds enhance toughness of dual polybutadiene networks. Polymer 87:123–128

Goosey MT (1985) Epoxide resins and their formulation. In: Goosey MT (ed) Plastics for electronics. Springer, Netherlands, Dordrecht, pp 99–136

Harmon JP, Bass R (2014) Self-healing polycarbonate containing polyurethane nanotube composite. University of South Florida; US Patent 8,846,801 B1, Sep. 30

Huang M, Yang J (2011) Facile microencapsulation of HDI for self-healing anticorrosion coatings. J Mater Chem 21:11123

Jasra R, Maiti M, Srivastava V. (2015) Reliance Industries Limited, US Patent 20150045496, Feb. 12

Jolley ST, Williams MK, Gibson TL, Smith TM, Caraccio AJ, Li W (2012) Self-healing polymer materials for wire insulation, polyimides, flat surfaces, and inflatable structures. National Aeronautics and Space Administration (NASA); Dec. 20

Jones AR, Watkins CA, White SR, Sottos NR (2015) Self-healing thermoplastic-toughened epoxy. Polymer 74:254–261

Keller MW, Hampton K, McLaury B (2013) Self-healing of erosion damage in a polymer coating. Wear 307:218–225

Keller MW, White SR, Sottos NR (2007) A self-healing poly(dimethyl siloxane) elastomer. Adv Mater 17:2399–2404

Lee MW, An S, Jo HS, Yoon SS, Yarin AL (2015a) Self-healing nanofiber-reinforced polymer composites: 1. Tensile testing and recovery of mechanical properties. ACS Appl Mater Interfaces 7:19546–19554

Lee MW, An S, Jo HS, Yoon SS, Yarin AL (2015b) Self-healing nanofiber-reinforced polymer composites: 2. Delamination/debonding, and adhesive and cohesive properties. ACS Appl Mater Interfaces 7:19555–19561

Lee MW, An S, Kim YI, Yoon SS, Yarin AL (2018) Self-healing three-dimensional bulk materials based on core-shell nanofibers. Chem Eng J 334:1093–1100

Lee MW, An S, Lee C, Liou M, Yarin AL, Yoon SS (2014a) Self-healing transparent core–shell nanofiber coatings for anti-corrosive protection. J Mater Chem A 2:7045–7053

Lee MW, An S, Lee C, Liou M, Yarin AL, Yoon SS (2014b) Hybrid self-healing matrix using core−shell nanofibers and capsuleless microdroplets. ACS Appl Mater Interfaces 6:10461–10468

Lee MW, Jo HS, Yoon SS, Yarin AL (2017a) Thermally driven self-healing using copper nanofiber heater. Appl Phys Lett 111:011902

Lee MW, Sett S, An S, Yoon SS, Yarin AL (2017b) Self-healing nano-textured vascular-like materials: Mode I crack propagation. ACS Appl Mater Interfaces 9:27223–27231

Lee MW, Sett S, Yoon SS, Yarin AL (2016a) Fatigue of self-healing nanofiber-based composites: static test and subcritical crack propagation. ACS Appl Mater Interfaces 8:18462–18470

Lee MW, Sett S, Yoon SS, Yarin AL (2016b) Self-healing of nanofiber-based composites in the course of stretching. Polymer 103:180–188

Lee MW, Yoon SS, Yarin AL (2016c) Solution-blown core−shell self-healing nano- and microfibers. ACS Appl Mater Interfaces 8:4955–4962
Lenhardt JM, Kim SH, Nelson AJ, Singhal P, Baumann TF, Satcher JH (2013) Increasing the oxidative stability of poly(dicyclopentadiene) aerogels by hydrogenation. Polymer 54:542–547
Li G, Ajisafe O, Meng H (2013) Effect of strain hardening of shape memory polymer fibers on healing efficiency of thermosetting polymer composites. Polymer 54:920–928
Lutz A, van der Berg O, Damme JV, Verheyen K, Bauters E, Graeve ID, Du Prez FE, Terryn H (2015) A shape-recovery polymer coating for the corrosion protection of metallic surfaces. ACS Appl Mater Interfaces 7:175–183
Mauldin TC, Rule JD, Sottos NR, White SR, Moore JS (2007) Self-healing kinetics and the stereoisomers of dicyclopentadiene. J R Soc Interface 4:389–393
Neisiany RE, Khorasani SN, Lee JKY, Ramakrishna S (2016) Encapsulation of epoxy and amine curing agent in PAN nanofibers by coaxial electrospinning for self-healing purposes. RSC Adv 6:70056–70063
Ou R, Eberts K, Skandan G (2015) Phase separated self-healing polymer coatings. NEI Corporation, US Patent 8,987,352 B1, Mar. 24
Park JH, Braun PV (2010) Coaxial electrospinning of self-healing coatings. Adv Mater 22:496–499
Patrick JF, Hart KR, Krull BP, Diesendruck CE, Moore JS, White SR, Sottos NR (2014) Continuous self-healing life cycle in vascularized structural composites. Adv Mater 26:4302–4308
Perring M, Long TR, Bowden NB (2010) Epoxidation of the surface of polydicyclopentadiene for the self-assembly of organic monolayers. J Mater Chem 20:8679–8685
Rahman MA, Sartore L, Bignotti F, Landro LD (2013) Autonomic self-healing in epoxidized natural rubber. ACS Appl Mater Interfaces 5:1494–1502
Raquez JM, Deleglisea M, Lacrampea MF, Krawczak P (2010) Thermosetting (bio)materials derived from renewable resources: a critical review. Prog Polym Sci 35:487–509
Saeed MU, Li BB, Chen ZF, Cui S (2016) Self-healing of low-velocity impact and mode-I delamination damage in polymer composites via microchannels. Express Polymer Letters 10:337–348
Shahabudin N, Yahy R, Gan SN (2016) Microcapsules of poly(urea-formaldehyde) (PUF) containing alkyd from palm oil. Mater Today Proc 3:S88–S95
Sinha-Ray S, Pelot DD, Zhou ZP, Rahman A, Wu X-F, Yarin AL (2012) Encapsulation of self-healing materials by coelectrospinning, emulsion electrospinning, solution blowing and intercalation. J Mater Chem 22:9138–9146
Spoljaric S, Salminen A, Luong ND, Seppälä J (2014) Stable, self-healing hydrogels from nanofibrillated cellulose, poly(vinyl alcohol) and borax via reversible crosslinking. Eur Polym J 56:105–117
Turkenburg DH, Hv B, Funke B, Schmider M, Janke D, Fischer HR (2015) Polyurethane adhesives containing Diels–Alder-based thermoreversible bonds. J Appl Polym Sci 132:41944
Urban MW, Ghosh B (2015) Self-repairing cyclic oxide-substituted chitosan polyurethane networks. University of Southern Mississippi. US Patent 9,200,089
Vahedi V, Pasbakhsh P, Piao CS, Seng CE (2015) A facile method for preparation of self-healing epoxy composites: using electrospun nanofibers as microchannels. J Mater Chem A 3:16005–16012
van der Zwaag S (ed) (2007) Self healing materials: an alternative approach to 20 centuries of materials science. Springer, Heidelberg
Wang W, Xu L, Li X, Yang Y, An E (2014) Self-healing properties of protective coatings containing isophorone diisocyanate microcapsules on carbon steel surfaces. Corros Sci 80:528–535
White SR, Moore JS, Sottos NR, Krull BP, Cruz WAS, Gergely RCR (2014) Restoration of large damage volumes in polymers. Science 344:620–623
White SR, Sottos NR, Geubelle PH, Moore JS, Kessler MR, Sriram SR, Brown EN, Viswanathan S (2001) Autonomic healing of polymer composites. Nature 409:794–797
Willocq B, Bose RK, Khelifa F, Garcia SJ, Dubois P, Raquez JM (2016) Healing by the Joule effect of electrically conductive poly(ester-urethane)/carbon nanotube nanocomposites. J Mater Chem A 4:4089–4097

Wu X-F, Rahman A, Zhou Z, Pelot DD, Sinha-Ray S, Chen B, Payne S, Yarin AL (2013) Electrospinning core-shell nanofibers for interfacial toughening and self-healing of carbon-fiber/epoxy composites. J Appl Polym Sci 129:1383–1393

Wypych G (2017) Self-healing materials: principles and technology. ChemTec Publishing, Toronto

Xiao Y, Huang H, Peng X (2017) Synthesis of self-healing waterborne polyurethanes containing sulphonate groups. RSC Adv 7:20093

Yang J, Keller MW, Moore JS, White SR, Sottos NR (2008) Microencapsulation of isocyanates for self-healing polymers. Macromol Rapid Commun 41:9650–9655

Yerro O, Radojevic V, Radovic I, Petrovic M, Uskokovic PS, Stojanovic DB, Aleksic R (2016) Thermoplastic acrylic resin with self-healing properties. Polym Eng Sci 56:251–257

Zhang H, Wang P, Yang J (2014a) Self-healing epoxy via epoxy–amine chemistry in dual hollow glass bubbles. Compos Sci Technol 94:23–29

Zhang H, Yang J (2014) Development of self-healing polymers via amine–epoxy chemistry: I. Properties of healing agent carriers and the modelling of a two-part self-healing system. Smart Mater Struct 23:065003

Zhang P, Li G (2015) Healing-on-demand composites based on polymer artificial muscle. Polymer 64:29–38

Zhang X-C, Ji H-W, Qiao Z-X (2014b) Residual stress in self-healing microcapsule-loaded epoxy. Mater Lett 137:9–12

Chapter 3
Macroscopic Observations of Physicochemical Aspects of Self-Healing Phenomena

The spreading of droplets of liquid healing agents on both horizontal and tilted intact surfaces is considered and compared with that on porous nanofiber (NF) mats in Sects. 3.1 and 3.2, respectively. The intact surfaces and NF mats serve as macroscopic models of self-healing engineering materials with vascular networks, where the healing agents have been released from the NFs in a damaged domain. The spreading of droplets on NF mats show significant deviations from that on the intact surfaces because of the imbibition of liquid into the inter-fiber pores. The model macroscopic experiments with a single crack tip in Sect. 3.3 elucidate the self-healing mechanism, namely, that the epoxy resin and hardener released into the tip react with each other, yielding a cured and hardened epoxy that heals the crack tip. Then, in Sect. 3.4, a microfluidic chip-like setup comprising a vascular system of microchannels alternatingly filled with either a resin monomer or a curing agent is used to study the additional intrinsic aspects of the physical healing mechanism in self-healing engineering materials. The model demonstrates that, as a pre-notched crack propagates across the chip, the resin and curing agent are released from the damaged channels, wet the surrounding matrix, spread over the banks of the crack, mix, and finally polymerize. Moreover, the polymerized domains form a system of pillars, which stitch the crack banks on opposite sides, thus preventing further propagation of the crack.

3.1 Spreading of Released Drops of Healing Agents on Horizontal Surfaces

Self-healing materials hold great promise for engineering applications, as concerns relating to the durability, reliability, and sustainability of engineering products have emerged as major issues in various industrial and military applications (Trask et al. 2007; Wu et al. 2008; Samadzadeh et al. 2010; Blaiszik et al. 2010; Hager et al. 2010; Stankiewicz et al. 2013; Binder 2013; Herbst et al. 2013; Yang and Urban 2013; Wei et al. 2014; Yang et al. 2015; Hillewaere and Du Prez 2015; Wei et al. 2015; Thakur

A. L. Yarin et al., *Self-Healing Nanotextured Vascular Engineering Materials*, Advanced Structured Materials 105, https://doi.org/10.1007/978-3-030-05267-6_3

and Kessler 2015; Diesendruck et al. 2015; Bekas et al. 2016; Silva et al. 2017; Behzadnasab et al. 2017). Among the numerous approaches proposed to introduce self-healing properties into engineering materials, the embedded vascular system with encased self-healing agents attracted significant attention for its great potential, as discussed in Sects. 1.1 and 1.4. In works related to core-shell NFs containing self-healing agents, the optimum core-shell NF formation conditions were explored (cf. Chap. 4), as were the recovery of mechanical and adhesive properties, suppression of microcrack growth and propagation, and the corrosion protection performance (cf. Chaps. 7−10). However, the detailed internal mechanisms of self-healing on the macroscopic level accessible to direct observations must also be studied, starting from the release of liquid healing agents from a damaged material and their spreading in vascular NF mats, as it was reported by An et al. (2017a).

3.1.1 Experimental Observations

Two self-healing agents, dimethylvinyl-terminated dimethyl siloxane (DMS, resin monomer) and dimethyl-methyl hydrogen-siloxane (DMHS, curing agent) (see Sect. 2.2) were used in these experiments as the model core agents. They were spreading over NF mats electrospun from polyacrylonitrile [PAN, $M_w = 150$ kDa in the solvent N,N-dimethylformamide (DMF, 99.8%); see Sect. 4.1]. These materials are typically employed for self-healing nanotextured engineering vascular materials based on core-shell NF mats (Lee et al. 2014a, b, 2015a, b, 2016a, b, c; An et al. 2015). To fabricate the NF mats, an 8 wt% PAN solution was prepared first by dissolving PAN in DMF with magnetic stirring for 1 day at room temperature. Then, the PAN solution was supplied to a fixed syringe equipped with an 18-gauge needle using a syringe pump with a flow rate of $Q_{es} = 800$ μl/h. Simultaneously, a high DC voltage of $V_{es} = 12.5$ kV was applied to the needle by using a DC power supply. The PAN solution jet issuing from the needle exit underwent electrically-driven bending instability in flight (Yarin et al. 2014), the accompanying thinning, and solvent evaporation; a dry electrospun NF mat was formed on the collector counter-electrode. The mat thicknesses were in the 33–135 μm range, which is typical for electrospun mats. Varied thicknesses were intended to elucidate the effect of enhanced mat imbibition on the drop spreading and coalescence. During electrospinning, the collector was a drum rotating with the angular speed of 200 rpm. The distance between the needle and the collector was 12 cm. The drum collector was used to form large-area NF mats; each NF mat had an area of 1130 cm^2. This was sufficiently large to conduct all the experiments using samples cut from the same batch. NF mat thicknesses of $h_{NF} = 33 \pm 1.4$, 68 ± 1.5 and 135 ± 1.6 μm were obtained by varying the electrospinning time (t_{es}). Each thickness value was an averaged value, obtained by measuring the thickness at ten different locations on a folded mat and considering the number of folds. The area densities corresponding to the mat thicknesses $h_{NF} = 33 \pm 1.4$, 68 ± 1.5 and 135 ± 1.6 μm were 0.023, 0.047, and 0.069 g/cm^2, respectively. These NF mats were used as one of the substrates in the droplet coalescence

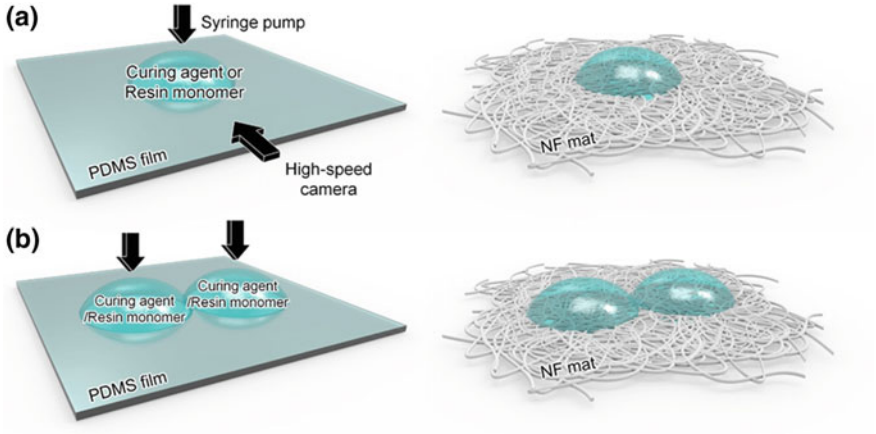

Fig. 3.1 Schematic of **a** the wetting and **b** the coalescence experiments with two droplets, either on PDMS film (left) or NF mat (right). Reprinted with permission from An et al. (2017a)

experiments. A polydimethylsiloxane (PDMS) film, used as another substrate in the droplet coalescence experiments, was formed by mixing the resin monomer and the curing agent solutions at the volume ratio of 10:1 and drying for 48 h at room temperature. Figure 3.1 depicts the experimental process of the wetting and coalescence of droplets of the self-healing agents. In the wetting experiment, either a curing agent or resin droplet dripped from a syringe attached to a syringe pump with a flow rate of $Q_w = 3$ μl/min. The droplets issued from a 23-gauge needle attached to the syringe. The distance between the needle and substrate (PDMS film or NF mats) was 6 mm.

In the coalescence experiments, the curing agent and resin monomer droplets were deposited at different flow rates of $Q_c = 200$ μl/h and $Q_c = 800$ μl/h, respectively. The distance between the needle and the substrates was 7 mm. All wetting and coalescence experiments were performed on stainless steel substrates to flatten the samples and avoid significant wrinkles.

A high-speed camera (Vision Research, USA), which was vertically aligned over the height of the substrate (PDMS film or NF mat) height, was used to observe the spreading droplets. An electronic caliper was used to measure the mat thickness and I'MEASURE software was used to measure the radius (a), the height (h), and the bridge height (H_b) of the droplets. The viscosity (μ) and surface tension (σ) values of the self-healing agents were measured by using a rotational rheometer and a contact-angle analyzer based on the pendant drop method, respectively (Stauffer 1965; Hansen and Rødsrud 1991; Arashiro and Demarquette 1999). The sample temperature during the measurements was maintained at 25 °C. The surface roughness was measured using a non-contacting optical profiler (see Sect. 5.1) and the roughness value (R_q) was calculated by the root-mean-square deviation (RMSD) method.

3.1.2 *Wetting of Self-Healing Agents on Porous Electrospun NFs*

The observed impact velocity (V_0) of droplets onto the substrate (PDMS film and NF mats) was relatively low at $V_0 \approx 0.2$ m/s because of the small nozzle-to-substrate distance (cf. Sect. 3.1.1). At such a low impact velocity, no splashing or bouncing occured (Yarin 2006). Figure 3.2 shows the experimental results for the curing agent and resin monomer droplets spreading over time, t, depending on the NF mat thickness, h_{NF}. The time ranges for the spreading of the curing agent and resin monomer droplets are 0–3 and 0–300 s, respectively.

On the PDMS film and the NF mat with the $h_{NF} = 33$ μm, the radius a of the spreading droplet is gradually increased as t increases, whereas the height (h) of the spreading droplet is decreased (Fig. 3.2a, b, e, f). A different radius trend is observed for the NF mats with higher thicknesses of $h_{NF} = 68$ and 135 μm, compared to that with $h_{NF} = 33$ μm. Namely, on these thicker NF mats, the radius is initially increased but then decreased after t = 1 and 0.5 s, respectively (Fig. 3.2c, d).

These different trends observed in droplet spreading on the thicker NF mats with $h_{NF} = 68$ and 135 μm compared to those on the thinner NF mat with $h_{NF} = 33$ μm and on the PDMS film are attributed to the enhanced effect of porosity in the thicker NF mats. The overall pore volumes in the thicker NF mats are significant, and liquid is gradually absorbed into them. The mats are wetted easily by the resin and curing agent, as illustrated in Fig. 3.3.

The surface roughness of the NF mats is also affected by the electrospinning time, t_{es} (which also affects the thickness h_{NF}), as shown in Table 3.1, where the surface roughness, R_q, is increased from 3.04 to 3.53 μm as h_{NF} increases. The contact surface area between the droplet and the NF mat is increased as R_q increases, which facilitates the absorption of liquid into the NF mats.

For a resin monomer droplet, its footprint a on the mat with $h_{NF} = 68$ μm exhibits a slight increase (Fig. 3.2g). This is also true for the resin monomer droplet on the mat with $h_{NF} = 135$ μm; however, in both these cases, the increase of a with time ceases after the initial increase, and in the latter case a is decreased after t = 100 s (Fig. 3.2h). In addition, the dimensionless capillary numbers ($Ca = \mu U/\sigma$, with U being the edge-spreading velocity) in all cases are similar, namely $Ca \approx 8 \times 10^{-3}$. Such spreading regimes are generally considered as viscosity-dominated rather than capillarity-dominated (Ringrose and Bentley 2015). Furthermore, it should be emphasized that the magnitude of the rate of variation of the droplet height h is increased as the NF mat thickness h_{NF} increases (cf. Fig. 3.2).

Table 3.1 Surface roughness values of NF mats

	NF mat thickness		
	33 μm	68 μm	135 μm
R_q (μm)	3.04	3.13	3.53

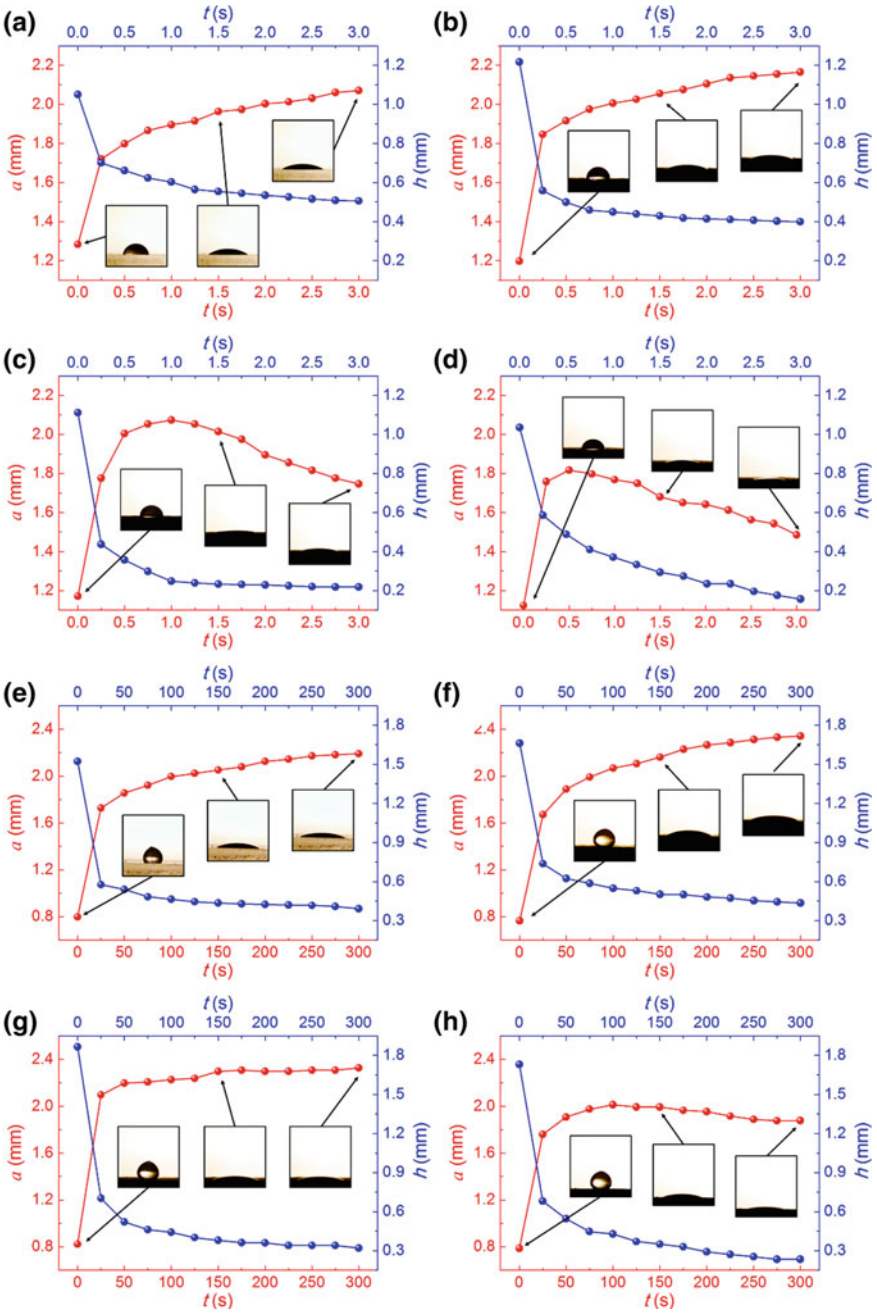

Fig. 3.2 Droplet radius a as a function of time t for (**a**, **c**, **e**, and **g**) the curing agent and (**b**, **d**, **f**, and **h**) the resin monomer droplets spreading on (**a** and **e**) the PDMS film, **b** and **f** the NF mat with $h_{NF} = 33$ μm, **c** and **g** the NF mat with $h_{NF} = 68$ μm, and **d** and **h** the NF mat with $h_{NF} = 135$ μm. Insets show the high-speed camera images of the spreading droplets. Reprinted with permission from An et al. (2017a)

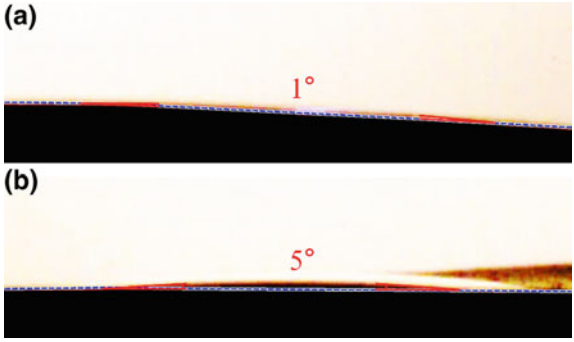

Fig. 3.3 Side-view images showing the static contact angles of **a** the curing agent and **b** the resin monomer on an intact flat PAN film. Reprinted with permission from An et al. (2017a)

3.1.3 Coalescence of Droplets of Self-Healing Agents on Porous Electrospun NFs

Figures 3.4, 3.5 and 3.6 show the side-view images of two coalescing droplets on the PDMS film and the NF mat with $h_{NF} = 68$ μm. Figures 3.4, 3.5 and 3.6 show the coalescence of the curing agent–curing agent, resin monomer–resin monomer, and curing agent–resin monomer droplet pairs, respectively. Unlike the wetting experiments discussed in Sect. 3.1.2, the time ranges for the cases involving the resin monomer (the resin monomer–resin monomer and resin monomer–curing agent cases, shown in Figs. 3.5 and 3.6, respectively) are each 30 s, sufficient for the completion of the coalescence process.

Figure 3.4 shows the coalescence of two droplets of the curing agent on different substrates. On the PDMS film (Fig. 3.4a), the bridge height of the two merging droplets, H_b, is increased until $t = 2$ s and then remains constant after $t = 2$ s. In coalescence on the NF mat with the thickness of $h_{NF} = 68$ μm, H_b is also increased until $t = 1$ s (Fig. 3.4b), but is thereafter decreased. This phenomenon is attributed to the imbibition of liquid into the NF mat as revealed by the wetting experiments (cf. Sect. 3.1.2).

Figure 3.5a, b illustrate the coalescence of two resin monomer droplets on the PDMS film and the NF mat with the thickness of $h_{NF} = 68$ μm, respectively. Similarly to the merging of two curing agent droplets on the PDMS film (cf. Fig. 3.4a), the bridge height H_b is increased until $t = 7.5$ s (image is not shown in Fig. 3.5a). After that, H_b is gradually decreased. On the NF mat with $h_{NF} = 68$ μm (Fig. 3.5b), H_b is also increased until $t = 7.5$ s and thereafter decreased. The comparison of Fig. 3.5a, b reveals slight difference between the two resin monomer droplet coalescence behavior on the PDMS film and the NF mat with the thickness of $h_{NF} = 68$ μm.

Figure 3.6 shows the coalescence of different droplets on different substrates, where the droplet on the left is the curing agent, and that on the right is the resin monomer. Both droplets are initially equal in size. In Fig. 3.6a, the bridge height H_b on the PDMS film is increased until $t = 1$ s (image is not shown in the figure), and then gradually decreased. In Fig. 3.6b, H_b on the NF mat with $h_{NF} = 68$ μm is

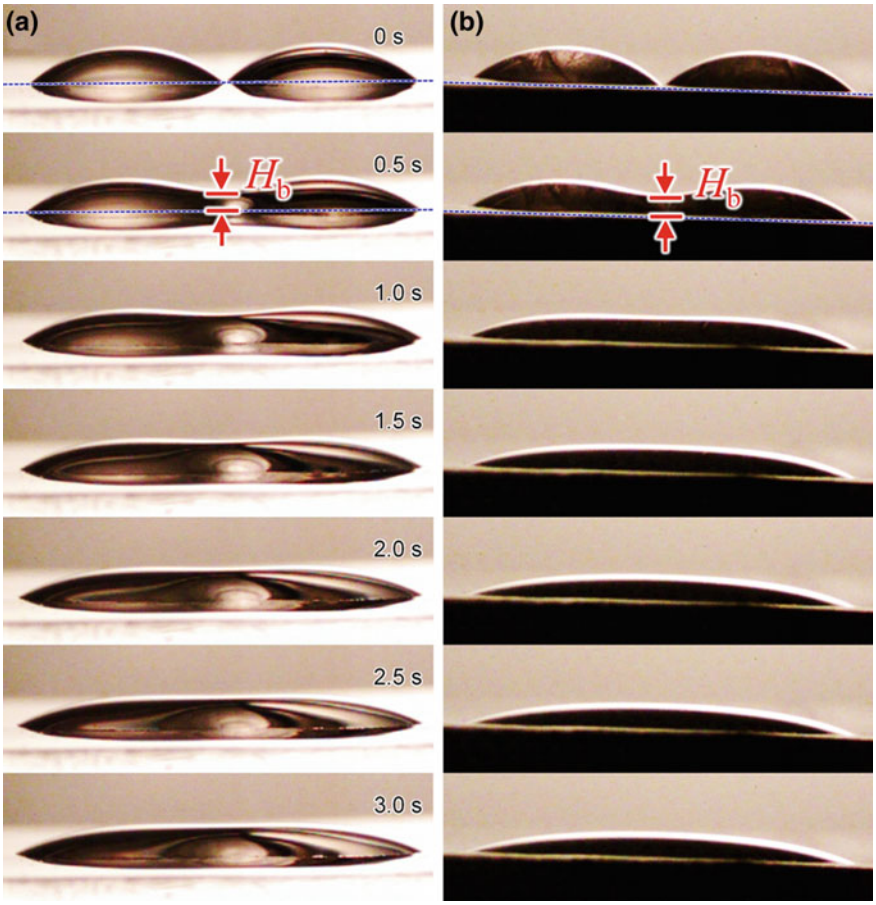

Fig. 3.4 Side-view images of the coalescing curing agent–curing agent droplets at different times on two substrates: **a** the PDMS film and **b** the NF mat with $h_{NF} = 68$ μm. Reprinted with permission from An et al. (2017a)

increased until t = 0.3 s (image is not shown in the figure), and thereafter decreased as well. Despite of the presence of the resin monomer droplet in this pair, here, unlike in Fig. 3.5, a significant decrease in H_b on the NF mat is clearly observed compared to that on the PDMS film (Fig. 3.6a). This is attributed to the lowered overall viscosity because of the mixture of the resin monomer with the curing agent. Therefore, when self-healing agents are released by microcracks from mutually entangled core-shell NFs, the relatively fast polymerization reaction between the curing agent and resin monomer is mainly caused by the fast imbibition of the curing agent into the surrounding matrix (Lee et al. 2014a, b, 2015a, b, 2016a, b, c; An et al. 2015). It should be emphasized that the compressibility of electrospun NF mats under the droplet weight or because of the impact impulse of the droplet, as well as the local redis-

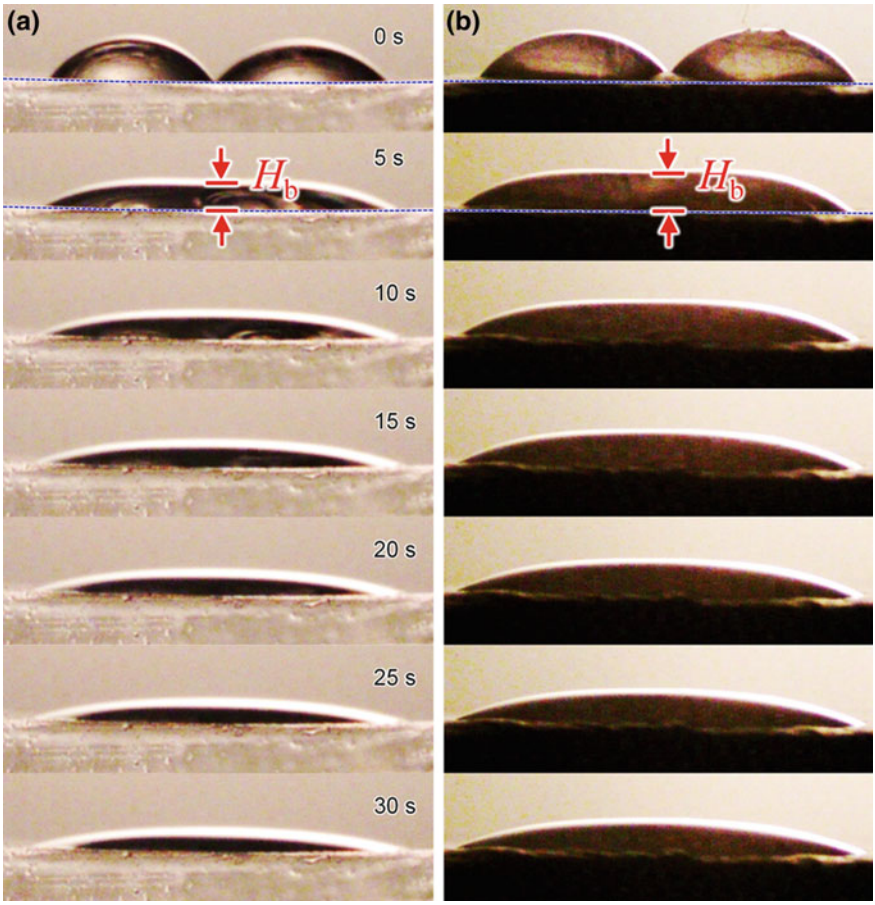

Fig. 3.5 Side-view images of the coalescing resin monomer–resin monomer droplets at different times on two substrates: **a** the PDMS film and **b** the NF mat with $h_{NF} = 68$ μm. Reprinted with permission from An et al. (2017a)

tribution of filament links under the pulling action of the liquid, are both negligibly small, even for droplet impacts with velocities reaching 3.5 m/s (Sahu et al. 2012). This is because the electrospun NF mats are thoroughly entangled on the micrometer scale, two to three orders of magnitude smaller than the droplet size. Accordingly, these effects are even less significant in the present case of soft deposition and slow motion of the droplets on the electrospun NF mats.

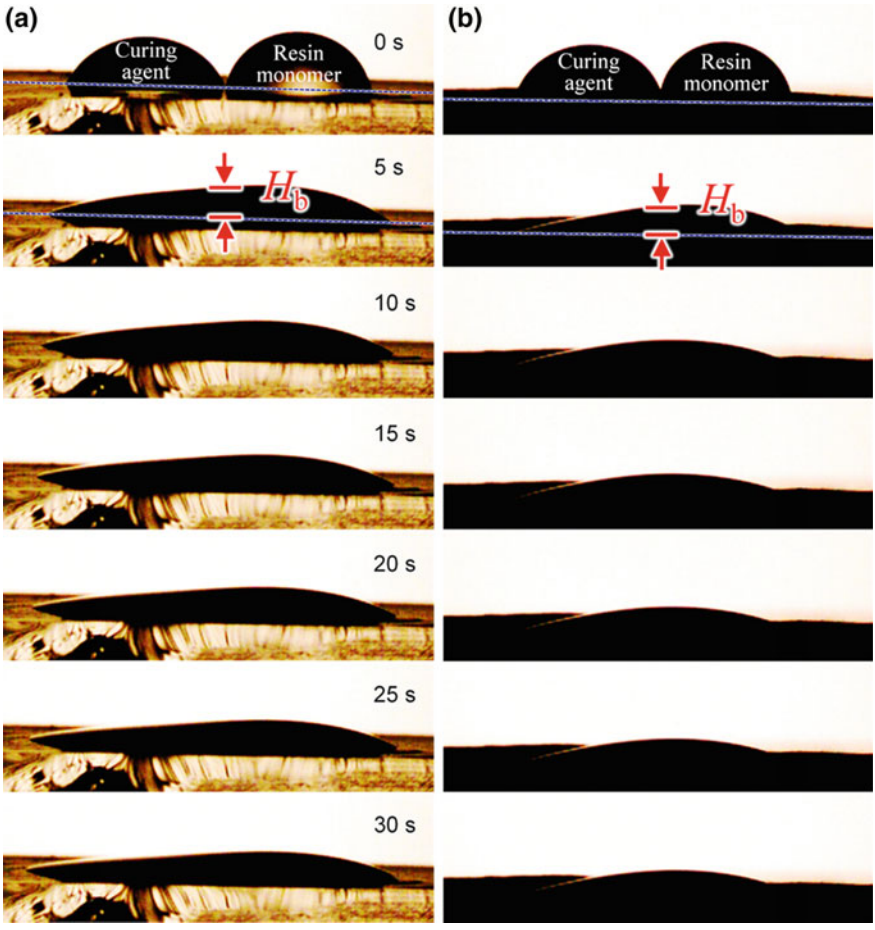

Fig. 3.6 Side-view images of the coalescing curing agent–resin monomer droplet pairs (left–right, respectively) at different times on two substrates: **a** the PDMS film and **b** the NF mat with $h_{NF} = 68\ \mu m$. Reprinted with permission from An et al. (2017a)

3.1.4 The Hoffman–Voinov–Tanner Law and Droplet Footprint Spreading on Wettable Intact Surfaces and NF Mats

To ascertain the hydrodynamic details of the spreading of the released healing agents over NF mats characteristic of self-healing nanotextured vascular materials, the spreading behaviors should be discussed in contrast with those on the intact surfaces. Figure 3.3 reveals that the static contact angles of the curing agent and resin monomer on an intact flat PAN film are approximately 1° and 5°, respectively. On an intact PDMS surface, another important case in the framework of self-healing

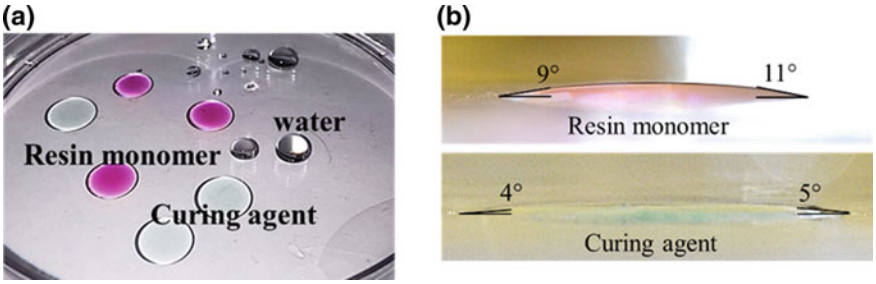

Fig. 3.7 **a** Resin monomer (magenta), curing agent (cyan), and water (transparent) droplets on PDMS surface and **b** static contact angles of resin monomer and curing agent on PDMS surface. As both the resin monomer and the curing agent are transparent, they were dyed using pigments to aid visualization. The colors of the pigments used for dyeing the resin monomer and curing agent are visible as magenta and cyan under certain lighting conditions. The amounts of the pigments used in the resin monomer and curing agent are negligibly small, but the pigments are distinguishable in the Raman spectra of the materials. Reprinted with permission from Lee et al. (2017)

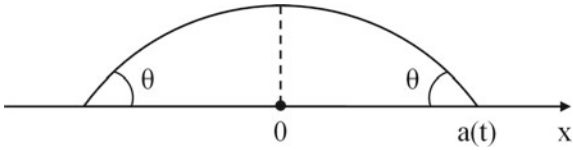

Fig. 3.8 Sketch of an axisymmetric droplet during wettability-driven spreading

materials, the static contact angles of the curing agent and resin monomer remain relatively small, about $\theta_0 = 5°$ and 10°, respectively (Fig. 3.7b). In the first approximation the intact PAN and PDMS substrates can be considered as nearly perfectly wettable by both the curing agent and resin monomer.

The Hoffman–Voinov–Tanner law describes the viscosity-dominated wettability-driven spreading of droplets on perfectly wettable intact substrates with which the liquid droplets show negligibly small static contact angles (Berg 1993). The law relates the current velocity of the contact line motion U during the spreading process to the current contact angle θ in the dimensionless form $Ca = C\theta^3$, where Ca is the capillary number introduced in Sect. 3.1.2, and $C = 0.0107$. In the dimensional form the Hoffman–Voinov–Tanner law reads

$$U = C\frac{\sigma}{\mu}\theta^3 \tag{3.1}$$

where θ should be sufficiently smaller than one.

A spreading axially symmetric droplet is sketched in Fig. 3.8; it can be approximated as a spherical cap. Using the elementary geometric considerations in the limit of $\theta << 1$, the footprint radius a of such a droplet can be expressed through θ as

$$a = \left(\frac{4V}{\pi}\right)^{1/3}\theta^{-1/3} \tag{3.2}$$

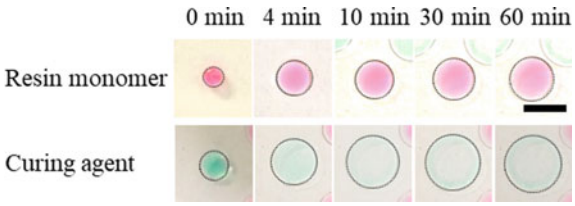

Fig. 3.9 Resin monomer and curing agent droplets spreading on a partially wettable PDMS surface (top view; elapsed times are listed above the images). Scale bar is 5 mm. Reprinted with permission from Lee et al. (2017)

Table 3.2 Properties of resin monomer and curing agent droplets used to acquire experimental data in Figs. 3.9 and 3.10 and their volumes

	σ (mN/m)	μ (Pa·s)	V (μl)
Resin monomer	20.9	5.729	13.8
Curing agent	18.5	0.0717	8.33

with $V = 4\pi a_0^3/3$ being the droplet volume and a_0 being the volume-equivalent droplet radius.

Considering that $U = da/dt$, with t being time, and excluding θ, Eqs. (3.1) and (3.2) yield the following differential equation which describes the footprint radius

$$\frac{da}{dt} = C\frac{\sigma}{\mu}\left(\frac{4V}{\pi}\right)^{1/3}\frac{1}{a^9} \tag{3.3}$$

The initial condition for this equation can be imposed exactly only at a certain remote asymptotic, where θ is already sufficiently small. Regardless, the formal integration with the initial condition $t = 0$, $a = 0$, yields

$$a = \left\{0.107\frac{\sigma}{\mu}\left(\frac{4V}{\pi}\right)^3 t\right\}^{1/10} \propto t^{1/10} \tag{3.4}$$

Note that surface tension σ stands here as a measure of the driving force, the surface tension of the solid-gas interface, as follows from Young's equation.

To verify the applicability of the scaling law $a \propto t^{1/10}$ predicted by Eq. (3.4), the spreading of the resin monomer and curing agent droplets on the PDMS surface is measured, as shown in Fig. 3.9. The corresponding results are compared in Fig. 3.10 with the scaling law predicted by Eq. (3.4). The properties of the resin monomer and curing agent and the droplet volumes used in these experiments are listed in Table 3.2. The experimental data for the axisymmetric droplets agree well with the scaling law following from Eq. (3.4) in the intermediate time range, when the effect of the initial conditions is already "forgotten", whereas the non-zero equilibrium contact angle still does not affect the spreading rate significantly.

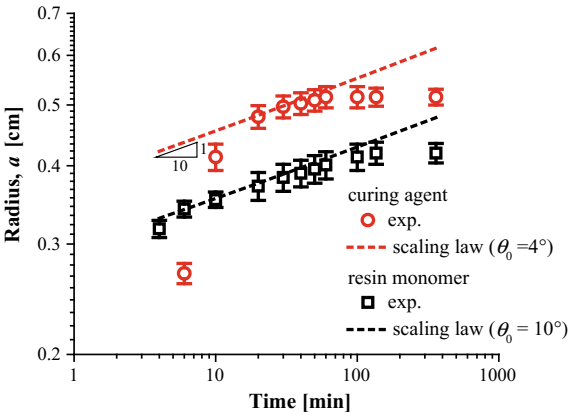

Fig. 3.10 Wettability-driven spreading of resin and cure droplets on PDMS surface. Experimental data are presented by symbols, while the scaling law corresponding to Eq. (3.4) is presented by dashed lines. Reprinted with permission from Lee et al. (2017)

The remarkable agreement of the Hoffman–Voinov–Tanner law with the data for the resin monomer and curing agent in Fig. 3.10 permits its extrapolation toward much shorter times and an elucidation of the healing process on the submicrometer scale. This reveals that the healing action of the resin monomer and curing agent on the length scale of 100–1000 nm is nearly instantaneous, requiring approximately 10^{-50}–10^{-30} s. These spatial and temporal scales cannot yet be measured instrumentally, but the estimate is encouraging regarding the self-healing of NF mats, because it shows that the limiting process is not the wettability-driven spreading, but rather the curing reaction itself, as confirmed by the experiments of Lee et al. (2014b, 2015a, b, 2016a) and An et al. (2015) discussed in Sects. 7, 8, and 10.

The experimental data in Figs. 3.9 and 3.10 were acquired at room temperature in open air. The resin monomer premixed with the curing agent in the ratio of 10:1, requires 24–48 h to cure. This time range is commensurate with the spreading time on the macroscopic scale attempted in these experiments. The spreading time on the submicrometer scale is much shorter, as mentioned above. Therefore, although the mixing of the resin monomer and curing agent released from the NFs proceeds very rapidly (much faster than in the presented model experiments of Figs. 3.9 and 3.10), the time required for the curing process remains on the scale of 1–10 h. It should be emphasized that the curing process can be accelerated at elevated temperatures; the curing time of a similar mixture would be decreased to 35 and 10 min at 100 and 150 °C, respectively.

The experimental results of Fig. 3.2 are compared with the theoretical predictions of the scaling law of Eq. (3.4) in Fig. 3.11 in the log–log scale, where the experimental and theoretical results are presented as solid and short dashed lines, respectively. Figure 3.11a, b show the case of the resin monomer and curing agent droplets on PDMS film. It should be emphasized that the physical properties of the resin monomer and curing agent in the experiments corresponding to Figs. 3.1, 3.2, 3.3, 3.4, 3.5, and 3.6 are slightly different from those listed in Table 3.2; the physical properties are presented in Table 3.3.

Note that the Hoffman–Voinov–Tanner law implies a perfectly wettable substrate, whereas PDMS is a nearly perfectly wettable substrate for the self-healing agents

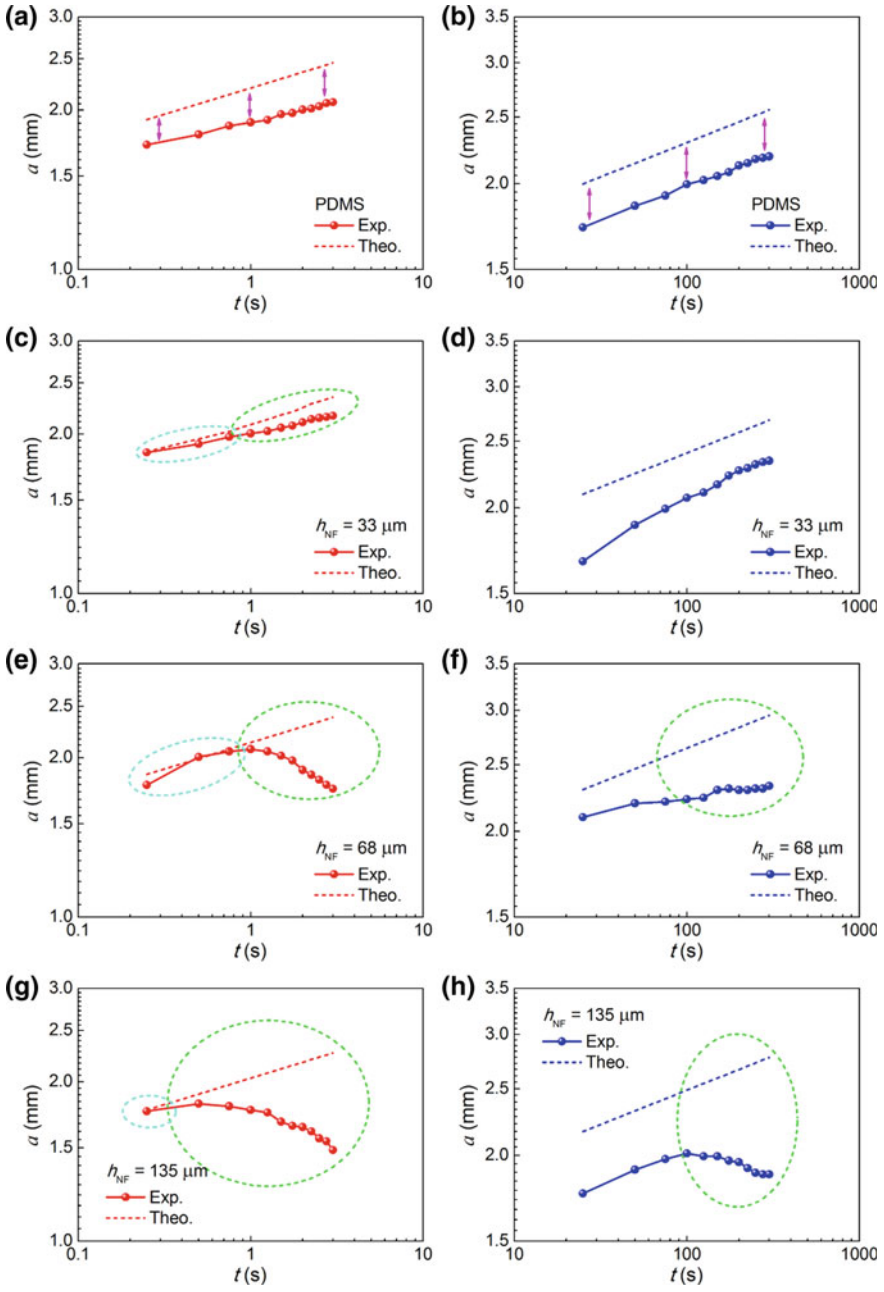

Fig. 3.11 Comparison of the experimental and theoretical values of the radius a as a function of time t for the spreading of (**a**, **d**, **e**, and **g**) curing agent and (**b**, **d**, **f**, and **h**) resin monomer droplets on (**a** and **b**) the PDMS film and (**c**–**h**) the PAN NF mats with different h_{NF}: **c** and **d** $h_{NF} = 33$ μm, **e** and **f** $h_{NF} = 68$ μm, and **g** and **h** $h_{NF} = 135$ μm. Reprinted with permission from An et al. (2017a)

Table 3.3 Viscosities and surface tension values of the curing agent and resin monomer used in the experiments of Figs. 3.1, 3.2, 3.3, 3.4, 3.5, and 3.6; $\dot{\gamma}$ denotes the shear rate in the simple shear experiments used to measure viscosities. The rheological behavior of the cure and resin monomer is close to those of Newtonian fluids

	$\dot{\gamma}$ (s^{-1})	μ (Pa·s)	σ (mN/m)
Curing agent	10	0.06	17.67
	500	0.05	
Resin monomer	10	4.97	23.94
	500	4.59	

(with the static contact angles of about 10° for the resin monomer and 5° for the curing agent). It should be emphasized that Eq. (3.4) is a remote asymptotic. As such, its comparison with experimental data corresponding to a definite initial condition can reveal only a scaling law rather than an overlap of the two lines (thus, the gap shown by arrows in Fig. 3.11a, b; cf. a similar shift in Fig. 3.10), which could cause a slight discrepancy between the theoretical and experimental results. It should be emphasized that the slopes of the experimental and theoretical dependences of a(t) in Fig. 3.11a, b are sufficiently similar.

Figure 3.11c–h show the comparison of the experimental results for curing agent droplets on NF mats of different thicknesses, h_{NF}, with the theoretical predictions of Eq. (3.4). Similarly to the PDMS film case (cf. Fig. 3.11a), the experimental results at early times agree well with the theoretical results obtained from Eq. (3.4) (marked by sky-blue loops in Fig. 3.11c, e, g). Furthermore, the perfect wettability of PAN by the curing agent, with the static contact angle of ~ 1° as revealed in Fig. 3.3a, brings the predictions closer to the experimental data, because it facilitates the rapid spreading corresponding to the remote asymptotic. However, significant deviations (marked by green loops in Fig. 3.11c, e, g) of the data on the NF mats from the predictions of Eq. (3.4) are observed after t = 1 s for the mat thicknesses $h_{NF} = 33$ and 68 μm (Fig. 3.11c, e), and after t = 0.5 s for the mat thickness of $h_{NF} = 135$ μm (Fig. 3.11g). In particular, this trend of deviation is intensified as both the time t and thickness h_{NF} are increased. Over time, it seems that the curing agent is increasingly imbibed by the NF mat bulk. On the other hand, the hydrodynamic relaxation time, $\tau_H \sim \mu/\sigma$, which controls the capillarity-driven flows of highly viscous fluids (the mat imbibition in the present case; Stachewicz et al. 2009), is relatively low for the curing agent, which facilitates its imbibition.

For resin monomer droplets on NF mats, Eq. (3.4) seems to deviate from the data even at earlier times t (Fig. 3.11d, f, h), which is attributed not only to the higher viscosity of the resin monomer compared to that of the curing agent (cf. Table 3.3) but also to the only partial, rather than perfect, wettability of PAN by the resin monomer (Fig. 3.3b, where the static contact angle is ~ 5°). At longer times, the growing disparity between the data and the predictions of Eq. (3.4) indicates resin monomer imbibition into the NF mats, which is not considered by Eq. (3.4) (marked by green loops in Fig. 3.11d, f, h).

3.1.5 Coalescence of Droplets on NF Mats

The wettability-driven suction of liquid into a porous medium can be described using the following diffusion-like equation (Luikov 1964, 1966):

$$\frac{\partial u}{\partial t} = \alpha_m \frac{\partial^2 u}{\partial x^2} \tag{3.5}$$

where u is the dimensionless moisture content, x is the horizontal coordinate with its origin at the droplet center, t is time, and α_m is the moisture transfer coefficient.

The solution of Eq. (3.5) is subjected to the following initial and boundary conditions

$$t = 0: \quad u = f(x) \tag{3.6}$$

$$t > 0: \quad x = \pm\infty, \quad u = 0 \tag{3.7}$$

where f (x) corresponds to the initial moisture distribution on the surface.

The moisture transfer coefficient is associated with wettability-driven liquid transport in the pores (Luikov 1964, 1966). The velocity v of the wettability-driven impregnation of pores can be evaluated using the Lucas–Washburn equation (Lucas 1918; Washburn 1921; Levich 1962; Lembach et al. 2010), $v \sim \sigma d/(8\mu H)$, where perfect wettability is assumed. In this equation, d denotes the characteristic cross-sectional pore diameter, σ the surface tension, μ the viscosity, and H the characteristic pore length. On the other hand, v can be expressed through the moisture transfer coefficient as $v \sim \alpha_m/(4H)$. Accordingly, $\alpha_m \sim d$. The permeability of porous media $k \sim d^2$, whereas the Kozeny–Carman equation (McCabe et al. 1993) relates the permeability to the porosity ε as $k \sim \varepsilon^3/(1-\varepsilon)^2$. Therefore, $d \sim \varepsilon^{3/2}/(1-\varepsilon)$, and thus $\alpha_m \sim \varepsilon^{3/2}/(1-\varepsilon)$. Namely, as the porosity increases, the moisture transfer coefficient increases. This dependence of the moisture transfer coefficient on the porosity reveals the dependence of all the subsequent results on the porosity.

The solution of the problem (3.5)–(3.7) is found as (Tikhonov and Samarskii 1990):

$$u(x,t) = \frac{1}{2\sqrt{\pi}} \int_{-\infty}^{\infty} \frac{1}{\sqrt{\alpha_m t}} \exp\left[-(x-\xi)^2/(4\alpha_m t)\right] f(\xi) d\xi \tag{3.8}$$

where ξ is the dummy variable.

It is assume that the two initial wet spots corresponding to the droplets in this model are fully wet, i.e., $u = 1$ at $t = 0$, at the following two symmetrically located sections: $-\ell - D \le x \le -\ell$ and $\ell \le x \le \ell + D$. At the other locations of the surface, no moisture is present at $t = 0$, i.e., $u = 0$. Note that D corresponds to the droplet size and 2ℓ corresponds to the initial distance between the closest droplet

edges. Accordingly, the function u = f (x) determining the initial distribution of the liquid is fully determined; thus, the integral in Eq. (3.8) can be easily evaluated. This yields

$$u = \frac{1}{2}\{\mathrm{erf}[M(x-\ell)] - \mathrm{erf}[M(x-\ell-1)] + \mathrm{erf}[M(x+\ell+1)] - \mathrm{erf}[M(x+\ell)]\} \tag{3.9}$$

where x and ℓ are rendered dimensionless by D, erf (•) denotes the error function, and the dimensionless function of time M depends on the dimensional time t as

$$M = \frac{D}{2\sqrt{\alpha_m t}} \tag{3.10}$$

Note that M varies from ∞ (which corresponds to t = 0) to 0 (which corresponds to t = ∞).

The experimental observations in Figs. 3.4, 3.5, and 3.6 are thus recast into the dependences of the bridge height H_b on time t as presented in Fig. 3.12. Note that the straight dashed lines in Fig. 3.12 illustrate the scaling trends which are suggested by the first three data points in each graph.

As discussed in Sect. 3.1.3, the bridge height H_b increases at the early times, but then begins to decrease because of the liquid surface rearrangement by surface tension. Surface tension is the only physical factor contributing to droplet coalescence on the intact PAN film. However, in coalescence on NF mat, the imbibition of liquid into the pores also affects the coalescence behavior. This latter factor induces the data deviation from the dashed lines (theoretical prediction), which is much more pronounced on the NF mats than on the intact PDMS film, especially in the curing agent–curing agent and the curing agent–resin monomer cases (Fig. 3.12b, f). The effect is less pronounced for the resin monomer–resin monomer droplets on the NF mat (Fig. 3.12d) because of the diminished imbibition, which arises from the relatively higher viscosity of the resin monomer and lower wettability of PAN by the monomer.

The data presented in Fig. 3.12 can be compared with the predictions of the theoretical Eqs. (3.9) and (3.10). Figure 3.13a, b depict the predicted moisture distributions for two coalescing curing agent–curing agent and resin monomer–resin monomer droplets, respectively, both on NF mat with $h_{NF} = 68\ \mu m$. These plots are obtained from Eqs. (3.9) and (3.10). In particular, the values of M and the initial conditions are established using the experimentally measured geometrical parameters D and ℓ for these two cases.

The results in Fig. 3.13 show that while the predicted values of M are varied from 1 to ~ 0 (meaning that the time t varies from approximately 0 to a certain sufficiently large value), the values of the moisture content u at the center x = 0 (corresponding to the bridge height H_b) in the curing agent–curing agent and resin monomer–resin monomer cases achieve the maximal values of u = 0.18 and 0.22 for M = 0.26 and 0.33, respectively. After these maxima, the values of u at x = 0 begin to decrease and approach 0. This general trend agrees with the experimental observation, although a

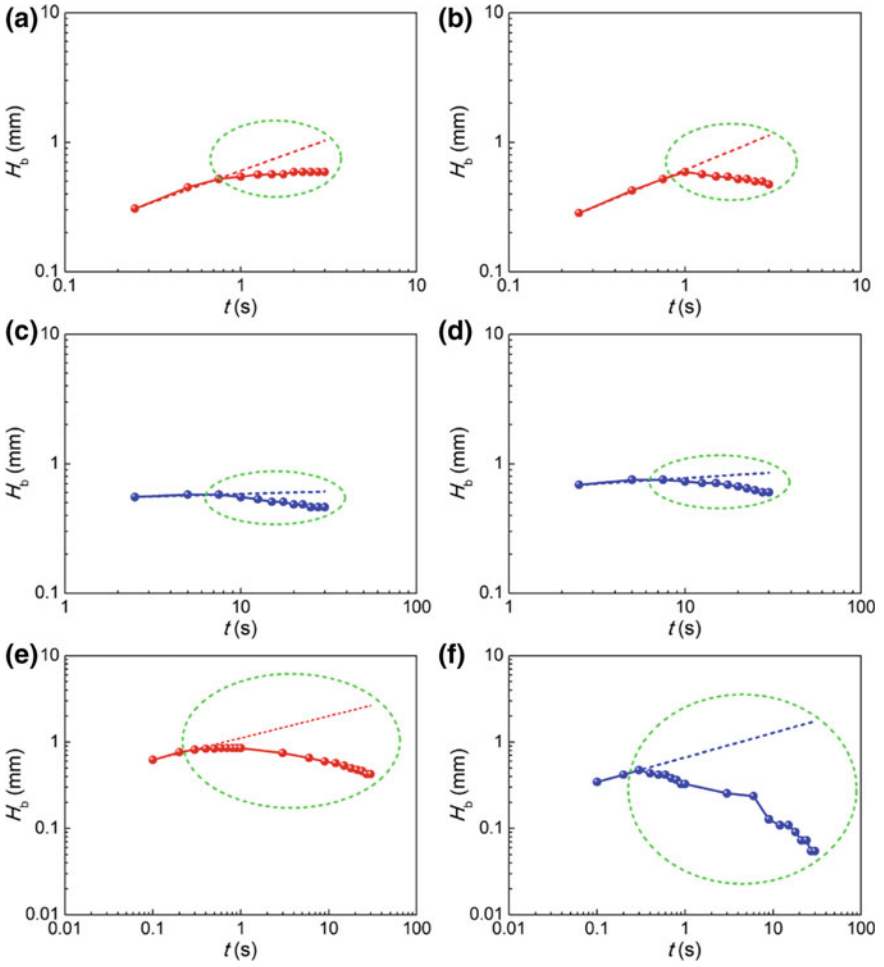

Fig. 3.12 The bridge height H_b as a function of time t for two coalescing (**a** and **b**) curing agent–curing agent, **c** and **d** resin monomer–resin monomer, and **e** and **f** curing agent–resin monomer droplets on (**a**, **c**, and **e**) an intact PDMS film and (**b**, **d**, and **f**) on the NF mat with $h_{NF} = 68$ μm. The data for the curing agent–curing agent, resin monomer–resin monomer and curing agent–resin monomer droplet pairs correspond to Figs. 3.4, 3.5, and 3.6, respectively. Reprinted with permission from An et al. (2017a)

detailed fit of the theory to the experimental data is possible only when the moisture transport coefficient α_m is selected appropriately. Accordingly, one finds the values of $\alpha_m = 1.2 \times 10^{-1}$ and 6×10^{-3} cm^2/s are appropriate for the curing agent–curing agent and resin monomer–resin monomer cases, respectively, for the NF mats with $h_{NF} = 68$ μm.

Figure 3.14 shows the comparison of the theory with the experimental data. In particular, Fig. 3.14a, b illustrate the unmatched values of the theoretically predicted

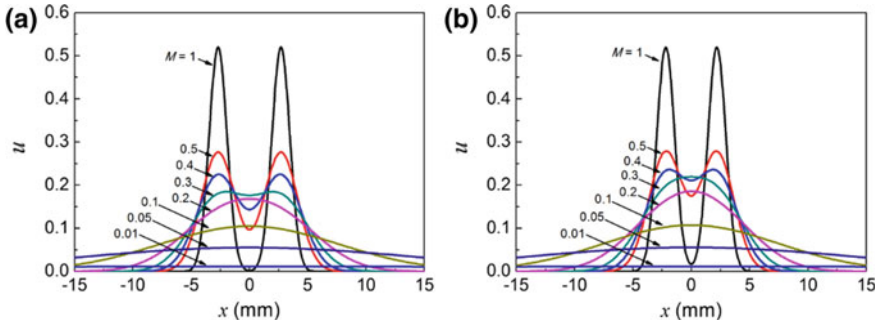

Fig. 3.13 Moisture distributions predicted using Eqs. (3.9) and (3.10) for two coalescing **a** curing agent–curing agent and **b** resin monomer–resin monomer droplet pairs on the NF mat with $h_{NF} =$ 68 μm. Reprinted with permission from An et al. (2017a)

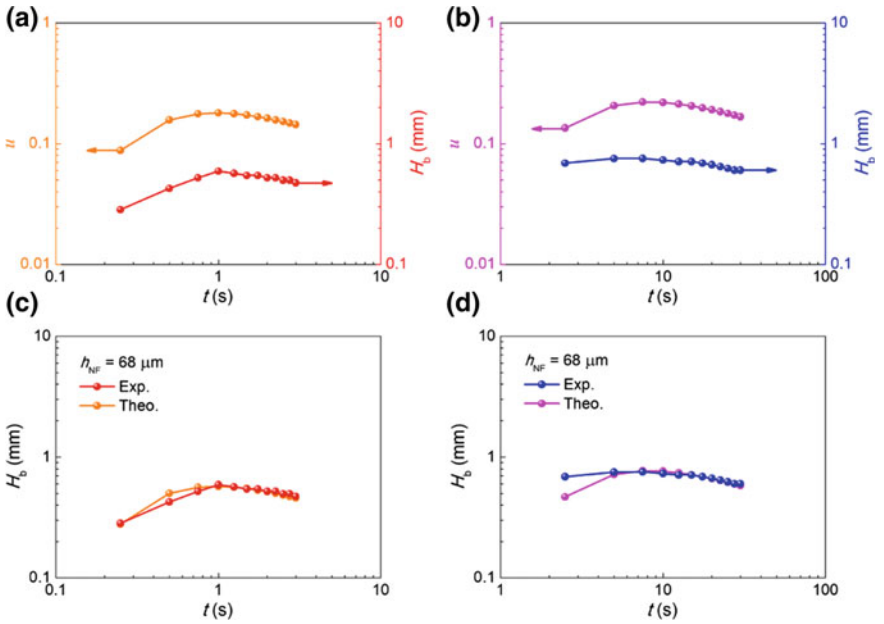

Fig. 3.14 The theoretically predicted (Theo.) bridge height (the value of u at x = 0) versus the experimentally measured (Exp.) bridge height H_b as functions of time t for two coalescing (**a** and **c**) curing agent–curing agent and (**b** and **d**) resin monomer–resin monomer paired droplets on NF mat with $h_{NF} = 68$ μm. Reprinted with permission from An et al. (2017a)

u at x = 0 and the measured H_b, which requires factors of 3.2 and 3.5 for the curing agent–curing agent and resin monomer–resin monomer cases, respectively. Then, the theoretical predictions

$$H_b = 3.2u$$

$$= 1.6\{\mathrm{erf}[M_c(x-\ell)] - \mathrm{erf}[M_c(x-\ell-1)] + \mathrm{erf}[M_c(x+\ell+1)] - \mathrm{erf}[M_c(x+\ell)]\} \quad (3.11)$$

$$H_b = 3.5u = 1.75\{\mathrm{erf}[M_r(x-\ell)] - \mathrm{erf}[M_r(x-\ell-1)] + \mathrm{erf}[M_r(x+\ell+1)] - \mathrm{erf}[M_r(x+\ell)]\} \quad (3.12)$$

where $\alpha_m = 1.2 \times 10^{-1}$ and 6×10^{-3} cm^2/s for the curing agent–curing agent and resin monomer–resin monomer cases, respectively, describe the experimental data well, as shown in Fig. 3.14c, d. Note also that M_c denotes the values of M for the curing agent–curing agent case, and M_r—for the resin monomer–resin monomer case.

The results of the present chapter show that droplets of the healing agents, dimethylvinyl-terminated DMS (resin monomer) and DMHS (curing agent), after release on NF mats, spread, make contact, and merge as driven by surface tension. Moreover, the PAN NF mats used in these experiments show wettability by both the resin monomer and curing agent with the static contact angles of 5° and 1°, respectively. Accordingly, the coalescence of two droplets on the NF mats is accompanied by significant imbibition of both resin monomer and curing agent into the pores. Therefore, the Hoffman–Voinov–Tanner law cannot describe drop spreading on the NF mats because of the significant effect of the imbibition, which is enhanced at greater mat thicknesses. The theory tracking the moisture content can describe the experimental time dependence of the bridge height between two coalescing droplets: an initial increase followed by a significant decrease, enhanced by the imbibition. The moisture transport coefficient values established are $\alpha_m = 1.2 \times 10^{-1}$ and 6×10^{-3} cm^2/s for the curing agent and the resin monomer, respectively. These values quantify the extent to which PAN NFs are more wettable by the the curing agent compared to the resin monomer.

3.2 Spreading on Tilted Surfaces

The physical mechanism of the self-healing process, in which the healing agents spread over porous PAN NF mats driven by wettability as discussed in Sect. 3.1, elucidated the rate of coalescence of the resin monomer and curing agent droplets on horizontal mats. Specifically, thicker NF mats, which possess a more developed porosities, facilitate the absorption of liquid agents, while reducing their wetted footprints at the surface. In the present chapter, the wettability-driven spreading of the liquid healing agents over inclined, or titled, NF mats is explored. In these cases, the effect of gravity can be significant and affect drop coalescence in a more pronounced way (An et al. 2017b).

Porous NF mats were fabricated by electrospinning (cf. Sects. 4.1 and 4.2). First, the 8 wt% PAN ($M_w = 150$ kDa) solution was prepared by dissolving PAN powder

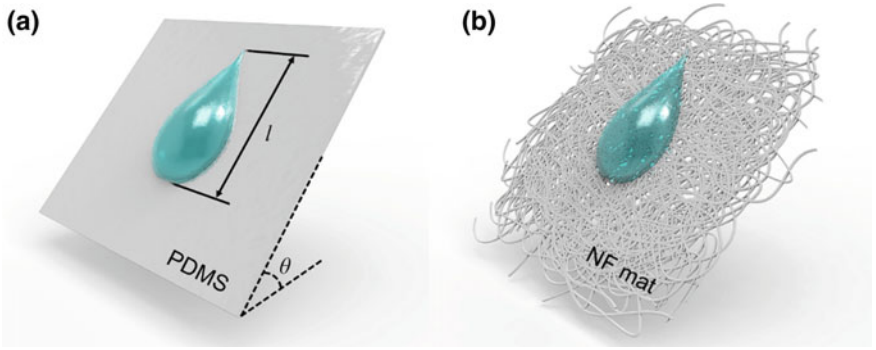

Fig. 3.15 Schematic of the wetting experiments with resin monomer or curing agent droplets on **a** an inclined flat PDMS film and **b** an inclined porous NF mat. Reprinted with permission from An et al. (2017b)

in DMF (99.8%) with magnetic stirring for 1 day at room temperature. Next, the PAN solution was electrospun with an 18-gauge needle-equipped syringe, a syringe pump, and a DC power supply. The flow rate of the solution was $Q = 800$ μl/h and the applied high DC voltage was 12.5 kV. The as-spun NFs were collected on a rotating drum. The angular speed of the drum was 200 rpm and the distance between the needle and drum was 12 cm. Different NF mats of thicknesses $h_{NF} = 33$, 68 and 135 μm were prepared by varying the electrospinning time (t_{es}); these mats had the average pore sizes of 0.64, 0.54, and 0.49 μm^2, respectively. The average pore size value of each NF mat was obtained by measuring 30 pores from 10 scanning electron microscopy (SEM) images.

A polydimethylsiloxane (PDMS) film was fabricated by blending dimethylvinyl-terminated DMS (resin monomer) and DMHS (curing agent) liquids (see Sect. 2.2) at the volume ratio of 10:1 and drying the blend for 2 days at room temperature.

Figure 3.15 depicts a schematic of the spread of a self-healing droplet on an inclined flat PDMS film or on an inclined porous NF mat. Several different inclination angles of $\theta = 30°$, 45°, 60°, and 70° were used in the experiments to observe the effect of the inclination on the droplet spreading behavior. The resin monomer or curing agent liquid was supplied to the substrates by a 23-gauge needle-equipped syringe with a flow rate of $Q = 3$ μl/min. The distance between the needle and the point at which the droplet touched the inclined substrate was 7.25 mm.

To capture images of spreading droplets, a high-speed camera was used. A side-view image was used to measure the contact length of the spreading droplet (l, cf. Fig. 3.15). The viscosity (μ) was measured by a rotational rheometer and the surface tension (σ) by a contact angle analyzer based on the pendant drop method (Stauffer 1965; Hansen and Rødsrud 1991; Dry 1996).

Figures 3.16a–d and 3.17a–d show the experimental results for the resin monomer droplet spreading on a flat PDMS film and different NF mats at several inclination angles (θ) from 30° to 70°. In all inclination cases, the side-view contact line length l

of the spreading droplets is increased as the time t increases. In the horizontal case $\theta = 0°$, that was studied in Sect. 3.1, the spreading resin droplet radii (a, which is half of the l value for the horizontal case) on the PDMS plane and the NF mat with thickness $h_{NF} = 33$ μm also increased as time t increased. However, on the thicker NF mats with $h_{NF} = 68$ and 135 μm at $\theta = 0°$, the increase in a (and thus, in $l = 2a$) ceased or, in some cases, a (and l) began to decrease because of the imbibition of the liquids into the thicker porous NF mats with significant pore volumes (cf. Sect. 3.1). Similarly, an enhanced imbibition into the thicker mats is revealed here for all inclination angle values (Fig. 3.16a–d). However, a decrease in l with increasing time is never observed (Fig. 3.16a–d). Furthermore, the values of l are increased for the same substrate as the inclination angle θ increases, because of the enhanced downward pull of gravity force along the surface. For example, for the PDMS film at t = 150 s, the value of l_{PDMS} is increased from 7.9 to 14.3 mm and for the 68-μm mat at t = 300 s the value of $l_{68\ \mu m}$ is increased from 6.7 to 10.4 mm as the inclination angle is increased from $\theta = 30°$ to 70°.

Although the lengths l of the curing agent droplets are lower compared to those of the resin monomer droplets depicted in Fig. 3.16a–d, similar trends are observed in the experimental results for the curing agent droplets shown in Fig. 3.16e–h. Note that the characteristic hydrodynamic time, $\tau_h = r\mu/\sigma$ (where r is the characteristic radius of the pores between NFs in the mat; cf. Sect. 3.1 and Stachewicz et al. 2009), of the curing agent ($\tau_{h,\text{curing agent}} = 1.4 \times 10^{-5}$ s) is relatively lower than that of the resin monomer ($\tau_{h,\text{resin monomer}} = 8.7 \times 10^{-4}$ s), which corresponds to a higher imbibition rate of the curing agent compared to that of the resin monomer. The value of r used for the estimate here is r = 0.42 μm, which is the average value obtained for different NF mats of thicknesses of $h_{NF} = 33$, 68, and 135 μm. For all tested inclination angles for the spreading curing agent droplets, the side-view length l is generally increased with time, with a saturation tendency appearing for the thicker NF mats. This tendency is more pronounced for the curing agent droplets compared to the resin monomer ones (cf. Fig. 3.16). Some anomalous behavior is recorded for the curing agent droplets; namely, the side-view length $l_{68\ \mu m}$ in the interval t = 2.0–3.0 s is smaller at $\theta = 60°$ than at $\theta = 70°$ [cf. Fig. 3.16g, h]. Furthermore, significantly different values of l on different substrates at t = 0 s are observed with the curing agent droplets at $\theta = 70°$ (Fig. 3.16h), unlike those of the resin monomer droplets (cf. Fig. 3.16d). This can be attributed to the combined effect of the lower viscosity of the curing agent (cf. Table 3.3 in Sect. 3.1) and the higher inclination angle, which causes instability in the initial sliding of the curing agent droplets. Such droplet instability is further enhanced when the inclination angle is increased up to $\theta = 80°$ (data not shown here).

The capillary numbers ($Ca = \mu U/\sigma$, where U is the velocity of the lowest tip of the contact line) of the droplets of the self-healing agents in the present experiments are relatively large, namely, $Ca = (7.5–8.8) \times 10^{-3}$. However, the spreading of droplets on the NF mats is considered as being viscosity-dominated rather than capillarity-dominated (Ringrose and Bentley 2015). In the case of no inclination ($\theta = 0°$), considered in detail in Sect. 3.1, the experimentally obtained values of the drop footprint radius a in the wettability-driven spreading resin monomer and

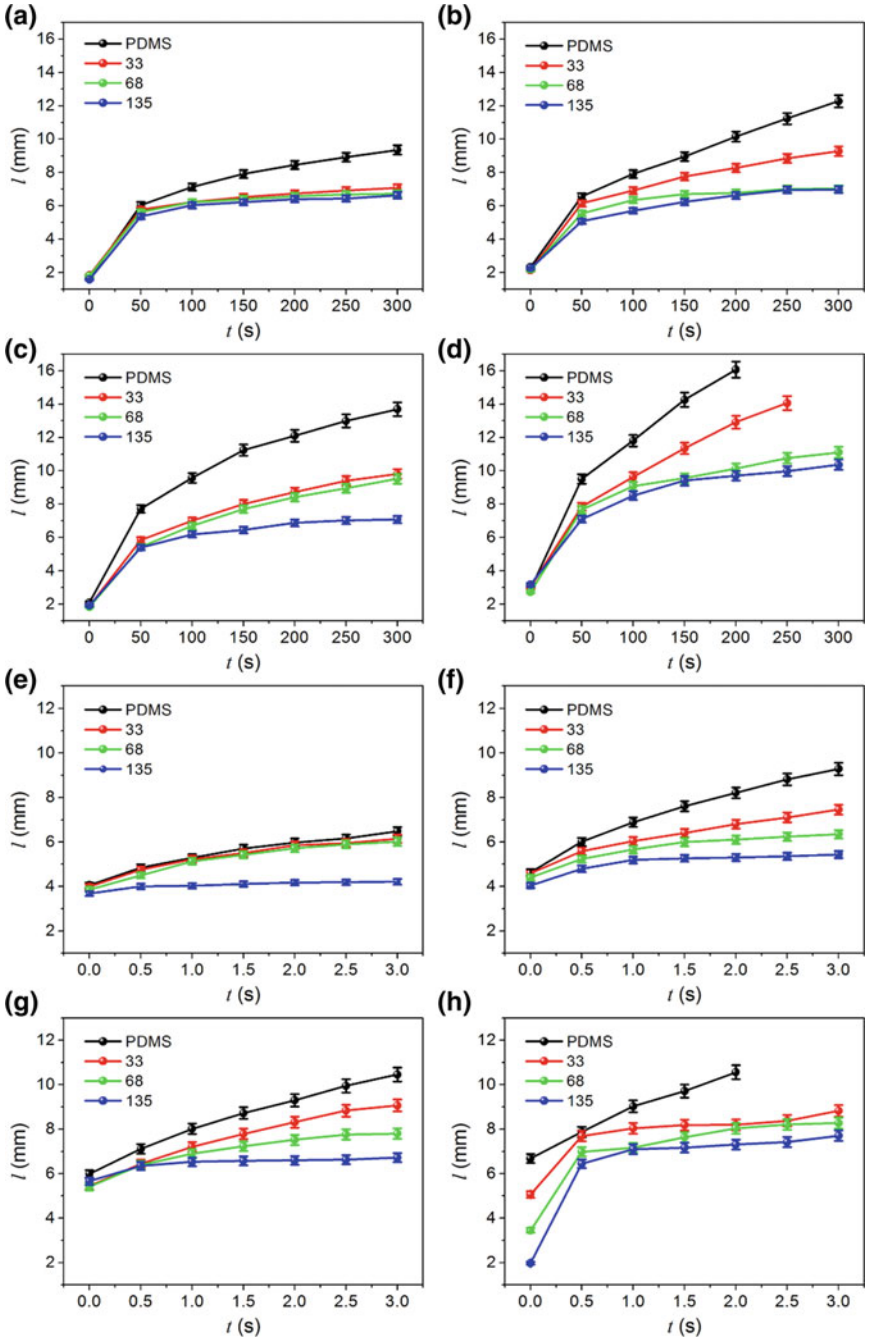

Fig. 3.16 Contact lengths of droplets l as a function of time t and the inclination angle θ for (**a**–**d**) the resin monomer and (**e**–**h**) the curing agent droplets spreading on the PDMS film and the NF mats with thicknesses $h_{NF} = 33$, 68, and 135 μm: **a**, **e** $\theta = 30°$, **b**, **f** $\theta = 45°$, **c**, **g** $\theta = 60°$, and **d**, **h** $\theta = 70°$. Reprinted with permission from An et al. (2017b)

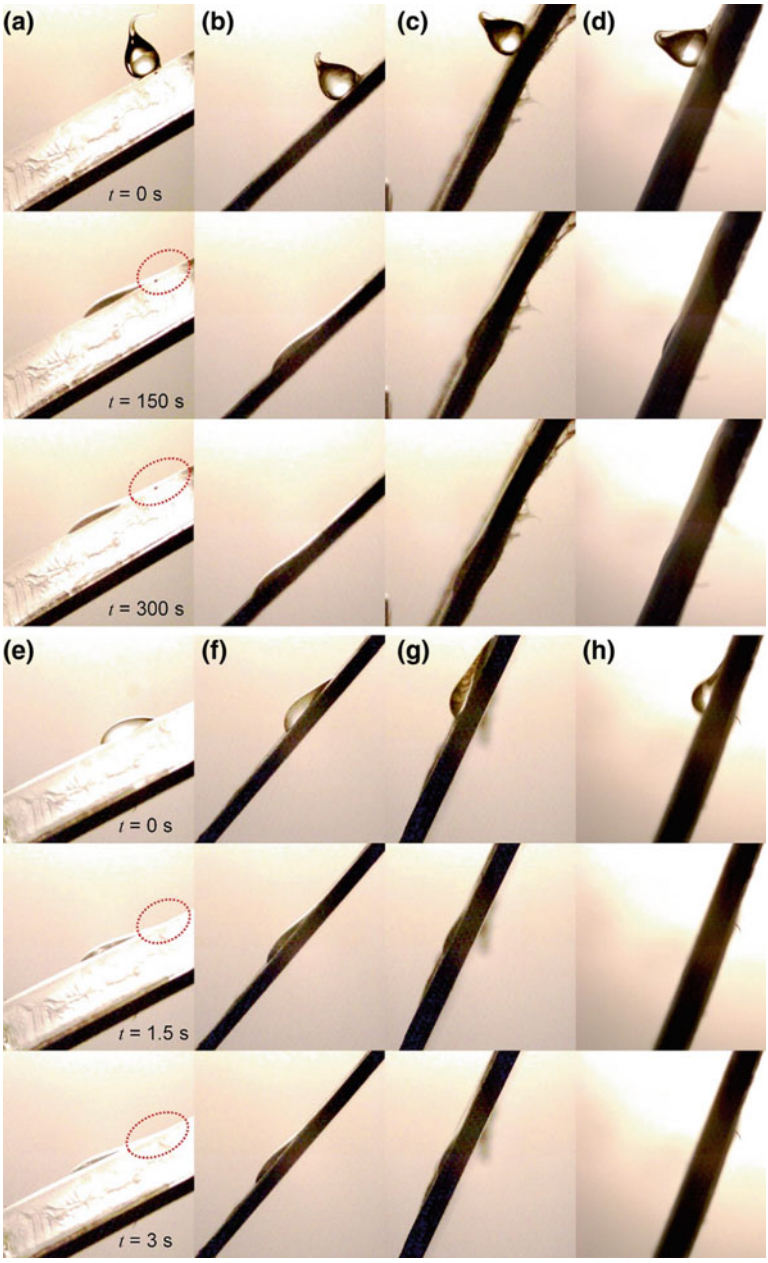

Fig. 3.17 Side-view images of spreading (**a**–**d**) resin monomer and (**e**–**h**) curing agent droplets at different times on different substrates at different inclination angles θ: **a**, **e** PDMS film at $\theta = 30°$, **b**, **f** NF mat with $h_{NF} = 33\ \mu m$ at $\theta = 45°$, (**c**, **g**) NF mat with $h_{NF} = 68\ \mu m$ at $\theta = 60°$, and (**d**, **h**) NF mat with $h_{NF} = 135\ \mu m$ at $\theta = 70°$. The red dotted ovals highlight the droplet tails. Reprinted with permission from An et al. (2017b)

curing agent droplets on the PDMS film and NF mats were compared with the Hoffman–Voinov–Tanner law, which is valid for intact perfectly wettable surfaces, thus yielding Eq. (3.4). The comparison showed that the data could disagree with Eq. (3.4) because of the imbibition of liquid into the NF mats, with the deviation becoming more pronounced for thicker mats (cf. Sect. 3.1).

On the other hand, Huppert theoretically studied the spreading of viscous fluid down inclined intact surfaces and found that the length of the droplet footprint depends on time in the form (Huppert 1982)

$$l_{\mathrm{Theo}} = \left(\frac{9\mathrm{A}^2 \mathrm{g} \sin\theta}{4\nu}\mathrm{t}\right)^{1/3} \tag{3.13}$$

where A and ν are the initial side-view cross-sectional area and the kinematic viscosity of the liquid, respectively, and g is the acceleration due to gravity. The observed curvatures of the sliding droplet surfaces are relatively small (Huppert 1982; Reznik and Yarin 2002), indicating that the surface tension effect can be neglected, as in Eq. (3.13). This is corroborated by the present Fig. 3.17 and particularly by the droplet tails, encircled by red dotted ovals in these images.

In Fig. 3.18, the experimental results (cf. Fig. 3.16) are compared with the theoretical predictions of Eq. (3.13), where the latter are shown by orange dashed lines. Similarly to the comparisons discussed in Sect. 3.1, the comparisons involving Eq. (3.13) exhibit slight discrepancies between the experimental and the theoretical results because of the uncertainty in the beginning of the asymptotic regime corresponding to Eq. (3.13). To eliminate this uncertainty, factors of 0.6 and 0.8 for the resin monomer and curing agent droplets, respectively, are used as multipliers in Eq. (3.13). Namely, the dependences of $0.6l_{\mathrm{Theo}}$ and $0.8l_{\mathrm{Theo}}$ are plotted in Fig. 3.18. These factors, obviously, cannot affect the scaling $l_{\mathrm{Theo}} \sim \mathrm{t}^{1/3}$ predicted by Eq. (3.13).

Figure 3.18 shows the experimental versus theoretical results for the spreading resin monomer and curing agent droplets, respectively, on the PDMS film and the NF mats of different thickness ($\mathrm{h_{NF}}$) at different inclination angles θ. In all cases of resin monomer droplets on PDMS film at different values of θ (Fig. 3.18a–d), the theoretical scaling predicted by Eq. (3.13) agrees well with the experimental data. However, on the NF mats, a significant decrease in the scaling exponent for l appears compared to the predictions of Eq. (3.13), as the mat thickness $\mathrm{h_{NF}}$ is increased. This arises from the imbibition of the resin monomer liquid into the NF mats, as described in Sect. 3.1 for the spreading behaviors on horizontal surfaces. Unlike the resin monomer droplets, the curing agent droplets show slight discrepancies from the theoretical predictions even on the PDMS films with different inclination angles θ (Fig. 3.18f–h). The overall slopes of the experimental dependences are seemingly decreased even more compared to the scaling predicted by Eq. (3.13). The greater decreases in slope are attributed to the lower viscosity of the curing agent compared to that of the resin monomer (Table 3.3 in Sect. 3.1), which enhances imbibition into the thicker NF mats and also invalidates the viscosity-dominated lubrication approximation implied by Eq. (3.13). At the large inclination angle $\theta = 70°$, even

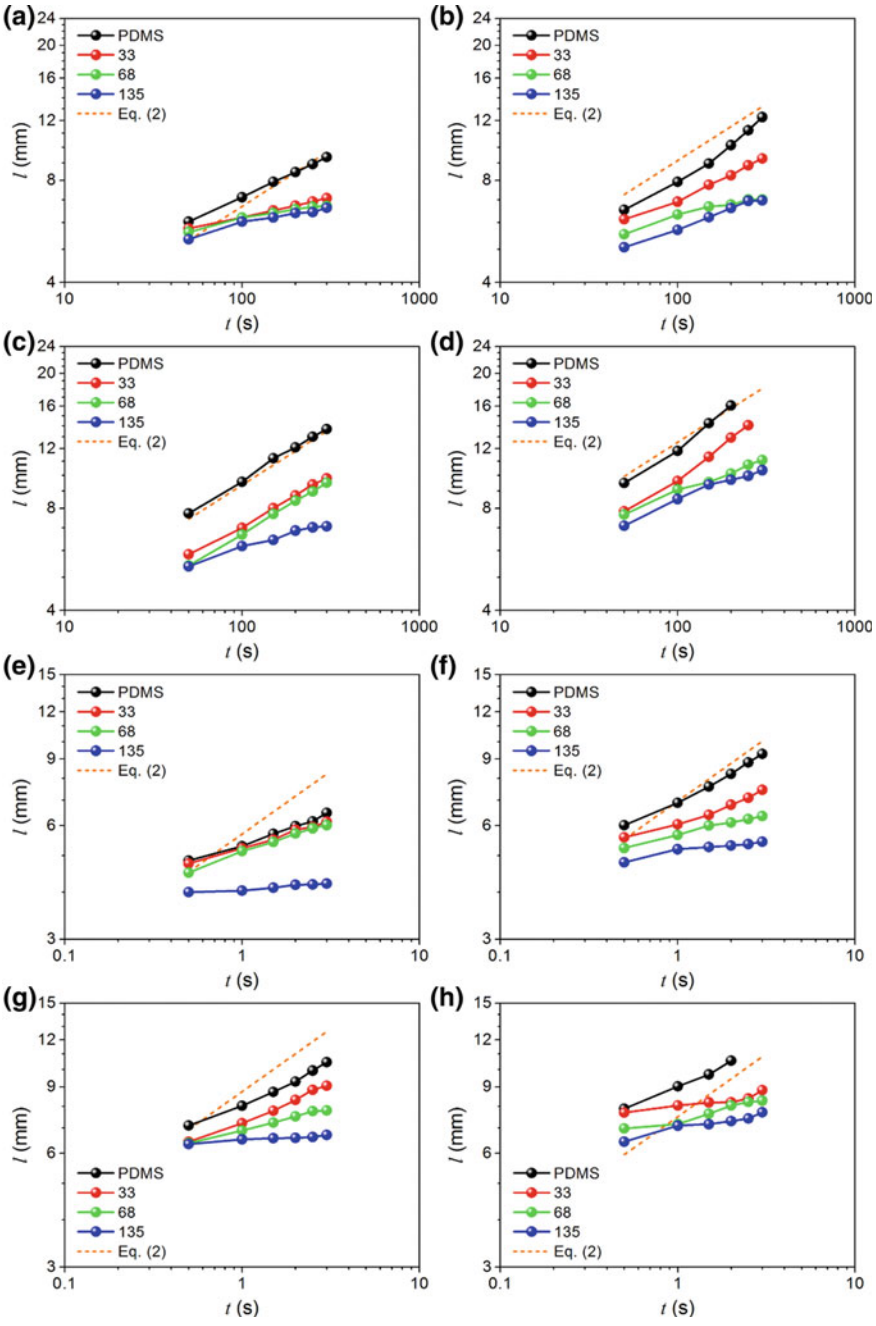

Fig. 3.18 Comparison of the experimental and theoretical results for the contact length l as a function of time t for (**a**–**d**) the resin monomer and (**e**–**h**) the curing agent droplets on PDMS film and the NF mats at different inclinations: **a**, **e** $\theta = 30°$, **b**, **f** $\theta = 45°$, **c**, **g** $\theta = 60°$, and **d**, **h** $\theta = 70°$. Reprinted with permission from An et al. (2017b)

the case of the PDMS film reveals a significant difference from the predictions of Eq. (3.13) because of the unstable behavior of the spreading curing agent droplet. It should be emphasized that the majority of the experimental dependencies shown in the log–log coordinates in Fig. 3.18, in fact, deviate from a linear fit. Therefore, they cannot be described by a power law, which is a direct consequence of the imbibition of the curing agent in the mats. Furthermore, the theory that describes the imbibition effect on the droplet spreading behavior on NF mats is currently applicable only for the case of zero-inclination case where $\theta = 0°$ (cf. Sect. 3.1.5).

In summary, the gravity-driven spreading of healing agent droplets over inclined electrospun porous NF mats revealed a significant wettability-driven imbibition effect, which was enhanced on thicker and/or more inclined mats. Because of this effect, Huppert's analytical solution (3.13) is inapplicable in the present case for estimating the droplet length in the direction of spreading on intact non-porous flat substrates. The imbibition effect revealed here is important for self-healing engineering materials with vascular NF-based delivery structure, because their effective operation is determined, in part, by spreading distance of healing agents from the location of damage.

3.3 Filling of Crack Tips

3.3.1 Macroscopic View of Epoxy Release and Hardening

Model macroscopic-scale experiments intended to elucidate the closure of cracks by healing agents were conducted by Lee et al. (2016b). They used a two-part commercial epoxy as the healing agent. The two components of the epoxy, the resin and hardener (see Sect. 2.4), had a 1:1 mixing ratio. When mixed, the resin set in 5 min and reached a fully cured state in 1 h at room temperature. Neither the resin nor the hardener of the epoxy were volatile. PDMS was used as a substrate material.

To visualize the intrinsic mechanism of crack healing by the release of the epoxy resin and hardener, the following macroscopic test was conducted. A channel with the dimensions of 63 mm × 5 mm × 3.2 mm (length × width × thickness) was cast on a PDMS substrate, leaving the top surface open to the air. Two drops of ~ 0.3 ml in volume, one of the epoxy resin and the other of the hardener, were gently placed at the right and left ends, respectively, of the channel. The hardener and the resin then spread from each side of the channel until making contact in the middle of the channel. The overlapping zone is located between the two vertical marks shown in the inset of Fig. 3.19. Photographs taken at regular time intervals allow the measurement of the mixing rate of the hardener and resin. The experimental data in Fig. 3.19 shows an increase in the width of the mixing zone, which manifests as a rippled surface texture. Assuming that mutual diffusion drives the initial stage of the mixing process, the width of the mixing zone depends on time t as $x = \text{const}\sqrt{Dt}$, where D is the binary diffusion coefficient. Taking for the estimate const ≈ 1, the diffusion coefficient D is 1.556×10^{-5} cm^2/s. However, this fits the experimental

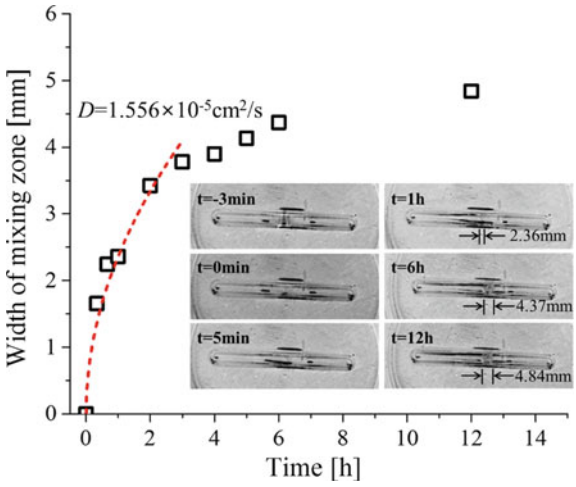

Fig. 3.19 Mixing of the two components, of epoxy resin (left) and the hardener (right). The experimentally measured width of the mixing zone is denoted in the images and depicted by square symbols. Its fit with the curve $x = \sqrt{Dt}$ is shown by the red dashed line. Reprinted with permission from Lee et al. (2016b)

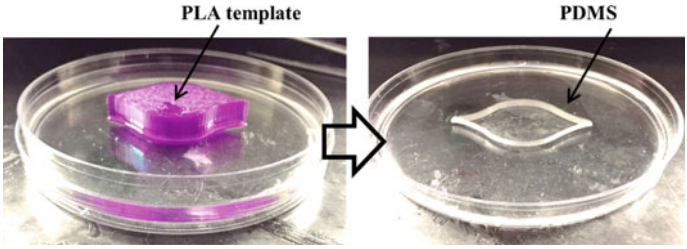

Fig. 3.20 (Left) 3D-printed crack-shaped PLA template pressed into the PDMS mold. (Right) Macroscopic crack-like domain formed in PDMS. Reprinted with permission from Lee et al. (2016b)

data only for t $\leq$ 3 h, with $R^2 = 0.9674$. For larger values of t, the epoxy-hardening reaction affects the mixing zone, which solidifies and thereby arrests further binary diffusion while the propagation of the reaction front becomes saturated.

3.3.2 Epoxy-Hardener Reaction Observed in a Macroscopic Crack-Tip-Shaped Mold

For a better understanding of the hardening of the two-part epoxy, the reaction of the resin and hardener in a crack-tip-like macroscopic mold was observed. Initially, a crack-like template was formed from polylactic acid (PLA) using a 3D printer, shown as the purple template in Fig. 3.20. This template was placed in a PDMS mold and left for 24 h. On removing the template, a macroscopic crack-like domain remained in the PDMS body (Fig. 3.20).

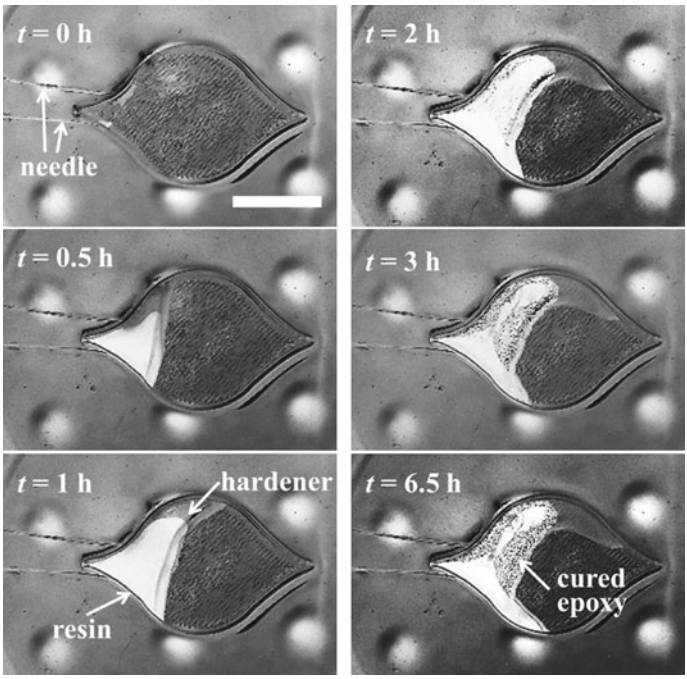

Fig. 3.21 Spreading and reaction of the epoxy resin and hardener released near the tip of the model crack. (Scale bar is 20 mm). Reprinted with permission from Lee et al. (2016b)

Two needles (25-gauge; inner diameter of 0.25 mm and outer diameters of 0.51 mm) were inserted, with the needle tips placed at the boundaries of the model crack in the solidified PDMS (Fig. 3.21). The two needles delivered the epoxy resin and hardener separately. The dark resin and bright hardener are seen in Fig. 3.21. The viscosity of the hardener, as reported by the manufacturer, was 400 mPa·s at 25 °C. The exact value of the viscosity of the epoxy resin was measured using a squeezing apparatus (Pelot et al. 2013). The measured viscosity of the resin was 8.1 ± 0.9 mPa·s at 25 °C. The resin and hardener were supplied through the needles to the bottom and top left sides, respectively, of the model crack tip, using two separate syringe pumps at flow rates of 1 ml/h. The syringe pumps were run for 10 min, with the total volumes of the supplied resin and hardener being ~160 μl each. The uncured resin and hardener appear to spread smoothly along the rim of the crack from the tips of their respective needles (Fig. 3.21). After 2 h, both the epoxy and hardener have stopped spreading; some of the cured epoxy is visible as a textured material in the photograph obtained at t = 6.5 h in Fig. 3.21.

In the self-healing vascular nanotextured composites, the diameters of the as-spun fibers containing the resin and hardener, which are embedded in PDMS matrix, are ~ 200–1400 nm. Hence, the volume of the epoxy components released by the rupture of these fibers during tensile tests (see Sect. 7.2) would be much smaller than

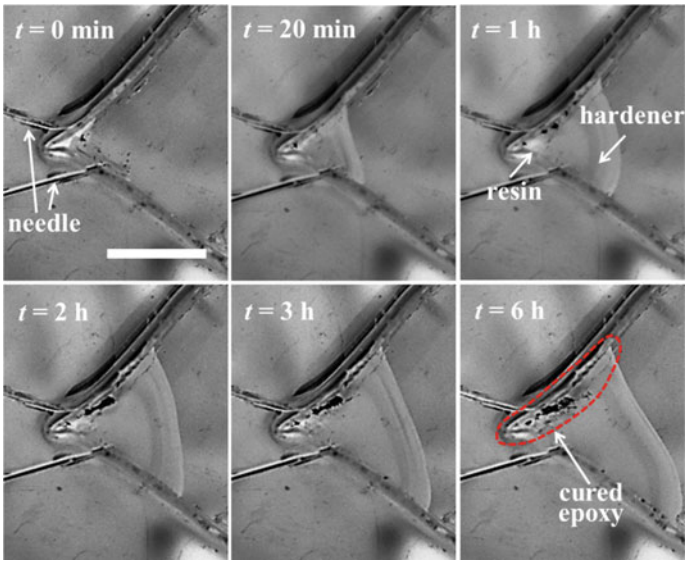

Fig. 3.22 Curing of a drop of the epoxy resin with excess hardener at the tip of the model crack. (Scale bar is 10 mm). Reprinted with permission from Lee et al. (2016b)

those used in the model crack experiment (Fig. 3.21). In the case of such nanofibers (NFs), tiny drops of both the resin and hardener would be released at the ruptured fiber tips and spread over the ruptured areas. The cured epoxy droplets covering such ruptured NF tips are visible in the SEM images of the cut NF mats presented in Lee et al. (2016c) and in Fig. 4.24b in Sect. 4.5. To mimic this observed healing process at the crack tip, drops of the epoxy resin are positioned in a model crack tip and excess of the hardener is supplied, as shown in Fig. 3.22. This causes strictly stoichiometric amounts of the resin and hardener to react at the crack tip. Curing then occurs along the tip rim, as seen in Fig. 3.22, where the cured epoxy appears as black dots in the panel corresponding to t = 6 h.

3.4 Stitching Cracks and the Corresponding Mechanical Properties

3.4.1 Macroscopic Model of Self-Healing Composite Materials with Embedded Microchannel System

The spread of released droplets of healing agents over nanofiber (NF) mats, as studied in Sects. 3.1 and 3.2, can lead to their mixing and reaction, as illustrated in Sect. 3.3. The matrix material in self-healing composites can also facilitate such phenomena,

yielding peculiar crack-healing mechanisms, as explored by Lee et al. (2017). They used polydimethylsiloxane (PDMS) in the component form of a resin monomer (DMS) and a curing agent (DMHS); see Sect. 2.2.

A model macroscopic setup was fabricated with embedded microchannels, which mimicked self-healing nanotextured vascular materials. The template for the microfluidic channels was composed of polycarbonate and contained two distinct sets of microchannels (see Fig. 3.23), which were filled with either the resin monomer or the curing agent. The dimensions of the individual microchannels were 1.5 mm × 30 mm × 0.29 mm (width × length × thickness), and the distance between the microchannels was 1 mm (Fig. 3.23). The premixed PDMS (10:1 volume ratio of resin to curing agent) was kept in a vacuum chamber to eliminate the captured bubbles for 1 h and then poured into the prepared template. After curing at room temperature for 2 days, the template was peeled away from the molding, and the molding was closed with a separate thin layer of PDMS. The two PDMS layers adhered together using a corona treater. The corona-treated PDMS layers were held for 1 day at room temperature to ensure the secure closing of the microchannel system. The thickness of the entire model was 2 mm. After the microchannel system was closed, the dyed resin monomer (red) and curing agent (green) were slowly injected into the empty microchannels.

The propagating crack in the pre-notched and stretched microchannel system and the released healing agents were photographed using digital cameras with a magnifying lens. The time intervals between the photographs were between 1 s and 30 min for different cases. Microscopic images of the system were obtained using an optical microscope and an SEM. The geometry of the released droplets was observed using an optical profilometer. A Raman spectrometer was used to verify that the resin monomer and curing agent were released successfully; a green 532-nm/50-mW diode laser was used as the radiation source. The changes in the mechanical properties of the macroscopic system with the embedded microchannels over the course of self-healing were investigated through tensile tests performed using an

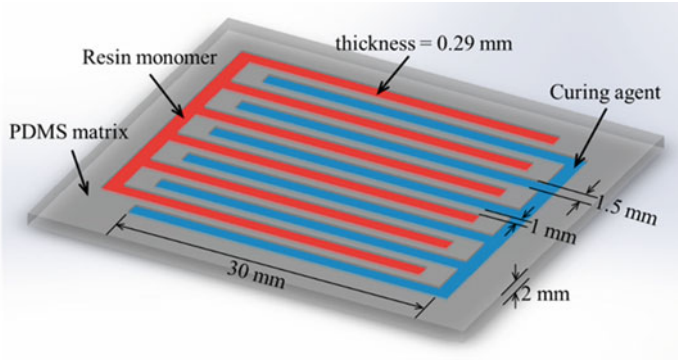

Fig. 3.23 Schematic of microchannel system. Reprinted with permission from Lee et al. (2017)

Instron 5942 system with a-100 N load cell. The test sample was fixed between the top and bottom grips and stretched at a constant strain rate of 10 mm/min until complete failure. The initial stretching of the pre-notched system was also conducted using an Instron 5942.

3.4.2 *Release and Mixing of Healing Agents*

When the microchannel system was pre-notched in the direction normal to the microchannel orientation and stretched by $\Delta l = 5$ mm along the direction parallel to the microchannel orientation, crack propagation was initiated. Light transmitted through the transparent PDMS specimen reveals that stress is concentrated near the crack tip, as shown in Fig. 3.24. The high-stress domain is represented by black spots in Fig. 3.24a. As the crack propagates across the inter-channel wall, the resin monomer leaks from the cut channel and wets the sample surface (Fig. 3.24b). Similarly, the curing agent also leaks from the microchannel cut by the propagating crack.

Care was taken to avoid squeezing any healing material from the notches in the samples when they were placed in the Instron 5942 machine and gripped at the edges. It was confirmed that the healing agents were released from the test samples in the tensile tests only after crack propagation had started. The healing agents were

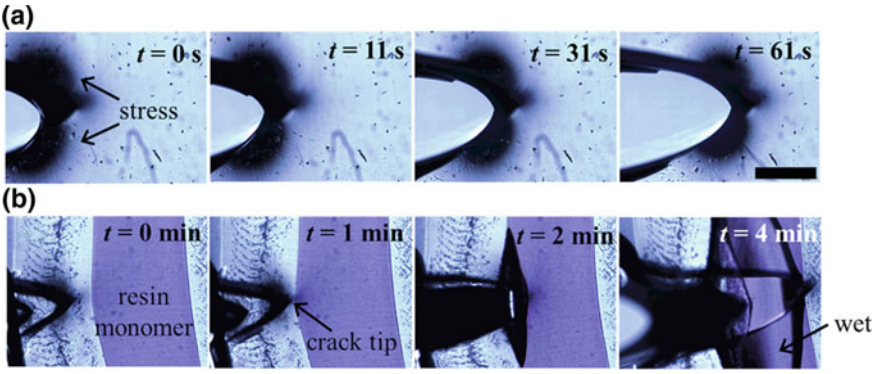

Fig. 3.24 **a** Crack tip and stress concentration in the surrounding area in a pure PDMS sheet. **b** Resin monomer-filled microchannel cut by a propagating crack, with the resin monomer leaking and wetting the sample. Scale bar (rightmost image in **a**, bottom right) is 500 μm. Respective times t are listed in the frames. The sample shown in panel **a** is a pure PDMS sheet (without any channels) of the same size as that in panel **b**; the latter is a PDMS sheet with channels filled with resin monomer. Both samples have a similar pre-notched cracks that begin propagating after the samples are stretched by $\Delta l = 5$ mm. Both rows show top views, and row panel **b** clearly reveals that the resin monomer is released from the channel, as the propagating crack has reached it. The black spots surrounding the tip of the propagating crack in panel **b** cannot be related to the resin monomer, because none is available in the present case. Instead, the black spots are rather associated with the stress-optical phenomenon described in the literature (Withers 2011). Reprinted with permission from Lee et al. (2017)

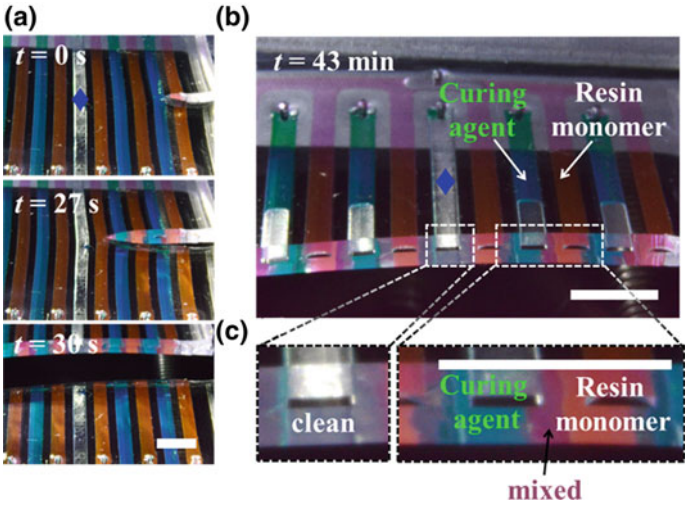

Fig. 3.25 Crack propagation and release of resin monomer and curing agent from damaged parallel microchannels. **a** Snapshots showing crack propagation through the system of parallel microchannels alternatingly filled with the resin monomer and curing agent. **b** Wettability-driven spreading and mixing of the resin monomer and curing agent on the cut surface of the crack banks. **c** Magnified view of a crack bank. Scale bar is 5 mm. Note that the spreading of the released healing agents is fully dominated by wettability (cf. Sects. 3.1 and 3.2), and they spread in all directions, in particular against the direction of gravity. Reprinted with permission from Lee et al. (2017)

visually observed to be released only from the growing crack. The released resin monomer and curing agent are spread on the cut surface (the crack banks), as shown in Fig. 3.25. The resin monomer and curing agent are colored in red and green, respectively, and the area where they make contact and mix appears purple.

3.4.3 Wettability-Driven Spreading and Polymerization of Healing Agents

In the planar case more closely resembling the spread of resin monomer and curing agent over the crack banks, Eq. (3.4) of Sect. 3.1, corresponding to the Hoffman–Voinov–Tanner law, is replaced by the following:

$$a = \left[0.253\frac{\sigma}{\mu}S^3 t\right]^{1/7} \propto t^{1/7} \tag{3.14}$$

where S is the cross-sectional area of a 'planar' droplet.

Equation (3.14) shows that the spreading of the healing agents over the crack banks occurs more rapidly than they do under axisymmetric stain (the $t^{1/7}$ scaling versus $t^{1/10}$).

The material in the mixing zone is cured PDMS, formed by the mixing of the resin monomer and curing agent released from the damaged channels and their subsequent

polymerization on the crack bank. This can be proven using Raman spectroscopy, optical imaging and optical surface profilometry, as described in Sect. 5.2.

3.4.4 *Recovery of Mechanical Strength*

The channels filled with the resin monomer and curing agent were cut with a sharp razor, and the crack bank was observed (see Fig. 3.26). The resin monomer and curing agent are spread along the crack bank because of their wettability; the empty areas of the channels are shown in Fig. 3.26. As the crack is narrow, the released resin monomer and curing agent fill it readily. Moreover, the overflowed resin monomer and curing agent wet the top (or bottom) surfaces of the sample; the wetting front on the surface is highlighted by lower arrows in Fig. 3.26.

The cracked sample was left to rest for 24 h and then subjected to tensile test. During the resting period, the released resin monomer was polymerized by the released curing agent. The polymerized resin (PDMS) filled the crack and partially healed the cut channel, acting as a glue between the crack banks. In Fig. 3.27a, the healed crack filled with the polymerized resin is clearly visible in panel 3. For the sample healed by the polymerized resin (Fig. 3.27a), under the same extension, the load required for stretching is 6–8 times higher than that for a cut sample with no resin or curing agent in the channels (Fig. 3.27b). The load–extension curves for the two samples are shown in Fig. 3.27c.

A long-term fatigue test was performed next. Samples containing channels filled with the healing agents and those with empty channels were pre-notched at the center normal to the channel orientation and subjected to the tensile strain ε of 9.09%. The images in Fig. 3.28 show the release of healing agents from the pre-notched crack banks and their filling of the crack within 2 min. A small amount of the

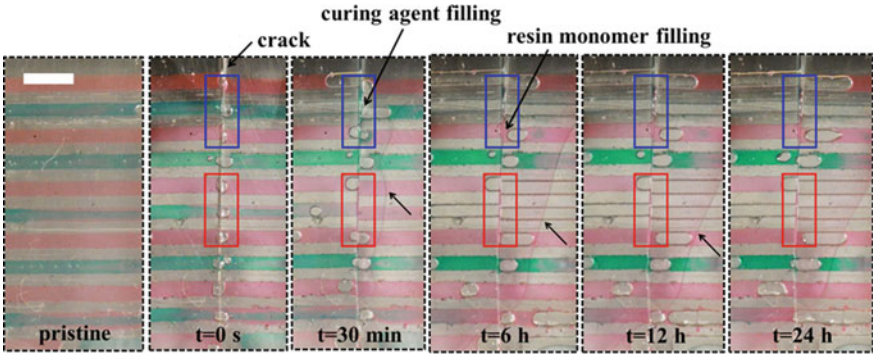

Fig. 3.26 Resin monomer (red) and curing agent (green) spreading in a narrow crack formed in the middle and spilling out over the sample surface. Scale bar is 5 mm. Reprinted with permission from Lee et al. (2017)

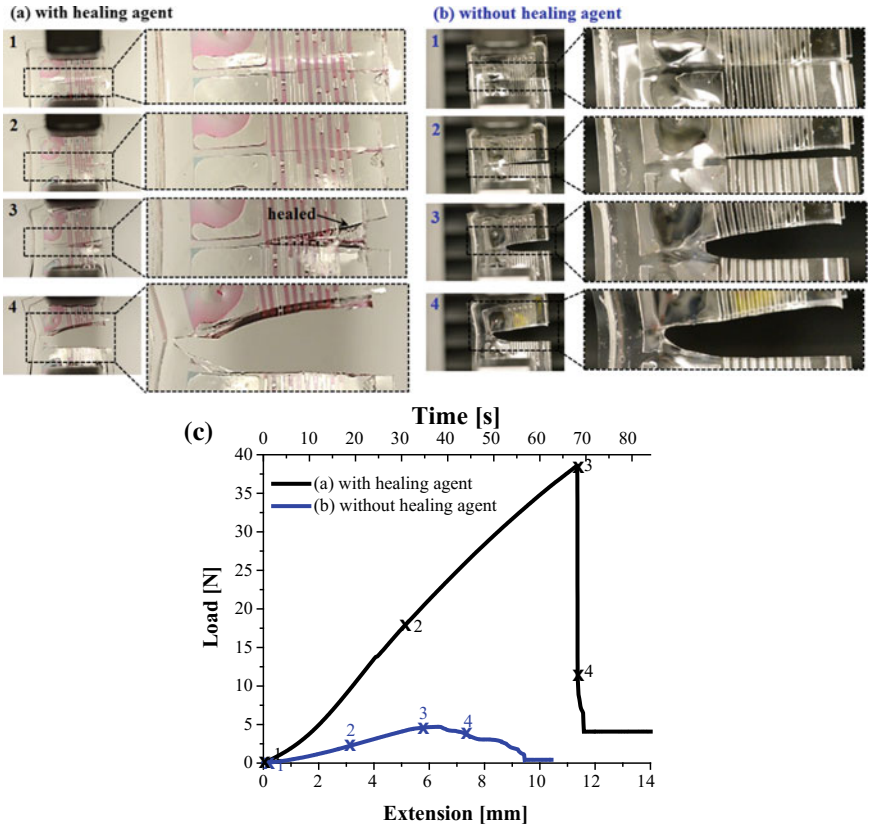

Fig. 3.27 **a** Cured sample after the resin monomer and curing agent spread from the cut channels, underwent polymerization, and covered the crack banks. **b** Cut sample without any resin monomer and curing agent in the channels. The empty crack is seen as a black void. **c** Load–extension curves of the samples shown in **a** and **b**. Numerals 1–4 on the curves correspond to frames 1–4, respectively, shown in panels **a** and **b**. Reprinted with permission from Lee et al. (2017)

healing agents spills onto the sample surface because of its wettability, as shown in the image in the second row in Fig. 3.28. The pillars formed by the polymerized resin (the polymerization occurs following the mixing of the resin monomer and the curing agent) span the upper and lower banks of the crack; crack propagation is arrested at t = 18 h. In the last image, which was obtained at t = 78 h, it can be seen that the crack remains contained without further propagation. On the other hand, the pre-notched crack in the stretched sample without healing agents has propagated freely, as shown in the images in the column on the right in Fig. 3.28.

The intrinsic physical mechanism responsible for self-healing in a damaged vascular system consisting of microchannels alternatingly filled with resin monomer (dimethyl siloxane) and curing agent (dimethyl-methyl hydrogen-siloxane) and embedded in a PDMS matrix is clearly illustrated in Fig. 3.28. When the microchan-

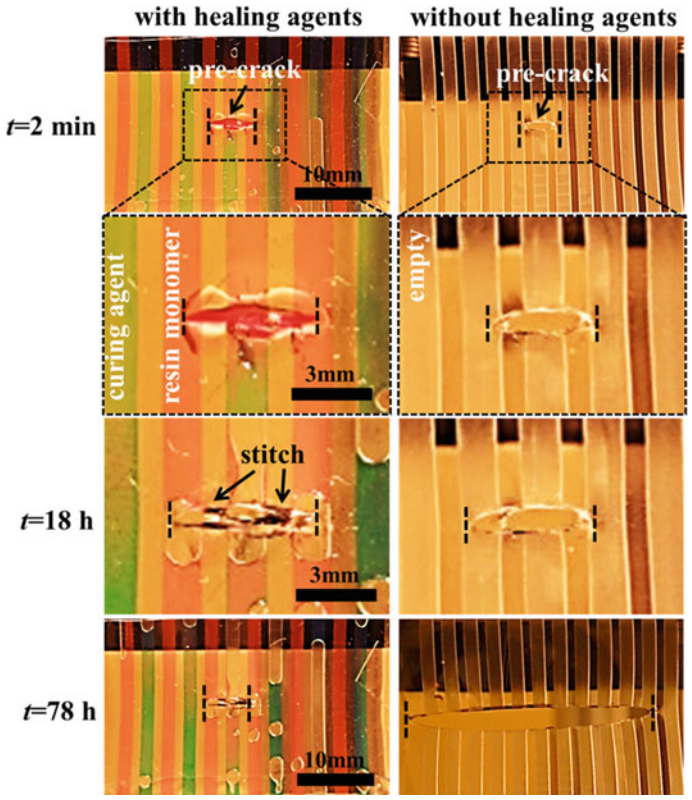

Fig. 3.28 Left column: Crack propagation in the pre-notched and stretched sample is arrested by the released healing agents, which form polymerized resin (PDMS). Right column: Unrestricted crack propagation in the pre-notched and stretched sample with no healing agents in the channels. Note that the spreading of the released healing agents is fully dominated by wettability, and the agents spread in all directions, including against the direction of gravity. It is seen that the crack is filled with a mixture of resin monomer and curing agent released from the channels within 2 min. The cured resin (PDMS) forms several bridges across the crack in 18 h, i.e. the self-healing process can be characterized as essentially "self-stitching". Reprinted with permission from Lee et al. (2017)

nel system is subjected to damage because of the propagation of a pre-notched crack under stretching, the healing agents, namely, the resin monomer and curing agent, are released from the damaged channels into the open crack space. Driven by their wettability, they spread over the crack banks in the PDMS matrix until they contact with the neighboring droplets as well as the droplets from the opposite bank. Then, the resin monomer and curing agent mix and undergo an organometallic crosslinking reaction, yielding resin polymerization. Raman spectroscopy (cf. Fig. 5.8 in Sect. 5.2) confirmed that the mixing and curing of the resin monomer occurred in the mixing zones, thus forming PDMS. Morphologically, pillars of the polymerized resin are formed; these stitch the opposing crack banks together, thus arresting further crack

propagation. This is the self-healing mechanism at work. In comparison, crack propagation in a PDMS matrix with initially empty channels (free of healing agents) continues unrestricted, and self-healing is impossible.

References

An S, Kim YI, Lee MW, Yarin AL, Yoon SS (2017a) Wetting and coalescence of drops of self-healing agents on electrospun nanofiber mats. Langmuir 33:10663–10672

An S, Kim YI, Yoon JY, Yarin AL, Yoon SS (2017b) Wetting of inclined nano-textured surfaces by self-healing agents. Appl Phys Lett 111:234101

An S, Liou M, Song KY, Jo HS, Lee MW, Al-Deyab SS, Yarin AL, Yoon SS (2015) Highly flexible transparent self-healing composite based on electrospun core–shell nanofibers produced by coaxial electrospinning for anti-corrosion and electrical insulation. Nanoscale 7:17778–17785

Arashiro EY, Demarquette NR (1999) Use of the pendant drop method to measure interfacial tension between molten polymers. Mater Res 2:23–32

Behzadnasab M, Mirabedini S, Esfandeh M, Farnood R (2017) Evaluation of corrosion performance of a self-healing epoxy-based coating containing linseed oil-filled microcapsules via electrochemical impedance spectroscopy. Prog Org Coat 105:212–224

Bekas D, Tsirka K, Baltzis D, Paipetis A (2016) Self-healing materials: a review of advances in materials, evaluation, characterization and monitoring techniques. Compos B 87:92–119

Berg J (ed) (1993) Wettability. Taylor & Francis, New York

Binder WH (ed) (2013) Self-healing polymers: from principles to applications. Wiley-VCH, Weinheim

Blaiszik B, Kramer S, Olugebefola S, Moore JS, Sottos NR, White SR (2010) Self-healing polymers and composites. Annu Rev Mater Res 40:179–211

Diesendruck CE, Sottos NR, Moore JS, White SR (2015) Biomimetic self-healing. Angew Chem Int Ed 54:10428–10447

Dry C (1996) Procedures developed for self-repair of polymer matrix composite materials. Compos Struct 35:263–269

Hager MD, Greil P, Leyens C, van der Zwaag S, Schubert US (2010) Self-healing materials. Adv Mater 22:5424–5430

Hansen F, Rødsrud G (1991) Surface tension by pendant drop: I. A fast standard instrument using computer image analysis. J Colloid Interface Sci 141:1–9

Herbst F, Döhler D, Michael P, Binder WH (2013) Self-healing polymers via supramolecular forces. Macromol Rapid Commun 34:203–220

Hillewaere XK, Du Prez FE (2015) Fifteen chemistries for autonomous external self-healing polymers and composites. Prog Polym Sci 49:121–153

Huppert HE (1982) Flow and instability of a viscous gravity current down a slope. Nature 300:427–429

Lee MW, An S, Jo HS, Yoon SS, Yarin AL (2015a) Self-healing nanofiber-reinforced polymer composites: 1. Tensile testing and recovery of mechanical properties. ACS Appl Mater Interfaces 7:19546–19554

Lee MW, An S, Jo HS, Yoon SS, Yarin AL (2015b) Self-healing nanofiber-reinforced polymer composites: 2. Delamination/debonding, and adhesive and cohesive properties. ACS Appl Mater Interfaces 7:19555–19561

Lee MW, An S, Lee C, Liou M, Yarin AL, Yoon SS (2014a) Self-healing transparent core–shell nanofiber coatings for anti-corrosive protection. J Mater Chem A 2:7045–7053

Lee MW, An S, Lee C, Liou M, Yarin AL, Yoon SS (2014b) Hybrid self-healing matrix using core − shell nanofibers and capsuleless microdroplets. ACS Appl Mater Interfaces 6:10461–10468

Lee MW, Sett S, Yoon SS, Yarin AL (2016a) Fatigue of self-healing nanofiber-based composites: static test and subcritical crack propagation. ACS Appl Mater Interfaces 8:18462–18470
Lee MW, Sett S, Yoon SS, Yarin AL (2016b) Self-healing of nanofiber-based composites in the course of stretching. Polymer 103:180–188
Lee MW, Yoon SS, Yarin AL (2016c) Solution-blown core−shell self-healing nano- and microfibers. ACS Appl Mater Interfaces 8:4955–4962
Lee MW, Yoon SS, Yarin AL (2017) Release of self-healing agents in a material: What happens next? ACS Appl Mater Interfaces 9:17449–17455
Lembach A, Tan HB, Roisman IV, Gambaryan-Roisman T, Zhang Y, Tropea C, Yarin AL (2010) Drop impact, spreading, splashing and penetration in electrospun nanofiber mats. Langmuir 26:9516–9523
Levich VG (1962) Physicochemical hydrodynamics. Prentice Hall, Englewood Cliffs
Lucas R (1918) Ueber das Zeitgesetz des Kapillaren Aufstiegs von Flussigkeiten. Kolloid Z. 23:15–22
Luikov AV (1964) Heat and mass transfer in capillary-porous bodies. Adv Heat Transfer 1:123–184
Luikov AV (1966) Heat and mass transfer in capillary-porous bodies. Pergamon Press, Oxford
McCabe WL, Smith JC, Harriot P (1993) Unit operations of chemical engineering. McGraw-Hill, New York
Pelot DD, Sahu RP, Sinha-Ray S, Yarin AL (2013) Strong squeeze flows of yield-stress fluids: The effect of normal deviatoric stresses. J Rheol 57:719–742
Reznik SN, Yarin AL (2002) Spreading of a viscous drop due to gravity and capillarity on a horizontal or an inclined dry wall. Phys Fluids 14:118–132
Ringrose P, Bentley M (2015) Upscaling flow properties. Reservoir model design. Springer, Heidelberg, pp 115–149
Sahu R, Sinha-Ray S, Yarin AL, Pourdeyhimi B (2012) Drop impacts on electrospun nanofiber membranes. Soft Matter 8:3957–3970
Samadzadeh M, Boura SH, Peikari M, Kasiriha S, Ashrafi A (2010) A review on self-healing coatings based on micro/nanocapsules. Prog Org Coat 68:159–164
Silva ACM, Moghadam AD, Singh P, Rohatgi PK (2017) Self-healing composite coatings based on in situ micro–nanoencapsulation process for corrosion protection. J Coat Technol Res 14:1–29
Stachewicz U, Dijksman JF, Burdinski D, Yurteri CU, Marijnissen JC (2009) Relaxation times in single event electrospraying controlled by nozzle front surface modification. Langmuir 25:2540–2549
Stankiewicz A, Szczygieł I, Szczygieł B (2013) Self-healing coatings in anti-corrosion applications. J Mater Sci 48:8041–8051
Stauffer CE (1965) The measurement of surface tension by the pendant drop technique. J Phys Chem 69:1933–1938
Thakur VK, Kessler MR (2015) Self-healing polymer nanocomposite materials: A review. Polymer 69:369–383
Tikhonov AN, Samarskii AA (1990) Equations of mathematical physics. Dover Publications, New York
Trask R, Williams H, Bond I (2007) Self-healing polymer composites: mimicking nature to enhance performance. Bioinspiration Biomimetics 2:1–9
Washburn EW (1921) The dynamics of capillary flow. Phys Rev 17:273–283
Wei H, Wang Y, Guo J, Shen NZ, Jiang D, Zhang X, Yan X, Zhu J, Wang Q, Shao L (2015) Advanced micro/nanocapsules for self-healing smart anticorrosion coatings. J Mater Chem A 3:469–480
Wei Z, Yang JH, Zhou J, Xu F, Zrínyi M, Dussault PH, Osada Y, Chen YM (2014) Self-healing gels based on constitutional dynamic chemistry and their potential applications. Chem Soc Rev 43:8114–8131
Withers PJ (2011) 3D crack-tip microscopy: Illuminating micro-scale effects on crack-tip behavior. Adv Energy Mater 13:1096–1100
Wu DY, Meure S, Solomon D (2008) Self-healing polymeric materials: a review of recent developments. Prog Polym Sci 33:479–522

Yang Y, Ding X, Urban MW (2015) Chemical and physical aspects of self-healing materials. Prog Polym Sci 49:34–59
Yang Y, Urban MW (2013) Self-healing polymeric materials. Chem Soc Rev 42:7446–7467
Yarin AL (2006) Drop impact dynamics: splashing, spreading, receding, bouncing…. Annu Rev Fluid Mech 38:159–192
Yarin AL, Pourdeyhimi B, Ramakrishna S (2014) Fundamentals and applications of micro- and nanofibers. Cambridge University Press, Cambridge

Part II
Fabrication Methods

Chapter 4
Fabrication of Vascular Nanofiber Networks with Encapsulated Self-Healing Agents for Mechanical Recovery

Several fabrication methods are used to prepare the components of self-healing nanotextured vascular materials. These include the general method of electrospinning discussed in Sect. 4.1 and its variant of co-electrospinning discussed in Sect. 4.2; the latter is used to form core-shell nanofibers (NFs) that contain healing agents in their cores. Another variant of electrospinning used to form such NFs is the emulsion spinning, which is described in Sect. 4.3. Instead of electrospinning, another general method of solution blowing (see Sect. 4.4) can be used to form NFs. This method is industrially scalable, and its variant of coaxial solution blowing can be used to rapidly manufacture core-shell NFs with healing agents in the cores (Sect. 4.5). Another variant of solution blowing—emulsion blowing—has also been used to form core-shell NFs with healing agents in the core (Sect. 4.6). All the abovementioned chapters discuss the fabrication of essentially two-dimensional self-healing materials. The subsequent Sect. 4.7 describes the methods of fabrication of two- and three-dimensional self-healing composites with embedded nanotextured vascular systems based on core-shell NFs.

4.1 Electrospinning

4.1.1 Charge Relaxation Time in Electrolytes

The electrospinning of polymer NFs employs polymer solutions belonging to the class of ionic conductors (i.e., electrolytes) (Melcher and Taylor 1969; Saville 1997; Yarin et al. 2014). To understand the fundamental aspects of electrospinning and co-electrospinning (considered further in Sect. 4.2), the electrodynamics of ionic conductors are considered here in brief. Because the magnetic effects in electrolytes are negligibly small (Castellanos and Perez 2007), the Maxwell equations simplify and reveal the following two equations determining the electric field:

A. L. Yarin et al., *Self-Healing Nanotextured Vascular Engineering Materials*, Advanced Structured Materials 105, https://doi.org/10.1007/978-3-030-05267-6_4

$$\nabla \cdot (\varepsilon \mathbf{E}) = 4\pi q \tag{4.1}$$

$$\nabla \times \mathbf{E} = 0 \tag{4.2}$$

where **E** is the electric field strength (boldfaced characters denote vectors), q is the bulk charge density (typically associated with ions in a solvent, rather than with a dissolved polymer), and ε is the relative permittivity, which is assumed to be constant. Here and hereinafter, Gaussian units are used.

Equation (4.2) shows that the electric field strength is a potential vector field, i.e.,

$$\mathbf{E} = -\nabla \varphi \tag{4.3}$$

with φ being the scalar potential.

Electrolytes possess electrical conductivity that is assumed to be ohmic, i.e., the electric current density vector $\mathbf{j}_e$ is determined by the potential gradient as

$$\mathbf{j}_e = -\sigma \nabla \varphi \tag{4.4}$$

with σ being the electrical conductivity, assumed to be constant.

On the other hand, bulk charges in a liquid at rest are redistributed by the electric current, and the charge-balance equation reads

$$\frac{\partial q}{\partial t} = -\nabla \cdot \mathbf{j}_e \tag{4.5}$$

where t is time and q is the bulk charge density.

Combining Eq. (4.1) with Eq. (4.3) and (4.4) with (4.5), the following system of two equations is derived

$$\nabla^2 \varphi = -\frac{4\pi q}{\varepsilon} \tag{4.6}$$

$$\frac{\partial q}{\partial t} = \sigma \nabla^2 \varphi \tag{4.7}$$

The substitution of the Poisson equation (4.6) into Eq. (4.7) yields a single equation for the bulk charge density

$$\frac{\partial q}{\partial t} = -\frac{4\pi\sigma}{\varepsilon} q \tag{4.8}$$

If at any place in an electrolyte at $t = 0$ an initial charge q_0 is injected, according to Eq. (4.7), it fades as

$$q = q_0 \exp(-t/\tau_C) \tag{4.9}$$

where

$$\tau_C = \frac{\varepsilon}{4\pi\,\sigma} \tag{4.10}$$

has units of time and is called the charge relaxation time. It is the characteristic time necessary for a charge to escape from an initially charged area because of the electric conductivity, however low it is.

In perfect conductors with very high electrical conductivities, the charge relaxation time approaches zero (i.e., the electric charges escape practically immediately), whereas in perfect dielectrics it should be infinite because they show zero conductivity. Electrolytes, however, possess finite and low electrical conductivities and thus show finite values of the charge relaxation times. For example, for water and oils the values of the charge relaxation times τ_C are between 1 μs and 20 s.

Accounting for the diffusion and convection of ions, the charge transport equation can be obtained as follows:

$$\frac{\partial q}{\partial t} + \nabla \cdot (q\mathbf{v}) = D\nabla^2 q - \frac{4\pi\,\sigma}{\varepsilon} q \tag{4.11}$$

which generalizes Eq. (4.8), where $\mathbf{v}$ is the flow velocity field, and D is the diffusion coefficient. The charge relaxation, being a purely electrical phenomenon is unaffected by the charge diffusion and convection, as reflected in Eqs. (4.10) and (4.11).

4.1.2 Formation of Electrospun Polymer NFs

The characteristic charge relaxation time of electrolytes significantly affects their possible interactions with electric fields in electrohydrodynamics. Any fluid flow possesses a characteristic hydrodynamic time τ_H, which may be associated with the residence time of material elements in the flow zone, correspond to the characteristic time of perturbation growth, or approach infinity in stationary situations. Therefore, a dimensionless group defined as the ratio of the two characteristic times can always be associated with flows of electrolytes:

$$\alpha = \frac{\tau_C}{\tau_H} \tag{4.12}$$

If, in a certain flow, the dimensionless charge relaxation time $\alpha << 1$, the electrolyte can be considered as a perfect conductor, even though its conductivity is relatively small. For example, in electrospinning, a polymer solution drop at the edge of the needle serving as one electrode, which is located at a certain distance from the counter-electrode (for example, a grounded plate), acquires stationary configurations with the liquid being at rest for a range of sub-critical voltages. In such cases, the characteristic hydrodynamic time $\tau_H = \infty$, and thus $\alpha = 0$, meaning that the electric

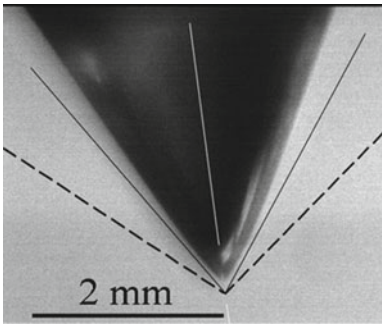

Fig. 4.1 Stationary drop shape under a sub-critical voltage near the critical voltage. The predicted critical shape corresponding to the Taylor cone with a half-angle of 49.3° at the tip (Taylor 1964), is shown by the dashed lines; the predictions of Yarin et al. (2001b) for the critical shape with the half-angle of 33.5° at the tip are shown by the solid lines. The reason for the difference between the Taylor cone and the experimentally observed critical shape is discussed in Yarin et al. (2001b) and Yarin et al. (2014). Reprinted with permission from Yarin et al. (2001b)

charges (ions) always have sufficient time to escape to the free surface and the liquid bulk becomes effectively uncharged. As a result, the bulk of the drop becomes effectively screened by the charges at its surface, which is identical to the case of perfect conductors. Therefore, such a drop in this case can be considered an equipotential perfect conductor. It is subjected to the electric Maxwell stresses pulling from the outside, in air, which describe the attraction of the net charges at the free surface to the counter-electrode. The balance of the Maxwell stresses with the surface tension determines the non-spherical stationary drop shape under such sub-critical voltages (Fig. 4.1).

Above the critical voltage, a stationary drop as shown in Fig. 4.1 is impossible, and jetting begins at the tip of the drop, as illustrated in Fig. 4.2. It is seen that in frame obtained at −28 ms the drop is already elongated by the Maxwell stresses associated with the applied electric potential. Then, the rounded tip becomes sharper, approaching a conical geometry, and a thin jet is issued from the tip. After the jet forms, elastic stresses and the surface tension both pull the cone back, while a rapidly elongating and thinning jet of polyethylene oxide (PEO) solution, carrying an electric charge, is continuously issued from the drop tip.

Electrified jets similar to that in Fig. 4.2 are prone to bending instability (Reneker et al. 2000; Yarin et al. 2014), such that a practically straight segment of the jet is followed by coils of increasing diameter (cf. Fig. 4.3). After several coils are formed, the electrical bending instability forms smaller coils on the larger coil, and so forth, as in a fractal, until the elongation stops, usually because of solvent evaporation and the solidification of the thin jet. In Fig. 4.3, the straight segment is red, the first bending coil is yellow, and the third bending coil is blue. Three turns or loops are presented in the yellow coil.

The characteristic growth time τ_H of the bending perturbations in electrospinning is very short ($\leq$1 ms). It is comparable or shorter than the charge relaxation time τ_C,

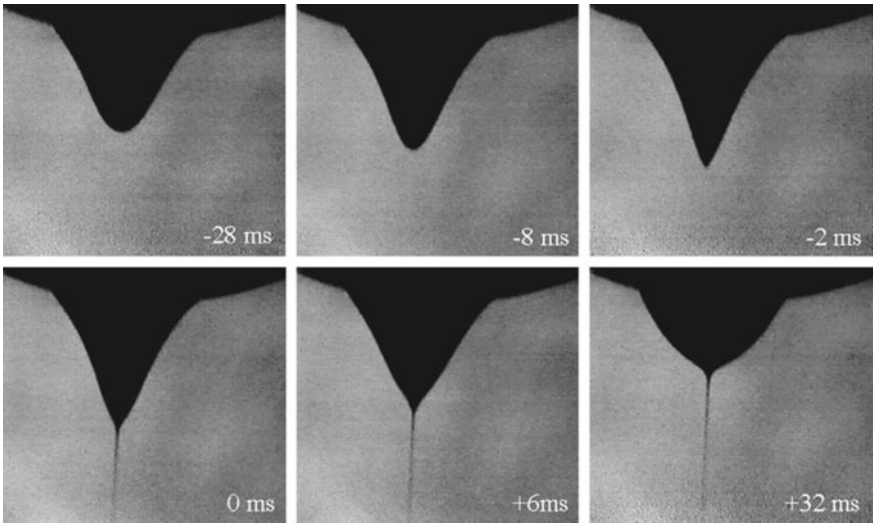

Fig. 4.2 Jetting from the drop tip subjected to a supercritical electric field (Fong and Reneker 2000). Selected images from a video in which a new image was recorded every 2 ms. The time zero is defined as the frame in which the jet first appears. The electrical potential is applied slightly more than 28 ms before the jet appears. The drop is PEO solution. Reprinted with permission from Reneker and Yarin (2008)

i.e., α of Eq. (4.12) is ≥ 1. This means that in a jet undergoing bending instability, charges do not have time to "relax", i.e., the electrical conduction practically ceases and the same liquid that behaves as a perfect conductor in the drop now behaves as a perfect dielectric, transporting only the charges embedded in it. Accordingly, when an inevitable bending perturbation occurs, a charge carried at the crest is pushed downward and outward by the Coulombic repulsion of the charges above the perturbed region (force $\mathbf{F}_{DO}$ in Fig. 4.4). Simultaneously, this perturbed segment is pushed upward and outward by the Coulombic repulsion of the charges below the perturbation (force $\mathbf{F}_{UO}$ in Fig. 4.4). The vector sum of these forces $\mathbf{F}_R$ is in the radial direction relative to the straight jet and sustains the growth of the radial displacement, i.e., it drives the bending instability. The local resulting electric force per unit length of the jet causing the electrically-driven bending instability is proportional to the local curvature k of the jet axis (Yarin et al. 2001a, 2014):

$$\mathbf{F}_R = -\delta^2 \ell n(L/a)|k|\mathbf{n} \tag{4.13}$$

where $\mathbf{n}$ is the local unit normal vector of the jet axis, δ is the electric charge per unit jet length, L is a certain cutoff length along the jet axis, and a is the local cross-sectional jet radius.

Bending perturbations in a fractal-like jet similar to that in Fig. 4.3 cause significant stretching, and thus the thinning of the jet. When the jet solidifies because of

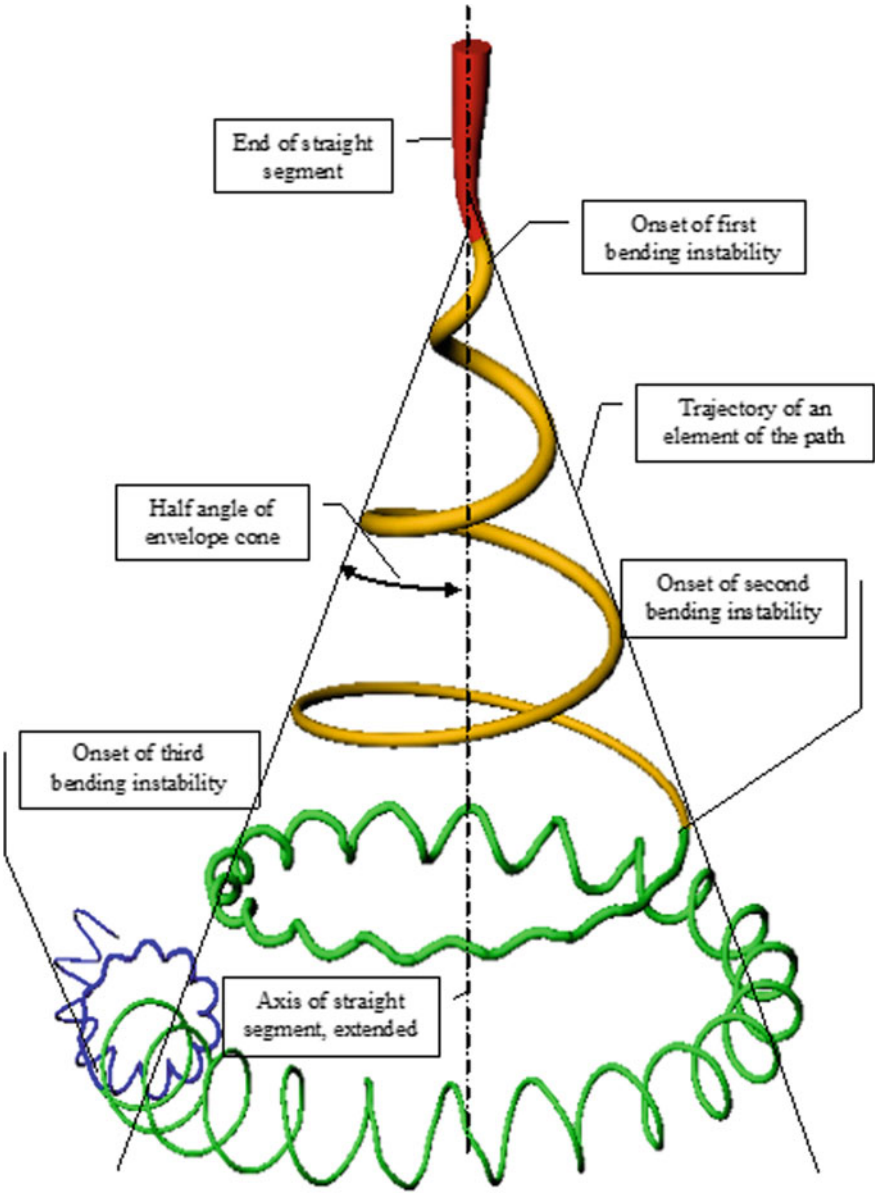

Fig. 4.3 Sketch of the prototypical instantaneous position of the path of an electrospinning jet containing three successive electrical bending instabilities. The straight segment is transformed into a three-dimensional coil. The jet path continues and is transformed to a smaller three-dimensional coil, with an axis following the curved path extrapolated from the first coil. The second spiral is eventually transformed to an even smaller spiral and so forth until the fractal-like jet is solidified by solvent evaporation. Reprinted with permission from Reneker and Yarin (2008)

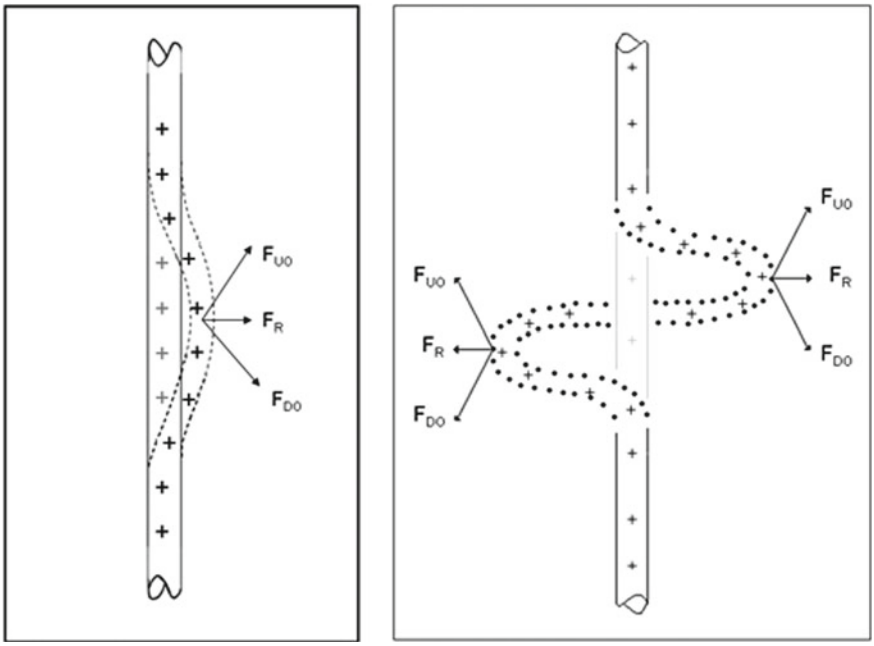

Fig. 4.4 A segment of an electrospinning jet at the location where a perturbed segment (shown in dotted lines) begins to grow in response to repulsive electric forces between the uniformly distributed charges carried by the jet. Reprinted with permission from Reneker and Yarin (2008)

solvent evaporation, its cross-sectional diameter is on the order of several hundred nanometers, i.e., NFs are formed by solidified jet.

The duality of the effective electric nature of electrolytes determined by the mutual rate of charge conduction and convection variation is reminiscent of the similar duality of polymeric liquids including polymer solutions used in electrospinning. Polymeric liquids are viscoelastic, i.e., they possess not only viscosity μ but also some elasticity characterized by the elastic modulus G. The ratio $\theta = \mu/G$ has units of time and is the elastic relaxation time, characterizing the effective duration of the shape memory of such liquids. In flowing polymeric liquids, the expected rheological behavior can be evaluated using the Deborah number $De = \theta/\tau_H$. If De << 1, the flow is termed weak; the liquid has sufficient time to "forget" any previous geometric configurations and to relax residual elastic stresses. In such a situation, a polymeric liquid behaves like a purely viscous Newtonian liquid. On the other hand, in strong flows with large De values, the elastic stresses do not have sufficient time to relax and instead become accumulated; the liquid behaves as a neo-Hookean elastic solid. Solid elastic bodies have infinite shape memories, and thus $De = \infty$. A ball of Silly Putty, which is mostly polydimethylsiloxane (PDMS) thrown against a wall bounces back elastically (De >> 1); the same ball placed gently on a table spreads slowly into a puddle (De << 1). When De is ~1, the polymeric liquid behaves as a viscoelastic

medium in which elastic stresses accumulate and relax in concert during flow and act simultaneously with viscous stresses. The analogy allows a conceptual interpretation of electrolytes as electrical Silly Putty.

It should be emphasized that polymeric liquids are spinnable when they can generate significant longitudinal stresses of elastic origin in stretching (Yarin et al. 2014). Spinnability is fundamental for any fiber-forming process, e.g., for electrospinning, co-electrospinning, solution blowing, emulsion spinning, and emulsion blowing, as discussed in the present chapter. The elastic stresses counteract bending and tend to diminish the radial spread of the jet paths, similar to the jet shown in Fig. 4.3.

4.2 Co-electrospinning

Co-electrospinning of core-shell micro- and NFs was first introduced by Sun et al. (2003). It was understood from the beginning that the shell material issuing from the annular needle surrounding the core needle should be a viscoelastic solution of a spinnable polymer, whereas the core material could be either a viscoelastic solution of a spinnable polymer or an inelastic liquid, e.g., oil, polymer monomer, salt solution, or any other solution, suspension, or emulsion. As with electrospinning, described in Sect. 4.1, co-electrospinning is driven by electric forces acting on ionic conductive liquids subjected to direct-current electric fields, which stretch core-shell jets by direct pulling, as well as by the growth of the electrically-driven bending instability. Co-electrospinning is discussed in detail in the monograph of Yarin et al. (2014). Here it should be emphasized that the possibility of encapsulating inelastic non-polymeric materials within the cores of core-shell NFs, inherent to co-electrospinning, is fundamentally important for forming NFs containing healing agents, which are materials of exactly this type.

Following Lee et al. (2015), the co-electrospinning of core-shell NFs is considered, with healing agents embedded in the cores of NFs used to fabricate self-healing composites. Polyacrylonitrile (PAN, $M_w = 150$ kDa) dissolved in N, N dimethylformamide (DMF, 99.8%) was used as a viscoelastic shell solution (8 wt% of PAN). The two components of PDMS (Sylgard 184), component A (resin monomer, dimethyl siloxane, DMS; cf. Sect. 2.2) and component B (curing agent, dimethyl-methyl hydrogen-siloxane, DMHS; also cf. Sect. 2.2) served as healing agents issuing from the core needles. The two components of PDMS are separately supplied to the core needles of the co-electrospinning apparatus for embedding within the individual NF cores, as shown in Fig. 4.5a. The resin monomer is diluted by n-hexane in the ratio of 2:1 (wt%), respectively, while the curing agent is used without further modification. As shown in Fig. 4.5a, for the first type of fiber, the diluted resin monomer solution (Q_{1R}) and PAN solution (Q_2) are separately supplied as the core and shell materials, respectively. For the second type of fibers, the pure curing agent solution (Q_{1C}) and PAN solution (Q_2) are separately supplied as the core and shell materials, respectively. Both types of fibers are simultaneously co-electrospun on the same rotating drum, forming a mutually entangled matrix.

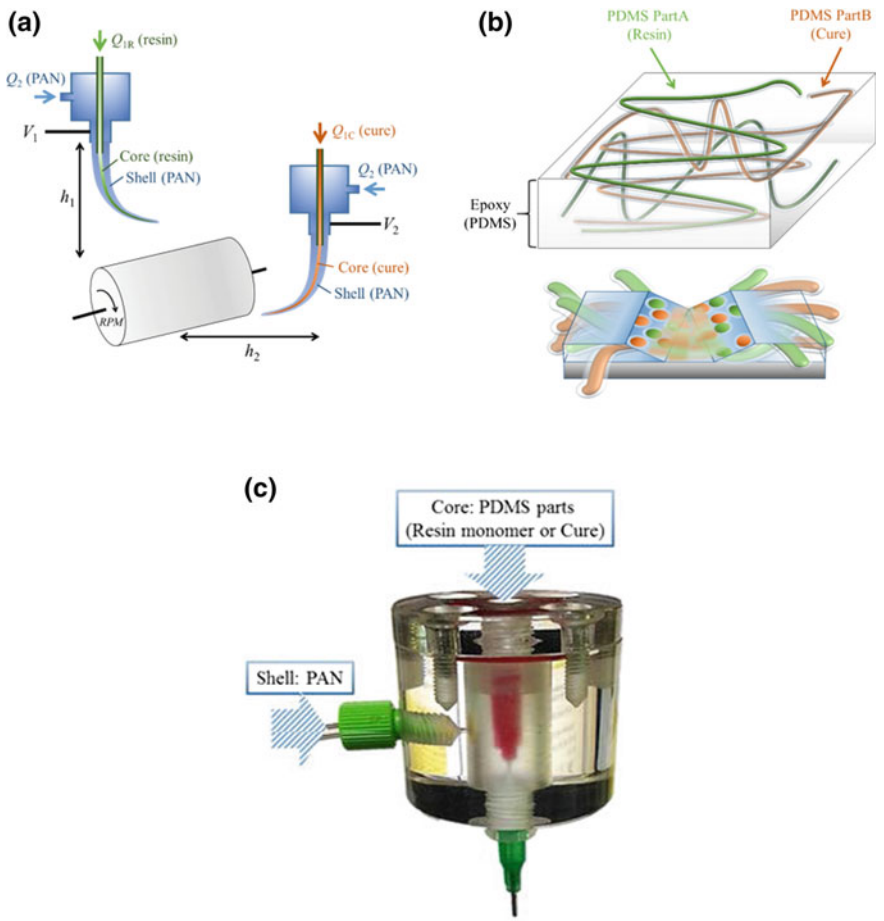

Fig. 4.5 **a** Schematic of experimental apparatus for simultaneous co-electrospinning of core-shell NFs containing separate binary components of self-healing agent in their cores. **b** Structure of self-healing fiber-reinforced composite: core-shell NFs with resin monomer and curing agent in the core are mutually-entangled and embedded in the PDMS matrix. When damage occurs, the resin monomer and curing agent are released; the polymerization reaction yields PDMS-reinforced healing. Reprinted with permission from Lee et al. (2015). **c** Image of the coaxial nozzles used to form self-healing core-shell NFs. Reprinted with permission from Lee et al. (2017a)

On the other hand, in Sinha-Ray et al. (2012), the co-electrospinning of core-shell fibers was realized using different healing agents of dicyclopentadiene (DCPD) and isophorone diisocyanate (see Sects. 2.1, 2.3, and 4.6).

Figure 4.5a demonstrates the supply of the core and shell solutions to the core and shell needles with flow rates of Q_1 and Q_2, respectively. Thus, the core materials (either the DMS resin monomer, or its curing agent) are stored in the liquid state within the cores of the core-shell fibers; each core is surrounded by a PAN shell

Table 4.1 Experimental parameters of the co-electrospinning apparatus in Lee et al. (2015)

		Flow rate	Voltage	Needle-to-collector distance	Angular velocity of collector drum
Core (ID: 0.61 mm/ OD: 0.91 mm)	Resin monomer	Q_{1R} = 0.07 ml/h	V_1 = 12–13 kV	h_1 = 10 cm	200 rpm
	Curing agent	Q_{1C} = 0.07 ml/h	V_2 = 12–13 kV	h_2 = 10 cm	
Shell (ID: 1.36 mm/ OD: 1.65 mm)	PAN	Q_2 = 0.9 ml/h	As for the core	As for the core	

ID—inner diameter, OD—outer diameter

in these separate NF types. As mentioned above, both types of co-electrospun NFs (containing either the resin monomer or curing agent in the core) are collected on a rotating drum collector for a period of 30 min (cf. Fig. 4.5a).

The parameters for the co-electrospinning process are listed in Table 4.1. The fiber-reinforced composite and the spreading of healing agents released in the damaged area are depicted in Fig. 4.5b. The resin monomer (green) and curing agent (orange) are encapsulated separately within the core-shell fibers; entire mutually-entangled NF mats are infiltrated by PDMS matrix. When the fibers are damaged by microcracks and the encapsulated liquid agents are released, the resin monomer and curing agent participate in a polymerization reaction, thus forming PDMS healing links.

The scanning electron microscopy (SEM) images of the pristine NF mats are shown in Fig. 4.6a (the PAN fiber mat) and 4.6b (the self-healing core-shell PAN–resin–curing agent, PRC fiber mat). The PAN NFs in Fig. 4.6a are uniform with the fiber cross-sectional diameter of 588 ± 135 nm. Furthermore, in the pristine self-healing PRC fiber mat, fibers with two different diameters of 1.32 ± 0.50 μm and 373 ± 105 nm can be distinguished; these are the fibers with the resin monomer and curing agent within the core, respectively, as demonstrated in Fig. 4.6b. Following stretching, it is observed that some of the originally intact PAN NFs are torn apart; and the suspended edges of these damaged fibers exhibit a curled appearance (cf. Fig. 4.6c). Moreover, the fiber diameter is decreased from 588 ± 135 nm to 544 ± 180 nm. As shown in Fig. 4.6d, after stretching some of the self-healing PRC fibers are also torn with tortuous edges. Spherical masses of released and polymerized PDMS are visible at the edges of the damaged fibers. The average diameter of the fibers is 578 ± 138 nm.

In addition, transmission electron microscopy (TEM) was employed to directly observe the core of the core-shell NFs. The results shown in Fig. 4.7 reveal the core-shell structures.

A similar approach was also employed by An et al. (2015). Figure 4.8a, b show the SEM images of resin monomer–PAN (R-PAN) and curing agent–PAN (C-PAN)

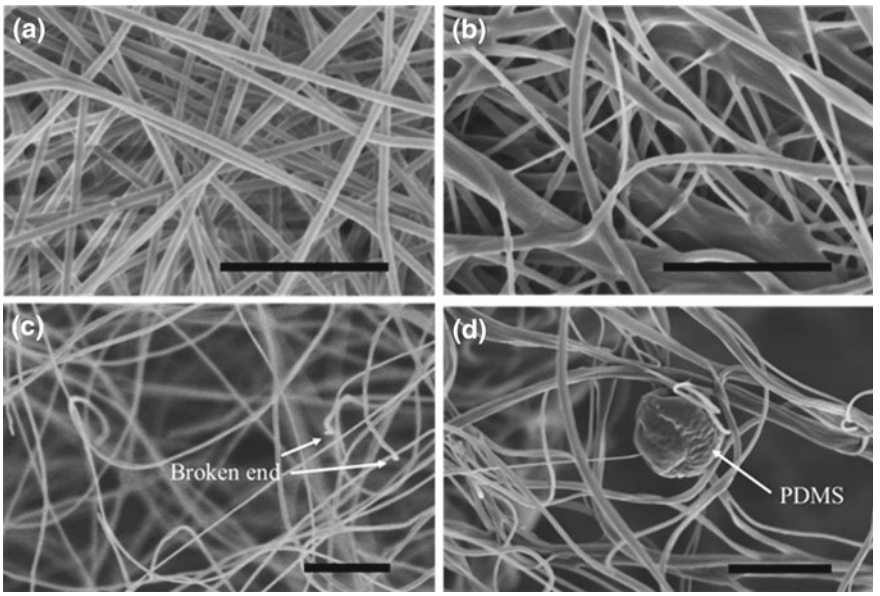

Fig. 4.6 SEM images of pristine fiber mats: **a** PAN NF mat, **b** the self-healing PRC nanofiber mat. The same mats following the repeated (third) tensile test: **c** PAN nanofiber mat with a fiber diameter of approximately 544 ± 180 nm, **d** PAN–resin–curing agent (PRC) NF mat, with the average fiber diameter of 578 ± 138 nm. The scale bars are 10 μm. Reprinted with permission from Lee et al. (2015)

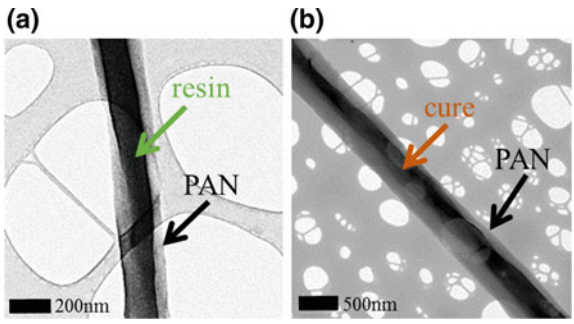

Fig. 4.7 TEM images of core-shell NFs. **a** Resin–PAN fiber, and **b** curing agent–PAN fiber. Reprinted with permission from Lee et al. (2015)

core-shell NFs. The NFs are sufficiently uniform with no beads observed. The diameter of the core-shell NFs is in the 300–350 nm range.

The presence of the core materials in these NFs was confirmed by pressing the NFs, deposited on a steel substrate, with tweezers. In Fig. 4.8c, d, the liquid core materials (the healing agents) are clearly seen after leaking from the ruptured NFs. It should be emphasized that the liquid state of the core materials is maintained throughout the entire co-electrospinning process, even after solvent evaporation, precipitation, and solidification of the shell (Reneker et al. 2000; Yarin et al. 2014).

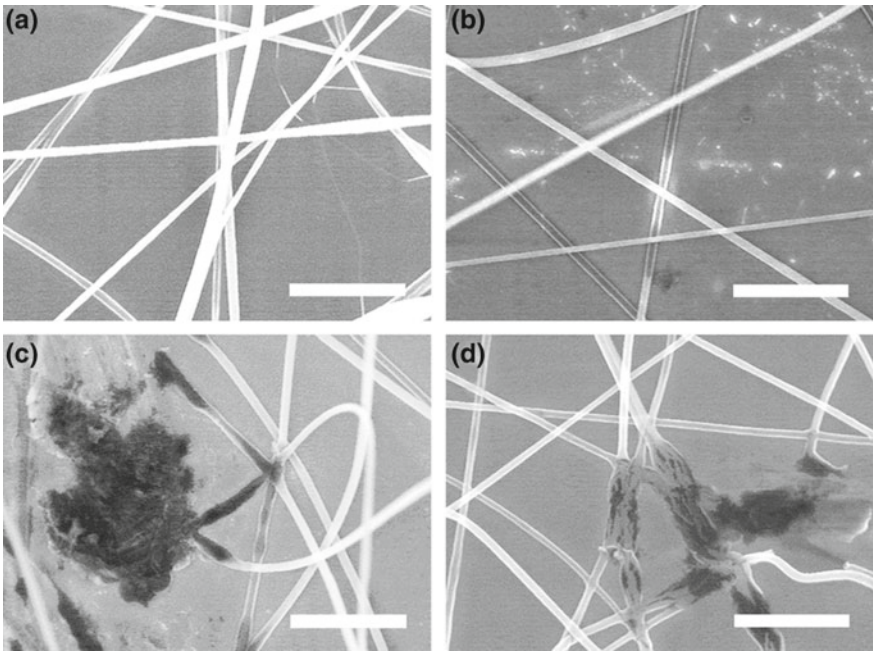

Fig. 4.8 SEM images of core-shell NFs. **a** R-PAN NFs, **b** C-PAN NFs, **c** ruptured R-PAN NFs, **d** ruptured C-PAN NFs. NFs shown in panels **c** and **d** were ruptured using a tweezer to observe release of the healing agent materials from the core. The scale bars are 6 μm. Reprinted with permission from An et al. (2015)

To further corroborate the core-shell structure of the NFs, TEM images were obtained as shown in Fig. 4.9. The TEM samples were prepared by depositing the NFs onto a copper grid for a few seconds. The interfacial boundary lines between the core and the shell are clearly visible in both the R-PAN and C-PAN NFs. The diameters of the whole core-shell NFs and their cores in the case of the R-PAN NFs are ∼293 nm and ∼189 nm, respectively. In the case of the C-PAN NFs, the diameter of the whole core-shell NFs and their cores were ∼360 nm and ∼195 nm, respectively.

Note also that Park and Braun (2010) used co-electrospinning from coaxial needles, similar to those in Fig. 4.5a, to fabricate self-healing core-shell-structured NFs. The core was filled with either part A (resin monomer) or part B (curing agent) of a siloxane-based healing agent, while a polyvinylpyrrolidone (PVP) solution in DMF was used to form the shell. The co-electrospun NFs were then embedded within a polymeric matrix to form a composite. It is known that beads are formed on electrospun NFs when the elastic forces in the polymer jet are insufficient to suppress capillary instability (Yarin 1993; Yarin et al. 2001a, 2014; Reneker et al. 2007; Lee et al. 2013a). Park and Braun (2010) fabricated bead-on-the-string NFs, rather than smooth NFs, such that the outer diameters of the "strings" and beads were on the

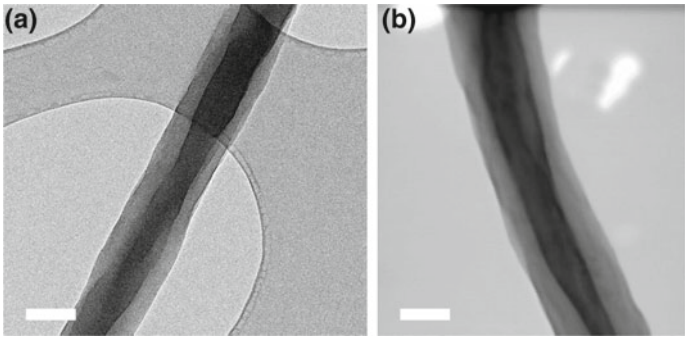

Fig. 4.9 TEM images of core-shell NFs. **a** R-PAN NFs. **b** C-PAN NFs. The scale bars are 200 nm. Reprinted with permission from An et al. (2015)

orders of hundreds of nanometers and several micrometers, respectively. Therefore, the healing agent was primarily present within capsule-like beads with the outer diameter of 2–10 μm. For this reason, the results presented by Park and Braun (2010) are more similar to those of the capsule-based approach discussed in Sect. 1.3.

Table 4.2 summarizes the parameters used to create the different fibers formed by co-electrospinning, emulsion spinning, solution blowing, coaxial solution blowing, and emulsion blowing, as discussed in Sects. 4.3–4.6.

4.3 Emulsion Spinning

The emulsion spinning of core-shell NFs was introduced in Bazilevsky et al. (2007) as a novel method derived from electrospinning. Emulsion spinning begins with the blending of two polymer solutions prepared in the same solvent. Over time, typically on the scale of several hours to one day, the spinodal decomposition occurs; one polymer solution forms droplets dispersed in a matrix formed by the other polymer solution. By manipulating the initial blend composition, the contents of the dispersed and matrix phases can be controlled. When such emulsions are electrospun from a single needle, dispersed droplets are periodically entrained and stuck at the source of the thin electrically-driven jet of the matrix solution (cf. Fig. 4.2). The solution droplet is entrained into the jet by viscous forces and occupies the core of the jet (Bazilevsky et al. 2007; Yarin 2011; Yarin et al. 2014). Because of the significant jet stretching in the course of the bending instability, one 100 μm diameter droplet can form a 1 m long core-shell NF. With dispersed droplets periodically entrained into the jet source, most of the length of the resulting NFs possesses a core-shell structure with only a few discontinuities in the core.

Self-healing NFs with healing agents in the core were formed using the emulsion spinning by Lee et al. (2014a, b). In these works, a platinum-catalyst-containing dimethylvinyl-terminated DMS (cf. Sect. 2.2) resin monomer was employed with an appropriate curing agent used as a healing agent. Specifically, the curing agent material DMHS (cf. Sect. 2.2) is emulsified in a PAN solution and electrospun into

Table 4.2 Characteristics of NFs formed by co-electrospinning, emulsion spinning, coaxial solution blowing, and emulsion blowing

Fabrication method	Shell material	Composite structure	Fiber diameter (nm)	Healing agent	Reference
Co-electrospinning	PVP	Polymeric matrix	Hundreds (OD, NFs) /Thousands (OD, beads)	Siloxane-based	Park and Braun (2010)
Co-electrospinning /emulsion spinning /emulsion blowing	PAN	–	1000–2000 (OD) /450–1000 (ID)	DCPD-based or isocyanate-based	Sinha-Ray et al. (2012)
Emulsion spinning	PAN	Epoxy matrix	444 (OD)	Siloxane-based	Lee et al. (2014a)
Emulsion spinning	PAN	Epoxy matrix	200–300 (OD, NFs) /600–1000 (OD, beads)	Siloxane-based	Lee et al. (2014b)
Co-electrospinning	PAN	Epoxy matrix	300–360 (OD) /190–200 (ID)	Siloxane-based	An et al. (2015)
Co-electrospinning	PAN	PDMS matrix	1320 (OD, resin part) /373 (OD, curing agent part)	Siloxane-based	Lee et al. (2015)
Coaxial solution blowing	PVDF/PEO	PDMS matrix	980 (OD)	Thiol-epoxy-based	Lee et al. (2016a)
Coaxial solution blowing	PVDF/PEO	–	1563 (OD, resin part) /675 (OD, hardener part)	Thiol-epoxy-based	Lee et al. (2016c)

ID—inner diameter, OD—outer diameter, PVP—polyvinylpyrrolidone, NFs—nanofibers, PAN—polyacrylonitrile, PDMS—polydimethylsiloxane

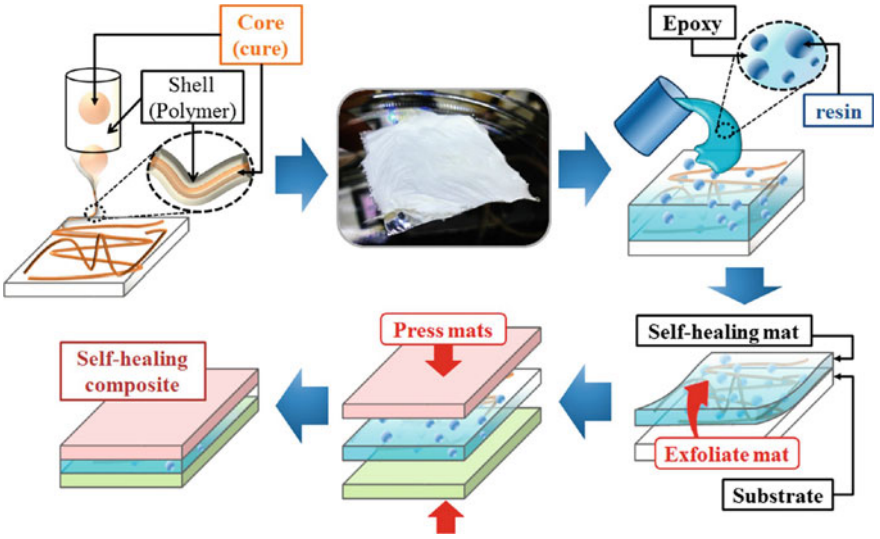

Fig. 4.10 Schematic of the emulsion electrospinning of core-shell NFs (on the left) and their encapsulation in an epoxy−resin emulsion to prepare a self-healing composite. Reprinted with permission from Lee et al. (2014b)

core-shell NFs, with the curing agent in the core and PAN in the shell, as depicted in Fig. 4.10. Note that in Sinha-Ray et al. (2012) the emulsion spinning of core-shell fibers was conducted with two different healing agents of dicyclopentadiene (DCPD) and isophorone diisocyanate (see Sects. 2.1, 2.3, and 4.6).

Using the emulsion electrospinning, core-shell NFs containing DMHS (curing agent) in the core were electrospun from the curing agent emulsion in a PAN-DMF solution onto several substrates. The curing agent droplets were dispersed in the 8 wt% PAN ($M_w = 150$ kDa) solution in DMF, denoted as PAN-DMF. Because it is electrospun from a single needle, this emulsion forms core-shell fibers with curing agent in the core and PAN shells. The weight ratio of the core-to-shell materials was 1:5. The resulting emulsion was mixed for 24 h using a magnetic stirrer. To refine the emulsified droplets, the emulsion was sonicated for 15 s eight times, with a total sonication time of ~2 min. Because the emulsion was metastable, it was electrospun within 1 h of preparation. The flow rate of the emulsion was 400 μl/h $< Q <$ 500 μl/h. The voltage applied to the needle was 7 kV $< V <$ 8.6 kV. The standoff distance between the needle exit and substrate was 7 cm. The inner and outer diameters of the needle were 0.84 and 1.27 mm, respectively. The durations of electrospinning were $t_{dep} = 3$ and 10 min, which yielded as-spun NF mats with different amounts of curing agent. The amount of curing agent can also be controlled by varying the curing agent concentration, flow rate, and standoff distance. However, Lee et al. (2014b) chose the deposition time as a parameter controlling the curing agent amount.

Figure 4.11a shows a NF mat deposited on an aluminum foil. The SEM image of that NF mat, reproduced in Fig. 4.11b shows NFs of 200−300 nm in diameter in regions without beads. Beads are formed because of the capillary instability (Yarin

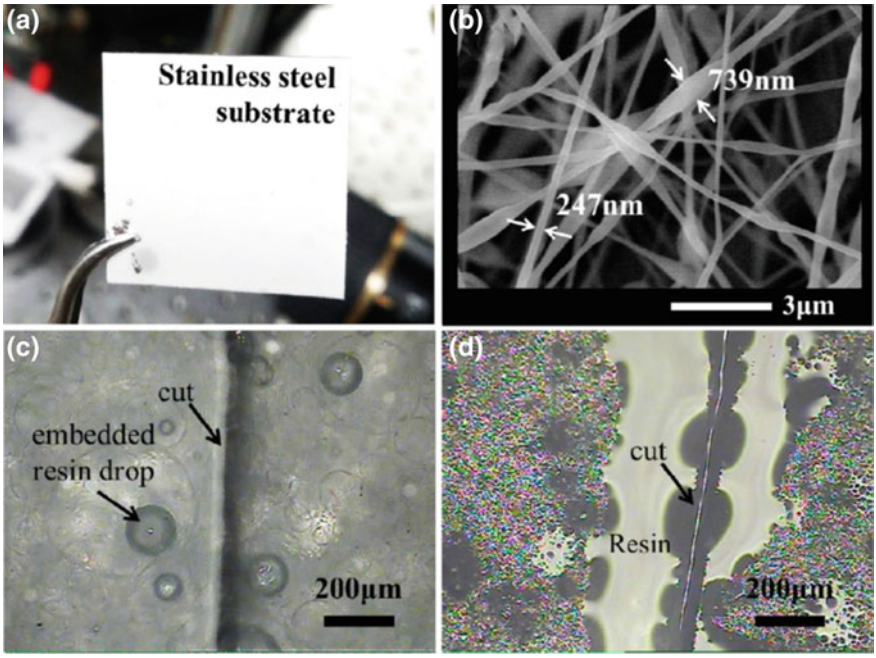

Fig. 4.11 **a** Macroscopic image of a mat of core-shell NFs with curing agent encapsulated in the core. **b** SEM image of core-shell NFs from the mat in panel **a**. **c** Optical microscopy (OM) image of a cut through a film of solidified epoxy with embedded resin droplets (a 20 wt% resin sample). **d** Resin released from the cut in panel **c**. Reprinted with permission from Lee et al. (2014b)

1993; Yarin et al. 2017). The uniformity of NFs could be improved by increasing the electrical conductivity and spinnability (elasticity) of the solution, as demonstrated for monolithic fibers electrospun from other polymer solutions (Lee et al. 2013a, b). However, in the work of Lee et al. (2014b), no additive was used in order to maintain the purity of the NFs to facilitate sample analyses.

In addition, an emulsion of DMS resin monomer droplets in epoxy was prepared and later poured into an as-spun NF matrix. The resulting material, composed of both curing agent-containing NFs and resin-containing epoxy, was solidified as a composite self-healing mat. In such an epoxy-based composite, the resin monomer and the catalyst were encapsulated in microdroplets, whereas the curing agent was encapsulated in the vascular system formed by core-shell NFs. Unlike the self-healing composite of Sect. 4.2, which incorporated both healing agents of the resin monomer and curing agent in the cores of two types of core-shell NFs, the hybrid composite of Fig. 4.10 incorporates the healing agents in microdroplets and NFs. DMS resin could also have been encapsulated in the NF cores; this approach was not adopted by Lee et al. (2014b) because it would require a significant amount of DMS. Indeed, the optimal curing reaction stoichiometry requires 10 times more DMS resin than curing agent, a difficult ratio to meet if the resin monomer is brought into the NF cores (Mata et al. 2005). However, the approach is still possible, as discussed later in this section. Therefore, it is preferable to deliver the curing agent as the NF cores,

Table 4.3 Viscosity of the resin monomer−epoxy emulsion

Resin concentration (wt%)	5	10	20
Viscosity [cP]	8600	10080	14100

while dispersing sufficient amount of DMS resin in the epoxy matrix, as sketched in Fig. 4.10. Furthermore, Lee et al. (2014b) adopted this approach because the emulsified resin monomer microdroplets within the epoxy are spherical and do not require any shell. When the epoxy solidifies, it encapsulates and preserves the resin monomer droplets. The resin monomer polymerizes in the presence of the curing agent to form PDMS resin when both agents are released from the microdroplets and NFs, respectively, after the hybrid material has been fractured.

The epoxy−resin emulsions are prepared by mixing 5, 10, and 20 wt% resin monomer relative to the weight of epoxy (Evergreen Pro, Samhwa Paint), as sketched in Fig. 4.10. The epoxy−resin emulsions were milky and turbid, with the resin monomer and epoxy dispersed and continuous phases, respectively. To fragment the resin monomer drops in the emulsion into finer droplets, the emulsion was sonicated for 2 min using an ultrasonicator (Q700; Qsonica, Newtown, CT). The temperature of the emulsion (70 °C) was monitored to remain below the boiling temperature of the solvent DMF ($T_b \sim 154$ °C). The emulsion preparation was conducted in air at room temperature.

Optical microscopy (OM) images of the resin monomer−epoxy emulsions with resin monomer concentrations of 5, 10, and 20 wt% are shown in Fig. 4.12. The resin monomer droplets in the emulsions are perfectly spherical. At least 10 OM images were used to measure a statistically sound droplet-size distribution and the average droplet size. Emulsions with higher resin monomer concentrations show larger resin monomer droplets. The average diameters of the resin droplets are 19, 23, and 27 μm for the 5, 10, and 20 wt% resin monomer concentrations, respectively, as shown in Fig. 4.12d. In Fig. 4.12e, the average drop diameter versus resin concentration is shown. The number of drops N is increased with the resin monomer concentration (Fig. 4.12e). In particular, for a 5−10 wt% concentration increase, nearly a 20% increase in the number of resin monomer droplets is observed compared to the initial droplet number N at 5wt% concentration. When the resin monomer concentration is increased from 10 to 20 wt%, an additional 20% increase in N is observed. An increase in the number and size of emulsified droplets with the concentration was also reported by Osborn and Akoh (2004), who studied oil-in-water emulsions. Higher resin monomer contents yield higher-viscosity emulsions, as summarized in Table 4.3. The later finding is also consistent with the observations of Chanamai and McClements (2000).

As a final step, the epoxy−resin monomer emulsion was poured onto the core-shell curing agent-containing NF mats. Approximately 24 h were required to solidify the epoxy−resin monomer layer. It should be emphasized that when NFs are embedded, the epoxy spreads because of the wettability of the matrix. If, during this process, significant pulling forces were developed and the NFs ruptured, the curing

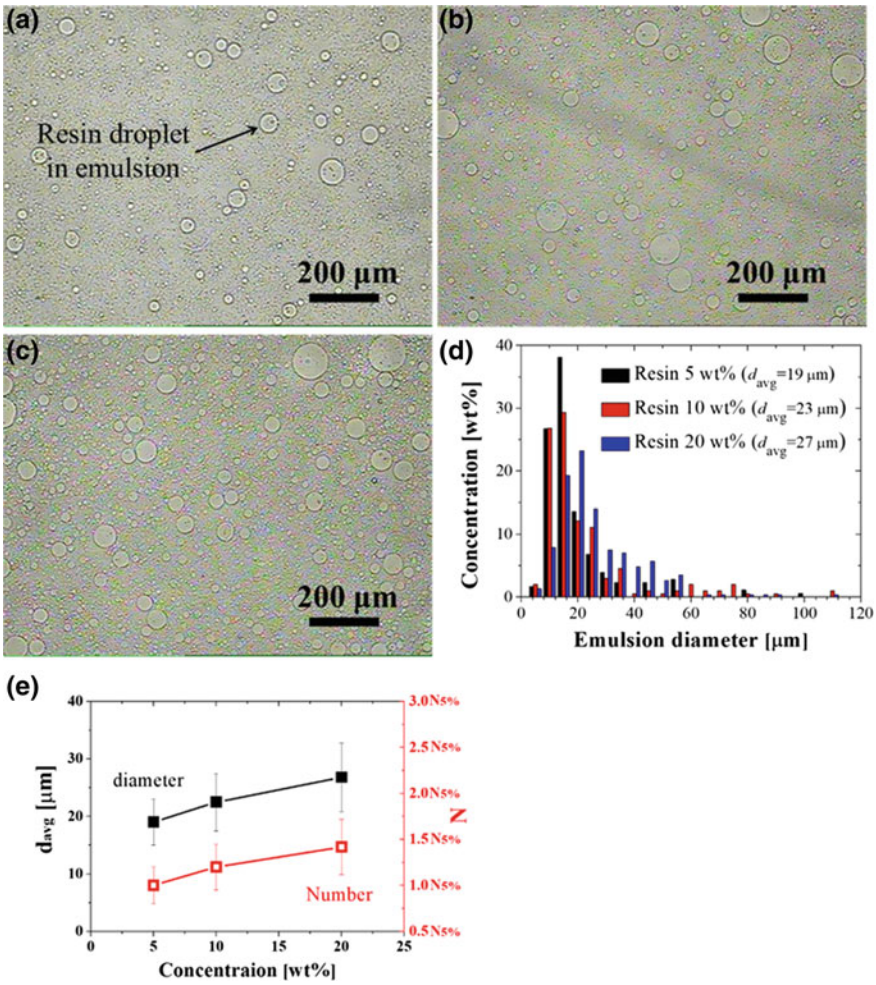

Fig. 4.12 Optical images of emulsions: **a** 5 wt% resin, **b** 10 wt% resin, and **c** 20 wt% resin monomer. **d** Size distribution of resin droplets in emulsions of different concentrations. **e** Emulsion droplet average diameter and the number of drops in the emulsion. Reprinted with permission from Lee et al. (2014b)

agent would be released and the resin monomer would polymerize, which would immediately stop the epoxy from spreading. Because the spreading proceeded, the NFs were not ruptured.

Panels **c** and **d** in Fig. 4.11 show OM images of the solidified epoxy-resin monomer matrix alone with no encased NFs for the sake of better visualization, with the encapsulated droplets containing liquid resin monomer in the solid epoxy matrix. The solidified epoxy-resin monomer film is prepared by drop-casting of 5 ml of the resin monomer-epoxy solution followed by 24 h drying and solidification. A deep cut was introduced with a razor through the solidified matrix, as shown in Fig. 4.11c.

The figure also shows that the size of a nearby embedded resin-monomer droplet, as highlighted by an arrow, is approximately 100 μm. These embedded resin droplets are fractured by the cut and thus release the liquid resin monomer. The OM image in Fig. 4.11d is obtained 2 h after the cut is inflicted. The material surrounding the cut-line is wet and impregnated with released resin monomer, as designed. The epoxy matrix is hydrophobic when solidified. Therefore, only oil-like substances such as the resin monomer can impregnate voids or cuts in the epoxy. The released resin monomer does not undergo polymerization and solidification unless it makes contact with the curing agent. Because the solidified matrix in Fig. 4.11 does not include curing agent-containing NFs, the released resin monomer remains a liquid.

Lee et al. (2014a) used emulsion spinning to form a fully vascular NF mat incorporating two mutually entangled networks of core-shell NFs containing either resin monomer or curing agent in the cores, rather than the hybrid system shown in Figs. 4.10 and 4.11. Figure 4.13 depicts the processes required for the dual-emulsion electrospinning and formation of a self-healing coating on a steel surface. A solution of the core material (dimethylvinyl-terminated DMS resin monomer) is prepared first using n-hexane as a solvent. Liquid curing agent (DMHS) is used with no solvent. Furthermore, a polymer solution of PAN in DMF is prepared to form the NF shell. The core liquids are separately emulsified in this PAN solution. Then the two emulsions of DMS in PAN matrix, and DMHS in PAN are electrospun from separate single needles to form a dual-NF mat containing mutually entangled NFs with cores of either DMS or DMHS, both encapsulated in PAN shells. Within the NF cores, both the resin monomer and curing agent are present as liquids. Finally, the dual-NF mat is intercalated with PDMS, which is solidified as an outer matrix for the self-healing composite. All these steps are performed under atmospheric conditions at room temperature.

Figure 4.13a shows that the shell material is prepared by dissolving PAN pellets (8 wt%) in DMF. To prepare one of the core solutions, the resin monomer is mixed with n-hexane at the volume ratio 1:1. This solution is emulsified in the PAN–DMF 20 wt% solution (Fig. 4.13a). The liquid curing agent is separately emulsified in a second batch of PAN–DMF 20 wt% solution. Thus, two separate emulsions are prepared for the dual-emulsion electrospinning. During the emulsion electrospinning illustrated in Fig. 4.13b, the shell material (PAN solution) forms a jet, while the tips of the droplets of either of the two core materials are entrained into the jet source and thus into the jet core by viscous forces. The dual-emulsion electrospinning of the DMS and DMHS emulsions in PAN matrices is performed onto a rotating drum collector, as depicted in Fig. 4.13c. As a result, a dual-NF mat containing NFs with either DMS resin or DMHS cores (blue or orange, respectively) is formed.

An optical image in Fig. 4.14a shows the catalyst-including resin monomer blended with the PAN–DMF solution. This image clearly illustrates that the resin monomer (DMS) is unsuitable for direct emulsification in the PAN–DMF solution. The DMS forms irregular chunks dispersed in the PAN–DMF solution. Even after 2 days of waiting, no reasonable emulsion is achieved; only the aggregation of these irregular chunks is observed. In general, to form an appropriate emulsion in PAN–DMF, the dispersed phase should be a non-polar fluid and the continuous

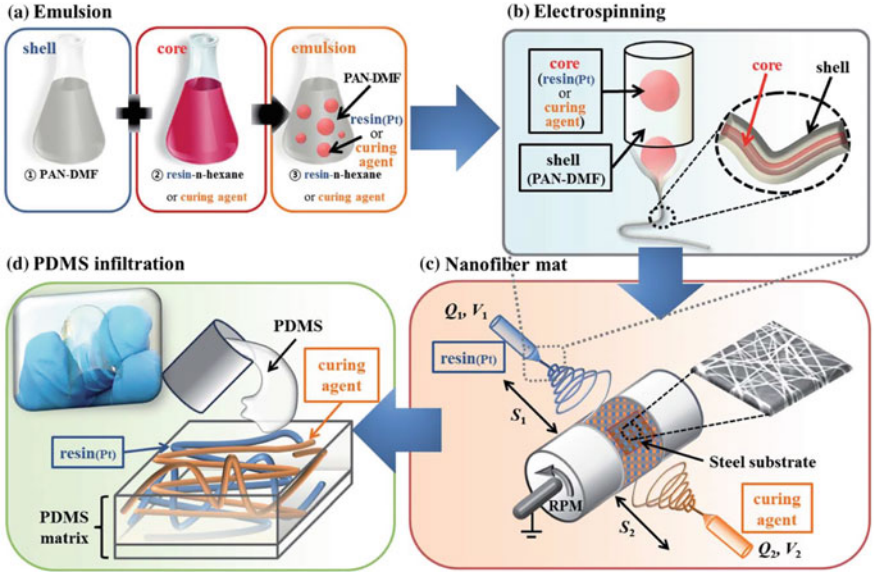

Fig. 4.13 Schematic. **a** Preparation of the shell polymer solution and two emulsions (DMF resin monomer and curing agent). **b** Emulsion electrospinning. **c** Dual-coating emulsion electrospinning setup. **d** PDMS matrix infiltration. Reprinted with permission from Lee et al. (2014a)

phase should be a polar fluid, or vice versa; these are immiscible and thus form a well-defined emulsion structure. In the present case, DMF (the continuous phase) is a polar fluid, and thus, the dispersed phase should be non-polar. However, the resin monomer DMS is a weak non-polar fluid, and thus, a strong non-polar fluid (such as n-hexane) should be added to it. Because both the resin monomer and n-hexane are non-polar, they mix well. This mixture is blended with the PAN–DMF solution, yielding the well-defined emulsion structure shown in Fig. 4.14b. In addition, mixing the resin monomer with n-hexane also provides the advantage of a moderate viscosity. It should be emphasized that even well-defined emulsions are only metastable. After 60 h, the emulsified droplets merged, forming stratified layers of the resin monomer–n-hexane solution and the PAN–DMF solution (not shown here).

The curing agent is easily blended and emulsified in the PAN–DMF solution without any additives; see Fig. 4.14c. Both core materials (resin–n-hexane and curing agent emulsions) were blended separately with the PAN–DMF solution (shell material) with the core-to-shell weight ratio of 1:5, as depicted in Fig. 4.13a. Figure 4.14d shows the size distribution of the core material droplets (resin–n-hexane or curing agent) indicating a range of diameters from ~10 to ~150 μm. The average sizes of the emulsified resin–n-hexane and curing agent droplets are 50 and 46 μm, respectively.

A photograph of the self-healing NF mat comprising both resin–n-hexane and curing agent NFs is shown in Fig. 4.15a. The mat is deposited onto an aluminum foil and is not intercalated with PDMS for visualization purposes. It has a milky appearance

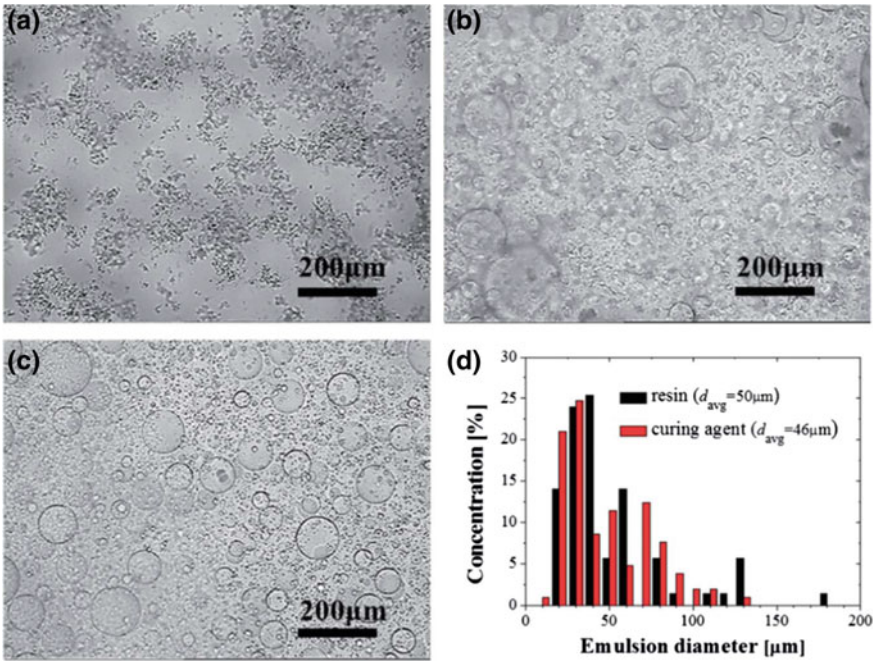

Fig. 4.14 OM images. **a** Emulsion of resin monomer (DMS) in PAN–DMF. **b** Emulsion of resin–n-hexane (1:1 v/v) in PAN–DMF. **c** Curing agent emulsion in PAN–DMF. **d** Emulsion droplet size distribution corresponding to panels **b** and **c**. Reprinted with permission from Lee et al. (2014a)

because of the submicrometer fiber size. The SEM images of the electrospun NFs are discussed next. The deposition time is set to only 30 s only to produce thin NF mats for visualization purposes. Because the core materials are encapsulated inside the NFs, they are invisible in the images (see Fig. 4.15b). To confirm the presence of the core materials in the NFs, the NFs are manually pressed at various locations using a pair of tweezers. The morphology of the pressed NF mat is seen in the SEM image in Fig. 4.15c. The image shows that the cores are ruptured and the core materials are squeezed out of the damaged NFs. This confirms the presence of the core materials in the liquid state within the NFs formed using emulsion electrospinning. The squeezed-out material seen in Fig. 4.15c has already solidified after polymerization between the released resin and curing agent. It should be emphasized that the damaged and self-healed sections of NFs would be definitely modified by the presence of the released polymerized material filling the cuts, as shown in Fig. 4.15c.

The size distributions of the resin–n-hexane and the curing agent NFs should not differ significantly. Despite having different core materials, their emulsified droplet sizes are comparable (see Fig. 4.14d). In addition, they use the same shell material (PAN–DMF). The electrospinning conditions, such as the needles, needle-to-substrate distances, applied voltages, and flow rates used to form these NFs are

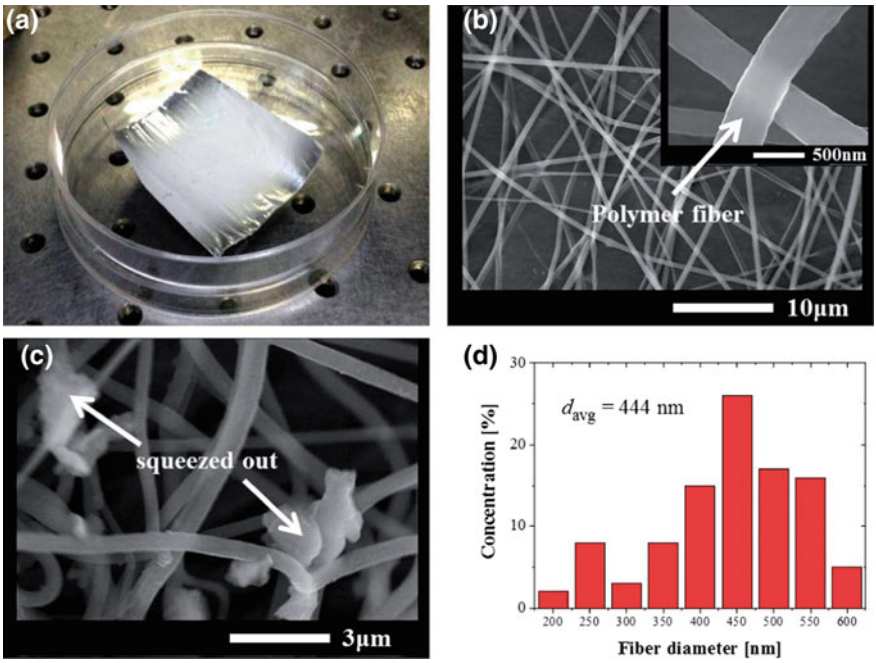

Fig. 4.15 NF mats and their SEM images. **a** Macroscopic photograph of NF mat. **b** SEM images of NFs in the mat. **c** Squeezed-out core materials. **d** Fiber diameter distribution. Reprinted with permission from Lee et al. (2014a)

identical. Therefore, the size distributions for the resin–n-hexane and curing agent NFs in Fig. 4.15d do not differ. The average diameter of these NFs was ~444 nm.

The characteristics of fibers formed by emulsion spinning, as reported in several works, are listed in Table 4.2.

4.4 Solution Blowing

In addition to the electrically-driven bending instability causing the formation of polymer NFs in electrospinning, as discussed in Sect. 4.1 and employed in Sects. 4.2 and 4.3, a perturbed (periodically curved) liquid jet moving in air or subjected to a co-flowing airflow blown with sufficiently high relative velocity experiences a distributed lateral force of aerodynamic origin. In other words, a curved element of such a jet experiences a distributed bending (lift) force, which appears because the air pressure over the concave side of a curved liquid jet element increases while that over the convex decreases. Detailed descriptions of the aerodynamic theory of such a distributed bending force can be found elsewhere (Entov and Yarin 1984; Yarin

1993). This theory yields the expression of the aerodynamic bending force acting per unit jet length in the same form as Eq. (4.13), namely,

$$\mathbf{F}_{\text{aerod}} = -\rho_a U^2 \pi a^2 |k| \mathbf{n} \tag{4.14}$$

where ρ_a is the air density, and U is the relative velocity of the jet and airflow directed as the unperturbed jet axis.

The aerodynamic force $\mathbf{F}_{\text{aerod}}$ enhances bending perturbations of the jet axis, causing their growth. This is the driving force of the aerodynamically-driven bending instability that transforms a slowly moving polymer solution jet in a high-speed airflow into NFs, similar to those achievable by the electrospinning, co-electrospinning and emulsion spinning processes described in Sects. 4.1, 4.2 and 4.3. Solution blowing and coaxial blowing yielding core-shell nanofibers (cf. Sect. 4.5) were introduced by Sinha-Ray et al. (2010), studied in detail in Sinha-Ray et al. (2015), and demonstrated for the first time on the industrial scale in Kolbasov et al. (2016).

The experimental setup used by Sinha-Ray et al. (2015) is sketched in Fig. 4.16. In the solution-blowing experiments conducted in that work, 15 wt% nylon 6 solutions in formic acid are used. The solution is supplied through a 16-gauge needle at the rate of 10 ml/h. The needle is located within a concentric nozzle that issues a high-speed air jet. The air line was connected to a house pressure line operating at 40–60 psi. The polymer solution issuing from the needle is entrained and stretched by the surrounding high-speed air jet. Then, the polymer jet is significantly thinned by air pulling and additionally thinned under aerodynamically-driven bending instability. As a result, polymer NFs are formed after the solvent evaporates in flight. High-speed imaging of the process was performed using a Phantom V210 camera operating at 3100 fps with an 8 μs exposure time. For a proper illumination, a light-emitting diode (LED)-based light source was used. A plano-convex lens was placed between the setup and the light source to render the light beam parallel for viewing through the camera.

In solution-blowing processes in general, and in the experiment of Fig. 4.16 in particular, the polymer solution is issued from a needle or die of ~1 mm diameter (13–16-gauge needles) at a flow rate of 5–10 ml/h. The concentric air-blowing occurs with a velocity of 150–200 m/s. As the viscoelastic polymer solution is issued from the needle, it remains straight and experiences aerodynamically-driven stretching within a distance of 0.94 mm from the nozzle exit (Fig. 4.17), similarly to electrospinning (Sect. 4.1). The stretching causes rapid thinning of the polymer jet as it is accelerated by the surrounding air jet (Fig. 4.17). Because the polymer jet remains quite thick at this short distance from the needle, it possesses a significant bending stiffness, and thus does not bend in this region (Fig. 4.17). After the polymer jet becomes sufficiently thin, a vigorous bending instability occurs, as shown in the images in Fig. 4.17.

An SEM image of a solution-blown NF mat and the corresponding fiber size distribution established in the experiments are shown in Fig. 4.18. The fiber sizes are 100–700 nm. The polymer supply rate can significant affect the fiber size distribution.

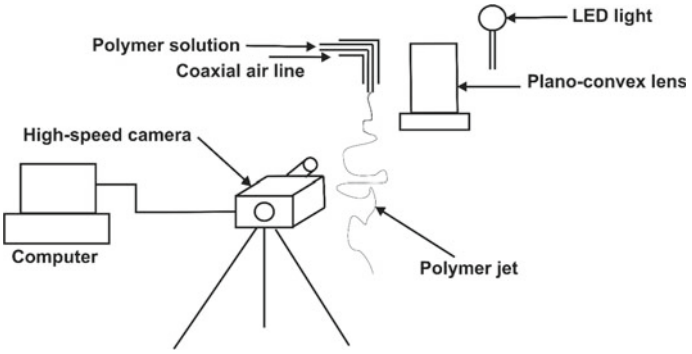

Fig. 4.16 Experimental setup for high-speed observation of solution blowing process. Polymer solution is pumped through the core of the core-shell nozzle, and air is blown at a very high speed through the annular nozzle surrounding the core needle. The low-speed polymer-solution jet is entrained by the surrounding air jet and stretched and bent by it. LED light illumination in conjunction with a plano-convex lens forms a parallel light beam, which facilitates recording using a high-speed camera at 3100 fps. Reprinted with permission from Sinha-Ray et al. (2015)

Kolbasov et al. (2016) scaled up the solution-blowing process from a single-needle setup like that shown in Fig. 4.16 and detailed in Fig. 4.19a to an intermediate six-needle nosepiece, as shown in Fig. 4.19b, and to the industrial-scale equipment, as demonstrated in Fig. 4.20.

In the industrial-scale solution-blowing process shown in Fig. 4.20a, the polymer solution is poured into a hopper and fed by gravity into a positive-displacement gear pump. The flow rate is controlled by adjusting the angular speed of the gear pump, with 1 rpm corresponding to 10 ml/min. Pump speeds of 0.5–3 rpm were used in Kolbasov et al. (2016). From the pump, the polymer solution is supplied to a redistribution chamber and then to the spinneret. The spinneret comprises an array of concentric annular nozzles with 41 nozzles per row and eight rows (Fig. 4.20b). The solution is discharged through the inner nozzles into a high-temperature, high-speed air jets issued from the outer nozzles. The air temperature is controlled by electrical heater.

4.5 Coaxial Solution Blowing

Dual coaxial solution blowing of polymer NFs containing healing agents in the core was developed in Lee et al. (2016c). The following materials were used: polyvinylidene difluoride (PVDF, $M_w \approx 180$ kDa), PEO ($M_w = 200$ kDa), DMF anhydrous 99.8%, and acetone. A PVDF solution for the shell material was prepared by mixing 5.0 g of PVDF solution (21 wt% in the acetone/DMF mixture, 2:3 wt%) and 2.0 g of PEO solution (4 wt% in the acetone/DMF mixture, 2:10 wt%). A two-part commercial epoxy kit (ClearWeld) was used as the healing agent embedded in the

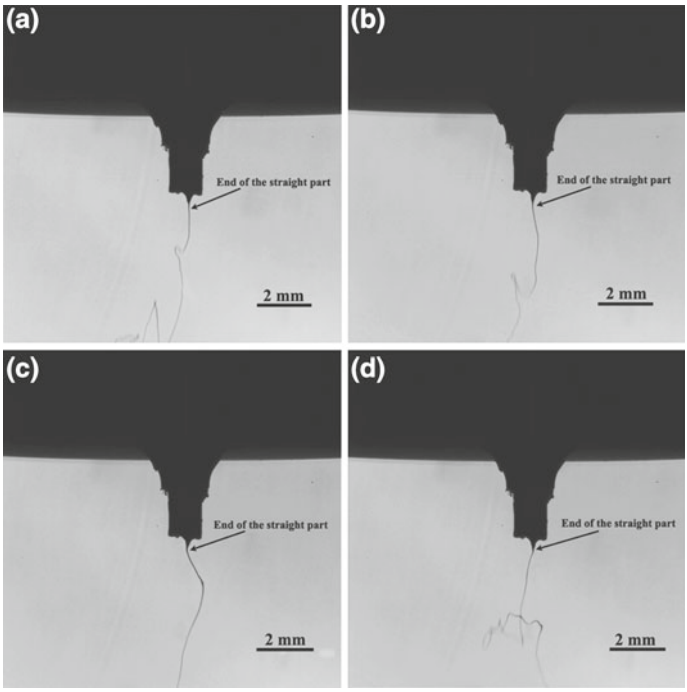

Fig. 4.17 Images from a high-speed recording of solution-blowing process where the polymer solution is issued at the flow rate of 10 ml/h into a parallel high-speed air jet. The air jet velocity is 144.5 m/s. The polymer jet possesses a short thinning straight region. At the end of the straight region (indicated by arrows in all the panels) a vigorous bending begins. The imaging was performed using a Phantom V210 camera operating at 3100 fps. Different panels show images obtained at different times: **a** 0.2 s, **b** 0.83 s, **c** 1.46 s, and **d** 1.69 s. Reprinted with permission from Sinha-Ray et al. (2015)

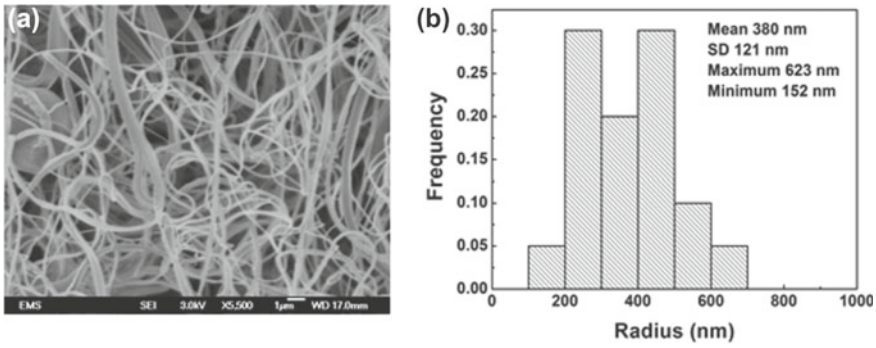

Fig. 4.18 **a** SEM image of solution-blown NF mat of nylon-6. **b** Fiber-size distribution. It should be emphasized that in the present case the NFs were deposited on a surface at rest. Reprinted with permission from Sinha-Ray et al. (2015)

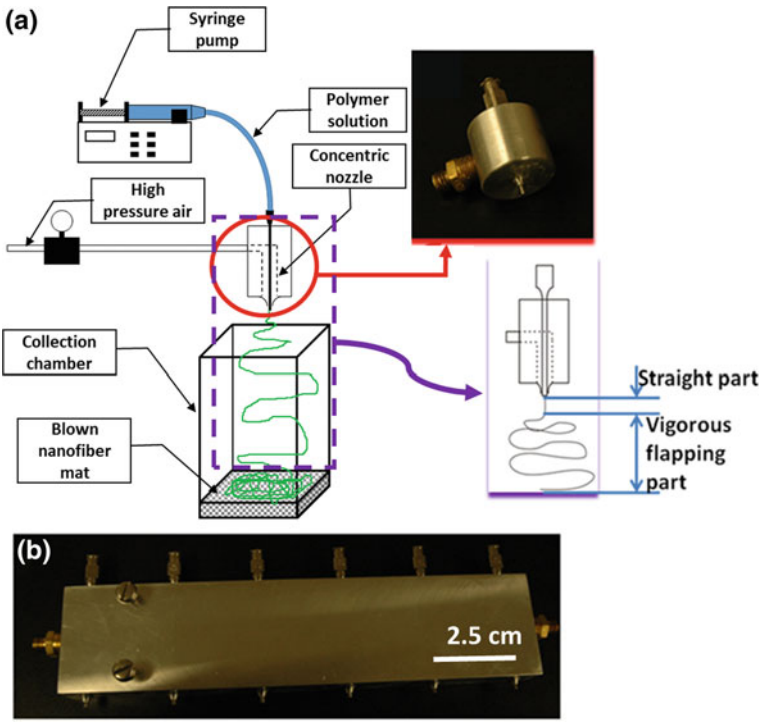

Fig. 4.19 **a** Schematic of a single-needle setup for solution blowing of monolithic NF mats. In the insets in panel **a**, an actual single-needle die and schematic of the solution blowing process are shown. **b** An actual intermediate scale multi-needle (single-row) solution-blowing die. In this die 13-gauge (outer diameter of 0.095") needles are used. Reprinted with permission from Kolbasov et al. (2016)

fiber cores. According to the manufacturer's specifications, it uses a mixing ratio of 1:1, sets in 5 min, and is fully cured in 1 h under ambient conditions. This is a commercial epoxy: the resin is a reaction product of epichlorohydrin (C_3H_5ClO) and bisphenol A ($C_{15}H_{16}O_2$) (CAS# 25085-99-8) 100% (cf. Sect. 2.4), while the hardener is predominantly a polyalkoxylated hydroxyalkyl thiol (<75%). Both the epoxy resin and hardener are nonvolatile materials. They were diluted with DMF (8:5 wt%) to lower their viscosities. A similar approach was used in Lee et al. (2016b) to form self-healing core-shell NF mats with epoxy and hardener in the cores.

PVDF is a safe and eco-friendly polymer that is durable under aging environments such as chemical pollution or UV radiation. Because pure PVDF is insufficiently spinnable to form NFs by solution blowing, a properly mixed PVDF solution with added high-molecular-weight PEO was used to enhance spinnability. No chemical interaction between PEO and PVDF in the NFs or with the surrounding matrix was possible, because PVDF is a highly inert material. In Sinha-Ray et al. (2012), the coaxial solution blowing of core-shell fibers using two different healing agents of

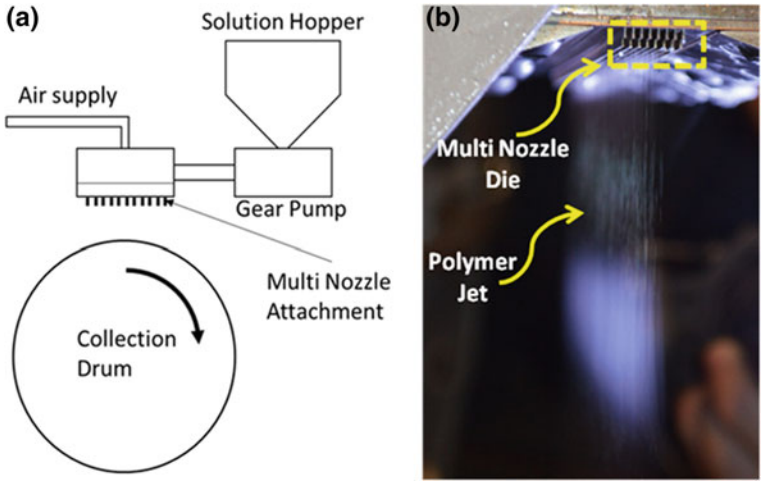

Fig. 4.20 **a** Schematic of the industrial-scale solution blowing setup used in the work of Kolbasov et al. (2016). **b** An actual multi-nozzle solution-blowing process using a Biax die nosepiece with 41 nozzles per row and eight rows. The distance between the collection drum and the spinneret is ~75 cm. The oncoming air flux is not deflected back, but rather spread over the drum and further down, being entrained by the drum rotation. The distance between each pair of adjacent nozzles is 3 mm. No special measures for vapor removal are taken, because only aqueous solutions are used. For non-aqueous solutions, the system would be modified with standard vapor removal equipment. Reprinted with permission from Kolbasov et al. (2016)

dicyclopentadiene (DCPD) and isophorone diisocyanate (see Sects. 2.1 and 2.3) was demonstrated.

The solution-blowing setup used in Lee et al. (2016c) to form self-healing core-shell NFs and microfibers (MFs), and the details of the core-shell needles and coaxial air nozzle used are shown in Fig. 4.21. In this case, the fiber mats are deposited on a grid. A similar setup with fiber deposition on a rotating drum was used by Lee et al. (2016a), as shown in Fig. 4.22.

The core solution, containing either the epoxy resin or hardener, and the shell solution (PVDF/PEO) are supplied separately to a core-shell needle with the flow rates of 1.0 ml/h for the core and 5.0 ml/h for the shell. Each core-shell needle is inserted into a coaxial air nozzle issuing pressurized air (at 40–50 psi). The resin- and hardener-cored fibers are produced simultaneously in two separate core-shell needle setups (Figs. 4.21 and 4.22). For the uniformly entangled deposition of the two types of fibers onto a permeable collector surface, the angle between the two needles is set to ~40° by an adjustable joint. The vacuum line installed under the permeable collector facilitates fiber adhesion to the collecting mesh. The air-blowing conditions are optimized by controlling the air pressure, needle-to-collector distance, flow rate, and other parameters. The solution-blown core-shell NFs and MFs are collected for 10–20 min and then peeled off the collecting mesh. It should be emphasized that the amount of self-healing material introduced and the rate of forming of core-shell

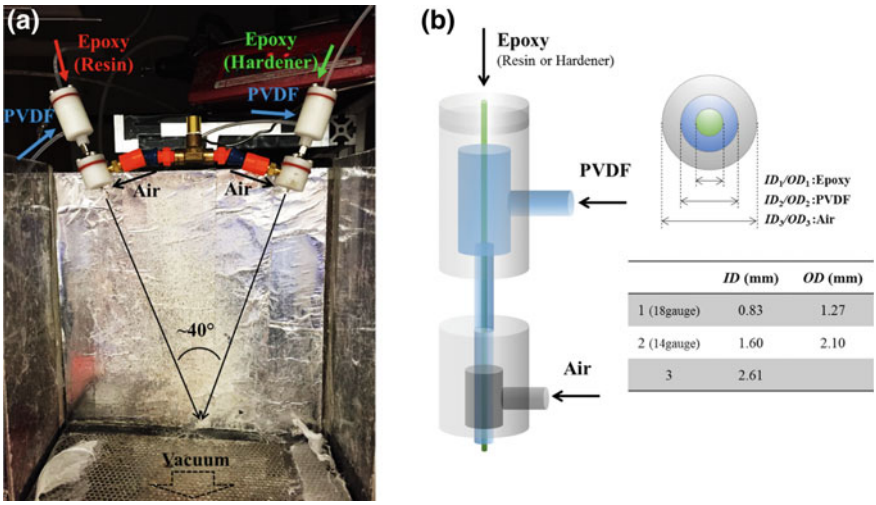

Fig. 4.21 Solution blowing of core-shell NFs and microfibers (MFs). **a** Experimental setup. **b** Design of core-shell needle with coaxial air-blowing nozzle. Epoxy- and hardener-core fibers are produced simultaneously and uniformly mixed in the deposited fiber mat. Reprinted with permission from Lee et al. (2016c)

fibers using solution blowing are both significantly higher than those in using the coaxial electrospinning method described in Sect. 4.2, as illustrated in Fig. 4.23. The core-to-shell mass ratio for solution co-blowing is 33 times (75.62%/2.29%) higher than that for co-electrospinning, while the total mass production rate is two times (1.524 g·h^{-1}/0.767 g·h^{-1}) higher.

In addition, for a direct comparison of the mass production rates of solution blowing (Sect. 4.4) and electrospinning (Sect. 4.1), Lee et al. (2016c) formed monolithic NFs using the same material, specifically, 12 wt% nylon-6 solution in formic acid. The maximum flow rates for reliable fiber formation using solution blowing and electrospinning without dripping, with the other parameters (nozzle-to-substrate distance, applied voltage or air pressure, nozzle diameter, etc.) held constant, were, respectively, $Q_{SB} = 5$–10 ml/h and $Q_{ES} = 0.1$–0.3 ml/h. In electrospinning, the voltage was in the 6.5–13 kV range, the needle-to-substrate distance was 15 cm, and the needle (18-gauge) had an ID and OD of 0.838 mm and 1.270 mm, respectively. Accordingly, the ratio of the mass production rate of solution blowing to that of electrospinning was 33.3 (as 10 ml·h^{-1}/0.3 ml·h^{-1}).

To study the fiber structure resulting from coaxial solution blowing, each MF mat was cut with scissors; the cut edges are shown in Fig. 4.24. The dissected PVDF MFs without stored epoxy in their cores show clear-cut edges, as seen in Fig. 4.24a. In comparison, the MFs with healing agents in their cores show accumulation of cured epoxy at the cut edges (see the red dashed circle in the middle part of Fig. 4.24b). The average diameters of the fibers without and with healing agents stored in their cores are 0.619 μm and 0.981 μm, respectively. In a separate experiment, the average

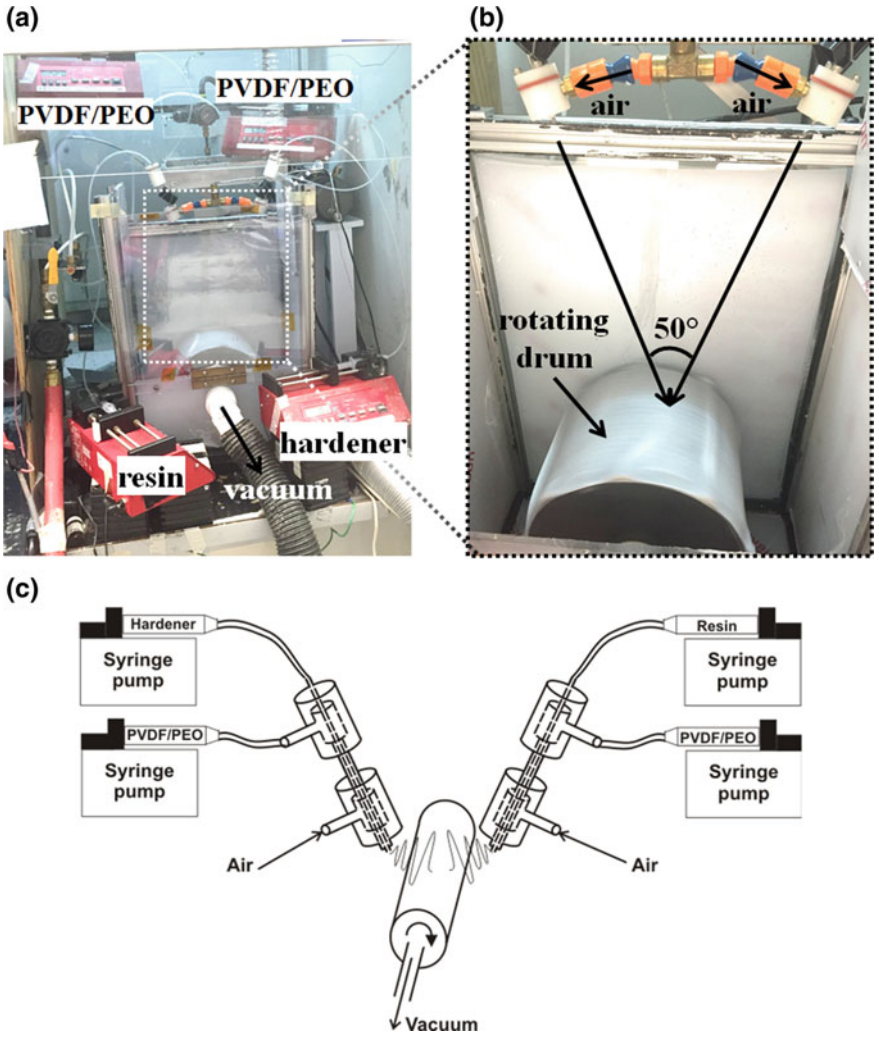

Fig. 4.22 **a** Experimental setup for dual solution blowing. The two components of the epoxy (the resin and the hardener) are issued in the fiber cores and encapsulated in the polymer (PVDF/PEO) shell. **b** The two types of the core-shell fibers are solution-blown separately and simultaneously deposited on a rotating drum. **c** Schematic of the experimental setup. Reprinted with permission from Lee et al. (2016a)

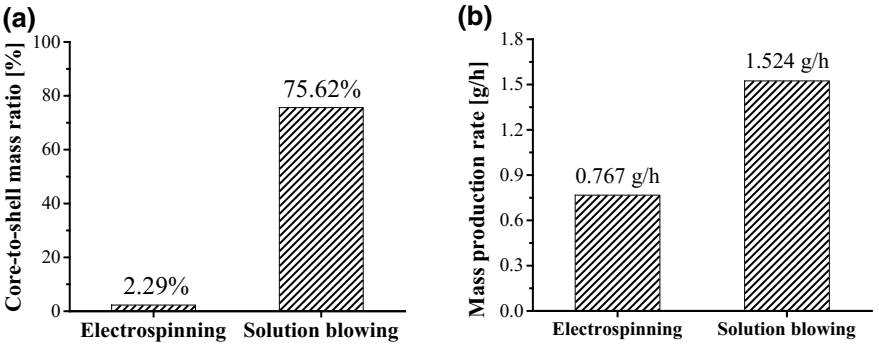

Fig. 4.23 Comparison of the **a** core-to-shell mass ratio, and **b** mass production rate for coaxial electrospinning and solution blowing of core-shell NFs and MFs. The core and shell materials for electrospinning are DMS resin monomer and PAN. The core and shell materials for solution blowing discussed in detail in the present section are epoxy resin and PVDF/PEO. Reprinted with permission from Lee et al. (2016c)

diameters of fibers with either resin or hardener were 1.563 μm or 0.675 μm, respectively. It should be emphasized that the resulting fiber diameters in solution blowing are controlled by the volumetric flow rates and the elongational viscosities of polymer solutions, the needle diameters, and the speed of air blowing (Yarin et al. 2014). The entrainment of the core material into the shell jet increased the outer diameter of the core-shell fibers compared to that of the fibers formed from a monolithic shell material.

To visualize the presence of the cores, a fiber mat with healing agents in the fiber cores was frozen by dipping in liquid nitrogen and then broken. Although most of the broken fibers rapidly released resin, the SEM image on the right-hand side in Fig. 4.25 reveals the fiber cores.

The characteristics of fibers formed by coaxial solution blowing are listed in Table 4.2.

4.6 Emulsion Blowing

The emulsion blowing of core-shell NFs with healing agents in the core was proposed by Sinha-Ray et al. (2012). They used the following material combination: PAN ($M_w = 150$ kDa), DMF anhydrous 99.8%, and healing agents of dicyclopentadiene (DCPD) (see Sect. 2.1) and isophorone diisocyanate (cf. Sect. 2.3). For emulsion solution-blowing, emulsions of DCPD in a solution of PAN in DMF and isophorone diisocyanate in a solution of PAN in DMF were prepared using the following route. A 12 wt% PAN solution in DMF was prepared first. Then, DCPD and DMF were added to achieve the concentrations of 8 wt% PAN and 5 wt% DCPD in DMF. To prepare an emulsion containing 8 wt% PAN and 5 wt% isophorone diisocyanate in DMF, all

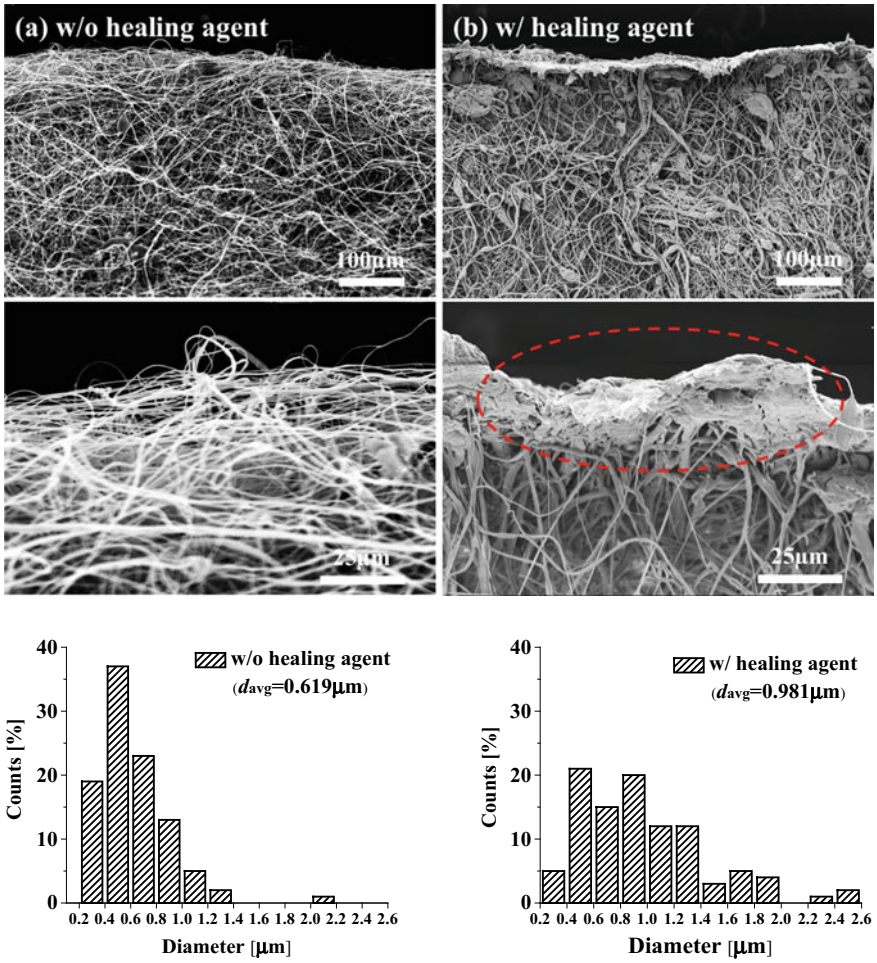

Fig. 4.24 SEM images of cut fiber mats (upper and middle images) and corresponding fiber size distributions (lower graphs). Column **a** without healing agents, and column **b** with healing agents in the fiber core. Reprinted with permission from Lee et al. (2016c)

three components were mixed simultaneously. Both solutions were prepared at the temperature of 75 °C under continuous stirring. Note that Sinha-Ray et al. (2012) also used these emulsions for emulsion electrospinning (cf. Sect. 4.3).

For the emulsion solution-blowing of core-shell NFs, an experimental setup similar to that of Figs. 4.16 and 4.19a was employed. In brief, a digital syringe pump supplied an emulsion to the needle tip, where it was subjected to coaxial high velocity (~150–200 m/s) airflow. The airflow was issued from an annular nozzle concentric to the needle supplying the emulsion. The airflow stretched the emulsion jet and also

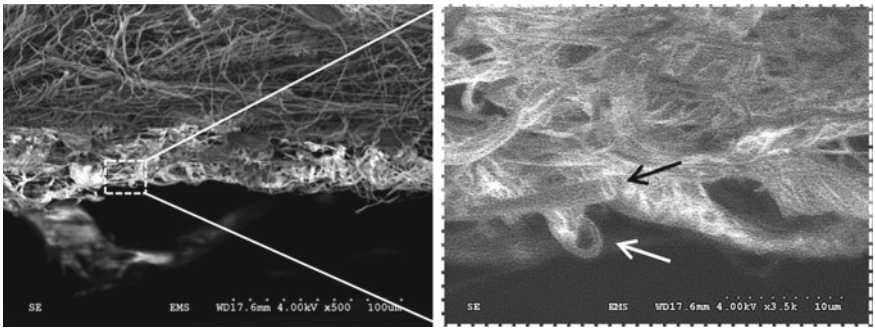

Fig. 4.25 Frozen and broken fiber mat. In the right-hand side image, the two arrows indicate visible fiber cores. Reprinted with permission from Lee et al. (2016c)

Table 4.4 Experimental parameters of the emulsion blowing of the two emulsions, namely, PAN and DCPD in DMF, and PAN and isophorone diisocyanate in DMF

Emulsion	Needle-to-collector distance (cm)	Air pressure (psi)	Flow rate (ml/h)
PAN/DCPD/DMF	30–35	30	6
PAN/isophorone diiso-cyanate/DMF	30–35	30	6

caused a vigorous bending instability, as discussed in Sect. 4.4. The parameters for the emulsion blowing of the two emulsions are listed in Table 4.4.

The fibers blown from the two emulsions were collected on glass slides for 1–3 min and inspected by OM. Micrographs of the fibers obtained from the emulsions of PAN/DCPD in DMF and PAN/isophorone diisocyanate in DMF are shown in Fig. 4.26a, b, and Fig. 4.26c, d, respectively. The majority of the collected fibers show core-shell structures. Figure 4.26a, b reveal that, for PAN/DCPD in DMF, the shell diameter is approximately 1.35 μm–3.00 μm, while the core diameter is 0.44–1.30 μm. For PAN/isophorone diisocyanate in DMF (Fig. 4.26c, d), the shell diameter is 1.80–2.90 μm, while the core diameter is 0.40–0.95 μm. The characteristics of the fibers formed by emulsion blowing are included in Table 4.2.

To demonstrate the presence of the healing agents in the fiber core, a fiber crush test was employed in Sinha-Ray et al. (2012). First, the fibers were collected on a copper plate roughened by sandpaper (600-grit) and the catalyst for the corresponding self-healing process was distributed on a second roughened copper plate. Then, the plates were pressed against each other under a mass of 1 kg overnight. For the isophorone diisocyanate/PAN fibers, water was used as the catalyst, whereas for DCPD/PAN fibers tungsten (VI) chloride was used. The fibers were observed before and after pressing. The fibers before pressing are shown in Fig. 4.27a, b (isophorone diisocyanate/PAN) and 4.27c, d (DCPD/PAN). The same fibers after pressing are shown in Figs. 4.28 (isophorone diisocyanate/PAN) and 4.29 (DCPD/PAN). The fibers are smooth before pressing; they develop different protrusions at their surfaces

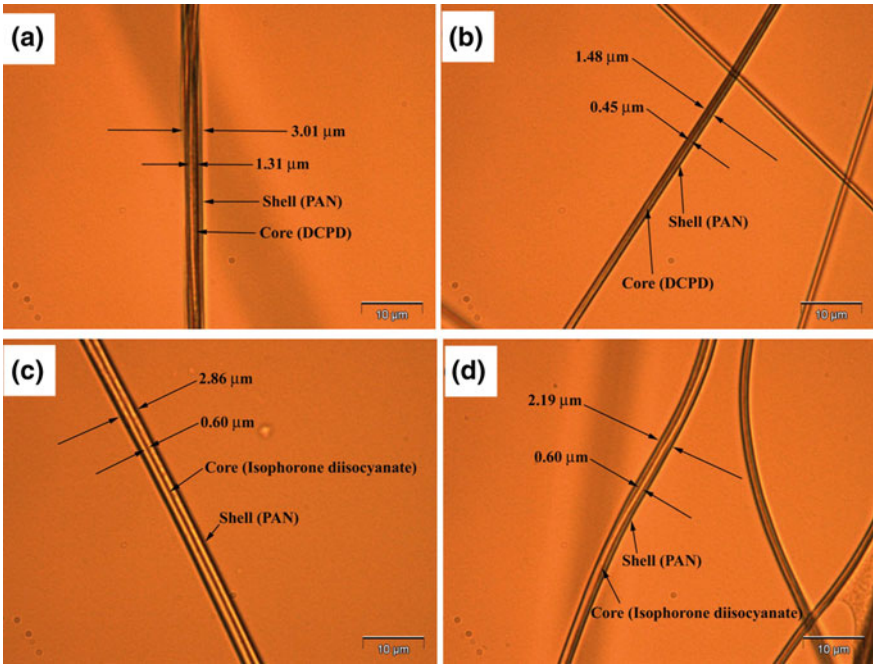

Fig. 4.26 OM images of the core-shell fibers obtained by emulsion blowing. Panels **a** and **b** show the core-shell fibers obtained from the emulsion of DCPD in PAN and DMF, while panels **c** and **d** show the core-shell fibers obtained from the emulsion of PAN and isophorone diisocyanate in DMF. The scale bars in all images are 10 μm. Reprinted with permission from Sinha-Ray et al. (2012)

with pressing. Namely, the fiber shells are ruptured at some locations and the encapsulated healing agents are released from the cores. At the fiber surfaces, these agents make contact with their catalysts, polymerize, and solidify to form the protrusions. The release of the healing agents from the fiber cores is also observed in the axial direction; solidified blobs are formed at the fiber edges (Fig. 4.29).

4.7 Two- and Three-Dimensional Self-Healing Materials

4.7.1 Two-Dimensional Planar Self-Healing Composites

Vascular self-healing materials are composites embedded with core-shell NFs containing healing agents in their cores. NF mats formed by coaxial electrospinning, emulsion spinning, coaxial solution blowing, and emulsion blowing, as described in Sects. 4.2, 4.3, 4.5, and 4.6, respectively, are essentially two-dimensional planar

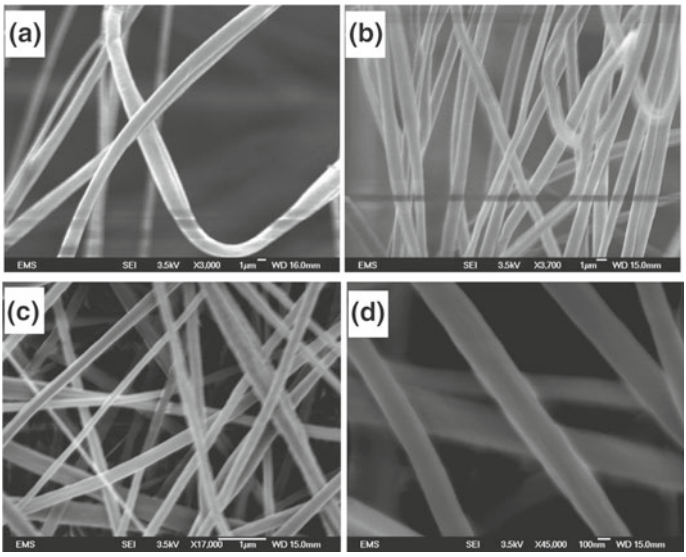

Fig. 4.27 SEM images of undamaged core-shell fibers. Panels **a** and **b** show isophorone diisocyanate/PAN core-shell fibers before pressing, and panels **c** and **d** show DCPD/PAN core-shell fibers before pressing. It is seen that the core-shell fibers have no protrusions on their walls. Reprinted with permission from Sinha-Ray et al. (2012)

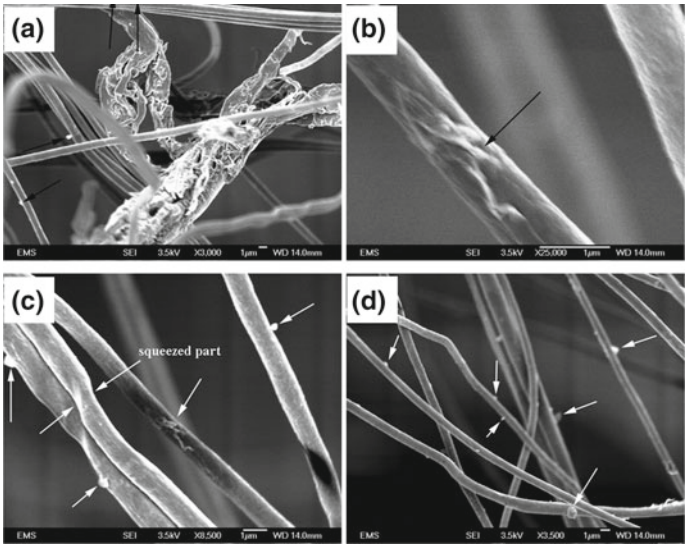

Fig. 4.28 SEM images of pressed isophorone diisocyanate/PAN core-shell fibers. Panels **a**–**d** illustrate different morphological aspects. The arrows indicate solid protrusions found on the fiber walls. Under pressing, isophorone diisocyanate is released from the fiber core, makes contact with the catalyst (water) and solidifies, forming visible protrusions. Reprinted with permission from Sinha-Ray et al. (2012)

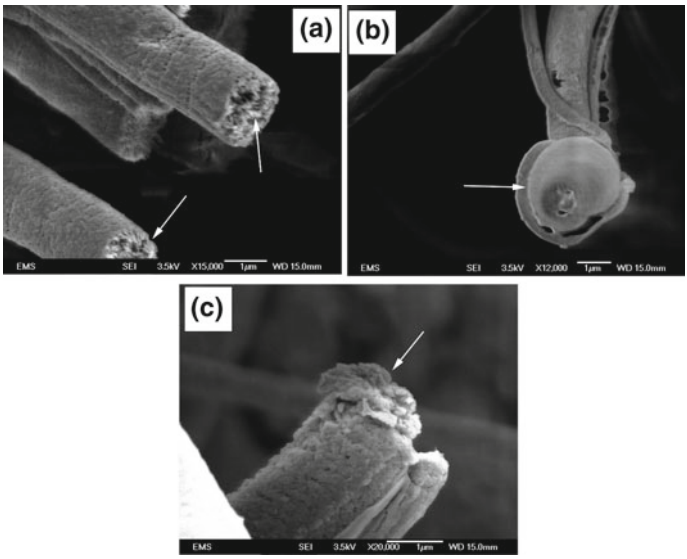

Fig. 4.29 SEM images of pressed DCPD/PAN core-shell fibers. In panel **a** the arrow shows the rough cross-section of a fiber. In **b** the arrow indicates a solid blob protruding from the core, and in panel **c** the arrow shows the solid protrusion formed at the end of a fiber. As a result of pressing, DCPD is released from the fiber core, comes in contact with the tungsten (VI) chloride catalyst, and solidifies. Reprinted with permission from Sinha-Ray et al. (2012)

materials with the thicknesses on the scale of 100 μm. Accordingly, in the majority of cases, composites incorporating these mats are also laminated two-dimensional planar materials (see the sketch in Fig. 4.5b). Several examples of such materials are given below.

In Lee et al. (2016a) the collected fiber mats with and without healing agents (epoxy or hardener) were cut into 20 mm × 60 mm strips. A mixture containing DMS resin monomer and curing agent in a 10:1 mass ratio was prepared separately. The fiber strips were then embedded in this mixture. The PDMS matrix with the embedded fibers was left to cure in open air at room temperature for 24–48 h. The content of NFs with and without healing agents in the PDMS matrices were ~3.21 and 2.68 wt%, respectively. It should be emphasized that no interfacial mismatch or extra chemical reaction between the embedded solidified PVDF/PEO NF mat and the surrounding PDMS matrix in the composite is observed (cf. Fig. 4.30).

Hybrid composites reported by Lee et al. (2014b) with embedded mats of core-shell NFs with healing agent (curing agent) and capsule-less resin monomer micro-droplets are depicted in Fig. 4.31. The SEM images in this figure show a cut cross-section of the 20 wt% epoxy-resin solidified matrix with the embedded curing agent-containing core-shell NFs deposited during $t_{dep} = 10$ min. In this case, the cut releases the curing agent, but the solidified matrix is rinsed with water immediately after the cut; thus, no self-healing is allowed for observation purposes. In particular,

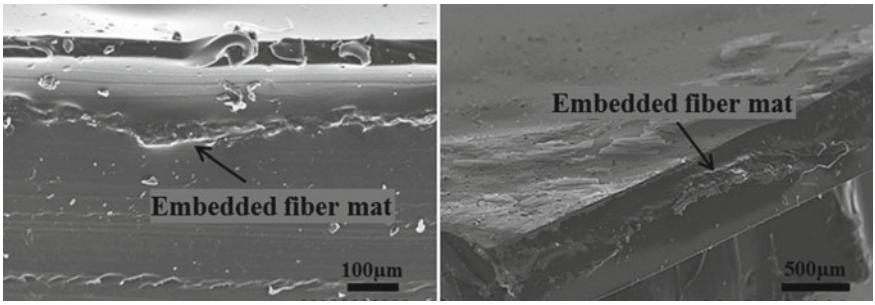

Fig. 4.30 SEM images of PVDF/PEO NF mat embedded in PDMF matrix. Here, it is impossible to distinguish individual NFs, since the magnification was chosen to better observe the interfaces. Reprinted with permission from Lee et al. (2016a)

the presence of the embedded resin monomer droplets is visualized by the elliptical holes previously occupied by the liquid resin monomer, which is also released by the cut. The magnified view in Fig. 4.31b shows ellipsoidal holes with semi-axes of a = 28.13 μm and b = 19.2 μm on the left and a = 43 μm and b = 17 μm on the right. The ellipsoidal (essentially spheroidal) shape is caused by the cut. The volume-equivalent radius of the cut droplet is then $r^3 = ab^2$, giving r values of 21.81 μm and 23.16 μm for the left and right holes, respectively. The average hole size is in agreement with the emulsion droplet size shown in Fig. 4.12d. Figure 4.31c depicts a section of a NF sticking out from the matrix. It shows that some NFs are not fully encased by the epoxy-resin matrix despite being wetted by the matrix material. This is evident from the protruding fiber (~6–7 μm in thickness) as shown in Fig. 4.31c. Figure 4.31d shows an SEM image of the cut cross-section of the matrix. The cross-section is textured with circular marks, indicating the NFs embedded in the epoxy-resin matrix.

4.7.2 Three-Dimensional Self-Healing Composites

Lee et al. (2018) embedded electrospun core-shell NFs containing healing agents into a three-dimensional bulk matrix using a simple and versatile process. Two types of healing agents (resin monomer and curing agent) were encapsulated inside the NF cores. Then, the core-shell fibers were encased in a macroscopic three-dimensional bulky material. To achieve this, the electrospun core-shell fibers containing two components of PDMS (either the resin monomer or curing agent) were directly embedded into an uncured PDMS bath and dispersed there, forming a monolithic bulky composite (Process A). In addition, core-shell fibers that had been chopped into short filaments were embedded into a highly porous sponge-like medium (Process B). Bulky self-healing materials are of interest in multiple engineering application, including biomimetic and biomedical applications. Sponge-like materials are beneficial because of their low densities and softness. They are tremendously effective as

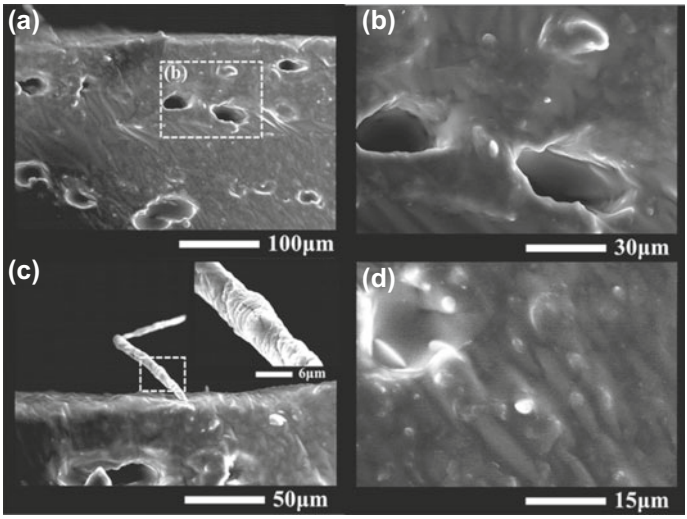

Fig. 4.31 **a**, **c** Cross-sectional SEM image of epoxy-resin matrix with embedded NFs. **b** Magnified image of the area within the box in panel (**a**), with the volume-equivalent diameters of the two holes (the cut resin droplets) of 21.81 μm and r = 23.16 μm, comparable with the droplet average diameter in the 20 wt% emulsion of 27 μm. **d** NFs embedded in the matrix cut by the razor. Reprinted with permission from Lee et al. (2014b)

liquid absorbers (Jiang et al. 2017), compression-shock dampers, and cleaners. Their intrinsic porosity facilitates the embedding of self-healing NFs, and their self-healing properties would mimic many natural materials derived from humans, animals, and plants.

In both Processes A and B the following materials and fiber-forming method were used: PDMS, PAN (M_w = 150 kDa) and DMF (99.8%). The two components of PDMS, the DMS resin monomer and DMHS curing agent, were embedded separately within the cores of individual core-shell fibers with PAN shells by coaxial electrospinning (see Sect. 4.2). The overall co-electrospinning conditions were similar to those used in Lee et al. (2015) and An et al. (2015), except for the substrate. The co-electrospun core-shell fibers had either resin monomer or curing agent in the cores and PAN shells. The resin monomer and curing agent stored in the fiber cores would remain liquid until they interacted with each other after damage to the composite material.

It should be emphasized that a specific polymer is chosen according to the required spinnability for different spinning systems. In Lee et al. (2016c) and Yarin et al. (2014), PVDF/PEO blends in acetone/DMF were used in the coaxial solution-blowing process (cf. Sect. 4.5), whereas in the present case PAN in DMF was used in co-electrospinning. The spinnability of a particular polymer solution typically depends on its viscoelasticity (associated primarily with the polymer molecular

weight and concentration in solution) and spinning conditions; cf. Yarin et al. (2014). The spinning conditions determine the driving forces of the process, and in particular, the rates of stretching involved. Some polymer solutions that work properly in electrospinning are not suitable for solution blowing and vice versa. In the present case, however, both PVDF/PEO and PAN could be used. PAN in DMF is a relatively easily co-electrospinnable, and thus an attractive material combination.

In Process A, the premixed (10:1 ratio) PDMS (volume of 55 ml), which was not cured yet, was placed in a petri dish located under the co-electrospinning needles as shown in Fig. 4.32. Then, the fibers containing the two separate components of PDMS (either the resin monomer or curing agent) were simultaneously co-electrospun onto the uncured liquid PDMS (the pre-mixed but unpolymerized resin and curing agent) in the petri dish for 30 min to 2 h, using the fixed core and shell flow rates of 90 μl/h and 550 μl/h, respectively. The bottom of the PDMS bath was a grounded steel substrate. The voltage applied to both co-electrospinning syringes was 11.5 kV, and the distance between the needle and uncured PDMS was 8 cm. The co-electrospun fibers, which touched the surface of the liquid PDMS, were wetted by and submerged in the liquid. Afterward, the sample in the petri dish was dried for 48 h to permit solidification at room temperature. To prepare a three-layered three-dimensional block of self-healing material, the uncured PDMS was firstly prepared as a single layer. Then, the first co-electrospinning was conducted for 30 min, as described above. To form the second layer on the first layer, the NF-embedded uncured PDMS was half-dried for 24 h and the second co-electrospinning was then performed for 30 min. Similarly, the third layer was prepared by the same process as the second layer. The second and third drying times were 24 h and 48 h, respectively.

In Process B, a self-healing three-dimensional sponge was prepared. A sugar frame for the sponge was prepared with sugar grains (organic turbinado raw cane sugar) purchased at a local grocery. Core-shell fibers with self-healing agents were co-electrospun from a coaxial needle. In addition, 8 wt% of PAN was dissolved in DMF to form the shell material. For the core, the DMS resin monomer was diluted with n-hexane at a 2:1 wt% ratio, while the DMHS curing agent was used as-is. The fiber mat was deposited onto a rotating drum collector for 3 h. The details of the preparation of the self-healing fiber mat are the same as those described above for Process A.

A porous three-dimensional PDMS sponge was prepared as depicted in Fig. 4.33. The as-spun fiber mat (0.2 g, PAN or PRC, i.e., the core-shell fibers with one of the healing agents in the core) was chopped using a commercial food chopper for 4 min in 50 ml of resin. Some of the healing agent was released from the edges of the chopped fibers, similarly to the observations of the release process on a larger scale (Lee et al. 2017b; cf. Sect. 3.4). However, the partial recovery of the mechanical properties after damage, as discussed in Sect. 8.6, revealed that sufficient healing agents remained in the cores of the chopped core-shell NFs embedded in the sponge. The chopped fibers were roughly 20–50 μm in length (see Fig. 4.34b). Then, 5 ml of the curing agent was added to the colloidal suspension and mixed well (PDMS with chopped fibers premixed in the ratio of 10:1 to the curing agent). Afterward, the fiber–PDMS mixed solution was poured onto the sugar skeleton and placed in

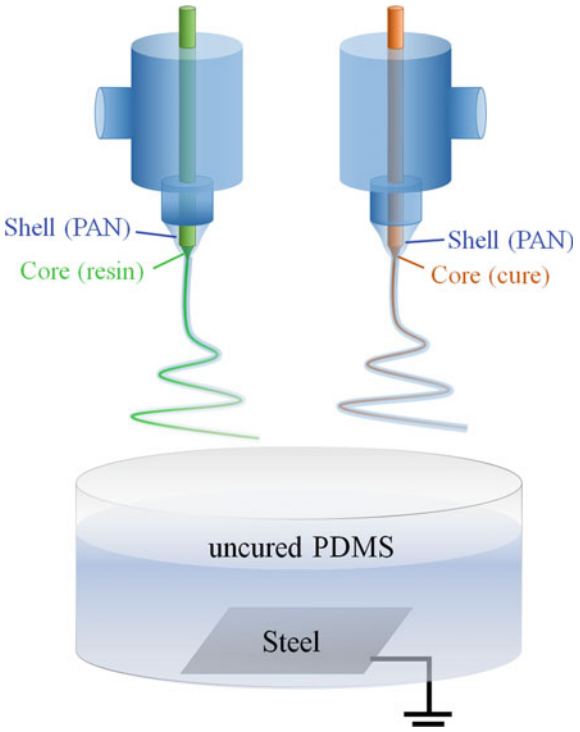

Fig. 4.32 Schematic of dual coaxial-electrospun core-shell fiber mats submerged into uncured PDMS in a petri dish with grounded steel bottom. Reprinted with permission from Lee et al. (2018)

a vacuum chamber for 24 h for the curing. The PDMS-infiltrated sugar frame was rinsed in a hot water bath and sonicated for 10 min, facilitating removal of the sugar from the sponge (see Fig. 4.33). The PDMS–PAN (or –PRC) sponge, shaped by the sugar skeleton but containing no sugar, was then dried in an oven for 30 min at 100 °C. The mass ratio of the embedded fibers to the PDMS matrix in the sponge was found as 0.2 g/(55 ml × 0.965 g/ml) × 100% = 3.77%, and the core-to-shell mass ratio in the embedded co-electrospun fibers was 2.29%, as in Lee et al. (2016c).

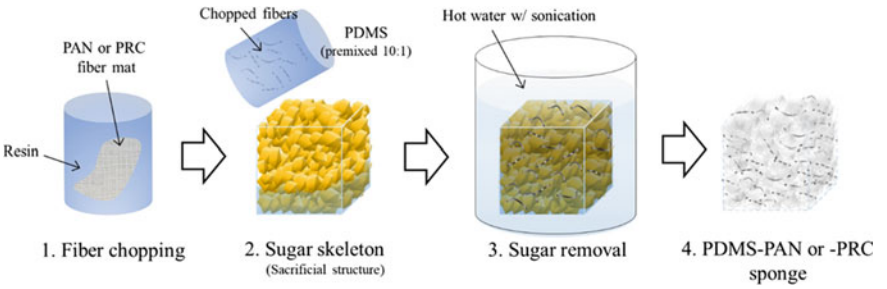

Fig. 4.33 Fabrication of self-healing sponge. Reprinted with permission from Lee et al. (2018)

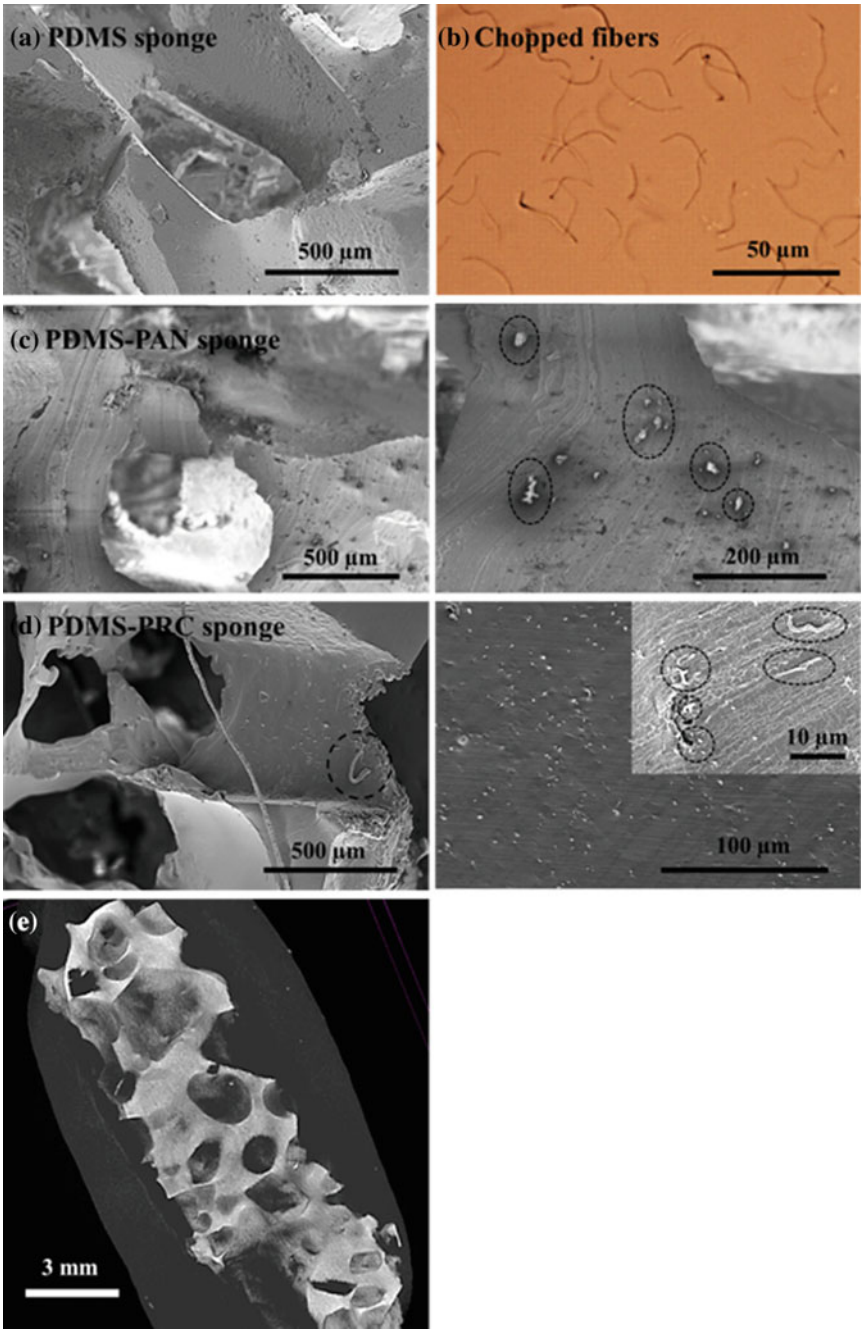

Fig. 4.34 **a** PDMS sponge. **b** Chopped fibers. **c** PDMS–PAN sponge. **d** PDMS–PRC sponge. In panels **c** and **d** in the enlarged images on the right, several cut or aligned NFs are encircled by dashed curves. Magnification: ×80, ×800, ×70/×200, and ×80/×500 for panels **a**–**d**, respectively. **e** Micro-CT image of PDMS–PRC sponge. Reprinted with permission from Lee et al. (2018)

The as-prepared sponges were observed using SEM and OM. The irregular and non-uniform structure of the PDMS sponge is seen in Fig. 4.34a, b, c, d. The tails of the PAN and PRC fibers embedded in the PDMS matrix are seen at the cut surface of the sponge in the magnified second images in Figs. 4.34c, d. The sponge porosity is calculated by considering the amount of 30 ml PDMS in the sugar skeleton of 56.4 ml, as $(1–30/56.4)\times 100\% = 46.81\%$. The pore size is approximated by the grain size of the sugar granules, ranging from 0.6 to 1.5 mm. It should be emphasized that when the core-shell fibers are observed at the microscale, the epoxy released from the cut fibers is easily observed (cf. Fig. 4.24 in Sect. 4.5). It is much more difficult to observe the epoxy released from the thin NFs because it is easily melted or burned under a focused SEM beam; thus, higher-magnification images of material released from a damaged individual fiber are impossible to obtain. In the present case, the repair of mechanical damage was chosen to demonstrate the effect of the released healing agents and the success of the healing process (cf. Sect. 8.6). Microscale computational tomography (micro-CT), a non-destructive imaging method, was also used to observe the porous structure of the sponge. However, this method could not visualize the embedded fibers in the matrix material, because the fiber cross-sectional diameter was smaller than the minimum resolution (~1 μm) of the micro-CT equipment (see Fig. 4.34e).

References

An S, Liou M, Song KY, Jo HS, Lee MW, Al-Deyab SS, Yarin AL, Yoon SS (2015) Highly flexible transparent self-healing composite based on electrospun core–shell nanofibers produced by coaxial electrospinning for anti-corrosion and electrical insulation. Nanoscale 7:17778–17785

Bazilevsky AV, Yarin AL, Megaridis CM (2007) Co-electrospinning of core− shell nano/microfibers using a single nozzle technique. Langmuir 23:2311–2314

Castellanos A, Perez AT (2007) Electrohydrodynamic systems. Chapter C21 in Springer handook of experimental fluid mechanics (Eds. C. Tropea, A.L. Yarin and J. Foss), Springer, Berlin

Chanamai R, McClements DJ (2000) Dependence of creaming and rheology of monodisperse oil-in-water emulsions on droplet size and concentration. Colloids Surf A 172:79–86

Entov VM, Yarin AL (1984) The dynamics of thin liquid jets in air. J Fluid Mech 140:91–111

Fong H, Reneker DH (2000) Electrospinning and the formation of nanofibers. In: Salem DR, editor. Structure formation in polymeric fibers (Salem DR, Ed.). Munich, Hanser Publishing, pp. 225–246

Jiang S, Duan G, Kuhn U, Mörl M, Altstädt V, Yarin AL, Greiner A (2017) Spongy gels by a top-down approach from polymer fibrous sponges. Angewante Chemie, Int Ed 56:3285–3288

Kolbasov A, Sinha-Ray S, Joijode A, Hassan MA, Brown D, Maze B, Pourdeyhimi B, Yarin AL (2016) Industrial-scale solution blowing of soy protein nanofibers. Ind Eng Chem Res 55:323–333

Lee MW, An S, Jo HS, Yoon SS, Yarin AL (2015) Self-healing nanofiber-reinforced polymer composites: 1. Tensile testing and recovery of mechanical properties. ACS Appl Mater Interfaces 7:19546–19554

Lee MW, An S, Joshi B, Latthe SS, Yoon SS (2013a) Highly efficient wettability control via three-dimensional (3D) suspension of titania nanoparticles in polystyrene nanofibers. ACS Appl Mater Interfaces 5:1232–1239

Lee MW, An S, Kim YI, Yoon SS, Yarin AL (2018) Self-healing three-dimensional bulk materials based on core-shell nanofibers. Chem Eng J 334:1093–1100

Lee MW, An S, Latthe SS, Lee C, Hong S, Yoon SS (2013b) Electrospun polystyrene nanofiber membrane with superhydrophobicity and superoleophilicity for selective separation of water and low viscous oil. ACS Appl Mater Interfaces 5:10597–10604

Lee MW, An S, Lee C, Liou M, Yarin AL, Yoon SS (2014a) Self-healing transparent core–shell nanofiber coatings for anti-corrosive protection. J Mater Chem A 2:7045–7053

Lee MW, An S, Lee C, Liou M, Yarin AL, Yoon SS (2014b) Hybrid self-healing matrix using core−shell nanofibers and capsuleless microdroplets. ACS Appl Mater Interfaces 6:10461–10468

Lee MW, Sett S, An S, Yoon SS, Yarin AL (2017a) Self-healing nano-textured vascular-like materials: Mode I crack propagation. ACS Appl Mater Interfaces 9:27223–27231

Lee MW, Sett S, Yoon SS, Yarin AL (2016a) Fatigue of self-healing nanofiber-based composites: Static test and subcritical crack propagation. ACS Appl Mater Interfaces 8:18462–18470

Lee MW, Sett S, Yoon SS, Yarin AL (2016b) Self-healing of nanofiber-based composites in the course of stretching. Polymer 103:180–188

Lee MW, Yoon SS, Yarin AL (2016c) Solution-blown core−shell self-healing nano- and microfibers. ACS Appl Mater Interfaces 8:4955–4962

Lee MW, Yoon SS, Yarin AL (2017b) Release of self-healing agents in a material: What happens next? ACS Appl Mater Interfaces 9:17449–17455

Mata A, Fleischman AJ, Roy S (2005) Characterization of polydimethylsiloxane (PDMS) properties for biomedical micro/nanosystems. Biomed Microdevices 7:281–293

Melcher JR, Taylor GI (1969) Electrohydrodynamics: a review of the role of interfacial shear stresses. Annu Rev Fluid Mech 1:111–146

Osborn HT, Akoh CC (2004) Effect of emulsifier type, droplet size, and oil concentration on lipid oxidation in structured lipidbased oil-in-water emulsions. Food Chem 84:451–456

Park JH, Braun PV (2010) Coaxial electrospinning of self-healing coatings. Adv Mater 22:496–499

Reneker DH, Yarin AL (2008) Electrospinning jets and polymer nanofibers. Polymer 49:2387–2425

Reneker DH, Yarin AL, Fong H, Koombhongse S (2000) Bending instability of electrically charged liquid jets of polymer solutions in electospinning. J Appl Phys 87:4531–4547

Reneker DH, Yarin AL, Zussman E, Xu H (2007) Electrospinning of nanofibers from polymer solutions and melts. Adv Appl Mech 41:43–195

Saville DA (1997) Electrohydrodynamics: the Taylor-Melcher leaky dielectric model. Annu Rev Fluid Mech 29:27–64

Sinha-Ray S, Pelot DD, Zhou ZP, Rahman A, Wu X-F, Yarin AL (2012) Encapsulation of self-healing materials by coelectrospinning, emulsion electrospinning and solution blowing and intercalation. J Mater Chem 22:9138–9146

Sinha-Ray S, Sinha-Ray S, Yarin AL, Pourdeyhimi B (2015) Theoretical and experimental investigation of physical mechanisms responsible for polymer nanofiber formation in solution blowing. Polymer 56:452–463

Sinha-Ray S, Yarin AL, Pourdeyhimi B (2010) The production of 100/400 nm inner/outer diameter carbon tubes by solution blowing and carbonization of core–shell nanofibers. Carbon 48:3575–3578

Sun Z, Zussman E, Yarin AL, Wendorff JH, Greiner A (2003) Compound core/shell polymer nanofibers by co-electrospinning. Adv Mat 15:1929–1932

Taylor GI (1964) Disintegration of water drops in an electric field. Proc Roy Soc London A 280:383–397

Yarin AL (1993) Free liquid jets and films: Hydrodynamics and rheology. Longman Scientific & Technical and John Wiley & Sons, Harlow and New York

Yarin AL (2011) Coaxial electrospinning and emulsion electrospinning of core−shell fibers. Polym Adv Technol 22:310–317

Yarin AL, Koombhongse S, Reneker DH (2001a) Bending instability in electrospinning of nanofibers. J Appl Phys 89:3018–3026

Yarin AL, Koombhongse S, Reneker DH (2001b) Taylor cone and jetting from liquid droplets in electrospinning of nanofibers. J Appl Phys 90:4836–4846

Yarin AL, Pourdeyhimi B, Ramakrishna S (2014) Fundamentals and applications of micro- and nanofibers. Cambridge University Press, Cambridge
Yarin AL, Roisman IV, Tropea C (2017) Collision phenomena in liquids and solids. Cambridge University Press, Cambridge

Chapter 5
Characterization of Self-Healing Phenomena on Micro- and Nanoscale Level

This chapter describes and discusses some of the characterization methods employed to verify the physical and chemical aspects of self-healing on the micro- and nanoscale levels. These methods are used to confirm that the healing agents are encased and released from nanofibers (NFs), spread, reacted, and solidified. The methods discussed in this section are also used to elucidate the morphological changes in the damaged material caused by the released healing agents. Characterization methods including visualization (Sect. 5.1), spectroscopy (Sect. 5.2), and thermal analysis (Sect. 5.3) are discussed below.

5.1 Visualization

To ensure that the healing materials are encapsulated in the fiber cores, defect-free and bead- or blob-free uniform fibers are preferred. The overall morphologies of fibers containing healing agents can be inspected using optical microscopy (OM, Sett et al. 2015), scanning electron microscopy (SEM, An et al. 2014), atomic force microscopy (AFM, Sinha-Ray et al. 2013), and optical profilometry (Ghosal et al. 2016). However, only the exterior features can be observed by these methods. The core-shell architecture is one of the most important structural features of self-healing fibers. Thus, the presence of a core filled with a healing agent must be confirmed using transmission electron microscopy (TEM), which allows for imaging through sufficiently thin shells (An et al. 2015; Lee et al. 2015). Fluorescence imaging can also be used to observe the encased core material if it is blended with a fluorescent dye or contains fluorescent markers (Sinha-Ray et al. 2011; Pang and Bond 2005a, b). The internal damage incurred within a composite can be investigated using ultrasonic C-scanning or X-radiography (Bleay et al. 2001; Pang and Bond 2005a, b). NF images obtained using the methods described in this chapter are shown in Fig. 5.1. It should be emphasized that Fig. 5.1 illustrates the observation methods, with not necessarily core-shell fibers containing healing agents (some fibers in Fig. 5.1 are not of this

A. L. Yarin et al., *Self-Healing Nanotextured Vascular Engineering Materials*, Advanced Structured Materials 105, https://doi.org/10.1007/978-3-030-05267-6_5

type). A number of additional SEM, TEM and fluorescent images of core-shell NFs filled with healing agents can be found in Chaps. 1 and 4.

5.2 Spectroscopic Characterization

The elemental composition of the released healing agents can be analyzed using energy-dispersive X-ray spectroscopy (EDX). For example, the presence of dimethyl siloxane resin monomer (C_2H_6OSi, DMS; cf. Sect. 2.2) in the core encapsulated in the polyacrylonitrile [$(C_3H_3N)_n$, PAN] shell of core-shell NFs was confirmed by EDX analysis. The spectrum of the NFs contained a distinct peak related to silicon (Si) at the Kα value of ~1.8 keV (see Fig. 5.2) (Lee et al. 2014b, 2015).

The presence of a curing agent (dimethyl-methyl hydrogen-siloxane, DMHS) within NFs formed by emulsion electrospinning (Sect. 4.3) was confirmed by EDX in Lee et al. (2014b). Figure 5.3 compares SEM images and the EDX data for the uniform parts of NFs and in the beads on the fibers. The beads should contain more curing agent, as they are bulkier sections with more space to store the curing agent. Figure 5.4 confirms the greater amount of curing agent in the beads on the fibers through a comparison of the silicon contents in different detection domains corresponding to Spectra 3 and 4. The peak corresponding to the silicon content is higher for the bead on the fibers. Silicon is also detected in the uniform parts of these fibers, indicating continuous curing agent cores throughout these core-shell NFs. It should be emphasized that the curing agent is uniformly distributed in the cores of multiple long sections of NFs spanning the beads. Therefore, a 3D network of such NFs allows uniform coverage of the surface, which is hard to achieve with an approach involving capsules.

In Sinha-Ray et al. (2012), EDX was employed to detect healing agents of dicyclopentadiene (DCPD; cf. Sect. 2.1) or isophorone diisocyanate (cf. Sect. 2.3) in the fiber cores. The fibers were formed using co-electrospinning, emulsion electrospinning, and coaxial solution blowing described in Sects. 4.2, 4.3 and 4.5, respectively. The quantification of light elements by EDX is extremely difficult and may be inaccurate because of the absorption of low-energy X-rays in a specimen, in the detector window and the silicon dead layer. In addition, to avoid any possible interference, samples cannot be sputter-coated with metal. Therefore, samples should be inspected in a differential-pressure SEM chamber, which employs gas ions to neutralize the electric charge. This causes the beam to widen, which can introduce difficulties with localization for any analysis conducted. This widening can begin from a submicrometer-sized spot in an ultra-high vacuum SEM to a spot of ~100 μm in a differential-pressure SEM (in addition to the possible movement of the NF mat under an electron beam).

When EDX is employed, materials are characterized based on their Kα energy shell. In the core-shell NFs studied by Sinha-Ray et al. (2012), the shell consisted of PAN and the core comprised either DCPD ($C_{10}H_{12}$) or isophorone diisocyanate ($C_{12}H_{18}N_2O_2$). In the PAN/DCPD core-shell system, it was implied that the EDX

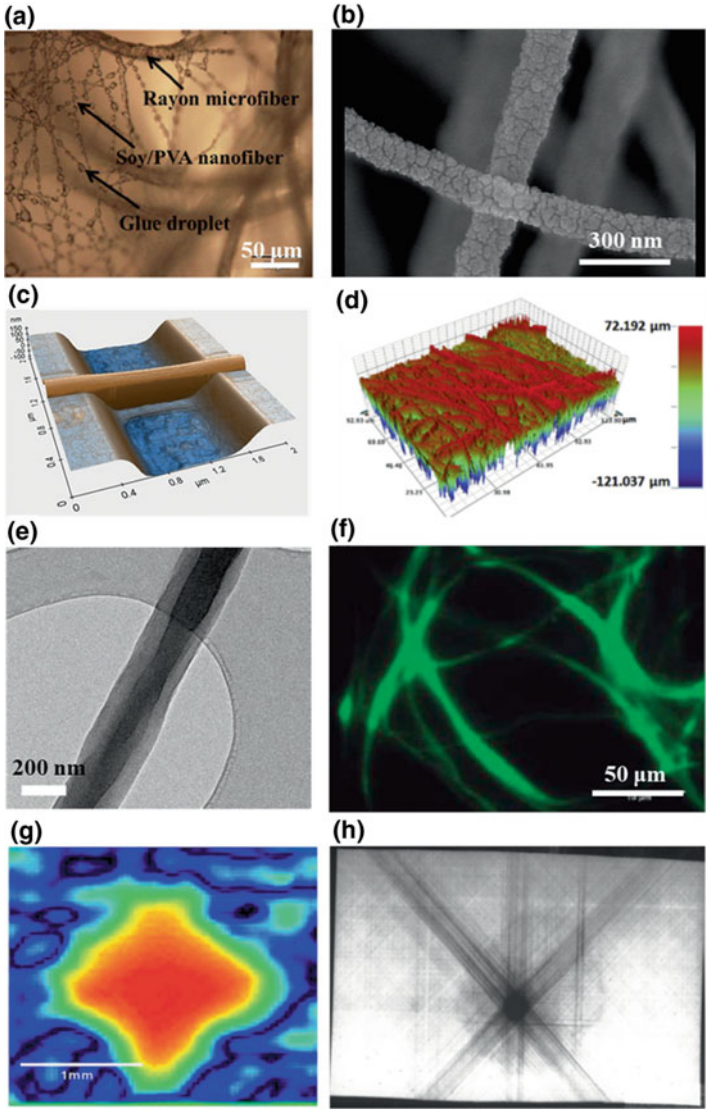

Fig. 5.1 **a** OM image of as-deposited soy protein/poly(vinyl alcohol) (PVA) NFs on a rayon pad. Reprinted with permission from Sett et al. (2015). **b** SEM image of electrospun polyacrylonitrile (PAN) NFs sputter-coated by platinum. Reprinted with permission from An et al. (2014). **c** AFM landscape-mode image of nylon-6 fiber deposited over a trench. Reprinted with permission from Sinha-Ray et al. (2013). **d** Optical profilometry image. Reprinted with permission from Ghosal et al. (2016). **e** TEM image of resin monomer (core)-PAN (shell) NF; cf. Fig. 4.9 in Sect. 4.2. Reprinted with permission from An et al. (2015). **f** Fluorescence microscopy image of fibers of nylon-6/soy protein blend. Reprinted with permission from Sinha-Ray et al. (2011). **g** Ultrasonic C-scanning image after impact damage at the impact energy of 0.8 J (i.e., indentation at 1400 N). Reprinted with permission from Pang and Bond (2005b). **h** X-radiograph of quasi-isotropic hollow glass/fiber composite after impact test obtained using opaque X-ray dye incorporated within the impact region. Reprinted with permission from Bleay et al. (2001)

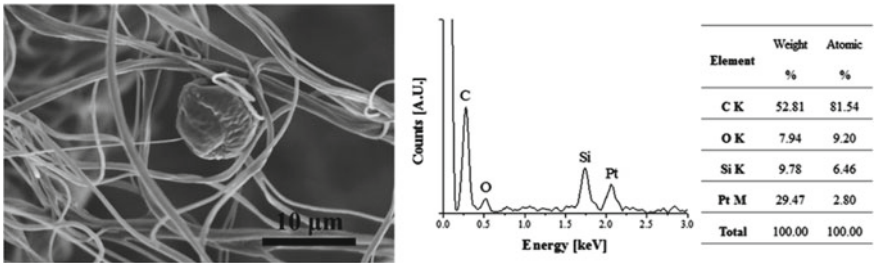

Element	Weight %	Atomic %
C K	52.81	81.54
O K	7.94	9.20
Si K	9.78	6.46
Pt M	29.47	2.80
Total	100.00	100.00

Fig. 5.2 SEM image of a spherical mass of DMS resin monomer released from damaged co-electrospun NFs (cf. Fig. 4.6d in Sect. 4.2) and EDX analysis results for this mass. Reprinted with permission from Lee et al. (2015)

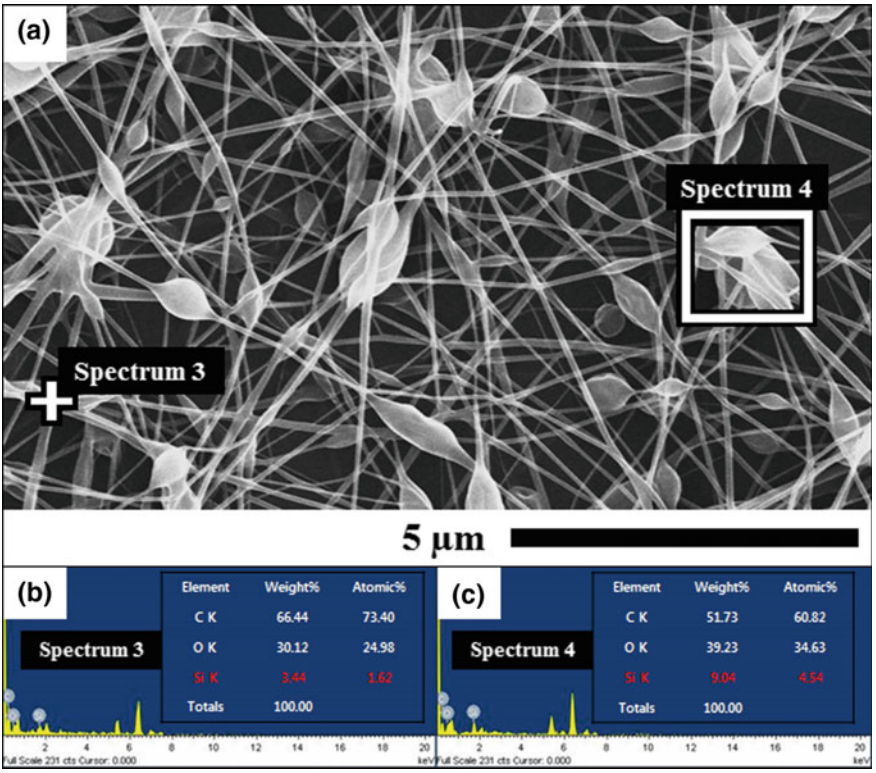

Fig. 5.3 **a** SEM and **b**, **c** EDX data for NFs formed by the emulsion electrospinning with curing agent in the cores. Data were obtained in **b** the region of a uniform fiber, Spectrum 3, and in **c** the region of a bead on the fiber, Spectrum 4. Reprinted with permission from Lee et al. (2014b)

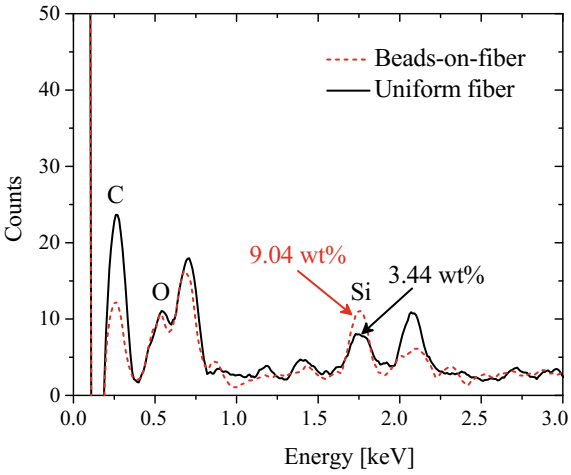

Fig. 5.4 EDX data for core-shell NFs with curing agent in the core. A silicon peak at 1.739 keV implies the presence of curing agent withing NFs. Reprinted with permission from Lee et al. (2014b)

spectrum of the DCPD core, which contained little or no nitrogen, should be easily distinguishable from the shell spectrum, which contained nitrogen. A careful observation of the EDX series revealed that carbon and nitrogen corresponded to the Kα value of 0.277 keV and 0.392 keV, respectively. The energy resolution of the detector was ~0.140 keV, meaning that, in the EDX spectrum, the peaks of nitrogen and carbon would overlap, impeding reliable characterization based on the presence or absence of nitrogen. Indeed, it is shown in Fig. 5.5a and b for the PAN/DCPD core-shell fibers that the nitrogen peak is completely obscured by the neighboring carbon peak, thus making it impossible to prove the existence of DCPD in the core by EDX. However, the spectrum of a cross-section of PAN/isophorone diisocyanate NFs (Fig. 5.5c) is more informative. Figure 5.5c shows that the oxygen peak in the core in such fibers is much higher (~8%; Fig. 5.5c) than that in the shell (~3%; Fig. 5.5a). This indicates the presence of isophorone diisocyanate in the fiber core. However, the difference in the oxygen peaks is not very pronounced, and the comparison of Fig. 5.5a and c is more qualitative than quantitative.

An additional question arises in relation to the released healing agents: whether they mix, polymerize, and solidify, or remain unmixed and liquid. Solidification does not occur in any individual fiber core alone because the cores contain either DMS resin monomer or the curing agent in separate fibers, as in Lee et al. (2017a). Solidification occurs only when the healing agents are released from the ruptured fiber cores, mixed, and polymerized. It should be emphasized that neither X-ray diffraction (XRD), EDX, nor Raman spectroscopy can determine whether a mixed drop containing both resin monomer and curing agent is polymerized, and thus solidified. This can be determined only by observing the change in the surface texture of a drop, as was shown in Sect. 3.3; cf. Figs. 3.21 and 3.22. Such a change can also be noted via a detailed inspection of the images like those in Fig. 5.6, demonstrating that polymerization and solidification occurred in the drops shown.

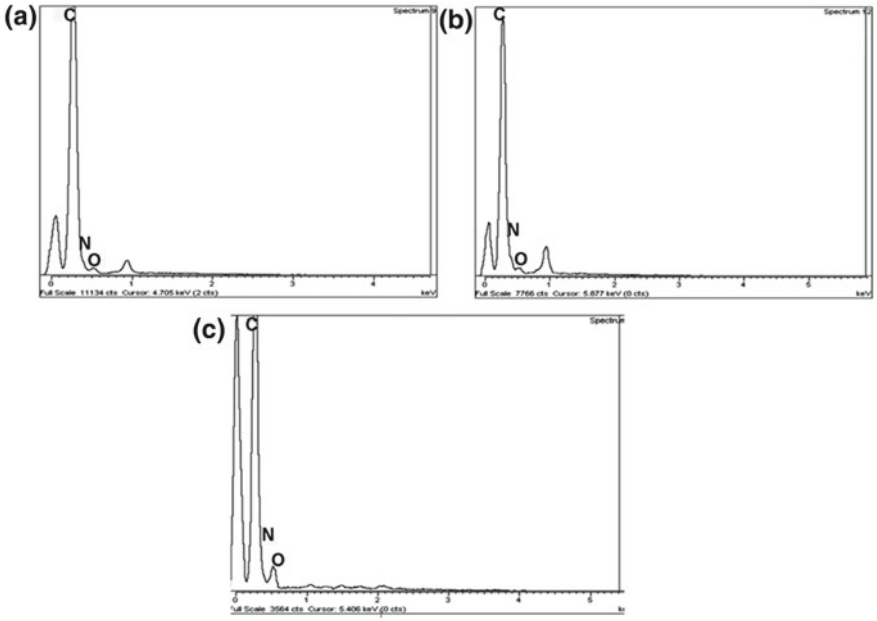

Fig. 5.5 EDX spectra of **a** NF shell (PAN), and **b** a cross-section of PAN/DCPD NF. The presence of nitrogen is masked by the neighboring carbon peak in the spectrum because of the energy resolution of the detector. Panel **c** shows a cross-sectional EDX spectrum of a PAN/isophorone diisocyanate NF. Panel **c** reveals a visible increase in the oxygen peak compared to that in panel **a**. This rise is attributed to the presence of the oxygen-containing isophorone diisocyanate in the fiber core. Reprinted with permission from Sinha-Ray et al. (2012)

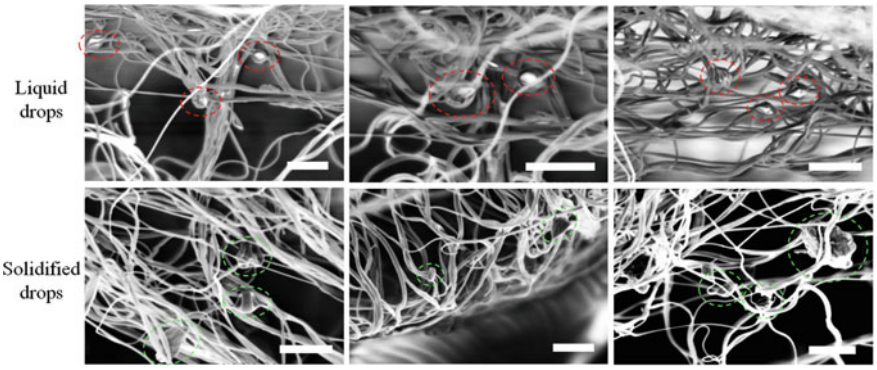

Fig. 5.6 SEM images of cut zone in a PRC (PAN–resin-curing agent) nanofiber mat (scale bars are 5 μm). The surrounding vacuum could have facilitated drop release from the fibers; however, such a release was also observed in open air under ambient pressure and temperature in An et al. (2015). Reprinted with permission from Lee et al. (2017a)

Fourier-transform infrared (FTIR) and Raman spectroscopies performed at room temperature in open air can also be used as nondestructive imaging techniques. The healing process, that is, the polymerization of the released healing agents, can be investigated using these techniques (Zanjani et al. 2015, 2017; Yerro et al. 2016). For example, in the case of DCPD, the bands at wavenumbers of 1572 cm^{-1} and 1614 cm^{-1} are assigned to the $\nu(C = C)$ stretching vibrations of the DCPD monomer (see Fig. 5.7). The occurrence of the healing process is confirmed by the fact that the disappearance of the peak at 1572 cm^{-1} and the red-shifting of the peak at 1614 cm^{-1}, which suggest the polymerization of DCPD (Yerro et al. 2016). FTIR analysis has also been used to confirm the encapsulation of hardener and epoxy within a fiber structure. Figure 5.7c and d show the FTIR spectra of hardener and resin, respectively. The peak at 1592 cm^{-1} corresponds to N–H bending vibrations, while the strong peak at 1150 cm^{-1} is related to the stretching of C–N bonds, confirming the presence of the amine-based hardener in the fiber structure (Fig. 5.7c). Furthermore, the peaks at 815 and 840 cm^{-1}, which belong to the oxirane groups, verify the presence of the epoxy resin within the triaxial fiber structure formed in Zanjani et al. (2015) (Fig. 5.7d).

Raman spectroscopy is another method used to determine the chemical compositions of specific healed or unhealed regions in self-healing materials. The Raman spectrum of PDMS in the healed crack studied by Lee et al. (2017b), mentioned in Sect. 3.4, was used to confirm that the resin and curing agent were released and that the resin was cured on the PDMS surface of the surrounding matrix. The bonds in the PDMS molecule, namely the Si–O–Si, Si–C, and CH_3 bonds, exhibit peaks at the wavenumbers of 492 cm^{-1}, 618/712 cm^{-1}, and 1265 cm^{-1}, respectively, in the Raman spectrum of PDMS (Jayes et al. 2003). The spectral peaks for the resin monomer, curing agent, and dyes used (cf. Fig. 3.25), and their corresponding wavenumbers are listed in Table 5.1. The peaks were selected to distinguish between the released resin monomer and curing agent on the cured PDMS surface. In particular, the resin monomer/curing agent mixing zone was investigated to confirm that mixing and curing had occurred successfully. The peaks at 1541 cm^{-1} (⁎) and 2168 cm^{-1} (◆) seen in the spectra of the resin monomer (Fig. 5.8b) and the curing agent (Fig. 5.8c) are not seen in the spectrum of cured PDMS (Fig. 5.8a). These two peaks, which correspond to the CH_2–NH–CH_2 and Si–H bonds, respectively, disappear as the resin monomer is polymerized by the curing agent (Colthup et al. 1975). In addition, the dyed resin monomer and curing agent exhibit additional peaks (○ and ●), which correspond to the pigments used to color them. The Raman spectrum of the mixing zone exhibits the peaks described above. The mixing zone is also shown in the optical image in Fig. 5.9, marked (f). The Raman spectrum does not contain the peaks at 1541 cm^{-1} (⁎) and 2168 cm^{-1} (◆) seen from the uncured resin monomer and curing agent; thus, it is considered to correspond to the cured PDMS. It does contain peaks related to both the dyed resin (○) and the curing agent (●) released from the damaged channels (cf. Fig. 3.25 in Sect. 3.4). This proves that the material in the mixing zone is cured PDMS formed by the mixing of the resin monomer and the curing agent released from the damaged channels and their subsequent polymerization on the crack banks (see Fig. 3.28 in Sect. 3.4).

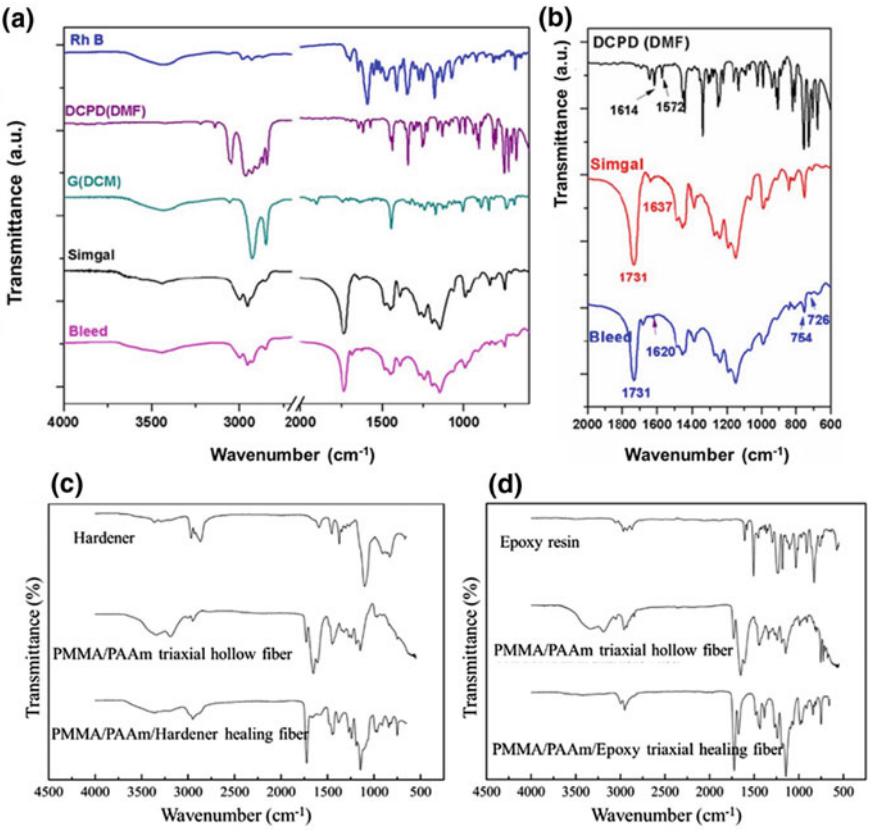

Fig. 5.7 **a** FTIR spectra of the initial materials and self-healing bleed. RhB: Rhodamine B; DCPD(DMF): 10 wt% DCPD solution in DMF; G(DCM): 1 wt% Grubbs' catalyst solution in methylene chloride (DCM); poly(DCPD) (RhB): ROMP (ring-opening metathesis polymerization) of polymer DCPD with RhB. **b** Spectra of DCPD(DMF), Simgal (a drug), and the bleed. Reprinted with permission from Yerro et al. (2016). **c** FTIR spectra of hardener, poly(methyl methacrylate)/poly(acrylamide) (PMMA/PAAm) triaxial hollow fibers, and PMMA/PAAm/hardener triaxial fibers. **d** FTIR spectra of epoxy resin, PMMA/PAAm triaxial hollow fibers, and PMMA/PAAm/epoxy triaxial fibers. Reprinted with permission from Zanjani et al. (2015)

Surface images from the same location of the microchannel system (in the mixing zone) are obtained using OM and analyzed using an optical surface profiler (see Fig. 5.9a and b, respectively; cf. Sect. 5.1). The pebble-like mixing zone between the two channel ends is clearly visible in Fig. 5.9a. The estimated height of this pebble-like zone is approximately 25 μm, according to the profilometry data.

Accordingly, it was found that in the macroscopic experiment of Lee et al. (2017b), the resin monomer and curing agent released into a crack were mixed and cured to

Table 5.1 Wavenumbers corresponding to the peaks seen in the Raman spectra

Wavenumber (cm^{-1})	Assignment
492	Si–O–Si symmetric stretching
618, 712	Si–C symmetric stretching
2907	CH_3 symmetric stretching
2965	CH_3 asymmetric stretching
1541 (∗)	marker for resin
2168 (⬥)	Marker for cure
1184, 1490 (○)	Marker for dye (resin)
1215, 1448 (●)	Marker for dye (cure)

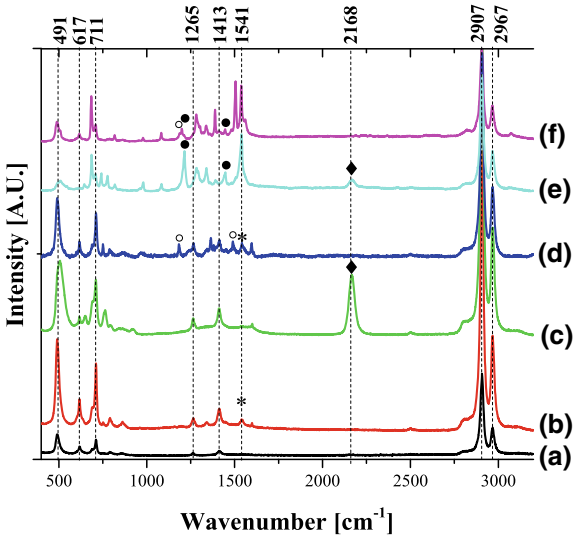

Fig. 5.8 Raman spectra: **a** cured PDMS, **b** pure resin monomer (∗), **c** pure curing agent (⬥), **d** dyed resin (○), **e** dyed curing agent (●), **f** mixing zone (the optical image is shown in Fig. 5.9a). Reprinted with permission from Lee et al. (2017b)

form additional PDMS chunks that helped to heal or stitch the crack banks together (cf. Fig. 3.28 in Sect. 3.4).

In addition, the self-healing of bisphenol A (BPA)-based epoxy resin was also studied using Raman spectroscopy in Patrick et al. (2014). The resin and hardener exhibited peaks at 1256 cm^{-1} (oxirane ring)/1610 cm^{-1} (phenyl ring) and 1656 cm^{-1} (amide-I), respectively (data is not shown here) (Farquharson et al. 2002; Merad et al. 2009; Maiti et al. 2004). Thus, based on the Raman spectrum of the fracture surface, the delivery of the healing agent and the occurrence of the healing (mixing and polymerization) processes were confirmed.

5.3 Thermal Analysis

Thermogravimetric analysis (TGA) and differential thermogravimetry (DTG) are useful in confirming the encapsulation of the self-healing cores in NF shells. Using these thermal analysis methods, the phase-change temperature can be determined (e.g., the melting or evaporation points). The change in the weight owing to the release of substantial amount of volatile substances or gasification during the phase-change process can be determined through TGA. DTG shows the first derivative of the weight-loss curve obtained by TGA and indicates the temperatures corresponding to the phase changes. According to the previous studies (Lee et al. 2014a, b; An et al. 2015), the evaporation temperatures of DMS resin monomer and its curing agent (uncured) are 576.3 °C (●) and 176.1 °C (⬥), respectively, while that of PAN is

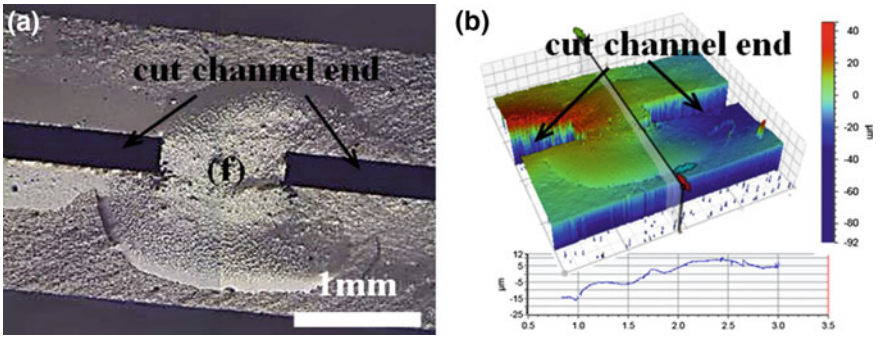

Fig. 5.9 **a** Optical image of cut surface (crack) on the microchannel system (cf. Figs. 3.25 and 3.28 in Sect. 3.4). **b** Optical profilometry image of the surface. Note that the spreading of the released healing agents is fully dominated by wettability, and they spread in all directions, including against gravity. Reprinted with permission from Lee et al. (2017b)

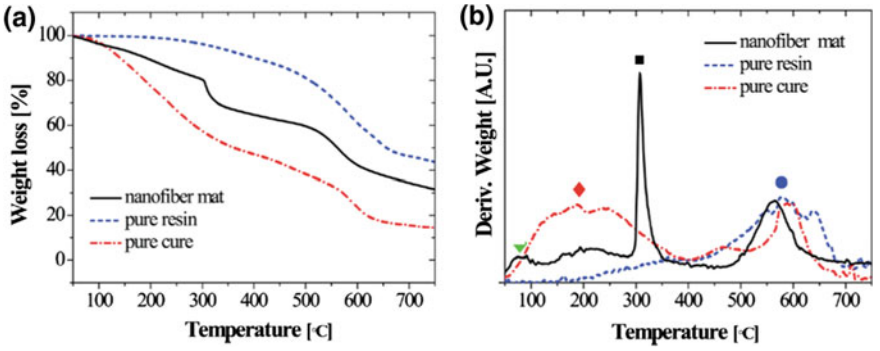

Fig. 5.10 Thermal analysis of core-shell NFs. **a** TGA curves of the core materials (DMS resin monomer and curing agent) and NF mat containing these materials within the cores. **b** DTG curves. The NF mat containing healing agents in the fiber core was obtained by emulsion electrospinning (cf. Sect. 4.3). Reprinted with permission from Lee et al. (2014a)

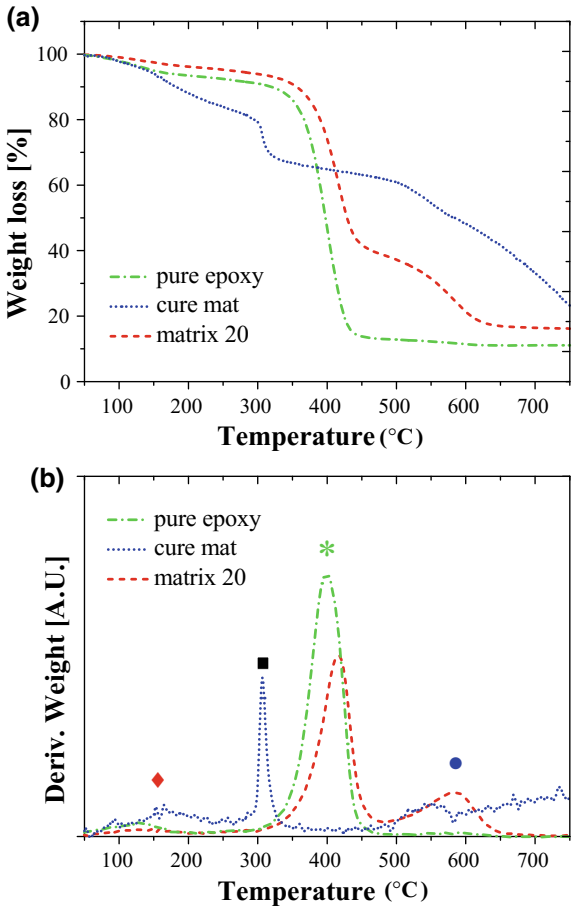

Fig. 5.11 **a** TGA results. **b** The corresponding DTG results. (◆ curing agent 176.1 °C, ■ PAN 305.0 °C, * epoxy–resin matrices with 20 wt% of resin monomer 416.1 °C, ● resin monomer 576.3 °C). Note that "matrix 20" herein refers to the epoxy–resin matrices with 20 wt% of resin monomer. The NF mat with curing agent in the fiber cores is denoted as "cure mat" herein. The NF mat containing curing agent in the fiber cores was obtained by emulsion electrospinning (cf. Sect. 4.3). Reprinted with permission from Lee et al. (2014a)

305.0 °C (■) (see Fig. 5.10, with the data for a fully vascular NF mat incorporating two mutually entangled networks of core-shell NFs containing either resin monomer or curing agent in the cores; cf. Sect. 4.3).

The results of the TGA of the hybrid self-healing materials (see Sect. 4.3) in Lee et al. (2014b) are presented in Fig. 5.11. The peak at 176.1 °C revealed by the NF mat corresponds to the curing agent, which is substantiated by a clearly distinct peak at ~305 °C, corresponding to PAN, agreeing with the results shown in Fig. 5.10. Indeed, 176.1 °C is the boiling temperature of the curing agent. In these materials, the epoxy matrices contained 5 wt% and 20 wt% NFs with curing agents in the cores (i.e., they are composite self-healing materials). Therefore, the peak at 176.1 °C should also be present in the data for the matrices. The magnification of the DTG data for these matrices near 176.1 °C reveals weak peaks, confirming the presence of the curing agent in the composite material. The DTG data for the matrices near 305 °C are difficult to resolve because of the relatively small amount of PAN. Lastly, the boiling

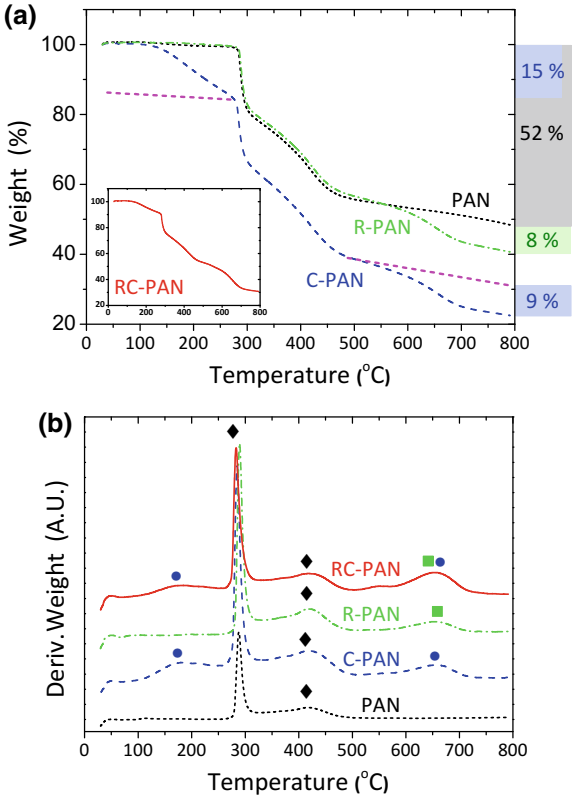

Fig. 5.12 Thermal analysis of PAN, R-PAN, C-PAN, and RC-PAN NFs. **a** TGA curves. The right-hand side column lists the total weight loss of the core and shell materials within the NFs (Gray: PAN, Green: resin monomer, Blue: curing agent; and purple line estimates the weight loss of curing agent). The insert graph shows the TGA results for RC-PAN NF mats. **b** DTG curves. The phase-transition temperatures of the core and shell materials are marked by black diamonds at 288 and 420 °C: PAN; green rectangles at 660 °C: resin monomer; blue circles at 180 and 660 °C: curing agent. The NF mats containing the resin monomer and curing agent in the fiber cores were obtained by co-electrospinning. Reprinted with permission from An et al. (2015)

temperature of the resin monomer in the matrices is 576.3 °C. At the resin monomer concentration of 5 wt%, the resin peak is indeterminate, with no distinctive peak, but rather a round peak. However, the resin monomer peak at 576.3 °C is clearly visible for the epoxy matrix containing 20 wt% of resin monomer.

The TGA was also conducted for NF mats with healing agents in the cores as formed using co-electrospinning (An et al. 2015; cf. Sect. 4.2). To determine the amount of the core or shell material contained in the NFs, TGA and DTG measurements are conducted, cf. Fig. 5.12. By comparing the TGA results (Fig. 5.12a) and the phase transition temperatures in the DTG results (Fig. 5.12b), the weight losses of the materials in question can be determined. In the temperature range of

0–800 °C, the weight losses of pristine PAN, curing agent, and resin monomer in the NFs are 52, 24, and 8%, respectively, consistent with the results of Lee et al. (2014a, b) discussed above. The weight loss of the curing agent was higher than that of the resin monomer because the volume of the resin monomer encapsulated in the resin-containing PAN (R-PAN) NFs is smaller than that of the curing agent encapsulated in the curing agent-containing PAN (C-PAN) NFs, since the resin monomer is mixed with n-hexane for stable co-electrospinning, as mentioned in Sect. 4.2. Because of the high evaporation rate of n-hexane, most of the n-hexane is evaporated before the samples are prepared for thermal analysis. Therefore, n-hexane is not detected in the TGA results, with no weight loss corresponding to n-hexane detected (not shown here). Figure 5.12 also shows the results for the mutually entangled R-PAN and C-PAN NF mats, which are denoted as RC-PAN NFs. It is instructive to see the differences in the phase-transition temperatures of the core and shell materials in NFs formed by different methods (cf. Figs. 5.10 and 5.11 with Fig. 5.12).

References

An S, Joshi BN, Lee MW, Kim NY, Yoon SS (2014) Electrospun graphene-ZnO nanofiber mats for photocatalysis applications. Appl Surf Sci 294:24–28

An S, Liou M, Song KY, Jo HS, Lee MW, Al-Deyab SS, Yarin AL, Yoon SS (2015) Highly flexible transparent self-healing composite based on electrospun core–shell nanofibers produced by coaxial electrospinning for anti-corrosion and electrical insulation. Nanoscale 7:17778–17785

Bleay SM, Loader CB, Hawyes VJ, Humberstone L, Curtis PT (2001) A smart repair system for polymer matrix composites. Compos A 32:1767–1776

Colthup NB, Daly LH, Wiberley SE (1975) Introduction to infrared and Raman spectroscopy, 3rd edn. Academic Press, New York

Farquharson S, Smith W, Rose J, Shaw M (2002) Correlations between molecular (Raman) and macroscopic (rheology) data for process monitoring of thermoset composite. J Process Anal Chem 7:45–53

Ghosal A, Sinha-Ray S, Sinha-Ray S, Yarin AL, Pourdeyhimi B (2016) Numerical modeling and experimental study of solution-blown nonwovens formed on a rotating drum. Polymer 105:255–263

Jayes L, Hard AP, Sene C, Parker SF, Jayasooriya UA (2003) Vibrational spectroscopic analysis of silicones: a Fourier transform-Raman and inelastic neutron scattering investigation. Anal Chem 75:742–746

Lee MW, An S, Jo HS, Yoon SS, Yarin AL (2015) Self-healing nanofiber-reinforced polymer composites: 1. Tensile testing and recovery of mechanical properties. ACS Appl Mater Interfaces 7:19546–19554

Lee MW, An S, Lee C, Liou M, Yarin AL, Yoon SS (2014a) Self-healing transparent core–shell nanofiber coatings for anti-corrosive protection. J Mater Chem A 2:7045–7053

Lee MW, An S, Lee C, Liou M, Yarin AL, Yoon SS (2014b) Hybrid self-healing matrix using core–shell nanofibers and capsuleless microdroplets. ACS Appl Mater Interfaces 6:10461–10468

Lee MW, Sett S, An S, Yoon SS, Yarin AL (2017a) Self-healing nano-textured vascular-like materials: Mode I crack propagation. ACS Appl Mater Interfaces 9:27223–27231

Lee MW, Yoon SS, Yarin AL (2017b) Release of self-healing agents in a material: What happens next? ACS Appl Mater Interfaces 9:17449–17455

Maiti NC, Apetri MM, Zagorski MG, Carey PR, Anderson VE (2004) Raman spectroscopic characterization of secondary structure in natively unfolded proteins: a-Synuclein. J Am Chem Soc 126:2399–2408

Merad L, Cochez M, Margueron S, Jauchem F, Ferriol M, Benyoucef B, Bourson P (2009) In-situ monitoring of the curing of epoxy resins by Raman spectroscopy. Polym Test 28:42–45

Pang JWC, Bond IP (2005a) 'Bleeding composites'—damage detection and self-repair using a biomimetic approach. Compos A 36:183–188

Pang JWC, Bond IP (2005b) A hollow fibre reinforced polymer composite encompassing self-healing and enhanced damage visibility. Compos Sci Technol 65:1791–1799

Patrick JF, Hart KR, Krull BP, Diesendruck CE, Moore JS, White SR, Sottos NR (2014) Continuous self-healing life cycle in vascularized structural composites. Adv Mater 26:4302–4308

Sett S, Lee MW, Weith M, Pourdeyhimi B, Yarin AL (2015) Biodegradable and biocompatible soy protein/polymer/adhesive sticky nano-textured interfacial membranes for prevention of Esca fungi invasion into pruning cuts and wounds of vines. J Mater Chem B 3:2147–2162

Sinha-Ray S, Lee MW, Sinha-Ray S, An S, Pourdeyhimi B, Yoon SS, Yarin AL (2013) Supersonic nanoblowing: a new ultra-stiff phase of nylon 6 in 20–50 nm confinement. J Mater Chem C 1:3491–3498

Sinha-Ray S, Pelot DD, Zhou ZP, Rahman A, Wu X-F, Yarin AL (2012) Encapsulation of self-healing materials by coelectrospinning, emulsion electrospinning, solution blowing and intercalation. J Mater Chem 22:9138–9146

Sinha-Ray S, Zhang Y, Yarin AL, Davis SC, Pourdeyhimi B (2011) Solution blowing of soy protein fibers. Biomacromol 12:2357–2363

Yerro O, Radojevic V, Radovic I, Petrovic M, Uskokovic PS, Stojanovic DB, Aleksic R (2016) Thermoplastic acrylic resin with self-healing properties. Polym Eng Sci 56:251–257

Zanjani JSM, Okan BS, Letofsky-Papst I, Menceloglu Y, Yildiz M (2015) Repeated self-healing of nano and micro scale cracks in epoxy based composites by tri-axial electrospun fibers including different healing agents. RSC Adv 5:73133–73145

Zanjani JSM, Okan BS, Yilmaz C, Menceloglu Y, Yildiz M (2017) Monitoring the interface and bulk self-healing capability of triaxial electrospun fibers in glass fiber reinforced epoxy composites. Compos A 99:221–232

Part III
Mechanical Behavior of Self-Healing Nanotextured Materials

Chapter 6
Failure, Cracks, Fracture, Fatigue, Delamination, Adhesion, and Cohesion

This Section is devoted to the description of several key ideas related to material failure, including several failure criteria (Sect. 6.1) and some necessary elements of the fracture mechanics, such as cracks, the Griffith theory, surface energy, and stress intensity factors for fracture in Modes I, II and III (Sect. 6.2). It also describes viscoelastic effects (Sect. 6.3) as well as subcritical (fatigue; Sect. 6.4) and critical (catastrophic) cracks and their propagation (Sect. 6.5). These elements of fracture mechanics are used in the discussion and analysis of the mechanical behavior of self-healing materials in Chap. 7. The present section also addresses interfacial phenomena at ply surfaces in composite materials such as delamination and de-bonding (Sect. 6.6), and introduces the fundamental aspects of measuring the adhesive and cohesive energies of stiff and soft materials (Sects. 6.7 and 6.8, respectively). These ideas are used in characterizing the mechanical aspects of delamination in Chap. 8. The present section also reviews the effect of nanofibers (not necessarily self-healing) on the toughening of ply surfaces in composites (Sect. 6.8).

6.1 Failure Criteria

The failure of loaded structure and devices has always accompanied practical engineering. Thus, the strength of materials as a scientific subject was researched extensively beginning in the 17th century; the search for failure conditions began with Galileo Galilei (Cherepanov 1979; Kachanov 2004; Barenblatt 2014). He, as well as Lamé and Rankine later, suggested that an ultimate normal stress σ_{max}, a material physical parameter, should determine the threshold to failure, and could be measured in uniaxial tensile tests. However, this assumption did not always agree with experimental data; Poncelet and Saint Venant proposed another failure criterion, namely, the ultimate strain at failure ε_{max}, which was also considered a material physical parameter measurable in uniaxial tensile tests. With the availability of further experimental data and the widespread introduction of additional types of materials to engineering practice beyond wood and stone, the formation of such macroscopic defects as slip

A. L. Yarin et al., *Self-Healing Nanotextured Vascular Engineering Materials*, Advanced Structured Materials 105, https://doi.org/10.1007/978-3-030-05267-6_6

and dislocations lines drew attention, and shear rather than normal stresses were investigated as failure criteria. Then, the failure condition can be formulated in the form of the Mohr–Coulomb criterion, namely (Tadmor and Gogos 2006):

$$\sigma_1 - \sigma_2 = |\sigma_1 + \sigma_2| \tan\beta + 2\alpha \tag{6.1}$$

where β is the angle of internal friction and α is the cohesion, both of which are material parameters. The principal stress difference is denoted as $(\sigma_1 - \sigma_2)$ and the principal stress sum as $(\sigma_1 + \sigma_2)$. As usual, the principal stresses correspond to the frame of reference in which shear stresses are zero (Green and Zerna 1954; Lurie 2005).

The condition of Eq. (6.1) arises from the maximum shear stress being equal to $(\sigma_1 - \sigma_2)/2$, while the normal stress acting at the surface of the maximum shear stress is equal to $(\sigma_1 + \sigma_2)/2$, and it is compressive (i.e. negative). Accordingly, when the Coulomb failure function F, defined as:

$$F = |\sigma_1 + \sigma_2| \tan\beta + 2\alpha - (\sigma_1 - \sigma_2) \tag{6.2}$$

becomes negative, the material fails; when F is positive, the material remains intact.

Therefore, the surface where $F = 0$ determines failure in shear. This essentially incorporates the Tresca failure criterion as well; Kachanov (2004).

It should be emphasized that in all the abovementioned failure criteria, the material behavior before failure is assumed to be linearly elastic, i.e., following Hooke's law (Landau and Lifshitz 1986; Yarin et al. 2017), whereas the behavior is not necessarily specified beyond the failure point, but typically assumed to be plastic. This was done, for example, by von Mises in proposing a failure criterion that is valid for the general three-dimensional case; the von Mises failure criterion encompasses the majority of the abovementioned stress-based failure criteria as particular cases. The criterion is formulated in terms of the second invariant of the stress tensor deviator $\boldsymbol{\tau}$ (excluding the isotropic part of the stress tensor), i.e., $I_2 = \mathrm{tr}(\boldsymbol{\tau}^2)$. Because the stress tensor and its deviator are implied to be symmetric, $\mathrm{tr}(\boldsymbol{\tau}^2) = \boldsymbol{\tau}{:}\boldsymbol{\tau}$, with the latter being the scalar product of $\boldsymbol{\tau}$ (Astarita and Marrucci 1974). Accordingly, the von Mises failure condition is formulated as:

$$\left(\frac{3}{2}\boldsymbol{\tau} : \boldsymbol{\tau}\right)^{1/2} - Y = 0 \tag{6.3}$$

where Y is the yield stress in uniaxial stretching, which is the material physical parameter characterizing the onset of plasticity.

Note that the invariant $I_2 = \tau_1^2 + \tau_2^2 + \tau_3^2$, where τ_i $(i = 1, 2, 3)$ denote the principal deviatoric stresses; furthermore $\tau_1\tau_2 + \tau_2\tau_3 + \tau_1\tau_3$ is also invariant (Lurie 2005). Therefore, another version of the second invariant can be introduced as:

$$I_2' = (\tau_1 - \tau_2)^2 + (\tau_2 - \tau_3)^2 + (\tau_1 - \tau_3)^2 = (\sigma_1 - \sigma_2)^2 + (\sigma_2 - \sigma_3)^2 + (\sigma_1 - \sigma_3)^2 \tag{6.4}$$

i.e., expressed through the principal stresses of the stress tensor $\boldsymbol{\sigma}$, rather than those of its deviator $\boldsymbol{\tau}$.

Then, the von Mises failure criterion can be written as:

$$\left\{\frac{1}{2}\left[(\sigma_1 - \sigma_2)^2 + (\sigma_2 - \sigma_3)^2 + (\sigma_1 - \sigma_3)^2\right]\right\}^{1/2} = Y \tag{6.5}$$

For an incompressible elastic body, Hooke's law reads (Yarin et al. 2017)

$$\boldsymbol{\tau} = 2G\boldsymbol{\varepsilon} \tag{6.6}$$

where G is the elastic shear modulus, and $\boldsymbol{\varepsilon}$ is the strain tensor.

Then, solving the elastic problem and using the von Mises criterion (6.3), one can determine the surface at which the material fails and plastic flow begins using the following equation (Yarin et al. 1995):

$$G(6\boldsymbol{\varepsilon} : \boldsymbol{\varepsilon})^{1/2} - Y = 0 \tag{6.7}$$

This failure condition appears adequate for problems of ballistic penetration (terminal ballistics; Yarin et al. 1995, 2017). In multiple other situations, the von Mises criterion or another of the abovementioned criteria adequately describe failure phenomena.

6.2 Cracks in Brittle Elastic-Plastic Media

Although there are many situations where the failure criteria discussed in Sect. 6.1 are reliable and accurate, they also fail in multiple other situations; material failure occurs at stresses and strains much lower than the expected σ_{max}, or ε_{max}, or Y determined from independent experiments (rather than calculated from molecular models, which typically provide gross overestimates). Griffith (1920) was the first to realize that real materials are far from ideal and uniform, as was assumed by solid mechanics and the abovementioned failure criteria. Real materials contain multiple microcracks, either pre-existing or developing during the deformation process. Under certain conditions, these microcracks can begin to grow and ultimately cause failure. In addition, several effects of surface dissolution (Joffe 1928) or treatment by surfactants (da C Andrade et al. 1950) can either enhance the strength of a crystalline body or reduce it, thus facilitating the onset of plastic flow. These effects cannot be explained in the framework of the solid-mechanics-based failure criteria considered in Sect. 6.1.

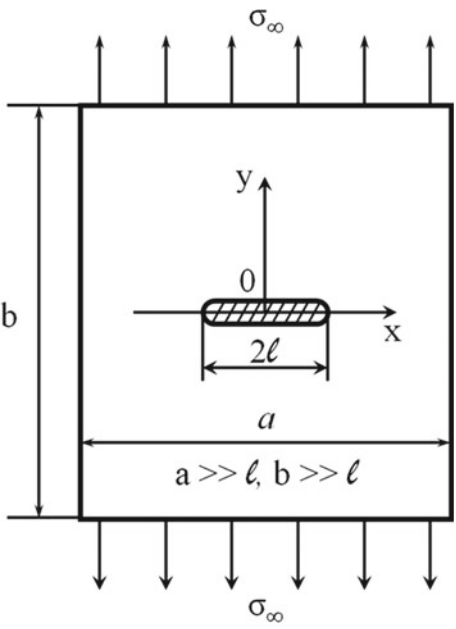

Fig. 6.1 Schematic of a crack in a body stretched normal to the crack. The crack is considered a cut following the x-axis; its detailed profile is not discussed here

The seminal idea proposed by Griffith, that cracks and their potential growth determine material failure, established the foundations of fracture mechanics. Following Griffith (1920), a single pre-existing crack of length 2ℓ in an infinite body (i.e., a body much larger than 2ℓ) is considered, which is stretched in the direction normal to the crack at infinity by the stress σ_∞ (Fig. 6.1).

If the crack propagates, i.e., its length 2ℓ increases, the elastic energy stored in the body, as well as the fields of strain and stresses in the body, are changed, and specifically decreased, because the process of crack propagation is self-sustainable, and thus the crack is unloading the body. The body is assumed to behave elastically with the elastic energy per unit volume $U \sim \sigma_\infty^2/E$ (E is the Young's modulus), following from the dimensional considerations. Consider a planar (a plane strain) problem, over a slice of length 1 in the direction normal to the xy–plane in Fig. 6.1. Then, the unloaded volume surrounding the crack is on the order of $\ell^2 \times 1$. Therefore, the reduction of the elastic energy due to the crack is $\Delta U \sim -(\sigma_\infty^2/E)\ell^2 \times 1$. As the crack propagates and elongates from ℓ to $\ell + \delta\ell$, the energy changes by

$$\delta(\Delta U) \sim \frac{\sigma_\infty^2 \ell}{E} \delta\ell \times 1 \tag{6.8}$$

The released elastic energy should be at least equal to the surface energy required to create a new surface for the extended crack, which is $\sim \gamma\delta\ell \times 1$, with γ being the surface energy per unit area (equivalent to the surface tension in fluid mechanics). Then, the condition for crack propagation is, according to Griffith (1920):

$$\delta(\Delta U) \sim \frac{\sigma_\infty^2 \ell}{E}\delta\ell \times 1 \geq \gamma\delta\ell \times 1 \tag{6.9}$$

Therefore, in the critical state when crack growth begins, Eq. (6.9) yields the following expression for the critical (minimum) stress required for a pre-existing crack of length ℓ to begin propagating:

$$\sigma_{\infty,c} = C\left(\frac{\gamma E}{\ell}\right)^{1/2} \tag{6.10}$$

where the dimensionless factor C could be a function of Poisson's ratio.

This factor can be found using the exact solution of the planar theory of elasticity in a plane with a crack. It is known that the solution is singular near the edge of the crack considered as a notch $-\ell \leq x \leq \ell$ and $y \equiv 0$, as in Fig. 6.1 (Cherepanov 1979). Then, asymptotically nearly all work δW by the elastic stresses that propagate the crack is exerted near the crack tip. Accordingly, only the normal stress $\sigma_{yy}\big|_{y=0}$ and the normal displacement $v|_{y=0}$ near the crack tip must be known. They are given by the following expressions:

$$\sigma_{yy}\big|_{y=0} = \frac{K_I}{\sqrt{2\pi r}} \tag{6.11}$$

$$v|_{y=0} = \frac{2(1-\nu)}{G}K_I\sqrt{\frac{\delta\ell - r}{2\pi}} \tag{6.12}$$

where r is reckoned over the x-axis from the crack tip at the beginning of the growth from $x = \ell$ to $x = \ell + \delta\ell$; G is the shear modulus and ν is Poisson's ratio (both being the material elastic parameters); K_I is the stress intensity factor of Mode I fracture, i.e., normal delamination near the crack tip (crack opening), the mode shown in Fig. 6.1.

It should be emphasized that, although the solutions given by Eqs. (6.11) and (6.12) are asymptotical and valid only near the crack tip, they do contain the "birthmark" of the global solution, for which they serve as asymptotes, namely, the stress intensity factor K_I. For the problem depicted in Fig. 6.1, it is given by Cherepanov (1979):

$$K_I = \sigma_\infty\sqrt{\pi\ell} \tag{6.13}$$

Because the force producing the work is $\sigma_{yy}\big|_{y=0}dr \times 1$ and the displacement is $v|_{y=0}$, and using Eqs. (6.11) and (6.12), the work done by the elastic forces on one side of the crack is:

$$\delta W = \int_0^{\delta\ell} \sigma_{yy}\big|_{y=0}\, v|_{y=0}dr \times 1 = 2\frac{K_I^2(1-\nu)}{\pi G}\int_0^{\delta\ell}\sqrt{\frac{\delta\ell - r}{r}}dr \times 1 \tag{6.14}$$

Evaluating the integral, and using Eq. (6.13) and the relationship $G = E/(1+\nu)$, the following is obtained:

$$\delta W = \frac{\sigma_\infty^2 \pi \ell (1-\nu^2)}{E} \delta\ell \times 1 \tag{6.15}$$

Equation (6.15) also yields an expression for the change in the elastic energy $\delta(\Delta U)$ due to propagation of the crack tip under consideration, because $\delta(\Delta U) = \delta W$, and thus (Irwin 1957):

$$\delta(\Delta U) = \frac{\sigma_\infty^2 \ell}{E} \left[\pi(1-\nu^2)\right] \delta\ell \times 1 \tag{6.16}$$

which is an accurate form of the estimate of Eq. (6.8).

During critical crack propagation, which is considered unhealable, the elastic energy is irreversibly consumed by the creation of the surface energy $2\gamma\delta\ell \times 1$, in which the factor 2 expresses the two banks of the crack. Then, using Eq. (6.16), the accurate condition of crack propagation replacing the estimate of Eq. (6.9) is obtained in the following form:

$$\frac{\sigma_\infty^2 \ell}{E} \left[\pi(1-\nu^2)\right] \delta\ell \times 1 \geq 2\gamma\delta\ell \times 1 \tag{6.17}$$

which yields the relation between the critical applied stress and the length of the crack beginning to propagate as:

$$\sigma_{\infty,c} = \left[\frac{2}{\pi(1-\nu^2)}\right]^{1/2} \left(\frac{\gamma E}{\ell}\right)^{1/2} \tag{6.18}$$

Therefore, the dimensionless factor C in Eq. (6.10) is $C = \left[2/\pi(1-\nu^2)\right]^{1/2}$.

The dependence of the critical stress on the crack length (6.18) is depicted in Fig. 6.2 by the dashed descending line. The initial crack length in the body is assumed to be ℓ_0. Then, according to Eq. (6.18) and Fig. 6.2, when the material is loaded by the stress $\sigma_\infty < \sigma_{\infty,c,0}$, where $\sigma_{\infty,c,0} = \left[2/\pi(1-\nu^2)\right]^{1/2} (E\gamma/\ell_0)^{1/2}$, the initial crack does not grow and remains subcritical. Only as the stretching stress approaches the value of $\sigma_\infty = \sigma_{\infty,c,0}$ does the crack propagation begin. The critical crack is unstable, because any inevitable small fluctuation in the value of σ_∞ above $\sigma_{\infty,c,0}$ induces crack growth. Therefore, even the value of $\sigma_{\infty,c,0}$ itself becomes supercritical for the enlarged crack (cf. the dashed curve in Fig. 6.2, which shows that an increasingly large crack requires an ever-decreasing critical stress for additional growth). Thus, the crack continues growing if the value of the stress $\sigma_{\infty,c,0}$ is not significantly decreased. If it decreased latter, the crack growth may stop. However, in the majority of materials such a crack would never heal; exceptions include materials with molecularly smooth crack banks, such as mica. Therefore, under the action of a constant load $\sigma_{\infty,c,0} \approx$ const, the crack growth becomes unstoppable and catastrophic.

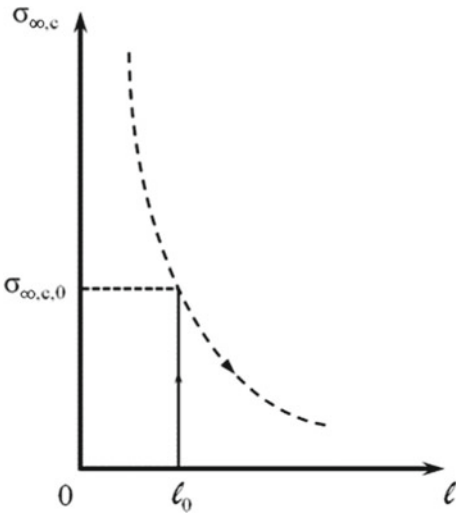

Fig. 6.2 Critical stress versus crack length

Equations (6.13) and (6.18) show that a critical minimum value of the stress intensity factor K_I required for crack growth exists, as:

$$K_{Ic} = \left[\frac{2\gamma E}{(1-\nu^2)}\right]^{1/2} \tag{6.19}$$

This result shows that the critical minimum value of the stress intensity factor K_{Ic} is essentially the materials parameter characterizing the proclivity of a material to fail by Mode I fracture because of pre-existing cracks. A crack remains subcritical, i.e., stable in the framework of the present theory, for $K_I < K_{Ic}$.

The result of the Griffith theory given by Eq. (6.18) agrees with the experimental data for such brittle materials as glass and mica, which have surface energy γ values approaching those predicted by physical theories considering the detailed molecular interactions in solid bodies (Cherepanov 1979). It should be emphasized that Eq. (6.18) is applicable to some other materials, such as metals, although the value of γ is three orders of magnitude larger than the theoretically expected surface energy. This is related to the significant plastic dissipation in such materials ahead of the crack tip; for crack propagation, the released elastic energy should be consumed by both the surface energy and the plastic dissipation. If the size of the plastic dissipation zone ahead of the crack d is much smaller than the crack length, i.e., $d \ll \ell$, the approximation of the crack tip as a singularity, as in Eqs. (6.11)–(6.17), remains valid, as does the result (6.18), with γ now understood as the overall energy loss per unit area including plastic dissipation (Orowan 1952; Irwin 1957). Accordingly, the value of the stress intensity factor K_I required for crack growth K_{Ic} increases. With the fracture toughness K_{Ic} as the physical parameter characterizing fracture and the yield stress Y as the physical parameter characterizing plasticity, the size of the plas-

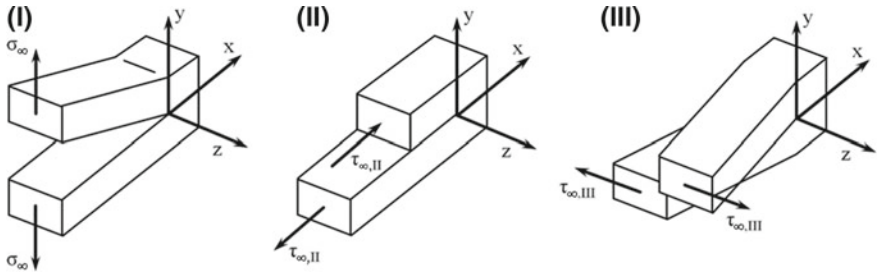

Fig. 6.3 Three different modes of crack growth

tic dissipation zone ahead of the crack can be evaluated as $d \sim (K_{Ic}/Y)^2$, because this is the only parameter combination that has units of length [cf. Eq. (6.13)]. Therefore, $K_{Ic} \sim Y\sqrt{d}$.

In addition to fracture by crack opening (Mode I), as considered above, two additional basic mechanisms exist for material failure due to cracks. They are in-plane shear (Mode II) and out-of-plane shear (tearing; Mode III), as depicted in Fig. 6.3.

The asymptotical singular solutions of the elastic problems for Modes II and III are well known and follow the same form as those in Eqs. (6.11) and (6.12) for the corresponding shear stresses and displacements (Cherepanov 1979). Accordingly, calculations similar to those done for Mode I yield the critical shear stress $\tau_{\infty,II,c}$ required for crack growth in Mode II as:

$$\tau_{\infty,II,c} = \left[\frac{2}{\pi(1-\nu^2)}\right]^{1/2}\left(\frac{\gamma E}{\ell}\right)^{1/2} \tag{6.20}$$

Similarly, in Mode III, the critical shear stress $\tau_{\infty,III,c}$ required for crack growth is expressed as:

$$\tau_{\infty,III,c} = \left[\frac{4}{\pi(1+\nu)}\right]^{1/2}\left(\frac{\gamma E}{\ell}\right)^{1/2} \tag{6.21}$$

6.3 Cracks in Viscoelastic Media

Plastic or viscous dissipation occurs near the crack tip in addition to the elastic phenomena, as mentioned in Sect. 6.2. This means that the behavior of a real material near the crack tip may be viscoelastic. It is tempting to include a viscoelastic zone in the near-tip domain of a growing crack, implying that the crack banks do not detach from each other instantaneously as in the brittle elastic case in Sect. 6.2, but instead experience a certain viscoelastic resistance at some length δ from the tip. Several models of this type incorporating viscous dissipation at the crack tip are known

in the literature (cf. the monographs of Cherepanov 1979 and Barenblatt 2014 and references therein). Here, the viscoelastic model of Entov and Salganik (1968) is discussed to some extent. One viscoelastic solid model is the Kelvin–Voigt model, which in its simplest form can be written as Rabotnov (1969):

$$\frac{\partial \varepsilon}{\partial t} + \frac{1}{\theta}\varepsilon = \frac{1}{\theta}\frac{\sigma}{E} \tag{6.22}$$

where ε is strain, σ is stress, t is time, and θ is the relaxation time, which is a physical parameter of the Kelvin–Voigt material, as is its Young's modulus E. It should be emphasized that such a material possesses the viscosity $\mu = E\theta$, which may be used as the second rheological parameter (in addition to the elastic parameter E) instead of θ.

Consider a linear Mode I crack propagating with velocity U against the direction of the x-axis (i.e., opposite to that of Fig. 6.3, I), with the y-axis being normal to it. The crack tip is located at the moment t at $x = \ell(t)$, with the crack occupying the domain $x > \ell(t)$, whereas the material ahead of it at $x < \ell(t)$ is intact. The global planar solution for a linear elastic body surrounding such a crack is known (Cherepanov 1979). Then, according to the Volterra elastic–viscoelastic correspondence principle (Rabotnov 1969; Rizzo and Shippy 1971; Cherepanov 1979; Paulino and Jin 2001; Mukherjee and Paulino 2003), the elastic solution can be substituted into the operator determined by Eq. (6.22) to formulate the corresponding viscoelastic problem for such a crack. Then, instead of Eq. (6.22), the following problem is obtained (Entov and Salganik 1968):

$$\frac{\partial}{\partial t}\left(\left.\frac{\partial v}{\partial x}\right|_{y=0}\right) + \frac{1}{\theta}\left(\left.\frac{\partial v}{\partial x}\right|_{y=0}\right) = \frac{1}{\theta}\frac{2(1-\nu^2)}{\pi E}\int_{\ell(t)}^{\infty}\frac{\sigma_{yy}(s,t)}{s-x}\sqrt{\frac{s-\ell(t)}{x-\ell(t)}}\,ds, \quad \text{for } x > \ell(t) \tag{6.23}$$

$$\frac{\partial}{\partial t}\left(\left.\frac{\partial v}{\partial x}\right|_{y=0}\right) + \frac{1}{\theta}\left(\left.\frac{\partial v}{\partial x}\right|_{y=0}\right) = 0, \quad \text{for } x < \ell(t) \tag{6.24}$$

Here, as in Sect. 6.2, v is displacement in the y-direction caused by material stretching in Mode I, and σ_{yy} is the corresponding normal stress over the still resisting to opening part of the crack near the tip that resists opening; s is a dummy variable. The role of the strain ε in Eq. (6.22) is played in Eqs. (6.23) and (6.24) by the strain $\varepsilon = \partial v/\partial x|_{y=0}$. Equation (6.24) expresses the cancelling of normal stresses in the intact material ahead of the crack tip.

In the still intact material within a propagating crack, the straining time is on the order of $[x - \ell(t)]/U$; accordingly:

$$\frac{\partial \varepsilon}{\partial t} \simeq \frac{\varepsilon}{[x-\ell(t)]/U} \tag{6.25}$$

For the locations within the intact part of the crack where $[x - \ell(t)]/U \ll \theta$, the rate of strain is very high compared to ε/θ and the material response according to Eq. (6.22) is viscous, i.e., $\sigma \simeq \theta E \partial\varepsilon/\partial t = \mu \partial\varepsilon/\partial t$. There, according to Eqs. (6.23) and (6.25), the former equation is reduced to the following:

$$\left.\frac{\partial v}{\partial x}\right|_{y=0} = \sqrt{x - \ell(t)}\frac{2(1-\nu^2)}{\pi E \theta U}\int\limits_{\ell(t)}^{\infty}\frac{\sigma_{yy}(s,t)}{\sqrt{s-\ell(t)}}ds \tag{6.26}$$

Implying the convergence of the integral, it is denoted as:

$$K = \int\limits_{\ell(t)}^{\infty}\frac{\sigma_{yy}(s,t)}{\sqrt{s-\ell(t)}}ds \tag{6.27}$$

which is the fracture toughness fully determined by the resistance to opening within the "glued" leading portion of the crack (Barenblatt 2014). It should be emphasized that the fracture toughness K differs by definition from the widely used fracture toughness K_{Ic} introduced in Sect. 6.2 and used elsewhere. Then, integrating Eq. (6.26) subjected to the boundary condition $v|_{y=0} = 0$ at $x = \ell(t)$, the following is obtained:

$$v|_{y=0} \simeq \frac{2}{3}[x - \ell(t)]^{3/2}\frac{2(1-\nu^2)}{\pi E \theta U}K \tag{6.28}$$

$$\text{for} \quad x - \ell(t) \ll U\theta \ll d \tag{6.29}$$

The crack profile given by Eq. (6.28) corresponds to the viscous domain at the leading part of the crack tip. The upper limit of this domain, d, is determined by the decay of the assumed resistance (stress) along the crack bank, which is essentially the effective cut-off length of the stress σ_{yy} from the crack tip.

However, in the domain where $[x - \ell(t)]/U \gg \theta$, i.e., significantly far (but not infinitely far) from the crack tip, $\partial\varepsilon/\partial t \ll \varepsilon/\theta$ and the response determined by Eq. (6.22) is elastic, i.e., $\sigma \simeq E\varepsilon$. Then, Eq. (6.23) yields:

$$\left.\frac{\partial v}{\partial x}\right|_{y=0} \simeq \frac{2(1-\nu^2)}{\pi E}\frac{1}{\sqrt{x-\ell(t)}}K \tag{6.30}$$

By integrating the latter equation, one finds:

$$v|_{y=0} \simeq 4\sqrt{x - \ell(t)}\frac{(1-\nu^2)}{\pi E}K \tag{6.31}$$

$$\text{for} \quad U\theta \ll x - \ell(t) \ll d \tag{6.32}$$

The crack profile (6.31) is valid in the elastic domain.

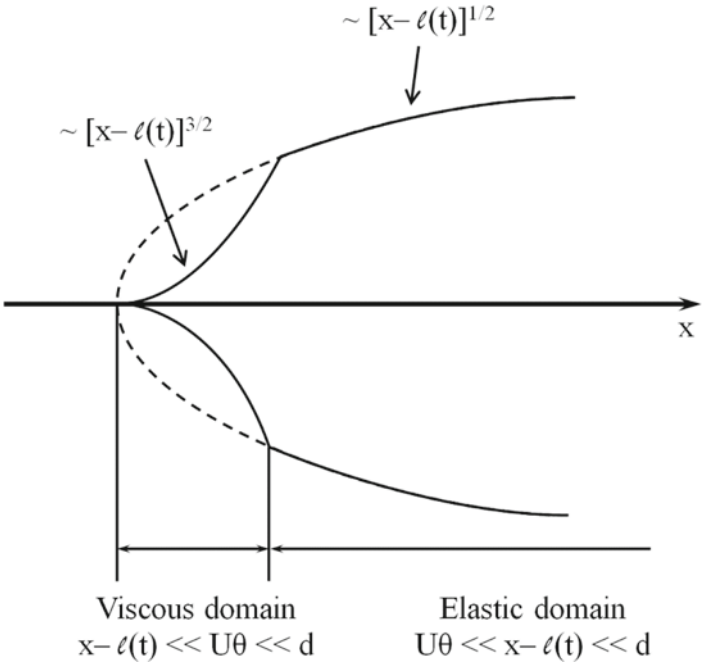

Fig. 6.4 Crack shape predicted for a viscoelastic material with resistance to crack opening in the leading part near the crack tip. Reprinted with permission from Lee et al. (2017)

Combining the results (6.28) and (6.29) with (6.31) and (6.32), the profile of a propagating crack with a zone of viscoelastic resistance to opening near the tip can be ascetrained as shown in Fig. 6.4. It should be emphasized that such a crack profile is predicted for a general viscoelastic resistance to the opening of the crack tip, not necessarily for the Kelvin–Voigt resistance (Landau and Lifshitz 1986).

6.4 Fatigue Cracks

Fatigue is considered a phenomenon associated with the growth of pre-existing cracks caused by periodic loading and unloading cycles, which eventually determine the lifetime of a body before a large magistral crack develops and causes catastrophic failure. Under cyclic Mode I loading and unloading the stress intensity factor $K_I = K_{I,max}$ can surpass the critical value K_{Ic}, thus causing the pre-existing cracks to grow. If the stress intensity factor K_I remained constant, the growth would immediately become catastrophic (Sect. 6.2). However, during the cyclic loading and unloading, the stress intensity factor K_I is periodically decreased below the critical level, and thus, the crack growth would stop during unloading stages. Cracks growth would resume during loading, and so on. In 1963, Paris (1964) and Paris and Erdogan (1963) proposed the following empirical law, known as Paris' law, which describes

the rate of crack growth per cycle for multiple materials, irrespective of their internal structure, at intermediate loads:

$$\frac{d\ell}{dn} = A(K_{I,max} - K_{I,min})^m \tag{6.33}$$

where ℓ is the crack length, $K_{I,min}$ is the minimum value of the stress intensity factor K_I per cycle (a sub-critical value), n is the number of cycles, which should be very large, A is the material constant, and the exponent m is between 2 and 10 for different materials (Cherepanov 1979; Suresh 1998; Barenblatt 2014).

For an external load that gradually and non-periodically increases in time t, $\sigma_\infty(t)$, increases in the pre-existing crack length $\ell(t)$ are stable when (Cherepanov 1979, Lee et al. 2017)

$$\frac{d\sigma_\infty}{d\ell} > 0 \tag{6.34}$$

This means that a pre-existing subcritical crack increases under the increasing load, but remains subcritical.

For a crack pre-notched at the center of a plate of width 2h, the stress intensity factor K_I is found as (Cherepanov 1979)

$$K_I = \sigma_\infty \sqrt{\pi \ell \sec \frac{\pi \ell}{2h}} \tag{6.35}$$

Note that Eq. (6.13) follows from Eq. (6.35) in the limit $h/\ell \to \infty$.

The critical stress intensity factor K_{Ic} is a material property that can be evaluated using Eq. (6.35) for the measured stress values corresponding to the ultimate strength. The yield stress Y can be obtained by fitting the stress–strain curve of an intact material to the phenomenological equation for uniaxial stretching (Green 1956):

$$\sigma = Y \tanh\left(\frac{E}{Y}\varepsilon\right) \tag{6.36}$$

where E is Young's modulus, σ is the tensile stress, and ε is the tensile strain.

Rendering Eqs. (6.34) and (6.35) dimensionless and introducing the dimensionless variables $\overline{\ell}$, $\overline{\sigma_\infty}$ and λ:

$$\overline{\ell} = \frac{\ell}{h}, \quad \overline{\sigma_\infty} = \sigma_\infty \frac{\sqrt{\pi h}}{K_{Ic}}, \quad \lambda = \frac{\pi K_{Ic}^2}{12 h Y^2} \tag{6.37}$$

the region of the unstable crack growth on the $\overline{\ell} - \overline{\sigma_\infty}$ plane is found as (Cherepanov 1979, Lee et al. 2017):

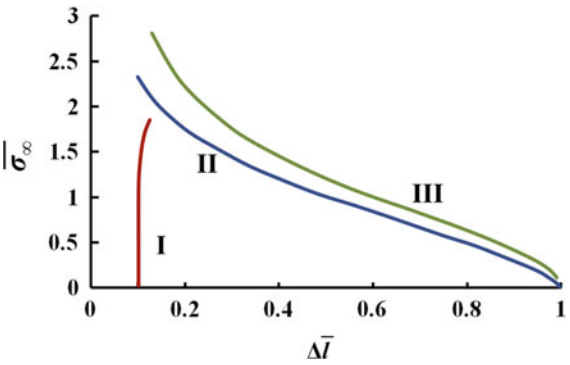

Fig. 6.5 The plane $\Delta\bar{\ell} - \overline{\sigma_\infty}$ with different domains of crack propagation. Red line I corresponds to Eq. (6.39), blue line II to Eq. (6.38), and green line III to Eq. (6.40). Reprinted with permission from Lee et al. (2017)

$$\cos\frac{\pi\bar{\ell}}{2} \le \bar{\ell}\overline{\sigma_\infty}^2\left[1 + \lambda\overline{\sigma_\infty}^2\left(1 + \frac{\pi\bar{\ell}}{2}\sec\frac{\pi\bar{\ell}}{2}\right)\sec\frac{\pi\bar{\ell}}{2}\right] \tag{6.38}$$

The equality in Eq. (6.38) corresponds to curve II (blue) in Fig. 6.5, where the domains below and above this curve correspond to stable and unstable (i.e., supercritical, catastrophic) crack growth, respectively. It should be emphasized that for an infinitely wide plate ($h/\ell \to \infty$) and a perfectly elastic material ($Y = \infty$), and considering Eqs. (6.19) and (6.37), Eq. (6.38) is reduced to the condition given by Eq. (6.18) (cf. Sect. 6.2).

The crack growth in the stable (subcritical) domain from an initial dimensionless crack length of $2\bar{\ell}_0$ is given by (Cherepanov 1979, Lee et al. 2017):

$$\bar{\ell} - \bar{\ell}_0 = -\lambda\left[\bar{\ell}\overline{\sigma_\infty}^2\sec\frac{\pi\bar{\ell}}{2} + \ln\left(1 - \bar{\ell}\overline{\sigma_\infty}^2\sec\frac{\pi\bar{\ell}}{2}\right)\right] \tag{6.39}$$

This is a quasi-static increase in length of a subcritical crack under an increasing but still subcritical stretching (disjoining) load $\overline{\sigma_\infty}(t)$. Equation (6.39) corresponds to the solid line of curve I (red) in Fig. 6.5.

A crack in any body begins to behave as an ideally brittle crack when the dimensional term $\Delta\bar{\ell} > 2$, where (Cherepanov 1979, Lee et al. 2017):

$$\Delta\bar{\ell} = \frac{12}{\pi}\frac{Y^2(\bar{\ell} - \bar{\ell}_0)}{K_{Ic}^2} \tag{6.40}$$

Equation (6.40) corresponds to curve III (green) in the unstable (supercritical, catastrophic domain) in Fig. 6.5.

The theoretical results depicted in Fig. 6.5 are compared to the experimental data on the crack propagation in self-healing nanotextured vascular materials in Sect. 7.4.

6.5 Critical Catastrophic Crack and Subcritical Crack Propagation

The experimental evidence in Sect. 7.3 reveals that pre-existing cracks can grow not only under periodic cyclic loading that temporarily enters into the unsteady domain, or under a transient increasing load crossing into the unsteady domain (both of which cases are considered in Sect. 6.4), but also under subcritical constant tensile loading. The latter cannot be explained by the theory in Sects. 6.1–6.4, and was analyzed recently by Lee et al. (2016), as discussed below.

According to Eq. (6.18) of Sect. 6.2, the half-length of a critical crack in Mode I, $\ell = \ell_*$, subjected to the tensile (disjoining) stress σ_∞ is given by the following expression:

$$\ell_* = \frac{2\gamma E}{\pi\sigma_\infty^2(1-\nu^2)} \tag{6.41}$$

It should be emphasized that a crack with the half-length ℓ_* is unstable and prone to growth, i.e., such a crack is catastrophic and can cause almost immediate failure of the loaded sample (cf. Sect. 6.2 and Barenblatt 2014). Shorter cracks of $\ell < \ell_*$, may self-heal (Cho et al. 2006), as observed with very smooth surfaces such as crack banks in mica. However, it is clear that in multiple materials, the cracks do not self-heal, even though they are not catastrophic with $\ell < \ell_*$. Therefore, specific physical mechanisms are suggested to explain the growth of subcritical cracks (Cherepanov 1979).

Here we explore a different plausible mechanism for the growth of subcritical cracks, which could also provide another perspective on the jump-like crack propagation observed in several materials (Cherepanov 1979; Lee et al. 2016; cf. Sect. 7.3). It should be emphasized that shorter subcritical cracks exist in materials that are subjected to perturbations and vibrations, which cause elastic sound waves to propagate. If a crack with length $\ell < \ell_*$ is oriented in the x-direction in a material that is stretched normally to the crack in the y-direction, the transversal elastic waves may affect the crack opening. Such waves are described by the following wave equation (Landau and Lifshitz 1986):

$$\frac{\partial^2 v}{\partial t^2} = C_t^2 \frac{\partial^2 v}{\partial x^2} \tag{6.42}$$

where v is the displacement in the y-direction and the velocity of the transverse elastic sound wave is given by:

$$C_t = \sqrt{\frac{E}{\rho(1+\nu)}} \tag{6.43}$$

in which ρ is the material density.

Taking the solution of Eq. (6.42) as $v = A\sin(kx - \omega t)$, where A is the amplitude, k the wavenumber, and ω the frequency, the average kinetic energy of the transverse elastic sound wave per unit area, $\overline{K}$, can be obtained from the following expression:

$$\overline{K} = 2A\left\langle \frac{1}{2}\rho\left(\frac{\partial v}{\partial t}\right)^2 + \frac{1}{2}\rho C_t^2\left(\frac{\partial v}{\partial x}\right)^2 \right\rangle = 2\rho A^3 C_t^2 k^2 \langle \cos^2(kx - \omega t)\rangle = \rho A^3 C_t^2 k^2 \tag{6.44}$$

Thus:

$$k^2 = \frac{\overline{K}}{\rho A^3 C_t^2} \tag{6.45}$$

The energy supplied by the elastic sound waves can cause the growth of subcritical (non-catastrophic) cracks with lengths $\ell < \ell_*$. Such cracks are located in materials subjected to random vibrations with numerous internal defects, e.g., in composites with embedded nanofiber mats containing healing agents. The theoretical analysis of the jump-like growth of subcritical cracks observed in experiments with such samples (cf. Sect. 7.3) addresses not a neat material, but materials with significant random defects in the internal structure, associated with the presence of the fibers. These factors can affect the evolution of the subcritical cracks with lengths $\ell < \ell_*$. Therefore, the length of such cracks cannot be treated deterministically, but rather statistically. The probability density function $\psi(x)$ is responsible for the localization of a subcritical crack at a certain length where it can exist as a metastable subcritical crack for some time. The probability of the localization of a crack can be described as a solution of the Schrödinger wave equation as

$$\frac{d^2\psi}{dx^2} = -k^2\psi \tag{6.46}$$

From Eqs. (6.45) and (6.46), we obtain:

$$\frac{d^2\psi}{dx^2} = -\frac{\overline{K}}{\rho A^3 C_t^2}\psi \tag{6.47}$$

The total energy of a crack per unit area is:

$$2\gamma = \overline{K} + U_{el} \tag{6.48}$$

where the elastic energy $U_{el} = \delta(\Delta U)$ is given by Eq. (6.16).

From Eqs. (6.16), (6.47), and (6.48), the following is derived:

$$\frac{d^2\psi}{dx^2} + \frac{1}{\rho A^3 C_t^2}\left[2\gamma - \frac{\pi(1-\nu^2)}{E}\sigma_\infty^2 \ell\right]\psi = 0 \tag{6.49}$$

Then, accounting for Eq. (6.41), Eq.(6.49) can be transformed to the following form:

$$\frac{d^2\psi}{dx^2} + \frac{2\gamma}{\rho A^3 C_t^2}(1 - \overline{L})\psi = 0 \tag{6.50}$$

where $\overline{L} = \ell/\ell_*$.

Crack localization imposes the following boundary conditions for Eq. (6.50):

$$x = -\ell, \psi = 0; \quad x = \ell, \psi = 0 \tag{6.51}$$

The solution of Eq. (6.50) subjected to the boundary conditions of Eq. (6.51) reveals that only a discrete spectrum of lengths of subcritical metastable cracks is possible. This spectrum is determined by the following cubic equation:

$$\overline{L}^3 - \overline{L}^2 + (nM)^2 = 0 \tag{6.52}$$

where n = 1, 2,…, and the dimensionless parameter M is given by the following:

$$M = \frac{\pi^2 \sigma_\infty^2 (1 - \nu^2)}{2\gamma E}\left(\frac{\rho A^3 C_t^2}{2\gamma}\right)^{1/2} \tag{6.53}$$

The solutions of Eq. (6.52) are elementary. Namely, for $(nM)^2 \ll 1$, the three roots of Eq. (6.52) are:

$$\overline{L}_1 \approx nM, \quad \overline{L}_2 \approx 1, \quad \overline{L}_3 \approx -nM \tag{6.54}$$

The first root determines a discrete set of short subcritical cracks corresponding to n = 1,2,…, which shows that the transition from a shorter to longer subcritical crack in this family can occur only in near-instantaneous leaps. The second root corresponds to the borderline catastrophic crack, which might be even smaller than its value as obtained from Eq. (6.41) corresponding to $\overline{\ell}_2 = 1$, because of the energy supplied by the elastic sound waves. Finally, the third negative set of roots $\overline{\ell}_3$ in Eq. (6.54) is unphysical.

For a wide range of values of the product nM, Cardano's formulae yield the solutions of Eq. (6.52), as illustrated in Fig. 6.6. Based on these solutions, the following conclusions can be made: roots 1 and 2 are real and positive for $1 \leq n \leq 38$ (for M = 0.01), whereas root 3 is always real and negative (and thus unphysical). The real root 1 describes the subcritical metastable half-lengths, which can increase only in a discretized manner by the energy supplied by the elastic sound waves. Moreover, in the asymptotic limit $(nM)^2 \ll 1$ corresponding to Eq. (6.54) the energy supply required for a jump in the crack size is given by:

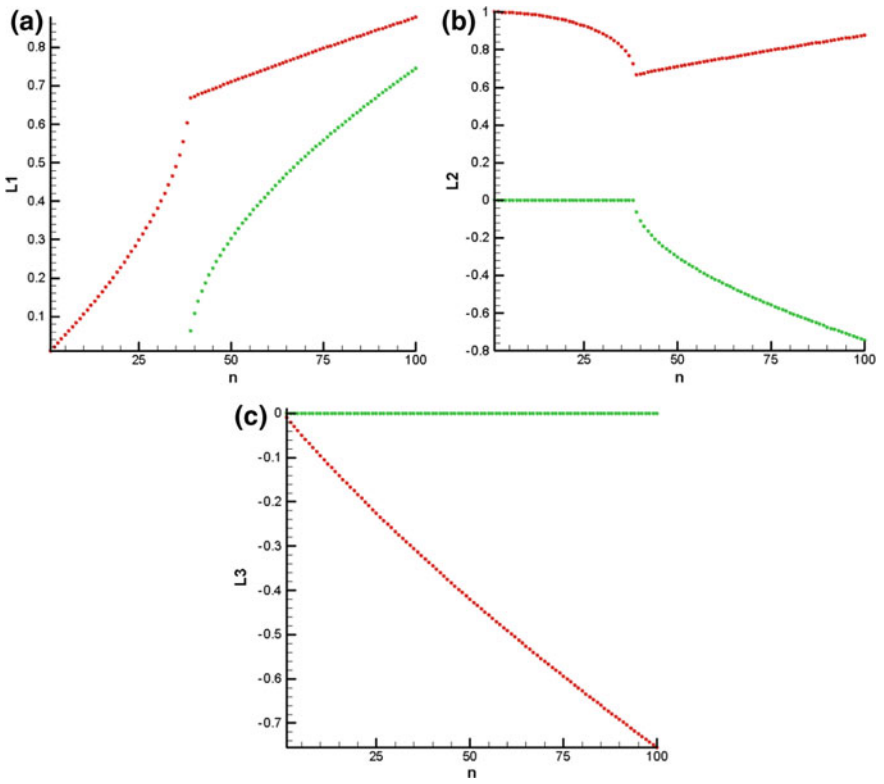

Fig. 6.6 **a** Root $\overline{L}_1$, **b** root $\overline{L}_2$, and **c** root $\overline{L}_3$. All roots are obtained at M = 0.01. Red and green symbols represent the real and imaginary parts, respectively. Reprinted with permission from Lee et al. (2016)

$$(\Delta\overline{K})_n = \Delta(2\gamma - U_{el})_n = (-\Delta U_{el})_n = \frac{\pi(1-\nu^2)\sigma_\infty^2(\ell_{1,n+1} - \ell_{1,n})}{E}$$
$$= 2\gamma\left[\frac{\pi^2\sigma_\infty^2(1-\nu^2)}{2\gamma E}\left(\frac{\rho A^3 C_t^2}{2\gamma}\right)^{1/2}\right] \tag{6.55}$$

This energy is independent of n. However, the latter is true only in the asymptotic limit $(nM)^2 \ll 1$, as indicated by Eq. (6.54) and Fig. 6.6a. The dependence of $\ell_{1,n}$ on n is linear for smaller values of n. However, as $\ell_{1,n}$ increases with n, the dependence of $\ell_{1,n}$ on n becomes nonlinear, as shown in Fig. 6.6a. Hence, $(\Delta\overline{K})_n$ increases with n. This implies that the transitions in size from one large subcritical metastable crack to a larger one becomes less probable.

On the other hand, according to Fig. 6.6b, the size of the catastrophic crack also depends on n, and $\ell_{2,n}$ decreases with n, i.e., a smaller crack becomes catastrophic under the effects of the vibrational energy supplied by the elastic sound waves. At the last possible steady state with M = 0.01, at n = 38, one obtains $\overline{L_2} = 0.726$ instead of $\overline{L_2} = 1$ in the absence of vibrations. Notably, the corresponding subcritical metastable crack at M = 0.01 and n = 38 has the half-length $\overline{L_1} = 0.603$, i.e., the

transition from this length to $\overline{L_2} = 0.726$ would be a final jump causing catastrophic failure for sufficient vibrational energy delivered by the elastic sound waves.

6.6 Delamination Cracks

Advanced polymer matrix composites (PMCs) comprising compliant polymeric matrices (typically epoxies) reinforced with high-performance macroscopic fibers (e.g., high-strength carbon fibers, etc.) are widely used as lightweight structural materials of choice in the automotive, aerospace and aeronautical industries because of their distinct advantages and superiority to traditional metallic materials. PMCs possess highly tailorable anisotropic materials properties, which permit high specific strength and stiffness, excellent formability and manufacturability, and superior protection from corrosion (Chou 1992; Jones 1999; Tsai 2005; Wu and Yarin 2013; Wu et al. 2013). Advanced PMCs were first developed for high-value military aircraft and spacecraft in the 1970s by the US Air Force. These advanced composites have contributed significantly to many in-service military aerospace and aeronautical systems that are 10–60% lower in weight than those based on metals with a typical weight savings of 20–30% as achieved by the US Air Force B2 bomber and F-22 Raptor (24%). Mature PMC technologies have rapidly proliferated in commercial transport aviation in the past decades. The Boeing 787 Dreamliner utilizes 50% PMCs by weight and ≥50% by volume. Embraer's E-Jets E2 will use composite materials for structural elements of flight controls (flaps, ailerons, elevators, rudder, and spoilers), landing gear doors, wing–fuselage fairings, and radomes. PMCs are also replacing increasingly more metal parts in ground vehicles and infrastructure as structural agility, fuel efficiency, and material renewability have become more valued worldwide. Vehicle weight reduction efforts have increased the use of PMCs in cars to approach 75%.

However, significant barriers and challenges remain before PMCs can be widely employed in the automotive, aerospace, and aeronautical industries. These include damage tolerance, fuel containment, repair, non-destructive inspection, modeling and failure prediction, and cost-effective manufacturing (Tenney and Pipes 2001). Current high-performance structural PMCs possessing highly anisotropic mechanical properties are typically fabricated by prepreg-based vacuum bag molding or vacuum-assisted resin transfer molding (VARTM) techniques. In the latter, in-plane macroscopic fibrous fabrics are commonly used. They serve as reinforcing frameworks for the resulting PMCs after the resin has been infused and cured. The in-plane fibrous fabric architecture strongly benefits for the in-plane uniaxial and biaxial mechanical properties of high-performance laminated PMCs. Some such PMCs could show mechanical properties similar to those of high-strength steels and alloys. However, compared to their superior in-plane mechanical properties, the out-of-plane properties of advanced PMCs are typically very poor. PMCs typically possess relatively low interfacial shear strength and poor inter-laminar adhesion. Microscopic imaging of the cross-sections of advanced PMCs reveals that ultrathin resin-rich interlayers of 1–50 μm in thickness exist between neighboring plies (laminas). Such interlayers can bear very low shear and normal stresses, especially for PMCs using thermosetting

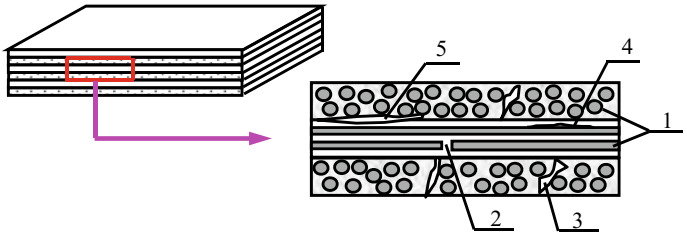

Fig. 6.7 Schematic of damage modes in a cross-ply PMC laminate: (1) reinforcing fibers, (2) fiber breakage, (3) matrix cracking, (4) fiber/matrix debonding, and (5) delamination; cf. with the experimental evidence in Fig. 8.22. Reprinted with permission from Wu and Yarin (2013)

resins. In fact, interlaminar fracture (delamination) is commonly observed in such composite materials: the problem has been a focus of research since the development of advanced laminated composites in the 1970s (Pipes and Pagano 1970, Pipes and Daniel 1971).

Because of the heterogeneous nature of fiber-reinforced laminated PMCs, the stress–strain fields and resulting failure processes of laminated PMCs are extremely inhomogeneous. Typically, the locus with a severe stress level may cause early microscopic damages (e.g., damage nucleation) in PMCs (Gdoutos et al. 2000), as in other fibrous inhomogeneous composites (Zhang et al. 2018). The inhomogeneity of the stress and strain fields and the randomness of the strength and toughness (K_{Ic}) of the composite constituents cause the typical failure process of laminated PMCs by progressive failure, associated with microcrack nucleation, matrix cracking, fiber breakage, fiber and matrix debonding, fiber pullout, and delamination (Cherepanov and Esparragoza 1995; Jones 1999; Tarpani et al. 2006; Wu and Yarin 2013; Wu et al. 2013). The typical damage modes in a cross-plied PMC laminate are illustrated in Fig. 6.7, including matrix cracking, fiber/matrix debonding, fiber breakage, and delamination. Delamination is a macroscopic failure phenomenon, usually a combination of one or more microscopic failure modes. The real damage and failure process in PMCs is much more complex and highly dependent upon the loading type, the fiber and ply architecture, and the physical properties of the constituents. In principle, the strength and toughness of PMCs arise from the combined effects of the strength and fracture toughness of the constituents (i.e., the reinforcing fibers and polymeric matrix), fiber–matrix interface properties (e.g., the interfacial physical and chemical properties, interfacial roughness, etc.), composite microstructure (e.g., fiber alignment, ply lay-up, volume fraction, etc.), dominant failure modes, and stress inhomogeneity (e.g., stress concentration). For one fiber/matrix combination, a practicable toughening technique that could enhance the strength and toughness of the resulting PMC system must address one or more dominant failure factors at an affordable cost.

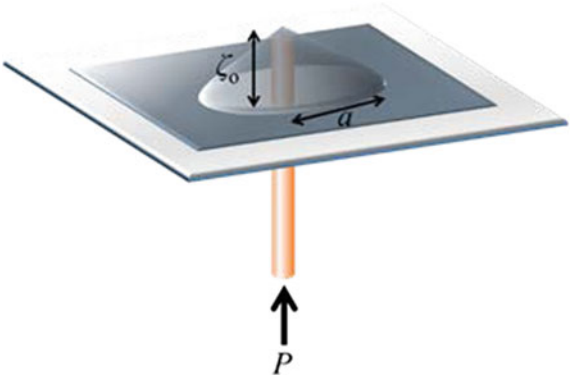

Fig. 6.8 Delamination and blister formation. Reprinted with permission from Lee et al. (2015)

6.7 Adhesion and Cohesion Energy: Stiff Materials

The delamination of one material layer from another is sketched in Fig. 6.8. The lower layer is bonded to a substrate; both of these have concentric stacking holes. On the other hand, the upper layer has no hole and is pushed upward by a shaft driven through the holes in the substrate and the lower layer. The driving force is P. At a certain instant, the upper layer detaches from the lower one and forms a membrane-like blister of height ζ_0 and radius a at its base (Fig. 6.8). The measurable parameters of the force P and blister radius a, essentially contain all information regarding the adhesion or cohesion energy of the layered structure.

If the lower and upper layers are each the same material, the cohesion energy must be overcome to detach one layer from the other. On the other hand, if the layers are different materials, the detachment energy is termed the adhesion energy. Blister growth proceeds by the work $\delta W = P\delta\zeta_0$ of the pushing force P, which is partially stored as the internal elastic energy in the blister membrane $\delta(\Delta U)$, and partially (irreversibly, for non-healing cracks) consumed as the new surface energy. This surface energy is associated with the new surface created between the upper and lower layers when the former delaminates from the latter. This is expressed by the following energy balance (Malyshev and Salganik 1965):

$$P\delta\zeta_0 = \delta(\Delta U) + T2\pi a\delta a \tag{6.56}$$

where T is the adhesion or cohesion energy and the membrane is assumed to be axisymmetric.

It should be emphasized that the adhesion or cohesion energy is intrinsically related to the surface energy γ introduced in the Griffith theory (Sect. 6.2). The only difference is that the surface energy γ is attributed separately to the two bank of a newly formed crack, whereas the adhesion or cohesion energy is attributed to the entire single link disconnected between the two banks of the separated layers.

To find the elastic energy stored in the blister membrane $\delta(\Delta U)$, the membrane shape must be predicted. The shape of a membrane in blister test (Fig. 6.8) is described by the following equation (Landau and Lifshitz 1986):

$$\frac{Eh^3}{12(1-\nu^2)}\nabla^4\zeta - \nabla\cdot[h\boldsymbol{\sigma}\cdot\nabla\zeta] = F \tag{6.57}$$

where h is the membrane thickness, E and ν are the Young's modulus and Poisson's ratio of the membrane material, respectively, ζ is the elevation of the membrane generatrix (i.e., its centerline), $\boldsymbol{\sigma}$ is the stress tensor in the membrane, and F is the distributed vertical force.

The first term on the left in Eq. (6.57) is associated with the moment of elastic forces in the membrane cross-section that resist bending, whereas the second term is associated with the resistance due to the elastic force arising from the membrane stretching. Accordingly, the first term is linear with the bending amplitude ζ, while the second is nonlinear. When the membrane material is sufficiently stiff, the first term is dominant, whereas the second is negligibly small because the stretching of such a materials is small. Indeed, the first term on the left in Eq. (6.57) is on the order of ζ, whereas the second one is on the order of ζ^3. The resistance to bending in stiff materials is associated with the moment of the elastic stresses in the membrane cross-section. For such stiff materials of interest in the present section, several formulae relevant for blister tests have been proposed in brief in Malyshev and Salganik (1965). The main formula contains a misprint, which is corrected below.

In detail, the pressing force F, as usual in cylindrical (axisymmetric) cases, is expressed as:

$$F = P\frac{\delta(r)}{2\pi r} \tag{6.58}$$

where the radial coordinate r measured from the membrane center (the shaft) is introduced and the Dirac delta function $\delta(r)$ expresses the pointwise nature the force.

Neglecting the second term in Eq. (6.57) and substituting Eq. (6.58) yields

$$\frac{1}{r}\frac{d}{dr}\left\{r\frac{d}{dr}\left[\frac{1}{r}\frac{d}{dr}\left(r\frac{d\zeta}{dr}\right)\right]\right\} = \frac{P}{D}\frac{\delta(r)}{2\pi r} \tag{6.59}$$

where

$$D = \frac{Eh^3}{12(1-\nu^2)} \tag{6.60}$$

Solutions of Eq. (6.59) are subjected to the following boundary conditions:

$$r = a: \quad \zeta = 0, \quad \frac{d\zeta}{dr} = 0 \tag{6.61}$$

i.e., it is assumed that the membrane of radius a is clamped at the periphery, and

$$r = 0: \quad \zeta = \zeta_0, \quad \frac{d\zeta}{dr} = 0 \tag{6.62}$$

at the membrane tip.

Additionally, for $P \equiv 0$, the membrane profile degenerates to $\zeta \equiv 0$.

Then, the following membrane profile is obtained:

$$\zeta = \frac{Pa^2}{4\pi D}\left(\frac{r}{a}\right)^2\left(\frac{\ln r/a}{2} - \frac{1}{4}\right) + \frac{Pa^2}{16\pi D} \tag{6.63}$$

Accordingly,

$$\zeta_0 = \frac{Pa^2}{16\pi D} \tag{6.64}$$

The elastic energy can be found as Landau and Lifshitz (1986):

$$\Delta U = \frac{1}{2}\int_V \boldsymbol{\sigma} : \boldsymbol{\varepsilon} dV \tag{6.65}$$

where the integral is evaluated over the membrane material volume V, and $\boldsymbol{\varepsilon}$ is the strain tensor; the colon denotes the scalar product of two second-rank tensors (Landau and Lifshitz 1986).

Accordingly, in the present case:

$$\Delta U = \frac{D}{2}\int_0^a \left[\frac{1}{r}\frac{d}{dr}\left(r\frac{d\zeta}{dr}\right)\right]^2 2\pi r dr \tag{6.66}$$

From Eqs. (6.63) and (6.66):

$$\Delta U = \frac{P^2a^2}{32\pi D} \tag{6.67}$$

Substituting Eqs. (6.64) and (6.67) into the energy balance (6.56) yields:

$$T = \frac{P^2}{32\pi^2 D} \tag{6.68}$$

According to Eq. (6.68) the adhesion or cohesion energy T is measured using the value of the pushing force P that forms a blister, regardless of the blister size. However, the elastic parameters and the thickness of the upper material must be known, as they determine D via Eq. (6.60). Note that Eq. (6.68) was first developed by Malyshev and Salganik (1965), although their first formula (2.6) for T, lacking a

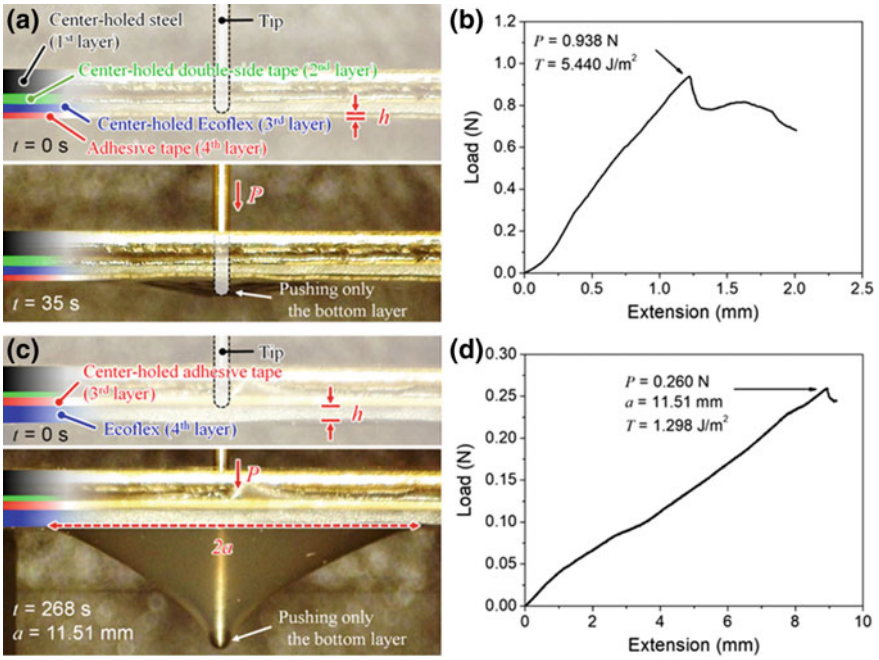

Fig. 6.9 Two blister tests used to measure the adhesion energy. **a** and **c** Photographic images; **b** and **d** the corresponding load–extension dependences. Panels **a** and **b** illustrate the case with the stiff blister; panels **c** and **d** illustrate the case with the soft blister. Reprinted with permission from An et al. (2018)

detailed derivation, contains the factor π in the denominator instead of the correct value of π^2, as in Eq. (6.68).

Equation (6.68) was recently used by An et al. (2018) for stiff membranes. The results are presented in Fig. 6.9 in the following chapter, along with those for the soft blister materials discussed next.

6.8 Adhesion and Cohesion Energy: Soft Materials

For soft materials, including nanofiber mats and some composites incorporating them, the first term in Eq. (6.57) is negligibly small, while the main resistance to bending arises from the material's resistance to stretching, as expressed in the second term on the left in Eq. (6.57). The theory of blister tests proposed by Wan and Mai (1995) rightly began at this point. However, the theory of Wan and Mai (1995) relies on an inappropriate approximation of the blister generatrix as a straight line, which is demonstrated below as incorrect. Therefore, the results of Wan and Mai (1995)

should be considered only as coarse approximations. In the present section, following Lee et al. (2015), a rigorous theory of blister testing for soft materials is developed.

Here, an axisymmetric blister with the radial coordinate r on the underlying substrate originating at the center of the substrate's hole, as in Sect. 6.7, is considered. Neglecting the first term on the left in Eq. (6.57) as negligibly small for soft materials, it is transformed to the following form:

$$\frac{1}{r}\frac{d}{dr}\left(h\sigma_{\tau\tau}r\frac{d\zeta}{dr}\right)+F=0 \tag{6.69}$$

where $\sigma_{\tau\tau}$ is the normal stress component directed along the blister generatrix, which has the unit vector $\boldsymbol{\tau}$.

The stress $\sigma_{\tau\tau}$ arises from the stretching of the blister generatrix, compared to its initial unstretched shape when it is aligned with the lower layer and substrate. The corresponding strain is expressed as $\varepsilon_{\tau\tau}=\sqrt{1+(d\zeta/dr)^2}-1\approx(1/2)(d\zeta/dr)^2$. Therefore, according to Hooke's law, $\sigma_{\tau\tau}=(E/2)(d\zeta/dr)^2$. The pressing force distribution is given by Eq. (6.58). Then, Eq. (6.69) takes the following form:

$$\frac{1}{r}\frac{d}{dr}\left[hr\frac{E}{2}\left(\frac{d\zeta}{dr}\right)^2\frac{d\zeta}{dr}\right]+P\frac{\delta(r)}{2\pi r}=0 \tag{6.70}$$

This equation is integrated using the first boundary condition (6.61), and considering that, if $P\equiv 0$, the membrane profile degenerates to $\zeta\equiv 0$. Note also that, for a blister, $d\zeta/dr<0$. Then, the following expression for the blister generatrix shape is obtained:

$$\zeta=\frac{3}{2}\left(\frac{Pa^2}{\pi Eh}\right)^{1/3}\left[1-\left(\frac{r}{a}\right)^{2/3}\right] \tag{6.71}$$

This expression for $\zeta(r)$ in Eq. (6.71) is nonlinear with r, thus invalidating the linear assumption made in Eq. (10) of Wan and Mai (1995), as well as all their final results based on that assumption. Notably, these inaccurate results were used for the analysis of blister test results in Na et al. (2012), rendering these later results inaccurate as well.

The blister height $\zeta_0=\zeta(r=0)$ is found from Eq. (6.71) as:

$$\zeta_0=\frac{3}{2}\left(\frac{P}{\pi Eh}\right)^{1/3}a^{2/3} \tag{6.72}$$

The elastic energy stored in the membrane is found using Eqs. (6.65) and (6.71) as:

$$\Delta U=\frac{3}{8}\left(\frac{P^4}{\pi Eh}\right)^{1/3}a^{2/3} \tag{6.73}$$

Then, the energy balance of Eq. (6.56) together with Eqs. (6.72) and (6.73) yields the following expression for the adhesion energy:

$$T = \frac{3}{8}\left(\frac{1}{\pi^4 Eh}\right)^{1/3}\left(\frac{P}{a}\right)^{4/3} \tag{6.74}$$

The expression following from Wan and Mai (1995), also used in Na et al. (2012), is slightly different

$$T = \left(\frac{1}{16\pi^4 Eh}\right)^{1/3}\left(\frac{P}{a}\right)^{4/3} \tag{6.75}$$

It should be emphasized that Eqs. (6.74) and (6.75) are very similar, only differing by the factor $3/8 = 0.375$ versus $16^{-1/3} \approx 0.397$. However, Eq. (6.74) is exact, while Eq. (6.75) remains an approximation. Therefore, the analysis of blister test results for soft materials should be based on Eq. (6.74).

The results of blister testing to measure the adhesion energies of stiff and soft materials are depicted and compared in Fig. 6.9. In the first blister test in An et al. (2018), a stiff adhesive tape is delaminated from a rigid substrate (see Fig. 6.9a). In the second blister test, a soft adhesive is delaminated from a rigid substrate (see Fig. 6.9c). The adhesion energies evaluated in the first test with the stiff blister [cf. Eq. (6.68) in Sect. 6.7] and in the second test with the soft blister [cf. Eq. (6.74)] are $T = 5.4$ and $T = 1.3$ J/m^2, respectively. Both values are evaluated at the moment at which the blisters are formed and detached (Fig. 6.9a and c).

References

An S, Kang DJ, Yarin AL (2018) Blister-like soft nano-textured thermo-pneumatic actuator as an artificial muscle. Nanoscale 10: 16591–16600

Astarita G, Marrucci G (1974) Principles of non-Newtonian fluid mechanics. McGraw-Hill, New York

Barenblatt GI (2014) Flow, deformation and fracture. Cambridge University Press, Cambridge

Cherepanov GP (1979) Mechanics of brittle fracture. McGraw Hill, New York

Cherepanov GP, Esparragoza IE (1995) The problem of fiber pullout. Mater Sci Eng A 203:332–342

Cho SH, Andersson HM, White SR, Sottos NR, Braun PV (2006) Polydimethylsiloxane-based self-healing materials. Adv Mater 18:997–1000

Chou TW (1992) Microstructural design of fiber composites. Cambridge University Press, Cambridge

da C Andrade EN, Randall RFY, Makin MJ (1950) The Rehbinder effect. Proc Phys Soc B 63:990–995

Entov VM, Salganik RL (1968) Cracks in viscoelastic bodies. Mech Solids 3:81–86

Gdoutos EE, Pilakoutas K, Rodopoulos CA (2000) Failure analysis of industrial composite materials. McGraw-Hill, New York

Green AE (1956) Hypo-elasticity and plasticity. Proc R Soc London A 234:46–59

Green AE, Zerna W (1954) Theoretical elasticity. Clarendon Press, Oxford

Griffith AA (1920) The phenomena of rupture and flow in solids. Phil Trans Roy Soc London A 221:163–198
Irwin GR (1957) Analysis of stresses and strains near the end of a crack traversing a plate. J Appl Mech 24:361–364
Joffe AF (1928) The physics of crystals. McGraw Hill, New York
Jones RM (1999) Mechanics of composite materials, 2nd edn. Taylor and Francis, Philadelphia
Kachanov LM (2004) Fundamentals of the theory of plasticity. Dover Publ, New York
Landau LD, Lifshitz EM (1986) Theory of elasticity. Reed Educational and Professional Publishing Ltd, Oxford
Lee MW, An S, Jo HS, Yoon SS, Yarin AL (2015) Self-healing nanofiber-reinforced polymer composites: 2. Delamination/debonding, and adhesive and cohesive properties. ACS Appl Mater Interfaces 7:19555–19561
Lee MW, Sett S, Yoon SS, Yarin AL (2016) Fatigue of self-healing nanofiber-based composites: Static test and subcritical crack propagation. ACS Appl Mater Interfaces 8:18462–18470
Lee MW, Sett S, An S, Yoon SS, Yarin AL (2017) Self-healing nano-textured vascular-like materials: Mode I crack propagation. ACS Appl Mater Interfaces 9:27223–27231
Lurie AI (2005) Theory of elasticity. Springer, Heidelberg
Malyshev BM, Salganik RL (1965) The strength of adhesive joints using the theory of cracks. Int J Fract Mech 1:114–128
Mukherjee S, Paulino GH (2003) The elastic–viscoelastic correspondence principle for functionally graded materials, revisited. ASME J Appl Mech 68:359–363
Na H, Chen P, Wan K-T, Wong S-C, Li Q, Ma Z (2012) Measurement of adhesion work of electrospun polymer membrane by shaft-loaded blister test. Langmuir 28:6677–6683
Orowan EO (1952) Fundamentals of brittle behaviour in metals. Fatigue and fracture of metals. John Wiley & Sons, New York, pp 139–167
Paris PC (1964) The fracture mechanics approach to fatigue. In: Proceedings of 10th Sagamore Army Materials Research Conference 1963. Syracose University Press, Raquette Lake, pp 107–127
Paris PC, Erdogan F (1963) A critical analysis of crack propagation laws. J Basic Eng Trans ASME D 85:528–534
Paulino GH, Jin Z-H (2001) Correspondence principle in viscoelastic functionally graded materials. ASME J Appl Mech 68:129–132
Pipes RB, Daniel IM (1971) Moire analysis of interlaminar shear edge effect in laminated composites. J Compos Mater 5:255–259
Pipes RB, Pagano NJ (1970) Interlaminar stress in composite laminates under uniform axial extension. J Compos Mater 4:538–548
Rabotnov YN (1969) Creep problems in structural members. North-Holland Publishing Company, Amsterdam
Rizzo FJ, Shippy DJ (1971) An application of the correspondence principle of linear viscoelasticity theory. J Appl Math 21:321–330
Suresh S (1998) Fatigue of materials. Cambridge University Press, Cambridge
Tadmor Z, Gogos CG (2006) Principles of polymer science, 2nd edn. John Wiley & Sons, Hoboken, NJ
Tarpani JR, Milan MT, Spinelli D, Bose WW (2006) Mechanical performance of carbon-epoxy laminates. Part I: Quasi-static and impact bending properties. Mater Res 9:115–120
Tenney D, Pipes RB (2001) Advanced composites development for aerospace applications. In: The 7th Japan International SAMPE Symposium and Exhibition, Tokyo, Japan, 13 Nov 2001
Tsai SW (2005) Three decades of composites activities at US Air Force Materials Laboratory. Compos Sci Technol 65:2295–2299
Wan K-T, Mai Y-W (1995) Fracture mechanics of a shaft-loaded blister of thin flexible membrane on rigid substrate. Int J Fract 74:181–197
Wu X-F, Rahman A, Zhou Z, Pelot DD, Sinha-Ray S, Chen B, Payne S, Yarin AL (2013) Electrospinning core-shell nanofibers for interfacial toughening and self-healing of carbon-fiber/epoxy composites. J Appl Polym Sci 129:1383–1393

Wu X-F, Yarin AL (2013) Recent progress in interfacial toughening and damage self-healing of polymer composites based on electrospun and solution-blown nanofibers: An overview. J Appl Polym Sci 129:2225–2237

Yarin AL, Rubin MB, Roisman IV (1995) Penetration of a rigid projectile into an elastic-plastic target of finite thickness. Int J Impact Eng 16:801–831

Yarin AL, Roisman IV, Tropea C (2017) Collision phenomena in liquids and solids. Cambridge University Press, Cambridge

Zhang W, Staszel C, Yarin AL, Shim E, Pourdeyhimi B (2018) Point-bonded polymer nonwovens and their rupture in stretching. Polymer 146:209–221

Chapter 7
Self-Healing of Mechanical Properties: Evaluation by Tensile Testing

In this Section the evaluation of the mechanical consequences of self-healing is discussed. In particular, the recovery of such mechanical properties as stiffness is addressed. The tensile testing of self-healing composites with different types of fibers are analyzed in Sects. 7.1 and 7.2. Fatigue testing under a static loads is discussed in Sect. 7.3. The case of increasing stresses and the effect of self-healing features on crack propagation are described in Sect. 7.4.

7.1 Tensile Testing: Stiffness Recovery in Composites with Co-electrospun Polyacrylonitrile–DMS Resin Monomer–Curing Agent Nanofibers

For the tensile testing of self-healing nanofiber (NF) mats and/or composites incorporating such mats, specimens are typically shaped as rectangular in shape; sometimes the dog-bone shape is used. Self-healing polyacrylonitrile (PAN)–DMS resin monomer–curing agent (PRC) NF mats formed by Lee et al. (2015) by co-electrospinning, as described in Sect. 4.2, were used to fabricate NF-reinforced composites with different matrices. To prepare composite specimens for tensile testing, both the non-self-healing monolithic PAN (used for comparison) and self-healing core-shell PRC NF mats were cut into specimens with dimensions of $\ell_0 \times w_0 =$ 90 mm $\times$ 23 mm (cf. Fig. 7.1a). These sections were sandwiched as middle layer between polydimethylsiloxane (PDMS, using pre-mixed resin monomer and curing agent at a ratio of 10:1) layers. The resulting PDMS-encased composites were cured at room temperature for 24 h. These specimens were subsequently used in tensile testing (see Fig. 7.1b). The initial thickness t_0 of each specimen was measured ten times using micrometer and the average of the ten measurements was recorded. The values of t_0 for the PAN and PRC NF-reinforced composites were 0.485 mm and 0.425 mm, respectively. Such layered composites present significant interest as self-

A. L. Yarin et al., *Self-Healing Nanotextured Vascular Engineering Materials*, Advanced Structured Materials 105, https://doi.org/10.1007/978-3-030-05267-6_7

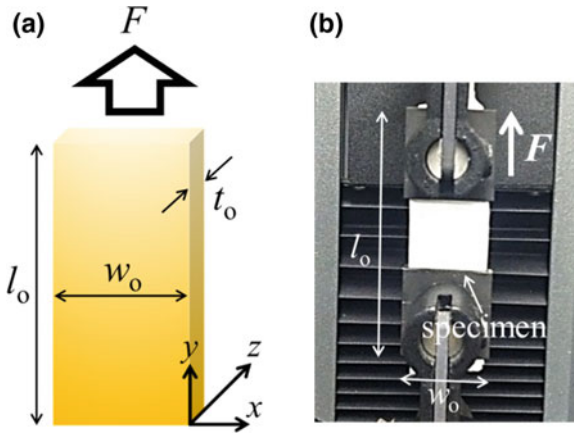

Fig. 7.1 **a** Specimen schematic and **b** photograph of apparatus for tensile testing. Reprinted with permission from Lee et al. (2015)

healing adhesive layers at ply surfaces in laminate composites (cf. Sects. 6.6 and 8.4); thus, mechanical testing of thin specimens was attempted.

The PDMS matrices of the prepared composites can be damaged and develop multiple microcracks during the stretching of such specimens, as occurs in the matrices of many other composites used in aerospace and other industries. However, in the present case, the PDMS matrices are embedded with mutually entangled core-shell NFs containing resin monomer and curing agent in their cores. These NFs are also damaged during stretching. Upon damage, they release resin monomer and curing agent into the surrounding microcracks of the PDMS matrix. Polymerization of the released resin in the presence of curing agent then occurs, and PDMS stitches spanning the banks of microcracks in the PDMS matrix are formed (see Sect. 3.4). This is the self-healing mechanism examined using tensile testing.

The first goal of any tensile test is to quantify the elastic behavior of the materials, as characterized by Hooke's law with the two material parameters of Young's modulus E and Poisson's ratio ν; all other elastic parameters used can be expressed using E and ν (Landau and Lifshitz 1986). In the tensile tests described below, only the specimen edges are loaded by the two pulling grips, whereas all the other sides are unloaded. Under such conditions, Hooke's law is reduced to the most elementary form:

$$\sigma_{xx} = E\varepsilon_{xx} \tag{7.1}$$

irrespective of the value of ν; σ_{xx} and ε_{xx} are the tensile stress and strain, with x being the stretching direction. Note that the value of E characterizes the specimen stiffness.

The PDMS-encased composite specimens were tensile tested by Lee et al. (2015) using an Instron 5942 machine. The initial specimen length (gauge length) between the upper and lower grips is set to 20 mm (cf. Fig. 7.1b). During the experiments, the stretching rate was 1 mm/min. Such low stretching rates are characteristic of many industrial applications, where the accumulation of mechanically generated

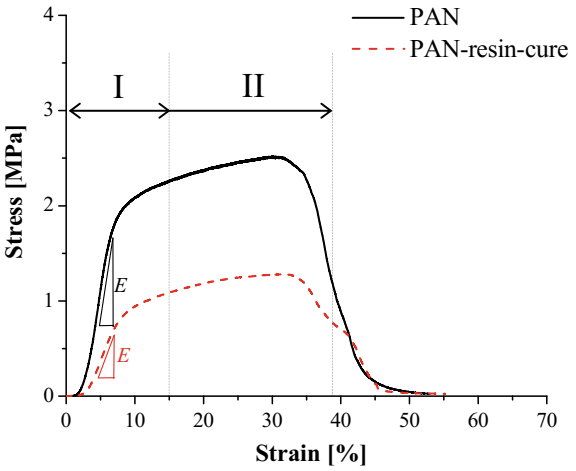

Fig. 7.2 Stress–strain curves measured in tensile testing of the PAN and PRC NF mats. Reprinted with permission from Lee et al. (2015)

microcracks occurs relatively slowly before suddenly causing a catastrophic event. The acquired data were presented as the stress–strain curves.

The procedure described below was used to evaluate the self-healing features of the PDMS-encased specimens containing the self-healing

core-shell PRC NFs. The specimens were stretched to strains of 15–18%, which caused internal damage. The accumulated damage at such strains was revealed during the experiments on the PDMS-encased specimens containing non-self-healing PAN NFs. These specimens did not recover their original stress–strain curves, as discussed below. The tested PDMS-encased specimens with self-healing core-shell PRC NFs were left for 24 h to ensure that polymerization occurred between the released resin monomer and curing agent from the damaged NFs. Subsequently, the self-healing specimens were further analyzed by tensile testing to evaluate the degree of recovery of their pre-damage stress–strain curves, wherein recovery would imply full self-healing.

Figure 7.2 shows the tensile test results for both PAN and self-healing PRC NF mats. The thicknesses of the PAN and PRC fiber mats are 0.089 mm and 0.191 mm, respectively; the PRC mat is 2.15 times thicker than the PAN mat. This is because the two additional components (dimethyl siloxane or DMS resin monomer and curing agent; cf. Sect. 2.2) were simultaneously supplied to the PAN solution during the co-electrospinning process (see Sect. 4.2). The Young's moduli E of the PAN NF mat and the self-healing PRC NF mat are measured as the slopes of the linear portions of the stress–strain curves in Fig. 7.2, according to Eq. (7.1). They are 46.45 MPa and 18.05 MPa for the PAN and self-healing PRC NF mats, respectively. This indicates that the fully solidified PAN NF mat is stiffer than the self-healing PRC NF mat containing liquid resin monomer or curing agent within the NF cores. The ultimate tensile strength of the PAN NF mat is also twice that of the self-healing PRC NF mat.

The results reveal two recognizable well-defined regimes of deformation within the stress–strain curves. In the elastic regime I, the stress-strain dependences are

initially linear and then, plasticity sets in; the intermediate plastic regime II, the dependences are non-linear; these initially regimes are followed by ultimate catastrophic failure. The regimes are typical for the different NF mats (Khansari et al. 2012; 2013, Sinha-Ray et al. 2012, 2014; Yarin et al. 2014).

Figure 7.3 shows the results of repeated tensile testing at strains reaching 15% (including the elastic regime I and the initial part of the plastic regime II) for both the PAN and PRC NF mats. Stretching to 15% (deep into the irreversible plastic regime) causes moderate damage to the mats. Each mat is initially stretched and then allowed "resting" for 24 h before the sequential tensile tests. Each mat was subjected to four sequential tensile tests. Figure 7.3a reveals that the PAN NF mat is deteriorating in its mechanical properties immediately after the first tensile test. During the second tensile test, the stress–strain curve shows catastrophic failure at the strain of 7.5%. During the sequential tensile tests, the PAN mat exhibits only a slight resistance to stretching; its stiffness and ultimate strength significantly decline during the sequential tests. On the contrary, the self-healing PRC specimen shows similar stress–strain curves for the four sequential tensile tests (cf. Fig. 7.3b). In Fig. 7.3c, the Young's moduli measured during the sequential tests are normalized by that obtained during the first test. The trends for the PAN mat and the self-healing PRC mat are drastically different. During the fourth sequential tensile tests, the Young's moduli are decreased (relative to the original values) by 90% for the PAN mat, but only by 30% for the self-healing PRC specimen. Specifically, the specimen healed over the rest time of 24 h by the release of the resin monomer and curing agent that were stored separately within the NF cores. It should be emphasized that the PAN NF mat is weakened significantly during the sequential tests and completely failed during the fourth tensile test, unlike the self-healing PRC mat, as shown in Fig. 7.3d.

In addition to the sequential tensile tests up to the strain of 15%, as illustrated in Fig. 7.3, similar tests are conducted by stretching the mats up to the level related to catastrophic failure (30% strain). The corresponding results are presented in Fig. 7.4. As Fig. 7.4d illustrates, during these tests, the stretched fiber mats shrink significantly in the middle unlike those shown in Fig. 7.3d. It should be emphasized that the specimens shown in Figs. 7.3d and 7.4d undergo different strain regimes. The specimens shown in Fig. 7.3d experience repeated stretching in the moderate strain range (regime I, strains ε_{xx} reaching 15%), whereas those shown in Fig. 7.4d are stretched beyond failure (regime II, strains ε_{xx} reaching 30%). The plastic deformation in regime II yields the dog-bone shape in the middle of the mats, characteristic of many materials in such situations.

Notably, the self-healing PRC mat shows behavior similar to that of the PAN specimen (see Fig. 7.4a and b). The self-healing mat only slightly outperforms the pure PAN specimen, as shown in Fig. 7.4c. Indeed, the normalized Young's moduli for the self-healing PRC material are only 11% and 15% greater than those of the pure PAN specimen during the second and third tensile tests, respectively. The experimental results for extensive sequential stretching imply that the ruptured NF sections are separated to such an extent that self-healing becomes practically impossible, despite the release of both resin monomer and curing agent from the cores of the ruptured NFs.

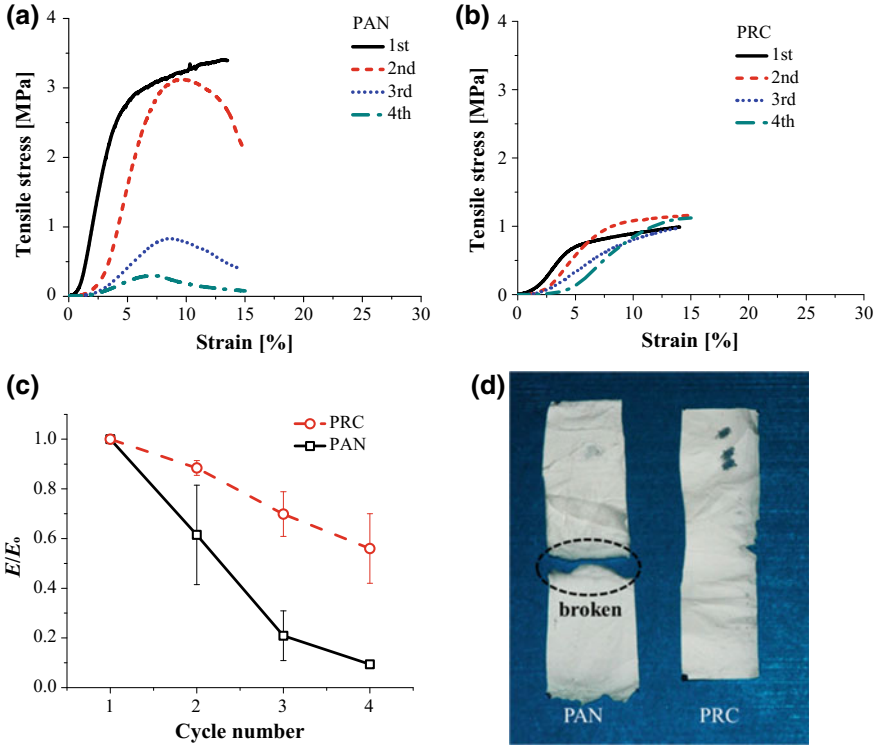

Fig. 7.3 Stress–strain curves measured during tensile tests with strain reaching 15% (elastic regime and the initial part of the plastic regime). **a** PAN NF mat, **b** PRC NF mat. **c** Relative variation in Young's modulus values during sequential tests; the Young's modulus measured during the first stretching is denoted E_0, while those measured during the sequential stretching tests of the same mat are denoted E. **d** Photographs of the specimens following the sequential tensile tests. Reprinted with permission from Lee et al. (2015)

Now the results of tensile testing for the corresponding composite specimens are considered. The PDMS-impregnated composite specimen with the self-healing PRC NFs were subjected to tensile tests every 24 h to strains of 15–18%. Figure 7.5 shows that the relative values of the ratio E/E_0 for the PRC composite specimens differ from those of both pure PDMS and the PAN-PRC-based composite specimens. The pure PDMS specimens are used as references; their Young's moduli are relatively unchanged over the four sequential tensile tests. This correlates with the results of the previous research (Kim et al. 2011), where the stress–strain curve of a PDMS specimen stretched to the 50% strain after ten tests is similar to the initial curve. In general, PDMS is regarded as a good elastomer.

Figure 7.5d shows that the stiffness of the PDMS composite with self-healing PRC fibers is not sustained, but enhanced following the sequential tensile tests. Indeed, after the fourth test, the Young's modulus of the composite is increased by a factor of

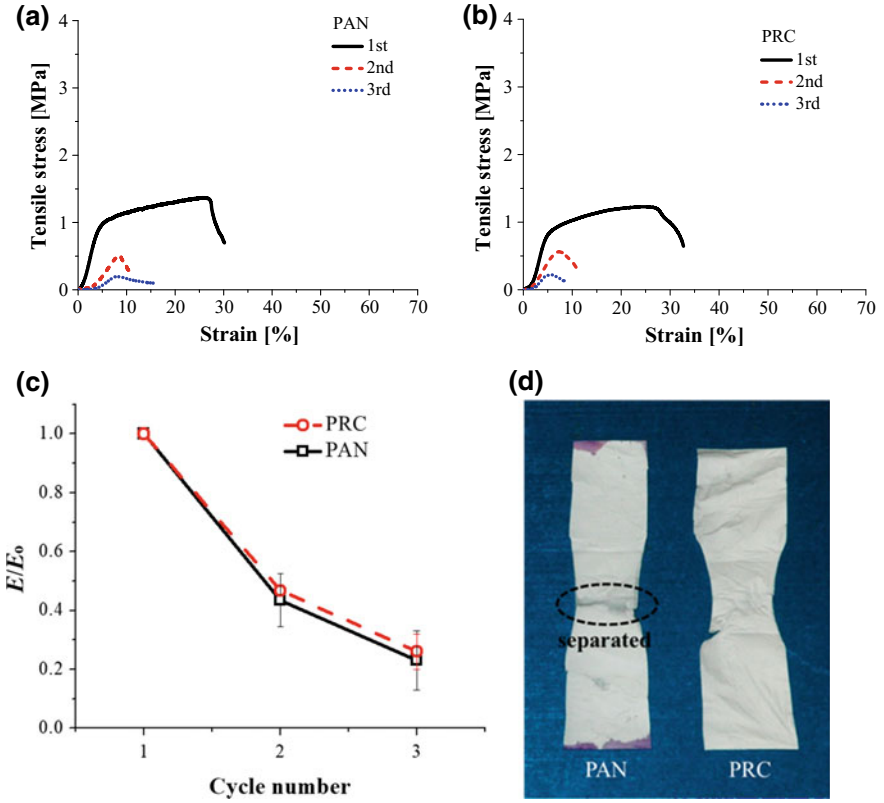

Fig. 7.4 Stress–strain curves measured during tensile tests to 30% strain (catastrophic failure regime). **a** PAN NF mat, **b** PRC NF mat. **c** Relative variation of the Young's moduli during the sequential tests; the Young's modulus measured during the first stretching is denoted E_0, while those measured during the sequential stretching tests of the same mat are denoted E. **d** Photographs of the specimens following the sequential tensile tests. Reprinted with permission from Lee et al. (2015)

1.4 compared to the initial measurement. This implies that both the resin monomer and curing agent were released from the damaged fiber cores; they not only heal the composite, but also strengthen it. The healing PDMS resin is identical to that of the matrix, facilitating compatibility. In contrast, the composite containing PAN NFs shows significant deterioration of its stiffness under repeated tensile testing.

It should be emphasized that the comparison between monolithic PAN and PRC core-shell fiber mats and composites embedded with them is based not on their respective stiffness, but on their respective abilities to recover their original stiffness after repeated moderate stretching or one catastrophic plastic deformation under tension. Therefore, the differences observed between the monolithic PAN NF mats and PRC fiber mats, as well as their respective composites, can be safely attributed

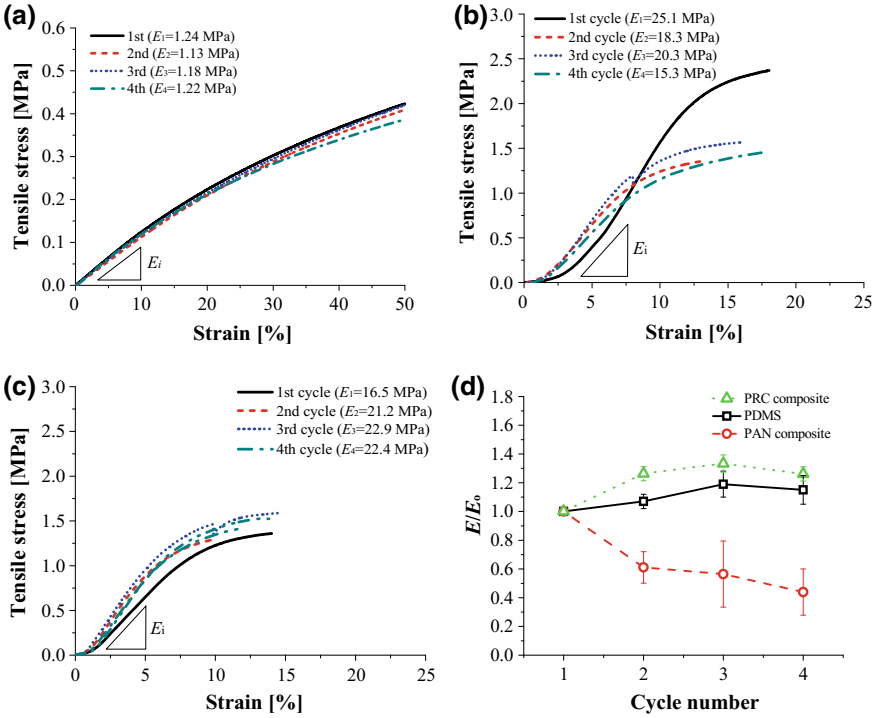

Fig. 7.5 Stress–strain curves of: **a** Pure PDMS, **b** PAN-based composites, **c** PRC self-healing composites, **d** relative Young's moduli; the Young's modulus measured during the first stretching is denoted E_0, while those measured during the sequential tensile tests of the same specimen are denoted E. Reprinted with permission from Lee et al. (2015)

only to the effect of the healing agents released from the damaged cores of the self-healing PRC NFs.

Note also that the restoration of mechanical properties in a 24-h rest period at room temperature, as demonstrated in this section, is an attractive result that fully meets practical requirements. In airplanes, fatigue microcracks accumulate for years, and their partial daily healing could probably prevent such catastrophic events as the opening of a "football-sized" hole in aircraft fuselages, as in 2009 and 2011 during commercial flights (cf. Sect. 1.1). Self-healing caused by different healing agents encased in capsules after the rest periods of 24–48 h at elevated temperatures was reported in Coope et al. (2011, 2014).

7.2 Tensile Testing: Stiffness Recovery in Composites with Solution-Blown PVDF/PEO/Epoxy/Hardener NFs

Solution-blown core-shell NF mats with epoxy resin and hardener (cf. Sect. 2.3) embedded as healing agents in the cores were formed by Lee et al. (2016a) using coaxial solution blowing, as described in Sect. 4.5. The epoxy resin and hardener solidify much faster than the DMS resin monomer and curing agent considered in Sect. 7.1. Therefore, faster self-healing is expected in the present case. The polyvinylidene fluoride/polyethylene oxide (PVDF/PEO) solution, as described in Sect. 4.5, was used to form the NF shells. The solution-blown NF mats with and without epoxy were cut into 20 mm × 60 mm strips. Separately, DMS resin monomer and curing agent were mixed in a 10:1 ratio and the cut fiber strips were cast into the premixed PDMS. The PDMS matrices with the encased fiber strips were allowed to cure in open air at room temperature for 24–48 h. The thickness of each composite specimen prepared according to this procedure was then measured at three different locations, with the average values recorded and listed below. The uniformity of the composites was not fully controlled because the NF mats were not distributed uniformly within the PDMS matrix. The thicknesses of the as-spun NF mat were approximately 0.11–0.12 mm, while the thicknesses of the composite specimens with and without epoxy resin and hardener in the NF cores were approximately 0.53–0.67 mm. An embedded NF mat in a similar PDMS matrix is shown in Fig. 4.30 in Sect. 4.7.

The PDMS–fiber composite specimens were used in tensile tests where the tensile stress was increasing over time in dynamic loading, as in Sect. 7.1. In the present dynamic tensile tests with pre-notched incisions (crack) the upper and lower ends of the composite specimens are tightly gripped by the grips of an Instron machine (model 5942) with a 100-N load cell. The initial gap between the upper and lower grips is 20 mm for all experiments. An initial horizontal incision is pre-notched in the middle of the specimen, as shown in the magnified image in Fig. 7.6. The specimens are then uniaxially stretched at strain rates of either $\dot{\varepsilon}_{xx} = 0.05$ mm/min (= 3 mm/h) or $\dot{\varepsilon}_{xx} = 0.025$ mm/min (= 1.5 mm/h) by the motion of the upper grip. The lower grip remains stationary. This initial stretching is done until the elongation reaches $\ell = 3$ mm in addition to the initial 20-mm gap (for 1 h or 2 h, depending on the stretching rate) or $\ell = 1.5$ mm in addition to the 20-mm initial length (for 0.5 h or 1 h, depending on the stretching rate).

The stretching is then stopped and the specimens are held in a stationary position with fixed grips for 1 or 2 h. Because the epoxy resin embedded in the fibers has a hardening time of approximately 1 h, this waiting time is considered sufficient for crack healing to occur in the specimens containing self-healing NFs.

At the end of the waiting time, the second stage of stretching begins. The specimen stretching is continued at the initial stretching rate until failure occurs by the central crack reaching a catastrophic size. The stress–strain curve for the entire experiment, including both the first and second stages of stretching, is measured by the Instron machine. Simultaneously, a digital camera is used to photograph the specimen with a focus on the propagating crack. Photographs are obtained at regular intervals of

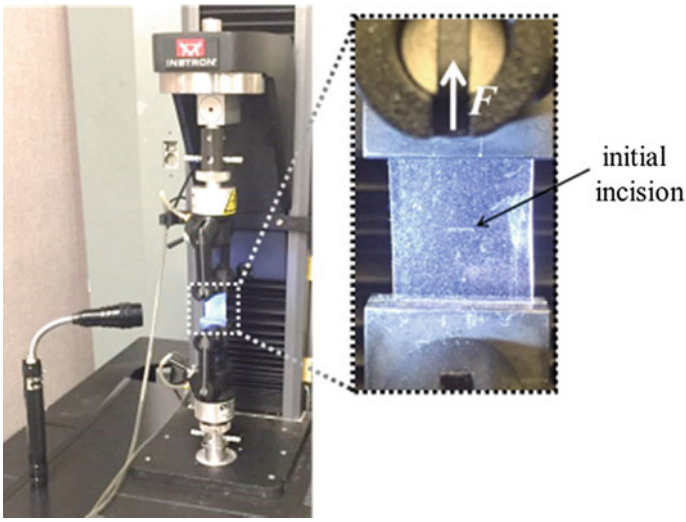

Fig. 7.6 Setup for dynamic tensile tests with crack growth for PDMS–fiber composites at fixed strain rates using Instron machine. The magnified image on the right shows the loaded specimen with the initial pre-notched incision before testing. The healing agents embedded in the fiber cores are the epoxy and hardener. Reprinted with permission from Lee et al. (2016a)

1 min until the specimen fails. All the experiments are repeated at least twice to corroborate the results.

The solution-blown NFs form randomly oriented nonwoven fabrics. The contents of NFs in the PDMS matrices in the composites studied here are approximately 3.21 wt% and 2.68 wt% core-shell NFs with epoxy resin or hardener in the cores and NFs without healing agents, respectively. The Young's moduli of the PVDF/PEO NF mats with and without epoxy and hardener are 2.13 and 2.73 MPa, respectively. Compared to the pure PDMS matrix (E = 0.85 MPa), the PVDF/PEO NF mats are stiffer and stronger by a factor of approximately 2.5–3.2 (see Fig. 7.7). It should be emphasized that the stretching of the NF mats is accompanied by fiber reorientation, predominantly in the stretching direction. Debonding and fiber rupture are minor for the strains of $\varepsilon_{xx} = 7.5$ or 15% explored in the experiments on self-healing depicted in Figs. 7.8 and 7.9, because the slopes of the stress–strain curves remain essentially unchanged.

The stress–strain curves, along with the time-dependent crack lengths, for the specimens containing NFs with and without epoxy components subjected to tensile testing at the constant stretching rate of 3 mm/h are shown in Fig. 7.8. In all cases, (#-1) indicates specimens with only PVDF/PEO fibers (non-self-healing fibers without healing agents), while (#-2) indicates specimens containing self-healing fibers with the epoxy components. Initially, the composite specimens are stretched for 1 h (3 mm, 15% strain) and then held for 1 h before further stretching (Fig. 7.8a-1 and a-2). By the nature of the epoxy, the 1-h holding time should be sufficient for the healing of the

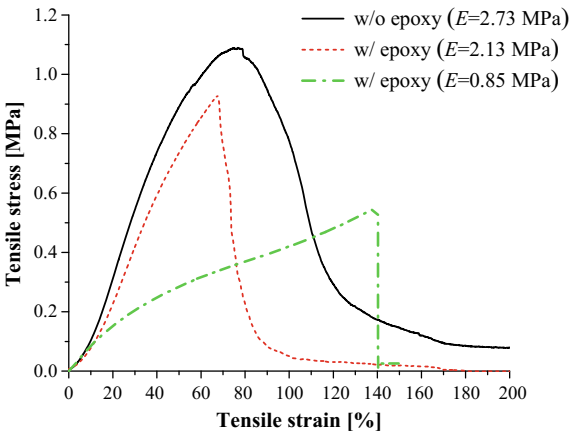

Fig. 7.7 Stress–strain curve of the as-spun PVDF/PEO NF mat with (w/) and without (w/o) epoxy resin and hardener and that of neat PDMS. Reprinted with permission from Lee et al. (2016a)

composite specimens with the epoxy–and hardener-containing NFs. In general, the composites fail at ~25% strain. Hence, 1 h of stretching causing 15% strain should provide moderate damage to the specimens, enough for the composites with the epoxy components to heal, but without causing irreparable damage. Moreover, this moderate damage ensures that only the NFs within the PDMS matrix are ruptured by stretching, while the external PDMS remains intact in the reversible region of elastic deformation. It should be emphasized that the encased NFs are both stiffer and stronger than the PDMS matrix (cf. Fig. 7.7), so the experiments reach the level of fiber damage that could trigger the observations of self-healing effects.

For the next set of tests, the initial stretching time is reduced to 30 min (1.5 mm, 7.5% strain), thereby inflicting less damage to the specimens (Fig. 7.8b-1 and b-2). The holding time remains 1 h.

For the third set of tests, the initial stretching time is 1 h (3 mm, 15% strain), as in the first set. However, the holding time is increased from 1 to 2 h, to elucidate the effects of the holding time on the reaction of the resin and hardener, solidification of the epoxy, and self-healing behavior of the composites.

For the first set of tests, the stress–strain curves for the composites containing PVDF/PEO NFs alone before and after the holding periods show nearly equal slopes, with a decrease of ~0.3% recorded after holding, indicating that no increase in stiffness occurs during the 1-h holding period (Fig. 7.8a-1). Because these NFs contain no self-healing material, the holding period should neither affect the stiffness nor induce healing of the composite. Meanwhile, the composites with NFs containing epoxy components show a remarkable enhancement in stiffness after the holding period (Fig. 7.8a-2). This indicates that the 1-h holding period is sufficient for the reaction between the two components (the epoxy resin and hardener) of the cured epoxy. The Young's moduli for these specimens are dramatically increased by 57.3% from $E_1 = 1.156$ to $E_2 = 1.818$ MPa in the post-holding stretching stage, implying significant self-healing of the composites.

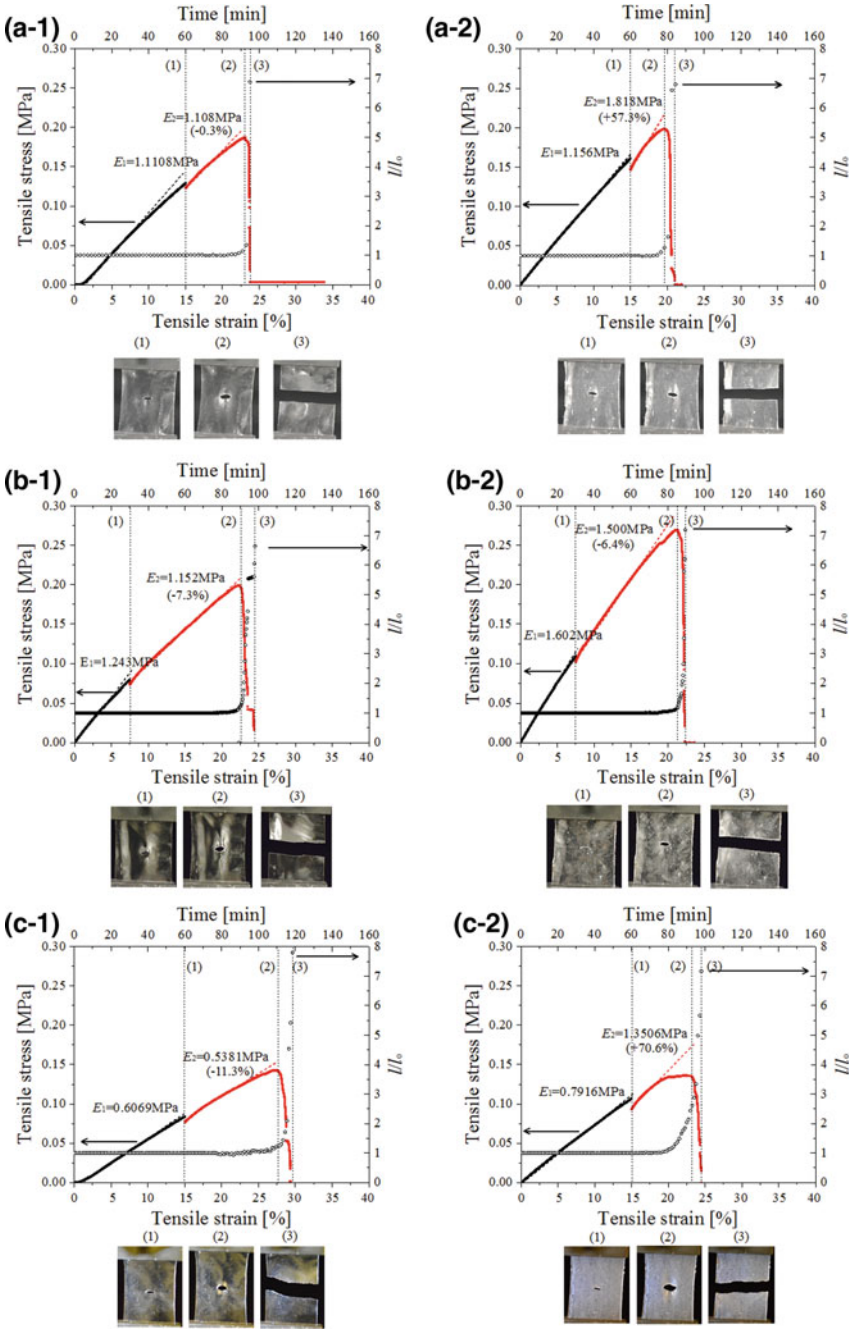
(a-1)
Time [min]
Tensile stress [MPa]
Tensile strain [%]
E₂=1.108MPa
(-0.3%)
E₁=1.1108MPa
(a-2)
E₂=1.818MPa
(+57.3%)
E₁=1.156MPa
(b-1)
E₂=1.152MPa
(-7.3%)
E₁=1.243MPa
(b-2)
E₂=1.500MPa
(-6.4%)
E₁=1.602MPa
(c-1)
E₂=0.5381MPa
(-11.3%)
E₁=0.6069MPa
(c-2)
E₂=1.3506MPa
(+70.6%)
E₁=0.7916MPa

◀**Fig. 7.8** Stress–strain curves and normalized crack lengths (ℓ/ℓ_0) in tensile testing of composites without and with epoxy components encapsulated in embedded NFs at the strain rate of 3 mm/h (= 0.05 mm/min). Panels **a**: stretching length 3 mm, holding period 1 h. Panels **b**: stretching length 1.5 mm, holding period 1 h. Panels **c**: stretching length 3 mm, holding period 2 h. Suffix–1 indicates specimens with PVDF/PEO fibers alone (no healing agents); suffix–2 indicates specimens containing NFs with epoxy components (healing agents) in the cores. In each panel, the black and red bold symbols indicate the initial and post-holding stretching stages, respectively. Black open circles indicate the dimensionless crack length versus time. The photographs of the composite specimens labeled (1), (2), and (3) beneath each stress–strain curve depict the specimens at the end of the holding period, the point of the maximum stress, and after complete failure. Reprinted with permission from Lee et al. (2016a)

For the second set of tests, in which the specimens are initially stretched for less time interval (30 min instead of 1 h), no increase in stiffness is observed, even for the composites containing NFs with the epoxy components (Fig. 7.8b-2). This indicates that the damage caused by 7.5% strain is insufficient to cause NF rupture and the release of the self-healing agents. Therefore, no healing is observed. The stiffness and Young's moduli of these composites, even those containing self-healing NFs are unchanged before and after the holding period.

For the third set of tests, a strain of 15% is applied to the specimens before the holding period. The holding time for these tests was increased to 2 h. As expected, the composites with PVDF/PEO NFs alone reveal no increase in stiffness during the stretching after the holding period (Fig. 7.8c-1). The stiffness is instead decreased by 11.3%. Meanwhile, the composites containing self-healing NFs show a remarkable increase in stiffness when the specimens are stretched after the 2-h holding period, with the Young's moduli increasing by ~ 70.6% from $E_1 = 0.7916$ to $E_2 = 1.3506$ MPa (Fig. 7.8c-2). The opposite trends in stiffness observed for the specimens with NFs with and without the epoxy components demonstrate that the latter specimens are damaged by stretching and inherently deteriorate in their mechanical properties, thereby showing reductions in stiffness. However, the composites with the epoxy components experience self-healing during the healing period of 2 h, causing enhancement of stiffness. The increase in stiffness for the epoxy-containing composites over the 2-h holding time is more pronounced than that observed over the shorter 1-h holding time, indicating that longer holding times permit greater healing in the specimens. Thus, in both cases when the self-healing specimens are moderately damaged, the epoxy cures the damaged sites, thus increasing the composite stiffness.

The crack length measurements over time reveal that the crack length remains nearly constant throughout the tensile tests, except during the final stages when the tensile stress is maximized. This is evident from the normalized crack length ℓ/ℓ_0 (where ℓ_0 is the initial crack length) remaining equal to 1 for most of the tensile test. However, this does not mean that the cracks do not grow and no damage is caused. Subcritical crack growth is possible, but visually difficult to detect [cf. Sect. 6.5 and Lee et al. (2016b), as well as Cherepanov (1979) and Barenblatt (2014)]. As the stress approaches the critical maximum value, the crack begins propagating rapidly, and

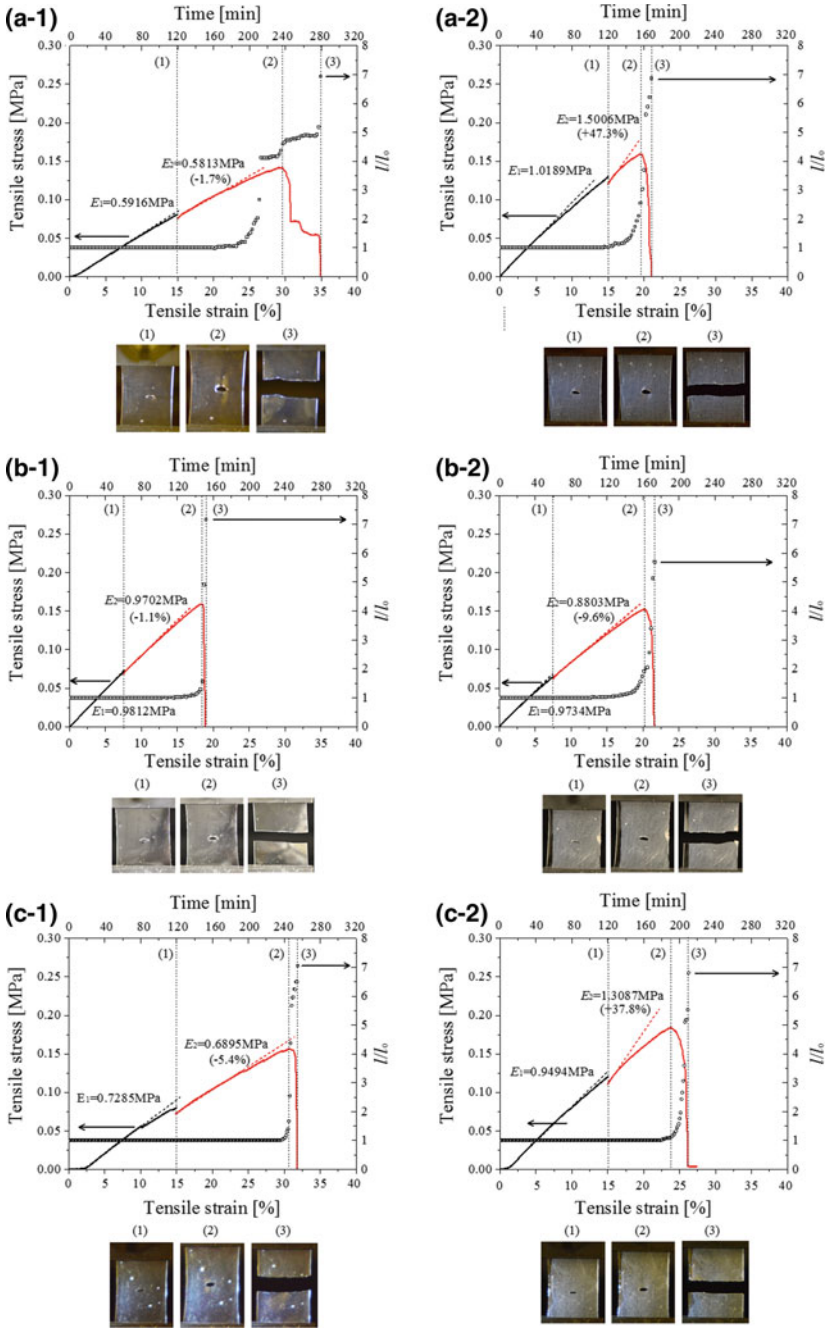
(a-1)
Time [min]
Tensile stress [MPa]
Tensile strain [%]
E1=0.5916MPa
E2=0.5813MPa
(-1.7%)
(a-2)
E1=1.0189MPa
E2=1.5006MPa
(+47.3%)
(b-1)
E1=0.9812MPa
E2=0.9702MPa
(-1.1%)
(b-2)
E1=0.9734MPa
E2=0.8803MPa
(-9.6%)
(c-1)
E1=0.7285MPa
E2=0.6895MPa
(-5.4%)
(c-2)
E1=0.9494MPa
E2=1.3087MPa
(+37.8%)

◀**Fig. 7.9** Stress–strain curves and normalized crack lengths (ℓ/ℓ_0) in tensile tests of composites without and with epoxy components at the strain rate of 1.5 mm/h (= 0.025 mm/min). Panels **a** : stretching length 3 mm, holding period 1 h. Panels **b** : stretching length 1.5 mm, holding period 1 h. Panels **c** : stretching length 3 mm, holding time 2 h. Suffix–1 indicates specimens with PVDF/PEO fibers alone (no healing agents) and suffix–2 indicates specimens containing fibers with epoxy components (the healing agents) in the cores. In each panel, the black and red bold symbols correspond to the initial and post-holding stages of stretching, respectively. The black open circles correspond to the dimensionless crack lengths versus time. The photographs of the composite specimens labeled (1), (2), and (3) underneath the stress–strain curves depict the specimens at the end of the holding period, the point of the maximum stress, and after complete failure. Reprinted with permission from Lee et al. (2016a)

the composite specimen fails within a few minutes. The sudden increase in the crack length is accompanied by the rapid decrease in the tensile stress to zero, indicating the catastrophic failure of the composite specimens.

To study the effect of the stretching rate on the self-healing of the composites, tensile tests are also performed at the lower strain rate of 0.025 mm/min (0.15 mm/h) for different initial stretching times and different holding periods. The results shown in Fig. 7.9, are similar to those in Fig. 7.8. Namely, the composites containing only PVDF/PEO fibers reveal, as expected, no enhancement in stiffness after the holding period (Fig. 7.9a-1, b-1, and c-1) regardless of the holding position or time. A significant increase in stiffness is observed for the composites containing fibers with epoxy components for the initial stretching of 3 mm (2 h of stretching to 15% strain). A holding period of 1 h yields a ~ 47.3% increase in the Young's modulus (Fig. 7.9a-2), whereas a 2-h holding period allows a ~37.8% increase (Fig. 7.9c-2). Unlike the case with the higher strain rate shown in Fig. 7.8, in the present case, the longer holding period does not cause further increases in stiffness. This could be because the lower stretching rate causes less damage to the epoxy-component-containing NFs compared to the previous case shown in Fig. 7.8.

Curing may occur at the initially pre-notched crack, as at any crack, but it elapses over several hours. Therefore, the initial incision may release the epoxy resin and hardener but curing cannot not happen immediately or during the stretching to the strains of $\varepsilon_{xx} = 7.5$ or 15% as shown in positions (1) in Figs. 7.8 and 7.9. During this first stage of stretching, the slopes of the stress–strain curves are not visibly changed, corroborating the lack of curing during these relatively short periods of time, despite the epoxy resin and hardener released from the initial and growing cracks. Afterward, a rest (holding) period of t = 1–2 h is given, which is sufficient for the curing reaction to proceed. Accordingly, in the second stretching stage after the holding period, an increase in stiffness is observed, which is caused by self-healing, i.e., curing and hardening of the released epoxy resin.

The microscopic phenomena accompanying self-healing are revealed in Fig. 7.10, showing SEM images of the specimen surface fractured by crack propagation. In the left-hand panel in Fig. 7.10, the fractured PDMS surface resembles a brick wall near the panel bottom. However, in the middle of the magnified specimen in the

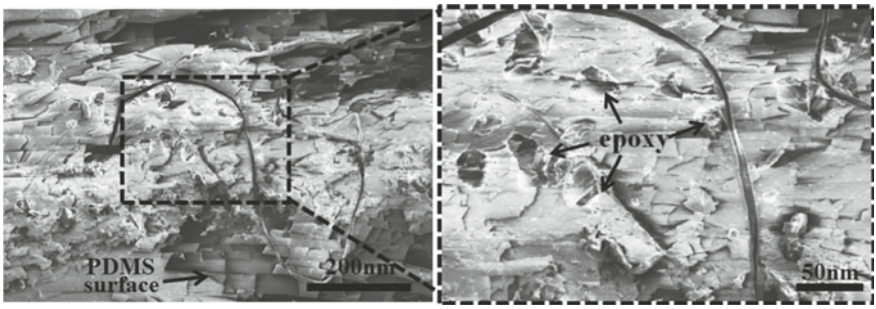

Fig. 7.10 SEM micrographs of fractured surface of a composite specimen containing self-healing NFs. Reprinted with permission from Lee et al. (2016a)

right-hand panel, several irregular epoxy chunks released from the fractured NFs are clearly visible.

Overall, the self-healing composites show the ability to restore and even enhance their mechanical stiffness after sustaining moderate damage, with healing times on the scale of 1 day for the DMS resin/curing agent (cf. Sect. 7.1) and 1 h for the epoxy/hardener healing agents, as shown in the present section. Repeatable self-healing is possible. However, self-healing is impossible after near-catastrophic damage.

7.3 Strength Recovery Under Static Fatigue Conditions

Considering the self-healing of fatigue cracks in self-healing composites, Lee et al. (2016b) studied composite materials with embedded epoxy/hardener-containing core-shell nanofibers formed by solution blowing (cf. Sect. 4.5). The shells of the core-shell solution-blown fibers were formed from a PVDF/PEO mixture. The core-shell fibers were encased in a PDMS matrix (see Fig. 4.30 in Sect. 4.7). An initial incision in the middle of a composite specimen stretched in a static fatigue test can, in principle, experience either crack propagation or healing, as observed in the present experiments.

The self-healing composite specimens are gripped between two vertical bars. The upper grip is fixed, while the lower one moves in the vertical direction (Fig. 7.11). Initially, a 20-mm-long specimen is clamped between the two grips (Fig. 7.12a). A 4-mm-long ($\ell_0 = 4$ mm) horizontal incision is introduced to the middle of the specimen. By lowering the lower grip mechanically, the specimens are stretched by 3, 3.5, or 4 mm, corresponding to 15%, 17.5%, or 20% of the initial length, respectively (Fig. 7.12b). A vertical micrometer fixed behind the grips facilitates the accurate measurements of the stretched specimen lengths. The horizontal incision in the original specimen is oval in shape. This is attributed to the initial stretching (cf. Fig. 7.12a and b). After the initial stretching, the upper and lower grips are fixed,

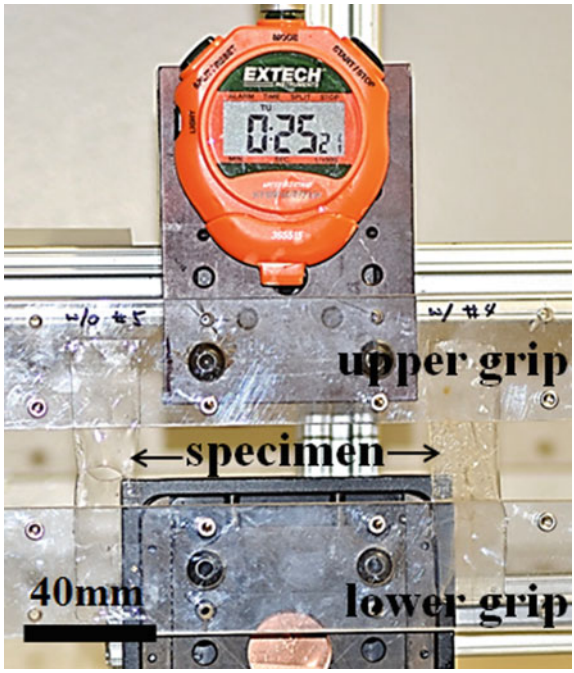

Fig. 7.11 Fatigue test setup with the fixed upper grip and movable lower grip. Reprinted with permission from Lee et al. (2016b)

thereby fixing the stretched specimen length in the vertical direction for a long time, during which the incision in the middle of the specimen is permitted to evolve. Hence, the stretching strain applied to the specimen in the vertical direction remaines fixed throughout the experiment. Snapshots of the specimen are taken every 30 min to monitor the increase in the crack length, ℓ, with time. It should be emphasized that the specimens are subjected to moderate tensile stresses and that the evolution of the fatigue crack in the self-healing or control specimens took hours or days, sufficient for self-healing.

Figure 7.13 shows the as-spun solution-blown fibers without epoxy before they are embedded in the PDMS matrix. The average diameter of fibers without and with epoxy components are 620 and 980 nm, respectively. Detailed descriptions of the fibers, their morphologies and diameter distributions are available in Sect. 4.5. The crack length ℓ is measured as a function of time using the photographs of the specimens obtained at various time moments t during the fatigue process. At $t = 0$, the dimensional length $\ell_0 = 4$ mm, and the dimensionless ratio $\ell/\ell_0 = 1$.

To explore the effects of the embedded NFs on the mechanical properties of the PDMS matrices, tensile tests of the different specimens were performed using an Instron 5942 with a 100-N load cell. The Young's modulus was measured using 20 mm × 60 mm specimens at a fixed strain rate of 10 mm/min. The Young's moduli of pure PDMS, self-healing PVDF/PEO NF mats, and non-self-healing mats were 1.24, 2.13 and 2.73 MPa, respectively. The Young's moduli of the PDMS–PVDF/PEO

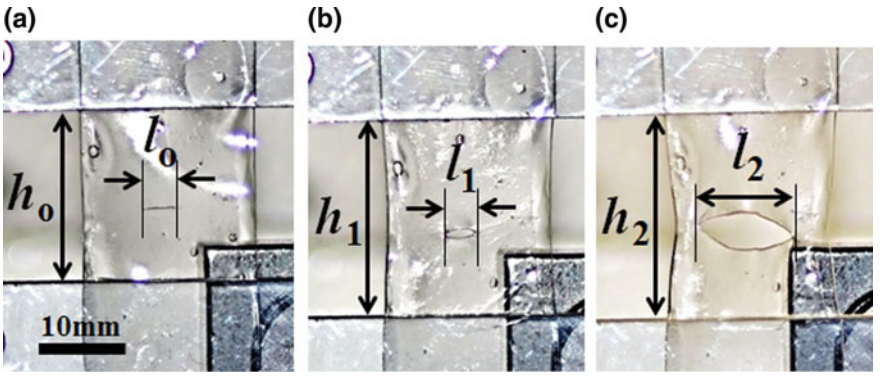

Fig. 7.12 Fatigue tests of PDMS–PVDF/PEO composites with and without epoxy and hardener in the cores of the embedded fibers. **a** The 20-mm-long specimens ($h_0 = 20$ mm) are initially clamped between the upper and lower grips, and **b** stretched by 3–4 mm ($h_1 = 23$–24 mm). **c** An increase in the crack length in time is revealed by a photograph taken at t = 6 days. Reprinted with permission from Lee et al. (2016b)

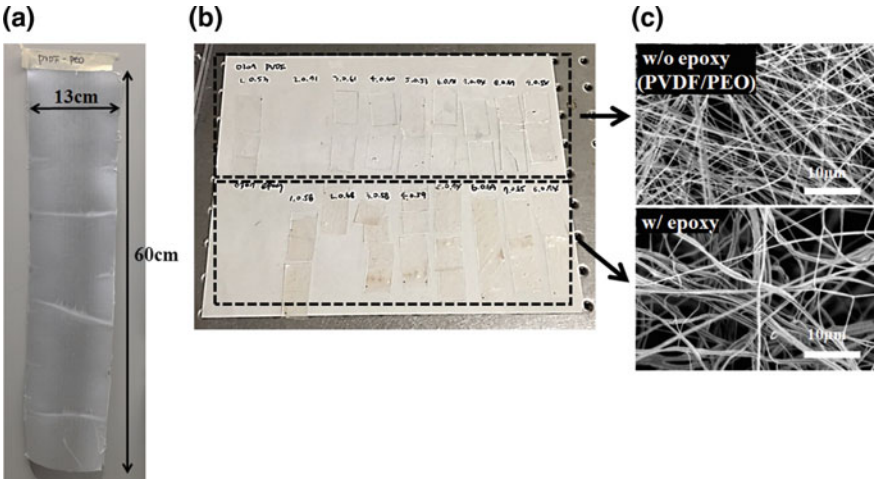

Fig. 7.13 **a** Solution-blown fiber mat collected on the plastic mesh of a rotating drum. **b** Specimens with the fiber mats encased in PDMS matrices. **c** SEM images of fibers with and without epoxy resin or hardener. Reprinted with permission from Lee et al. (2016b)

composites with and without epoxy and hardener in the NF cores were 1.53 and 1.44 MPa, respectively. Therefore, in this case the stiffness of the PDMS matrix was increased (not decreased) by 16–23% after the NFs were embedded.

In the experiments with the stretched composite specimens with cracks, distinctly different behaviors are recorded for the two types of specimens, i.e., for those with and without epoxy resin or hardener. For the composite specimens containing the PVDF/PEO fibers without epoxy resin or hardener, the crack length increases signif-

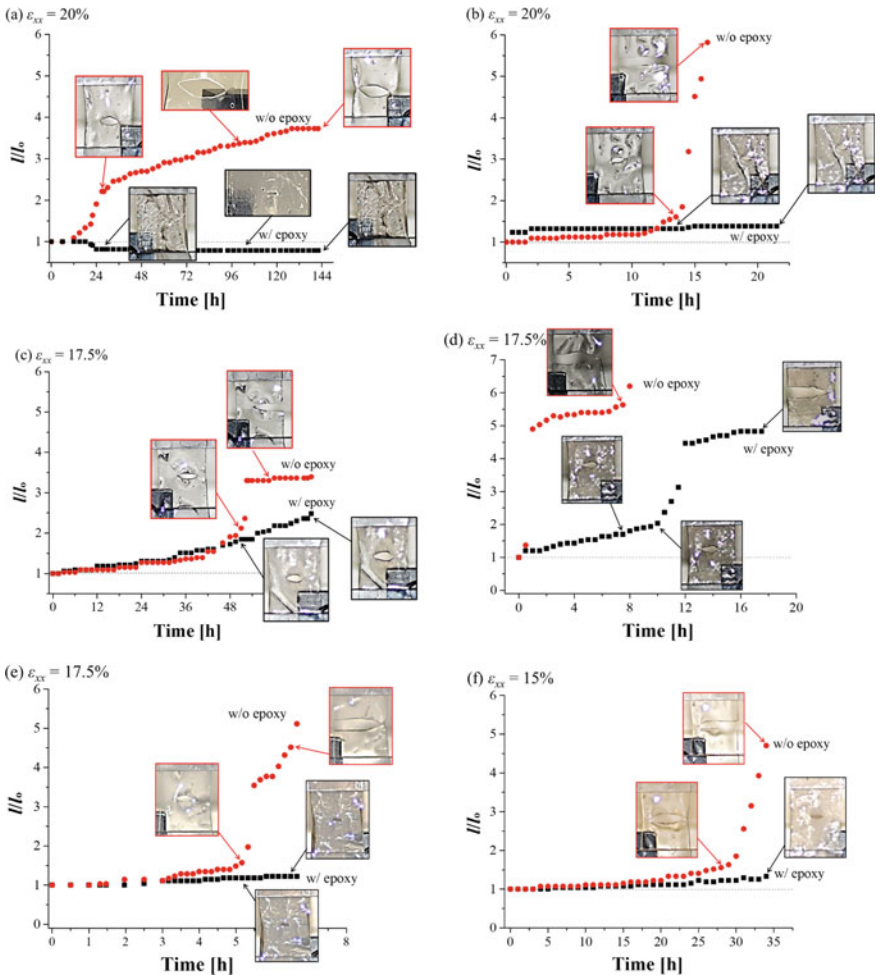

Fig. 7.14 Static fatigue test under fixed strain. The data for the composite specimens comprising PDMS matrices with embedded fibers without epoxy resin and hardener and those with epoxy resin and hardener are shown in red dots and black squares, respectively. The specimen thicknesses without and with epoxy are, respectively, **a** 0.44 and 0.63 mm, **b** 0.64 and 0.63 mm, **c** 0.77 and 0.49 mm, **d** 0.70 and 0.48 mm, **e** 0.60 mm for both, and **f** 0.53 and 0.58 mm. The strains ε_{xx} applied to the specimens are: **a**–**b** $\varepsilon_{xx} = 20\%$, **c**–**e** $\varepsilon_{xx} = 17.5\%$, and **f** $\varepsilon_{xx} = 15.0\%$. The thicknesses of the solution-blown fiber mats, both without and with epoxy components, before being encased in the PDMS matrix were in the 0.03–0.04 mm range. Reprinted with permission from Lee et al. (2016b)

icantly after the first 24 h and continues to increase until specimen rupture. However, for the specimens containing the fibers with epoxy resin and hardener, the crack propagation is much slower, indicating self-healing in the specimens. In fact, as Fig. 7.14a shows, the crack length in the self-healing specimens even decreases with time.

It should be emphasized that the composite specimens with the same contents, almost the same initial strains, and almost the same thickness can show different behaviors. These differences are attributed to several factors. First, the distribution of the fiber mat in the PDMS matrix cannot be precisely controlled; hence, after the setting, the fiber distribution is not uniform inside the PDMS matrix. Crack propagation is monitored in the center of the composite specimen, and the fiber content around the initial incision is uncontrollable for specimens both with and without epoxy. For the epoxy-containing specimens, the distribution of the epoxy within the encapsulated fiber is also unknown, because the core-shell fibers themselves are not uniform and the mat thickness near the initial incision may vary. Second, PDMS requires ~24–48 h to cure; although the initial thicknesses of the fiber mat-containing specimens are equal, the final thicknesses of the composites differ significantly. Accordingly, the time of specimen failure varies from 7 h to 6 days for the abovementioned reasons.

Under a fixed tensile strain, the crack length remains similar to the initial crack length ℓ_0 for some time. However, the crack length eventually begins to visibly increase. The increase in the crack length is much slower for the specimens containing fibers with the epoxy components, as the static fatigue tests are sufficiently long to allow the epoxy resin and hardener to escape the ruptured fibers, conglutinate, and solidify, and thus heal the specimen. The epoxy resin and hardener released from the separate broken fibers are cured along the crack and at the crack tip, which significantly delayed the crack propagation, as indicated by Fig. 7.14. The figure shows that the dimensionless crack lengths for the specimens with the embedded epoxy-component-containing fibers remain constant near 1 for most cases. Because the static fatigue tests last for several hours or days, while the epoxy requires only 1 h to cure, they facilitate the crack arrest in the self-healing specimens. It is also interesting to note that the subcritical cracks grow in a stepwise manner before reaching critical sizes, after which they grow continuously until they destroy the specimen. This trend is visible in both types of specimens, i.e., those with and without the epoxy resin and hardener. The stepwise growth of the subcritical fatigue cracks observed here is explained theoretically in Sect. 6.5.

The result shown in Fig. 7.14e is noteworthy. Here, the initial thicknesses of the composite specimens with and without epoxy are identical at 0.60 mm. Such specimens can be compared directly by ruling out the possible influence of the specimen thickness on the fatigue process. The self-healing epoxy-component-containing specimen still outlives that without epoxy, as shown in Fig. 7.14e, thus demonstrating the self-healing phenomenon. In addition, for the cases shown in Fig. 7.14c and d, the epoxy-component-containing self-healing specimens are thinner than those without epoxy. Regardless, the former outlive the latter because of the self-healing process.

7.4 Dynamic Situation: Mode I Crack Propagation

Co-electrospun PRC, PAN–resin (PR) and PAN–curing agent (PC) NF mats described in Sect. 4.2, and control electrospun pristine PAN mats were analyzed in tensile tests with progressively increasing stress to observe the influence of healing agents on the evolution and propagation of cracks pre-notched on one side in the middle of the mats (Lee et al. 2017). The Instron 5942 machine was used to conduct the tests. The tensile tests of the NF mats and the fiber-reinforced composite specimens were conducted according to ASTM D7565 standard (Standard 2017). The specimens were prepared by cutting the NF mats along the machine direction into rectangular strips of 60 mm × 25 mm (length × width) in size. These rectangular mats were then fixed in the Instron 5942 machine by clamping the upper and lower ends of the mats with pneumatic grips, with the two clamps separated by 20 mm. Thus, each exposed specimen had an initial area of 20 mm × 25 mm. A 5-mm-long sharp crack was pre-notched in the middle of each mat on the right-hand side, as shown in Fig. 7.15b. Then, the specimens are stretched at strain rates of 50, 10 and 1 mm/min until complete failure due to crack propagation (Mode I fracture; cf. Sect. 6.2). The load–displacement data obtained from the tensile tests were converted into the corresponding stress–strain curves; video imaging of crack propagation through the mats was conducted simultaneously. It should be emphasized that the cross-sectional area was evaluated as the product of the thickness and width of the mat, thus neglecting the cross-sectional porosity. Stretching is known to diminish the cross-sectional porosity of NF mats. Accordingly, the introduced inaccuracy is decreased as the stress and strain increase.

Representative stress–strain curves for the PAN and PRC specimens measured in tensile testing with Mode I crack propagation are shown in Fig. 7.16a. The corresponding stiffness associated with the initial linear segments of the curves and the ultimate strengths achieved are similar for the PAN and PRC NF mats in the present case. Significant differences between the two curves are observed beyond the ultimate strength point. The strain-at-failure of the PRC specimen is much larger than that of the PAN mat. The PAN mat experiences sudden failure immediately after the maximum stress point; the time interval before its complete failure ($t_{c,\,PAN}$) is short compared to that of the PRC specimen ($t_{c,\,PRC}$). The PRC NF mat cracks gradually for a much longer time. The crack propagation length before complete mat failure is 20 mm, i.e., equal to the difference between the mat width of 25 mm and the initial pre-notched crack length of 5 mm. This propagation length of 20 mm is divided by each crack propagation time (either $t_{c,\,PAN}$ or $t_{c,\,PRC}$) to evaluate the crack propagation speed V.

Several representative images of the PAN and PRC NF mats showing crack propagation during the tensile tests are depicted in Fig. 7.16b and c. The lower grip of the Instron 5942 machine remains fixed throughout the experiment, while the upper grip moves upward at a constant stretching rate. Figure 7.16b and c reveal that only the crack width increases initially, while the crack length remains constant at the pre-notched value of 5 mm. Once the tensile stress reaches its maximum value, indi-

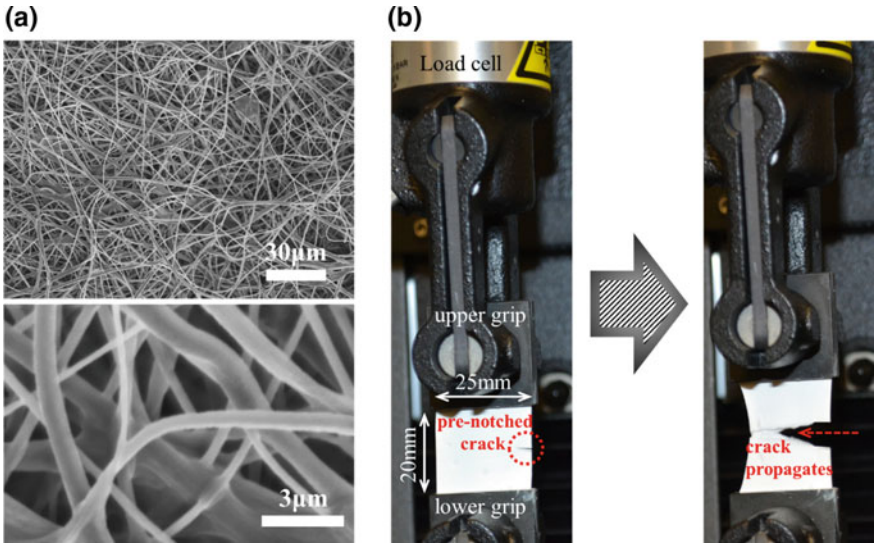

Fig. 7.15 **a** SEM micrographs of as-spun NF mat before damage. **b** The original specimen (as-spun NF mat) held between the grips of the Instron 5942 machine and propagation of the pre-notched crack during the tensile test. Reprinted with permission from Lee et al. (2017)

cating that the mat has reached its ultimate strength the crack propagates horizontally and its length begins to increase. From the images of the mat taken at regular time intervals, the crack propagation rate is measured after the ultimate strength point until the crack reaches the other edge of the mat (cf. the rightmost images in Fig. 7.16b and c).

The tensile tests of the PAN and PRC specimens are repeated at least four times (marked 1–4 in panels in Fig. 7.17a and b) for each stretching rate; thus the averaged Young's moduli and crack propagation speeds are established. Figures 7.17, 7.18, 7.19 summarize the results of the tensile tests conducted at the strain rates of 50, 10 and 1 mm/min, respectively. The catastrophic failure of the PAN NF mats occurs immediately after the maximum strength point, while that of the PRC specimens is delayed to a much larger strain, similar to the data in Fig. 7.16. The crack propagation speed of the PRC specimens is approximately 11% of that of the PAN specimens. In other words, the PRC specimens show much slower crack propagation during the tensile tests, while the Young's moduli of the PAN specimens are approximately 22% higher than those of the PRC specimens. The crack propagation is slowed by the presence of the uncured liquid agents in the cores of the core-shell PRC NF mats because the viscous liquids in the fiber cores provide another channel for energy dissipation. The specific value of the energy dissipation rate is on the order of $\mu(V/d)^2$, with μ being the zero-shear viscosity, V the crack propagation velocity, and d the cross-sectional fiber diameter. The viscous dissipation rate increases dramatically for sufficiently high liquid viscosities and small fiber diameters, as is the case here.

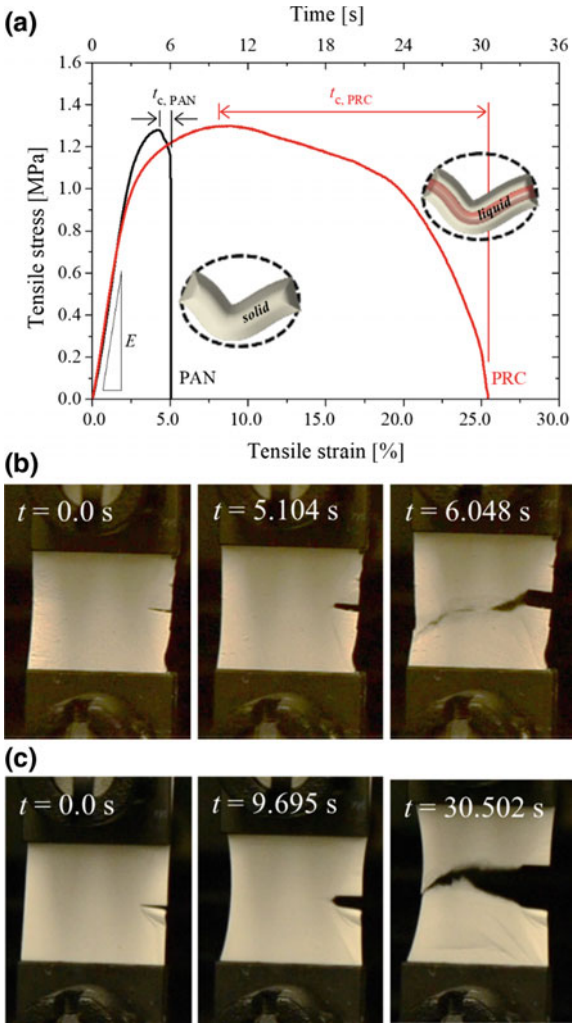

Fig. 7.16 **a** Stress–strain curves measured in tensile tests with pre-notched crack propagation in Mode I. Photographs of **b** PAN and **c** PRC specimens during the tensile tests reveal crack propagation in the horizontal direction beyond the ultimate strength point. The strain rate for the tensile tests is 10 mm/min for both cases. Reprinted with permission from Lee et al. (2017)

This is substantiated by the different rupture times of the PRC and PAN specimens, as Fig. 7.16a shows, of approximately 26 and 5 s, respectively, despite all conditions (fiber diameter, mat thickness, and strain rate) being equal. This indicates the retarding action of the liquid cores, although a detailed micro-mechanical theory for this phenomenon is currently unavailable.

The Young's modulus of the PRC specimens is gradually decreased as the strain rate increases from 1 to 50 mm/min (Fig. 7.20a). Slower stretching corresponds to higher measured stiffness in the PRC specimens, whereas the stiffness of the PAN specimens was approximately constant (cf. Fig. 7.20a). At the lowest stretching rate of 1 mm/min, the Young's moduli of the PAN and PRC specimens are similar. There-

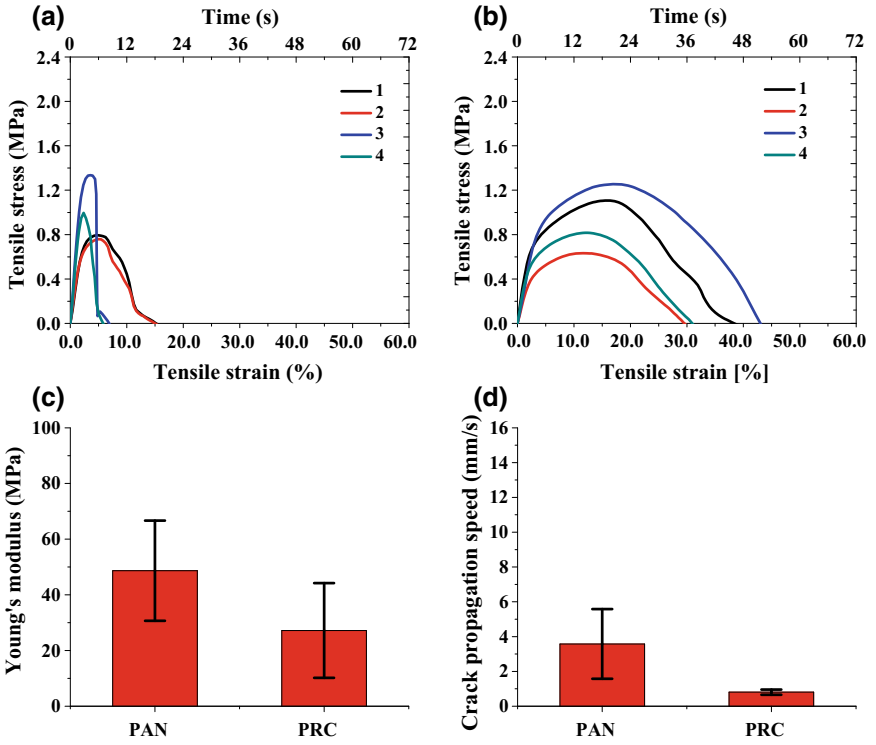

Fig. 7.17 Stress–strain curves of **a** PAN and **b** PRC NF mats in tensile tests with crack propagation. The numerals 1–4 in panels **a** and **b** indicate the four different trials. Averaged **c** Young's moduli and **d** crack propagation speeds for the PAN and PRC mats. Stretching rate is 50 mm/min. Here and hereinafter in Figs. 7.18 and 7.19, four different trials are used to evaluate repeatability. Reprinted with permission from Lee et al. (2017)

after, the Young's modulus is unchanged for the PAN mats, whereas it is decreased for the PRC specimens. The crack propagation speed of the PRC mats is approximately independent of the stretching rate and much lower than that of the PAN mats, which also show stretching rate dependence (Fig. 7.20b). At the lowest stretching rate of 1 mm/min, the crack propagation speeds for the PRC and PAN mats are similar. Thereafter on increasing the stretching rate, the crack propagation speed for the PAN mats is increased significantly, while that of PRC specimens is unchanged. Accordingly, the crack propagation speed at the strain rate of 10 mm/min is approximately 10 times lower for the PRC specimens than that of the PAN specimens.

The strains at which the ultimate stress is attained, denoted the ultimate strain, for the different PAN and PRC mats at different stretching rates are depicted in Fig. 7.20c. Because crack propagation begins only after the ultimate stress, higher ultimate strains imply longer elapsed times before the beginning of crack propagation. This time is denoted by t* in Fig. 7.20c. As seen in this figure, PRC specimens at all

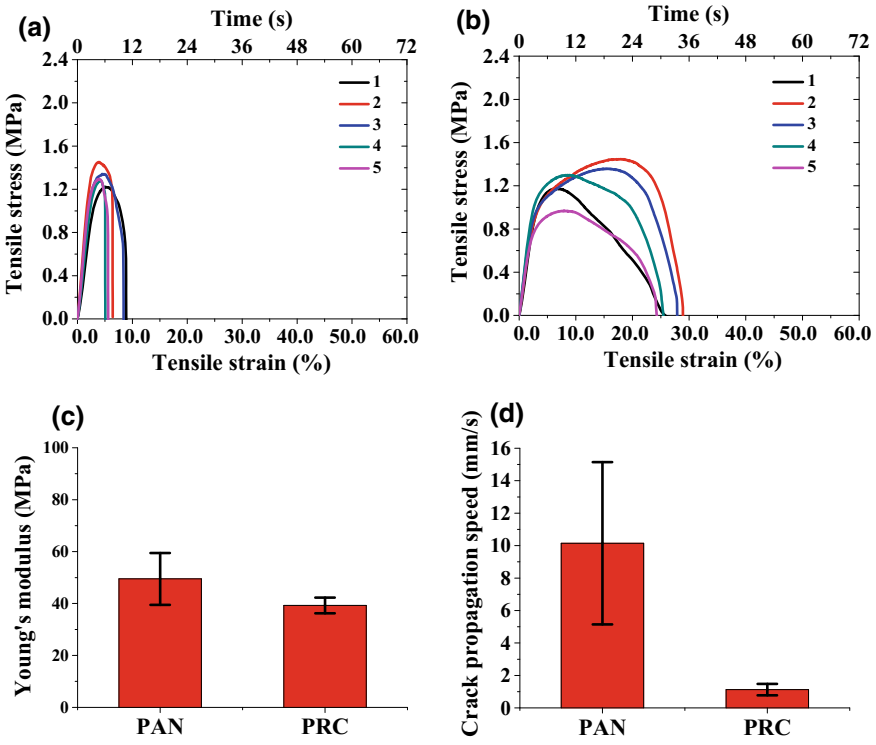

Fig. 7.18 Stress–strain curves of **a** PAN and **b** PRC NF mats in tensile tests with crack propagation. The numerals 1–4 in panels **a** and **b** indicate the four different trials. Averaged **c** Young's moduli and **d** crack propagation speeds for the PAN and PRC mats. Stretching rate is 10 mm/min. Reprinted with permission from Lee et al. (2017)

stretching rates show ultimate stresses at higher strain values than the corresponding PAN specimens. Thus, it can be concluded that the beginning of crack propagation in PRC specimens is delayed as compared to that in PAN specimens.

It should be emphasized that t* is the time interval from the beginning of the tensile tests until the ultimate stress point is reached, whereas t_c is the time interval from the ultimate stress point until a complete mat rupture. Thus, t* indicates the initial delay in crack propagation, while t_c indicates the crack propagation speed in the specimen. Figure 7.20 shows that both t* and t_c are longer for the PRC mats. Hence, it can be concluded that the cracks begin to grow later and more slowly in the PRC mats than those in their counterpart PAN mats.

In comparing the PR and PC fiber mats, their behaviors are quite similar. It should be emphasized that their Young's moduli, the ultimate stresses, and ultimate strains are slightly different from those of the PRC fiber mats. In Fig. 7.20a, the Young's moduli of the PR and PC fiber mats are higher than that of the PRC fiber mat, and even higher than that of the PAN mat at some points. The ultimate stresses and strains

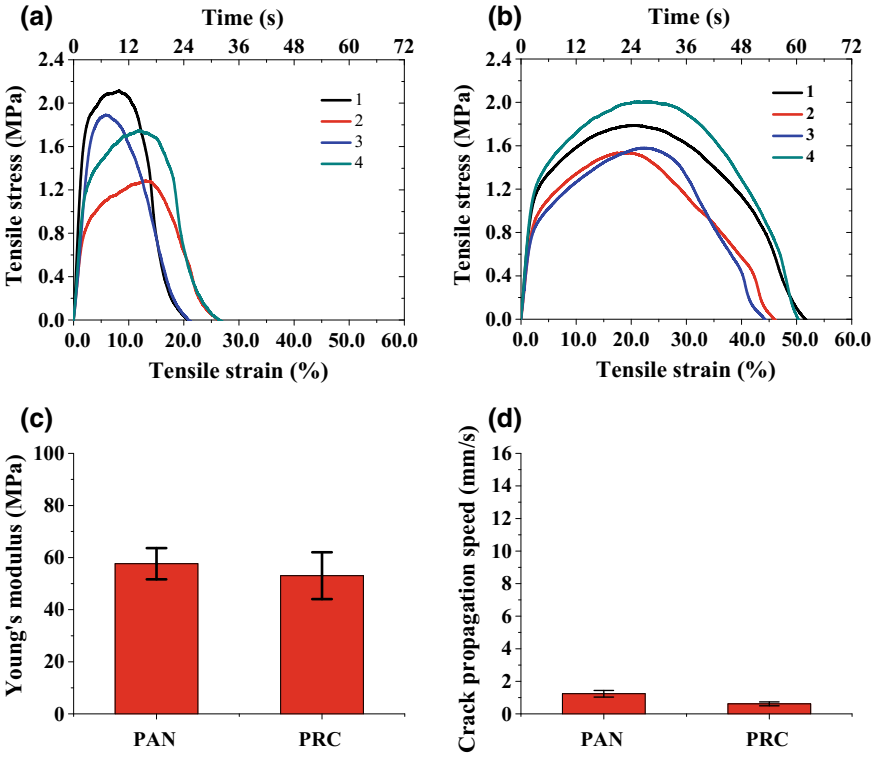

Fig. 7.19 Stress–strain curves of **a** PAN and **b** PRC NF mats in tensile tests with crack propagation. The numerals 1–4 in panels **a** and **b** indicate the four different trials. Averaged **c** Young's moduli and **d** crack propagation speeds for the PAN and PRC mats. Stretching rate is 1 mm/min. Reprinted with permission from Lee et al. (2017)

of the PR and PC fiber mats are higher and lower, respectively, than that of the PRC specimen (see Fig. 7.20c). However, the crack propagation speeds in the PR and PC specimens are similar to that in the PRC specimen, while being lower than that in the PAN specimen for all three strain rates.

Despite the data scatter involved, as manifested by the error bars, Fig. 7.20c reveals a clear delineation of the data for the PRC fiber mats from that for the PAN, PR, and PC fiber mats. Resin polymerization by the curing agents, associated with microscopic damage prior to crack propagation, is present only in the PRC fiber mats among all tested mats, and thus causes the recorded delays in PRC mat failure.

In general, higher applied loads correspond to shorter time intervals t* before the beginning of rupture (Parton and Morozov 1989). The longer time to failure of the PRC specimens as compared to that of the PAN specimens allows speculation that stress relaxation (viscoelastic memory effects) may occur in the PRC specimens. The stress relaxation in the PRC NFs is presumably associated with the presence of the liquid cores in these NFs. In addition to the elastic material parameter of the Young's modulus E associated with the solid polymeric shells of the fibers, another parameter of the zero-shear viscosity μ is associated with

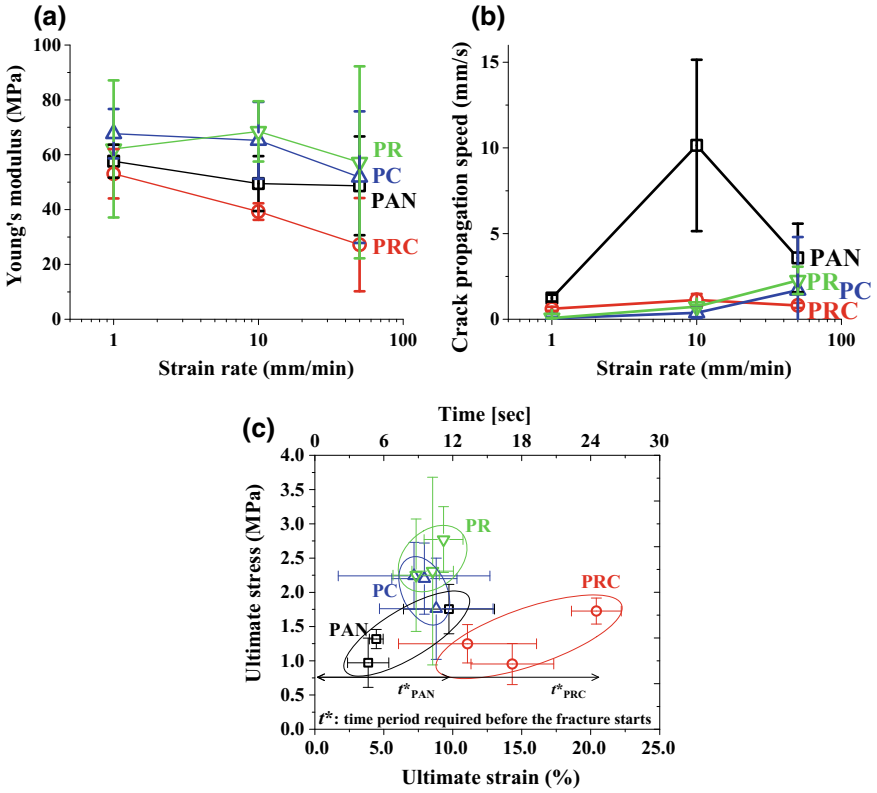

Fig. 7.20 Material parameters of the PAN, PRC, PC and PR mats. **a** Young's moduli. **b** Crack propagation speeds. **c** Ultimate stresses versus ultimate strains. Reprinted with permission from Lee et al. (2017)

the liquid cores. Accordingly, the characteristic stress relaxation time $\theta = \mu/E$ arises, which determines stress relaxation over time t, typically in the form of the exponential fading memory $\exp(-t/\theta)$ (Feng et al. 2002). In addition, liquid in the NF core may act as a plasticizer. Plasticizers are often added during manufacturing to improve the mechanical properties of polymers, facilitating chain rotation and motion with enhanced free volumes between the chains (Lim and Hoag 2013). Plasticizers decrease the Young's modulus and increase stretchability and resistance to cracking (Heinamaki et al. 1994; Leblanc et al. 2007; Joffe et al. 2015). In summary, the presence of liquid epoxy in the fiber cores of the PRC mats may provide an additional energy dissipation channel, granting viscoelasticity and stretchability as well as providing the ability to heal microscopic damage by means of the resin polymerization before and during crack propagation.

The as-spun PRC and PAN NF mats show irregular crack shapes and intermittent crack propagation, as in Fig. 7.16. Therefore, to study the crack shapes and propagation rates, composite specimens were formed with the co-electrospun PRC and electrospun PAN NFs embedded in them. The PAN/PRC NF mat was cut into pieces of 25 mm × 60 mm and then encased in a PDMS (10:1 wt. ratio) matrix. The thicknesses of such the PRC- and PAN-containing composites were 0.61 ± 0.16 mm and 0.52 ± 0.26 mm, respectively. Similarly to the tensile tests of the PRC and PAN NF mats, 5-mm-long sharp cracks were pre-notched in the middle of the right-hand sides of the composite specimens. Then, crack propagation under tension was observed. Similar observations were done using pure PDMS specimens (without the embedded NFs); however, the specimen stiffness in this case did not allow uniform crack propagation, as shown in Fig. 7.21a.

Figure 7.21b and c show the shapes of the cracks as they propagate across the PDMS–PRC and PDMS–PAN composite specimens, respectively. The theoretically predicted shape, assuming Kelvin–Voigt viscoelastic resistance near the tip of the opening crack, is sketched in Fig. 6.4 in Sect. 6.3. Such shapes can, to some extent, resemble the experimental images in Fig. 7.21b–i for various crack lengths and pre-notch positions. The PDMS–PRC and PDMS–PAN specimens with pre-notches at the right sides are shown in panels Fig. 7.21b–c, d, g and e, h with different initial incision lengths of 5, 2 and 10 mm, respectively. The initial incisions are located in the specimen centers in panels Fig. 7.21f and i for the PDMS–PAN and PDMS–PRC specimens, respectively. Overall, the PDMS–PAN and PDMS–PRC specimens show similar trends in crack propagation, smoothness, and uniformity in the crack boundaries and propagation rate. Especially, in Fig. 7.21d, the experimentally observed evolution of the crack shape at the final stages matches well with the theoretical predictions.

The PDMS–PAN composite specimens with the embedded rectangular strips of PAN NF mats have the width $2h = 25$ mm. An initial incision of the length of 5 mm is made at the specimen center (cf. Fig. 7.21f). The initial crack length is, accordingly, $2\ell_0$. The composite PDMS–PAN specimens are then stretched at a uniform stretching rate using an Instron 5942, while photographing the developing crack at regular time intervals. The dimensionless load $\overline{\sigma_\infty}$ is obtained from the stress–strain data, while the dimensionless crack length $\overline{\ell}$ is measured from the snapshots; the definitions of the dimensionless parameters are given in Eq. (6.37) in Sect. 6.4.

Figure 7.22 depicts the results of two experimental trials and compares them with the theoretical lines I and II. Because the parameters K_{Ic} and λ [cf. Eq. (6.37) in Sect. 6.4] are calculated using the values of the maximum stresses and yield stresses, the theoretical curves for each experimental set in Fig. 7.22a and b differ. Initially, the crack growth occurs in the stable subcritical domain, as is seen with the overlap of the experimental data with curves I. As the dimensionless load $\overline{\sigma_\infty}$ continues increasing, the crack length $\overline{\ell}$ crosses from the subcritical to the unstable supercritical and catastrophic domain (crossing curves II). The crack length then begins to increase in an unstable non-monotonic manner, similar to the ideal brittle crack trend (depicted by curves III). This continues beyond the ultimate stress point of the composite until complete specimen rupture.

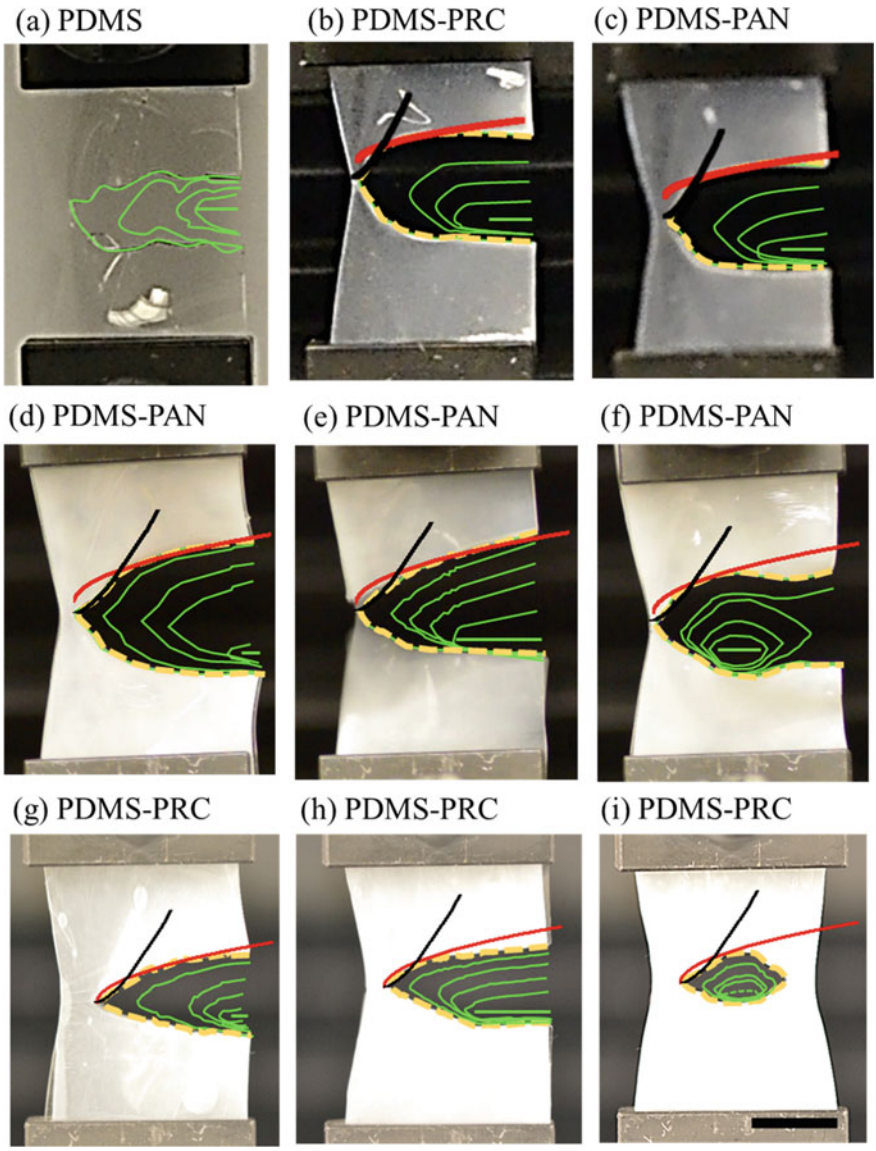

Fig. 7.21 Crack evolution in **a** pure PDMS, **b**, **g**–**i** PDMS–PRC, and **c**–**f** PDMS–PAN composite specimens. The lengths of the pre-notched incisions (shown by solid green horizontal bars): for **a**–**c**, **f**, and **i** $\ell_0 = 5$ mm; for **d**, **g** $\ell_0 = 2$ mm, and for **e**, **h** $\ell_0 = 10$ mm. Initial incision location is on the right side in panels (**a**–**e**, **g**–**h**), and at the center in panels (**f**, **i**). Four different colors are used to demarcate curves with different physical meanings: black is used for the near-field asymptotic, red for the far-field asymptotic, green for the intermediate contours of the propagating cracks, and dashed yellow lines for the final crack shapes. The theoretical predictions, shown by the black and red solid lines, correspond to the asymptotic expressions $[x - \ell(t)]^{3/2}$ and $[x - \ell(t)]^{1/2}$, respectively (cf. Sect. 6.3). The theoretical predictions are compared to the last photographs in all the panels, because the crack appears with the best resolution in these. Scale bar is 10 mm. Reprinted with permission from Lee et al. (2017)

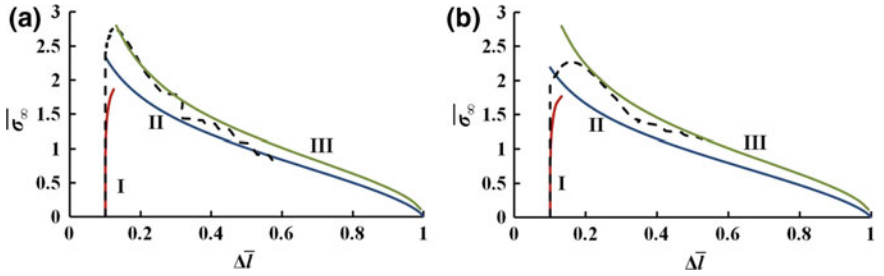

Fig. 7.22 Comparison of the experimental results on crack propagation with the theory of Sect. 6.4 developed for fatigue cracks propagating under load. Panels **a** and **b** indicate two different trials. Red lines I correspond to Eq. (6.39), blue lines II correspond to Eq. (6.38), and green lines III correspond to Eq. (6.40) from Sect. 6.4. The black dashed lines show experimental data. Reprinted with permission from Lee et al. (2017)

The PDMS–PAN specimens contain no healing agent; thus, the crack length ℓ is a straightforward consequence of the external load σ_∞. As seen in Figs. 7.16, 7.17, 7.18, 7.19, and 7.20, crack propagation in the PRC specimens is delayed significantly and specimen failure occurs at a much larger strains, attributed to the presence of the liquid cores and the associated viscoelastic stress relaxation. The theory of Sect. 6.4 considers continuous crack propagation under the external load σ_∞, without considering the effect of the liquid cores. Furthermore, the fracture toughness K_{Ic} of the specimen also changes when considering the liquid cores. The theory of Sect. 6.4 is based on the calculation of K_{Ic} at the ultimate strength and assumes a homogeneous composite material throughout the crack propagation distance. Currently, no method exists for calculating or measuring K_{Ic} for the PDMS–PRC specimens. Thus, the theory of Sect. 6.4 cannot be compared to the observed crack propagation behaviors of the PDMS–PRC specimens.

References

Barenblatt GI (2014) Flow, deformation and fracture. Cambridge University Press, Cambridge

Cherepanov GP (1979) Mechanics of brittle fracture. McGraw Hill, New York

Coope TS, Mayer UFJ, Wass DF, Trask RS, Bond IP (2011) Self-healing of an epoxy resin using scandium (III) triflate as a catalytic curing agent. Adv Funct Mater 21:4624–4631

Coope TS, Wass DF, Trask RS, Bond IP (2014) Metal triflates as catalytic curing agents in self healing fibre reinforced polymer composite materials. Macromol Mater Eng 299:208–218

Feng L, Li S, Li H, Zhai J, Song Y, Jiang L, Zhu D (2002) Super-hydrophobic surface of aligned polyacrylonitrile nanofibers. Angew Chem Int Ed Eng 41:1221–1223

Heinamaki JT, Lehtola VM, Nikupaavo P, Yliruusi JK (1994) The mechanical and moisture permeability properties of aqueous based hydroxypropyl methylcellulose coating systems plasticized with polyethylene-glycol. Int J Pharm 112:191–196

Joffe R, Madsen B, Nattinen K, Miettinen A (2015) Strength of cellulosic fiber/starch acetate composites with variable fiber and plasticizer content. J Compos Mater 49:1007–1017

Khansari S, Sinha-Ray S, Yarin AL, Pourdeyhimi B (2012) Stress-strain dependence for soy protein nanofiber mats. J Appl Phys 111:044906

Khansari S, Sinha-Ray S, Yarin AL, Pourdeyhimi B (2013) Biopolymer-based nanofiber mats and their mechanical characterization. Ind Eng Chem Res 52:15104–15113

Kim M-S, Shin H-J, Park Y-K (2011) Measurement of nonlinear mechanical properties of PDMS elastomer. Microelectron Eng 88:1982–1985

Landau LD, Lifshitz EM (1986) Theory of elasticity. Reed Educational and Professional Publishing Ltd, Oxford

Leblanc JL, Furtado CRG, Leite MCAM, Visconte LLY, de Souza AMF (2007) Effect of the fiber content and plasticizer type on the rheological and mechanical properties of poly(vinylchloride)/green coconut fiber composites. J Appl Polym Sci 106:3653–3665

Lee MW, An S, Jo HS, Yoon SS, Yarin AL (2015) Self-healing nanofiber-reinforced polymer composites: 1. Tensile testing and recovery of mechanical properties. ACS Appl Mater Interfaces 7:19546–19554

Lee MW, Sett S, Yoon SS, Yarin AL (2016a) Self-healing of nanofiber-based composites in the course of stretching. Polymer 103:180–188

Lee MW, Sett S, Yoon SS, Yarin AL (2016b) Fatigue of self-healing nanofiber-based composites: static test and subcritical crack propagation. ACS Appl Mater Interfaces 8:18462–18470

Lee MW, Sett S, An S, Yoon SS, Yarin AL (2017) Self-healing nano-textured vascular-like materials: Mode I crack propagation. ACS Appl Mater Interfaces 9:27223–27231

Lim H, Hoag SW (2013) Plasticizer effects on physical–mechanical properties of solvent cast Soluplus® films. American Association of Pharmaceutical Scientists 14:903–910

Parton VZ, Morozov EM (1989) Mechanics of elastic-plastic fracture, 2nd edn. Hemisphere Publishing Corporation, New York

Sinha-Ray S, Khansari S, Yarin AL, Pourdeyhimi B (2012) Effect of chemical and physical cross-linking on tensile characteristics of solution-blown soy protein nanofiber mats. Ind Eng Chem Res 51:15109–15121

Sinha-Ray S, Yarin AL, Pourdeyhimi B (2014) Meltblown fiber mats and their tensile strength. Polymer 55:4241–4247

Standard Test Method for Determining Tensile Properties of Fiber Reinforced Polymer Matrix Composites Used for Strengthening of Civil Structures (2017) ASTM D7565/D7565 m-10. West Conshohocken, PA

Yarin AL, Pourdeyhimi B, Ramakrishna S (2014) Fundamentals and applications of micro- and nanofibers. Cambridge University Press, Cambridge

Chapter 8
Self-Healing at Ply Surfaces: Adhesion, Cohesion, and Interfacial Toughening Evaluated Using Blister and Impact Tests

In this Section the adhesion (blister) test is discussed in Sects. 8.1 and 8.2 regarding the performances of two types of nanotextured vascular self-healing materials and their effects on the adhesion and cohesion energies. In Sect. 8.3, double-cantilever beam and bending tests, applied for the mechanical characterization of self-healing materials, are discussed. Sect. 8.4 outlines the interfacial toughening by means of nanofibers (NFs) intended to prevent delamination and crack propagation. In addition, damage to interfacial layers toughened by NFs is characterized by impact testing. Section 8.5 provides comprehensive data on mechanical recovery in self-healing vascular materials. In addition to the essentially two-dimensional self-healing materials discussed in Sects. 7.1–7.4 and 8.1–8.5, the mechanical behaviors of their three-dimensional counterparts are explored in Sect. 8.6.

8.1 Blister Testing: Recovery of Adhesion or Cohesion in Composites with Co-electrospun PAN/DMS-Resin/Curing Agent NFs

Various fatigue elements, such as microcracks and/or delamination surfaces, accumulate in engineering materials subjected to periodic loading and unloading. Under certain conditions, the growth of these defects can accelerate and cause catastrophic failure of a macroscopic component, despite the negligible sizes of most individual defects. In many cases, these defects occur in the material bulk, invisible to detection and thus evade inspection and repair. Composite materials, whose advanced mechanical properties and light weights have led to their wide use in industrial applications, are especially susceptible to these types of defects (see Sect. 6.6). Their original inhomogeneity facilitates, in particular, cracking and delamination at ply interfaces. NFs with embedded healing agents may effectively prevent microcracking and delamination at ply interfaces (Wu et al. 2013; Wu and Yarin 2013).

A. L. Yarin et al., *Self-Healing Nanotextured Vascular Engineering Materials*, Advanced Structured Materials 105, https://doi.org/10.1007/978-3-030-05267-6_8

To study the self-healing of delamination damage at ply interfaces, the adhesion energy and the effect of the released healing agents on it must be measured. The adhesion energy of a fiber membrane can be evaluated, for example, by the T-peel test (Ballarin et al. 2013), dead weight test (Najem et al. 2014; Sett et al. 2015), 180° peeling test (Sett et al. 2015), the double-cantilever test (Wu and Yarin 2013; cf. Sect. 8.3), and the blister test (Na et al. 2012; Wong et al. 2013). In the T-peel test, two long strips of a sample material are adhered under pressure and peeled away from each other. The adhesive strength is a function of the peel force, peel rate, and specimen dimensions. The dead weight test is used to evaluate the adhesive strength in shear. In this test, a specimen is adhered to a target substrate and pulled by a weight connected by a 90° pulley. The weight is provided by a vessel suspended on the pulley; this is gradually filled with water during the experiment. The weight of water that causes specimen detachment from the substrate is referred to as the dead weight transmitted to the adhesive interface. In the dead weight test, Mode II-type (see Fig. 6.3 in Sect. 6.2) detachment of the two surfaces is realized to evaluate the adhesion strength. In the double-cantilever test, like the T-peel test and 180º peeling test, Mode I-type (see Fig. 6.3 in Sect. 6.2) detachment of two cantilevers is realized to evaluate the adhesion strength. In blister testing, a mechanical shaft is used to push an adhesive membrane to induce its delamination from the substrate (see Fig. 6.8 in Sect. 6.7). The edge effect at the delamination, inevitable in the T-peel and the double cantilever tests, can be avoided by employing the conical axisymmetric geometry of the blister test, which is highly stable and reproducible (Obreimoff 1930; Hutchinson and Suo 1992).

Lee et al. (2015) studied the adhesion and cohesion of co-electrospun core-shell NF mats with dimethyl siloxane (DMS) resin monomer or dimethyl-methyl hydrogen-siloxane (DMHS) curing agent in the cores and polyacrylonitrile (PAN) shells, as self-healing PRC (PAN-resin-curing agent) NFs (see Sect. 4.2). Electrospun NF mats of monolithic PAN NFs were also used for comparison. Such NF mats were pressed onto polyethylene terephthalate (PET) substrates with holes in the middle, and these fiber mat–substrate layers were used as specimens for blister testing. Some specimens were subjected to periodic bending fatigue for several hours and then rested for 24 h to allow self-healing before the blister testing. For the blister tests, the specimens were bent with a fixed deflection of 3 mm at the frequency of 1 Hz for 3–5 h (see Fig. 8.1). The 10,800 total cycles of repeated bending induced fatigue in the adhered fiber mats. The function shape of the bending deflection applied during the fatigue is shown in Fig. 8.2.

The adhesion energies of the prepared NF mats were measured by blister tests. Most of the previous works on blister testing (Obreimoff 1930; Malyshev and Salganik 1965; Hutchinson and Suo 1992) addressed materials whose resistances to bending were associated with the bending stiffness (related to the moment of the elastic stresses in the cross-section), which were felt even at infinitesimally small bending amplitudes (cf. Sect. 6.7). On the contrary, NF mats are examples of blistering in soft materials, where the resistance due to specimen stretch-

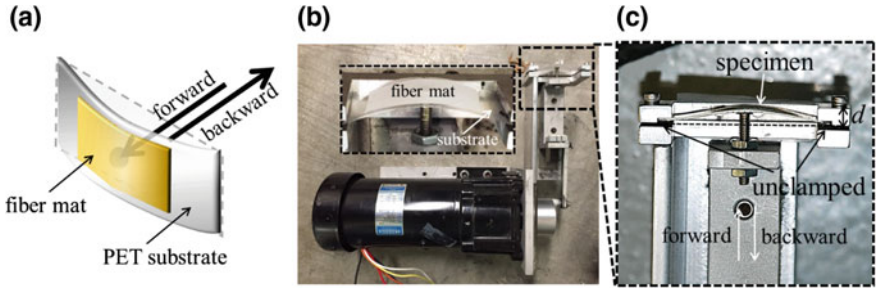

Fig. 8.1 Bending for fiber mat fatigue. **a** Schematic of specimen fatigue by bending. **b** and **c** Details of the experimental setup. Reprinted with permission from Lee et al. (2016c)

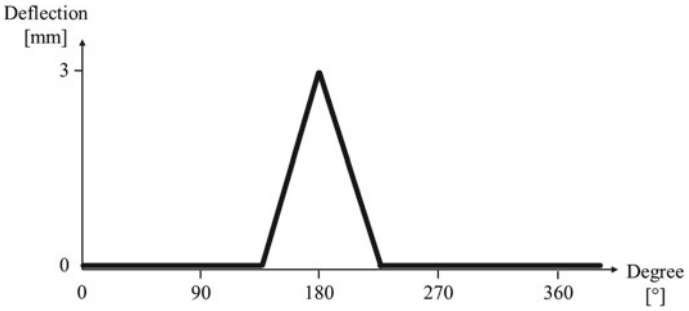

Fig. 8.2 Function shape of bending deflection applied during the fatigue. The deflection is applied using the conversion of the rotary motion of a motor (characterized in degrees on the horizontal axis) into the reciprocating motion of a punch used to bend the specimen. Reprinted with permission from Lee et al. (2015)

ing is dominant (cf. Sect. 6.8). The mats were cut into pieces with dimensions of 35 mm × 30 mm and placed on a flexible PET plate of 0.73 mm in thickness with a 3-mm-diameter hole in the middle. The NF mats are initially pressed to the PET substrates by pressing and rolling a metal roller over the mats, as shown in Fig. 8.3a. The force applied to the specimen through the roller is measured by a balance. The metal roller was rolled over the entire surface of each specimen more than 10 times to guarantee uniform loading and repeatability of the results. This procedure was previously used in the literature for similar purposes; it is known to enhance the degree of fiber adhesion to the substrate and to remove air entrapped in the fiber mat (Na et al. 2012; Wong et al. 2013). The pressure applied to the roller yields a non-zero contact zone (Derjaguin et al. 1975)

$$l = \left[\frac{3(1-\nu^2)\mathrm{RF}}{4\mathrm{E}}\right]^{1/3} \tag{8.1}$$

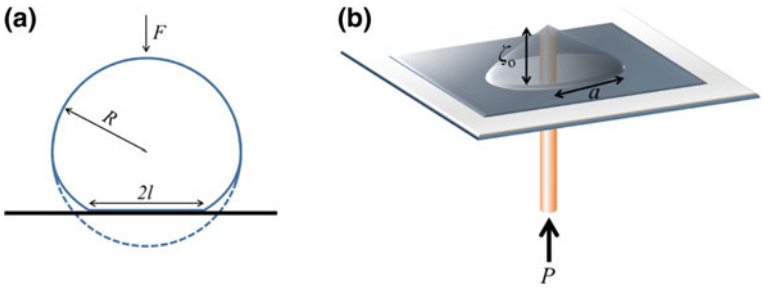

Fig. 8.3 **a** Deformation of an elastic roller pressed to a rigid plane. **b** Schematic of blister test. Reprinted with permission from Lee et al. (2015)

where l is the half-width of the contact area resulting from the roller deformation when it is pressed against the rigid surface under the substrate with NFs on top; E and ν are the metal roller's Young's modulus and Poisson's ratio, respectively; R is the roller radius; and F is the applied force. For a steel roller, E = 200 GPa and ν = 0.3. The roller radius R is equal to 45.5 mm. The hand-pressing force F $\approx$ 9.2 kgf = 9.2 kg $\times$ 9.81 m/s^2 = 90.25 N. Thus, according to Eq. (8.1), 2 l = 482 μm and the pressure P = F/(w $\times$ 2 l) (where the roller width w = 30.6 mm) applied to the mat was 6.12 MPa.

A shaft with a tip of 0.5 mm in diameter was inserted and pushed by an Instron 5942 through the hole in the PET substrate and used to delaminate the NF mat away from the substrate, while measuring the resistance force P (Fig. 8.3b). Simultaneously, the geometry of the detached NF mat was video-recorded to measure the height ζ_0 and radius a of the resulting blister.

Figures 8.4 and 8.5 show the results of the blister tests for both the PAN (control) and self-healing PRC NF mats. The thicknesses of the PAN and PRC fiber mats are 0.089 mm and 0.191 mm, respectively. The tests are conducted at different rates, as listed in the figure captions. Figure 8.4 shows photographs of the mat shapes at different stages of the delamination process.

In Fig. 8.5, the peak force reached in the blister tests strongly depends on the speed of the shaft motion, being lower at 2 mm/min than at 10 mm/min for both materials, whether fatigued or not. The loads recorded in the blister tests of the PRC fiber mats are significantly higher than those recorded in the tests of PAN fiber mats. This is because the core-shell PRC fibers have already sustained some damage during squeezing between the roller and the substrate. As a result, some DMS resin monomer and curing agent have already been released, permitting their polymerization as PDMS and thus enhancing the adhesion between the PRC fibers and the substrate.

Figure 8.5 also depicts the results of the blister tests conducted with PAN and PRC fiber mats after 5-h prior periodic bending. This experiment reveals the effects of prior damage accumulation on the mats' adhesive capacities, and evaluates the capability of the PRC fiber mats for preventing delamination. For both PAN and PRC specimens, the peak load achieved in the blister tests after prior periodic bending is

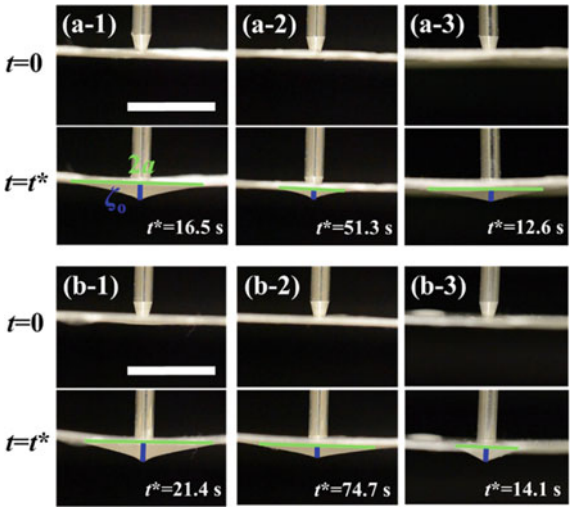

Fig. 8.4 Photographic images of different stages of blister (the adhesion) tests. PAN NF mat at shaft rates of (a-1) 10 mm/min (pristine mat), (a-2) 2 mm/min (pristine mat), and (a-3) 10 mm/min (specimen underwent prior periodic bending for 5 h followed by 24 h rest). PRC specimen at shaft rates of (b-1) 10 mm/min (pristine mat), (b-2) 2 mm/min (pristine mat), (b-3) 10 mm/min (specimen underwent prior periodic bending for 5 h followed by 24 h rest). Time t = 0 is the beginning of the test, time t^* is the time of blister formation. Values of the blister formation time t^* are displayed in the panels. Reprinted with permission from Lee et al. (2015)

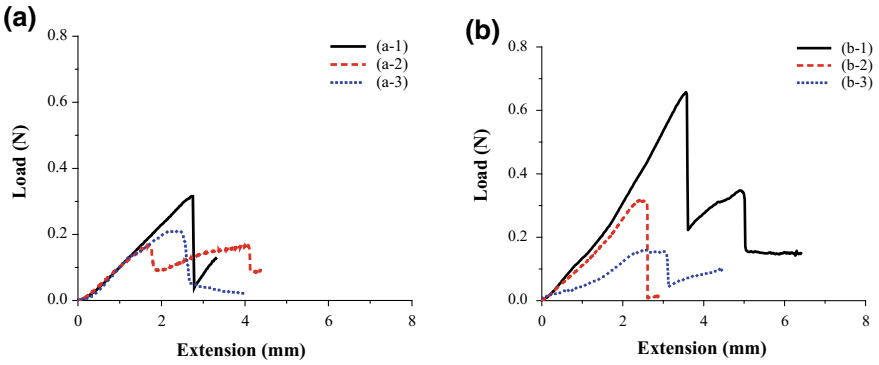

Fig. 8.5 Load–extension curves related to adhesion in blister tests: **a** PAN NF mat **b** PRC fiber mat. Shaft rate of (a/b-1) 10 mm/min, (a/b-2) 2 mm/min, (a/b-3) 10 mm/min after 5 h-long prior periodic bending. Reprinted with permission from Lee et al. (2015)

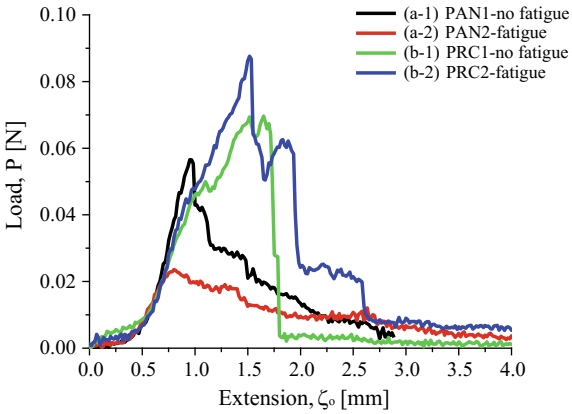

Fig. 8.6 Load–extension curves related to cohesion measured in blister (the cohesion) tests. Reprinted with permission from Lee et al. (2015)

decreased compared to that in the corresponding pristine specimens (compare curves a-3 and a-1, as well as b-3 and b-1, respectively). This indicates that the prior periodic bending caused significant damage, and in particular, induced fiber delamination from the substrate. Figure 8.5b shows that the PRC fiber mat does not recover its adhesive strength after periodic bending and a 24-h rest period. This indicates the insufficient release of DMS resin monomer and curing agent at the interface during the fatigue process.

It should be emphasized that the abrupt decreases in loads visible in Fig. 8.5 at later times are typically associated with the beginning of delamination propagation at the blister perimeter, similarly to a circular self-propagating crack.

The cohesion energy between identical NF mats was also measured using blister tests. For these specimens, a PAN or a PRC NF mat was fixed to the base PET substrate using dual-side tape, and then an identical NF mat was placed on top of it and finger-pressed. In Figs. 8.6 and 8.7, depicting the results of these tests, PAN1 and PRC1 denote the pristine specimens, while PAN2 and PRC2 denote the bending-fatigued ones (with deflection of 3 mm applied for 3 h with frequency $f = 1$ Hz; 10,800 bending cycles in total). The fatigued specimens were rested for 24 h after periodic bending for the self-healing PDMS polymerization reaction to proceed, allowing self-healing. The load–extension curves and photographs obtained during these blister tests are depicted in Figs. 8.6 and 8.7, respectively.

The adhesion energy T can be found from the experimental data using Eq. (6.74) from Sect. 6.8, which requires the measured values of the blister radius a and the blister formation force P. The dimensions of the blisters (2a and ζ_0) are measured using images similar to those in Fig. 8.4. The results are listed in Table 8.1. Notably, at the high shaft motion rate of 10 mm/min, the adhesion energy of PRC (experimental curve b-1 in Fig. 8.5) is almost three times higher than that of PAN (experimental curve a-1 in Fig. 8.5). Because of the slight bending of the PET substrate during the bending tests, the extensions corresponding to the curves in Fig. 8.5 are slightly higher than those in Fig. 8.4. As shown in Figs. 8.4 and 8.7, in most of the cases the PET

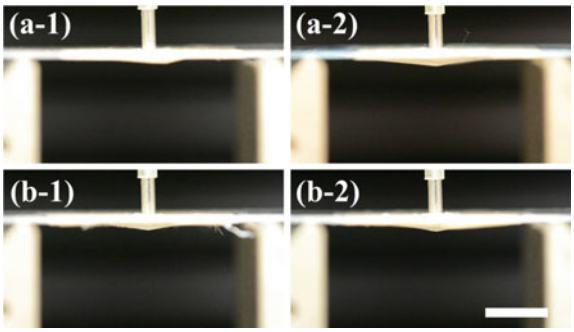

Fig. 8.7 Photographs of different stages of blister tests: (a-1) PAN1 without fatigue, (a-2) PAN2 with fatigue, (b-1) PRC1 without fatigue, (b-2) PRC2 with fatigue. Scale bar is 10 mm. Reprinted with permission from Lee et al. (2015)

Table 8.1 Adhesion energy T

Case in Fig. 8.5	Extension rate (mm/min)	Extension ζ_0 (mm)	a (mm)	P (N)	T (J/m^2 = N/m)
(a-1)	10	1.81	7.84	0.31578	0.7014
(a-2)	2	1.01	3.87	0.16691	0.7684
(a-3)	10	1.19	6.61	0.21218	0.5183
(b-1)	10	2.17	7.59	0.65736	2.0700
(b-2)	2	1.66	4.00	0.31542	1.8251
(b-3)	10	1.54	3.60	0.15276	0.7988

substrates do not bend at all in the blister tests. Because the same specimens should be used in the fatigue tests, the substrates must be flexible (as PET is) to undergo cyclic bending prior to blister tests, which excludes metal or ceramic substrates. Substrate bending occurs only in cases (a-1) and (b-1) in Fig. 8.4 and it is almost absent in the other cases. In cases (a-1) and (b-1), the extension values found from the Instron data (Fig. 8.5) are higher than the corresponding values measured from the images (Fig. 8.4) because of the substrate bending. For this reason, the extension value ζ_0 is determined in a manner minimizing the inaccuracy associated with substrate bending. As shown in Fig. 8.8a, the elevation at the blister center differs if it is measured from the base line corresponding to zero extension. To exclude the corresponding error in the measurement where substrate bending is observed, the end of the base line is set at the beginning of delamination (Fig. 8.8b). This practically excludes the possible inaccuracy associated with any substrate bending, because the extension is determined only by the real delamination of the NF mat from the substrate.

The adhesion energy is found using the measured blister geometry (the radius a) at the highest load P at the blister formation moment t^*.

For comparison, the results of the blister tests of the NF mats in Na et al. (2012) revealed the adhesion energy value of $0.206 \pm 0.026\,J/m^2$, significantly lower than

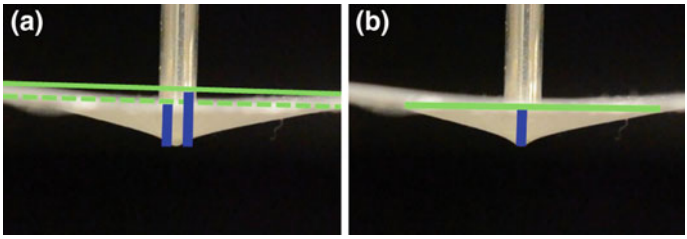

Fig. 8.8 Exclusion of the effect of the substrate bending (if any) on the measured extension value; blue line indicates extension; green solid and dashed lines indicate base lines established at beginning of experiment and beginning of delamination, respectively. Reprinted with permission from Lee et al. (2015)

Table 8.2 Cohesion energy T

Case in Fig. 8.6	Extension ζ_0 (mm)	a (mm)	P (N)	T ($J/m^2 = N/m$)
(a-1)	0.95	5.60	0.0566	0.2729
(a-2)	0.80	9.67	0.0236	0.0321
(b-1)	1.65	7.13	0.0696	0.3595
(b-2)	1.52	7.33	0.0876	0.3944

those shown in Table 8.1. This is despite the factor in Eq. (6.75) from Sect. 6.8, used in Na et al. (2012) and Wan and Mai (1995), being higher than that in Eq. (6.74) from the same chapter, used here. The difference is because Na et al. (2012) studied the adhesion of PVDF fibers on cardboard, rather than the material pair used in the present work.

In the cohesion-related experiments, as shown in Table 8.2 and Fig. 8.9, PAN and PRC specimens behave in diametrically opposed manner after prolonged bending fatigue. A significant decrease in the adhesion energy for the fatigued PAN specimen inevitably arises from delamination at the NF mat's interface with the PET substrate. Similarly, the cohesion between two PAN NF mats is also weakened by prolonged repeated bending, with no recovery from the damage sustained. Meanwhile, the fatigued PRC specimens containing DMS resin monomer and curing agent display an increase of approximately 10% in the measured cohesion energy. This implies that the healing agents are released from the NF cores during bending fatigue and polymerized, thus restoring and reinforcing the cohesion at the damaged interface.

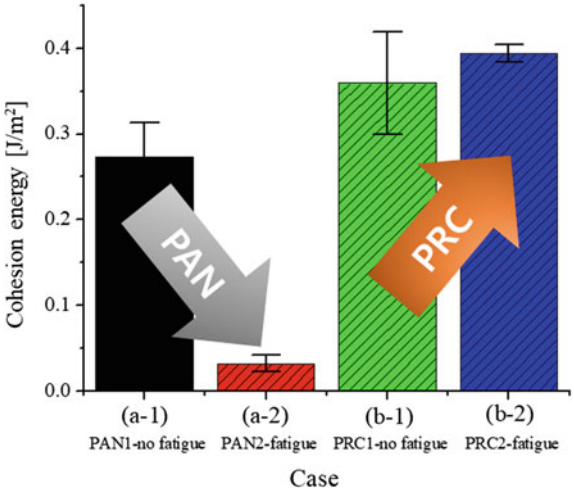

Fig. 8.9 Cohesion energies T. Reprinted with permission from Lee et al. (2015)

8.2 Blister Testing: Recovery of Adhesion or Cohesion in Composites with Solution-Blown PVDF/PEO/Epoxy/Hardener NFs

The DMS resin monomer and its curing agent considered in Sects. 7.1 and 8.1 comprise one of the most attractive available self-healing systems because of the chemical, mechanical, optical, and biocompatibility properties of PDMS. However, full curing and polymerization of PDMS requires 24–48 h at room temperature, and fully-cured PDMS is relatively soft and flexible. Therefore, it is not suitable for the applications requiring relatively fast response (shorter curing times) and sufficient rigidity of the solidified material (higher strength and stiffness).

Lee et al. (2016c) employed for the first time a commercial epoxy as a healing agent embedded in nano- and microfibers (NFs and MFs) formed using solution blowing (cf. Sects. 2.4, 7.2 and 7.3). The epoxy begins hardening rapidly (in ~5 min) after activation, and is fully cured in 1 h at room temperature. It provides a tensile strength reaching 30.33 MPa (4400 psi), as measured by the direct pulling of a test specimen from a substrate. For the study of self-healing systems, the two components of the epoxy resin monomer and hardener were encapsulated separately in the cores of NFs and MFs formed by the solution blowing of polyvinylidene difluoride (PVDF) using compressed air (Sect. 4.5). The self-healing properties of mats of these NFs and MFs were explored using the blister (adhesion/delamination) test preceded by periodic bending fatigue (for 1–9 h), as described in Sect. 8.1. The goal here is a fast-response (5–60 min) from self-healing materials for industrial applications, where they should be used to prevent delamination on ply surfaces, which are not exposed to environmental conditions. Specimens for the blister test were prepared similarly to those of Sect. 8.1.

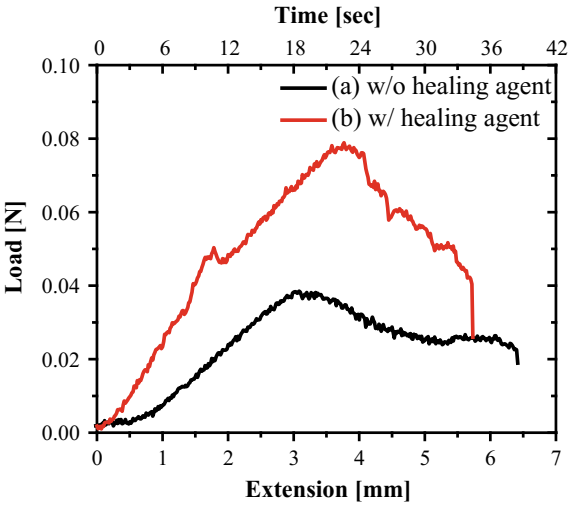

Fig. 8.10 Load–extension curves in blister tests quantifying specimen adhesion to the substrate. The specimens were finger-pressed to the substrate. Reprinted with permission from Lee et al. (2016c)

The adhesion tests of the fiber specimens on a PET substrate were conducted to confirm that the healing agents (the epoxy components) were encased in the fiber cores and to demonstrate the healing effect. For a control, monolithic PVDF fibers were formed without cores containing healing agents and also analyzed by blister tests. In these tests, the fiber mats without and with the epoxy components in the cores were placed onto flexible PET substrates and then pressed into place by hand. The adhesion energy associated with the detachment of these fiber mats from the substrate was measured by blister testing (cf. Sects. 6.8 and 8.1). The adhesion energies T found from the data (cf. Figs. 8.10 and 8.11) using Eq. (6.74) from Sect. 6.8 are $T = 0.307\ J/m^2$ (see Table 8.3) for the specimens containing the epoxy components in the fiber cores and $0.067\ J/m^2$ for the specimens without epoxy. The five-fold increase in the adhesion energy in the former case is caused by the release of the epoxy components from the cores upon the pressing of the fibers, thus bonding them to the substrate. This confirms the presence of the epoxy components in the fiber cores and their release under both pressure and bending.

For a more controlled method of adhering fiber specimens to the substrate, a metal roller was passed over the fiber mats on the substrates 10 times. Figures 8.12 and 8.13 show the data for these rolled specimens, revealing that the blister size and the load–extension dependence are significantly affected by the presence of the epoxy components in the fiber cores. The adhesion of the fiber specimens without epoxy components is deteriorated dramatically with fatigue. Specifically, after 1 h of bending fatigue (a-2), the adhesion energy T drops to approximately 40% of that in the pristine case (a-1) (cf. Table 8.4). For 9 h of of preceding bending (a-3), the

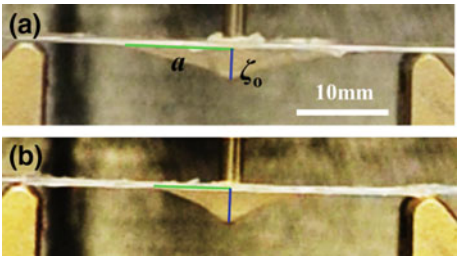

Fig. 8.11 Photographs of the blister test. The images correspond to the blister tests of the fiber mats in the following cases: **a** without healing agents **b** with healing agents in the fiber core. Reprinted with permission from Lee et al. (2016c)

Table 8.3 Adhesion energy T. The data corresponding to the blister tests is summarized in this table, with ζ_0 being the vertical extension at peak loading. Other parameters are defined as in Sect. 8.1, following Eq. (6.74) from Sect. 6.8. Rows (a) and (b) correspond to curves (a) and (b) in Fig. 8.10. Separate measurements revealed the Young's moduli of the fiber mats with either resin or hardener of 6.34 MPa or 1.85 MPa, respectively

Case	a (mm)	ζ_0 (mm)	P (N)	h (mm)	E (MPa)	T (J/m^2)
(a)	11.52	3.28	0.039	0.11	2.725	0.067
(b)	8.24	3.56	0.079	0.12	2.125	0.307

Table 8.4 Adhesion energy T. The table also summarizes all the parameters measured in the blister tests. The rows (a-1)-(a-3) and (b-1)-(b-3) correspond to the curves in Fig. 8.12, and are for specimens without and with epoxy components in the fiber cores, respectively

Case	a (mm)	ζ_0 (mm)	P (N)	h (mm)	E (MPa)	T (J/m^2)
(a-1)	10.31	3.63	0.037	0.09	2.725	0.071
(a-2)	10.06	1.65	0.018			0.028
(a-3)	13.81	1.52	0.019			0.021
(b-1)	1.63	2.52	0.300	0.08	2.125	15.354
(b-2)	1.69	2.87	0.316			15.575
(b-3)	2.06	2.28	0.189			3.735

adhesion energy is identical to that measured after 1 h, indicating that the main damage to the fiber mat and its adhesion to the substrate occur in this case during the first hour of bending fatigue.

For the specimens with epoxy components in the fiber cores, the adhesion energy of the non-fatigued specimens (b-1) is much higher than that of the non-fatigued specimens without epoxy components in the core (a-1). This result (with roller-pressing used) is similar to that with finger-pressing (cf. Fig. 8.10). However, for the specimens with epoxy components in the fiber cores, the adhesion energy remains unchanged after 1 h of bending (b-2), and drops to approximately 25% of the initial value after 9 h (b-3). The blister tests are conducted within several minutes of completion of either the 1 or 9 h of bending fatigue. It should be emphasized that the epoxy used sets in 5 min, which is comparable to the time between the bending

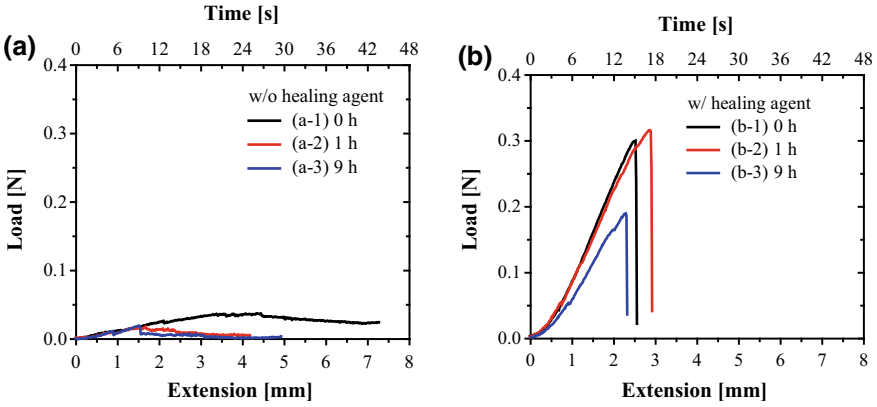

Fig. 8.12 Load–extension curves in blister tests quantifying specimen adhesion to the substrate: **a** without epoxy components and **b** with epoxy components in the fiber cores. All specimens were initially roller-pressed to the substrate (cf. Sect. 8.1). Curves marked as (-1) correspond to pristine (unfatigued) specimens, curves marked as (-2) correspond to specimens after 1 h of fatigue, and curves marked as (-3) correspond to specimens after 9 h of fatigue. Reprinted with permission from Lee et al. (2016c)

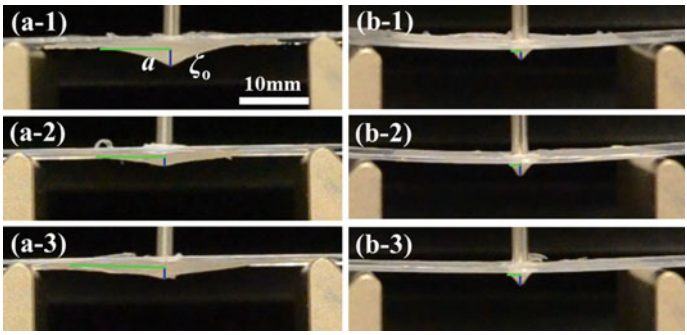

Fig. 8.13 Photographs of blister tests of specimens (a-#) without epoxy components and (b-#) with epoxy components in the fiber cores. All specimens were initially roller-pressed to the substrate. Fatigue levels (#) are as designated in Fig. 8.12. Reprinted with permission from Lee et al. (2016c)

fatigue and blister tests, and is thus sufficient for the curing of the damaged self-healing specimens. The adhesion between the substrate and the fiber mat may have recovered after 1 h of fatigue by self-healing, as shown in Fig. 8.12b although it is unclear whether sufficient specimen damage was caused by 1 h of bending fatigue to validate this conclusion. However, the data in Fig. 8.12b also shows that the specimen does not fully recover by self-healing from 9 h of fatigue in the allotted rest time.

For the cohesion experiments (i.e., testing the interfacial adhesion between two fiber mats instead that between a fiber mat and a substrate of different material), a layer of the fiber mat was attached to the substrate using dual-sided tape, another layer of a similar fiber mat was placed on it, and the fiber mat layers were pressed

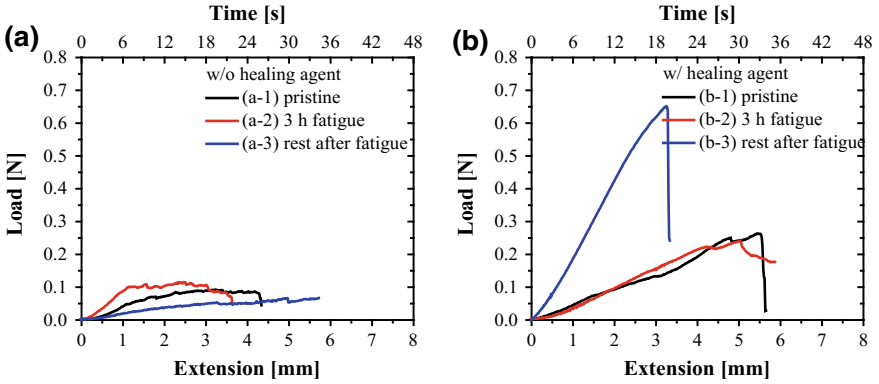

Fig. 8.14 Load–extension curves measured to quantify cohesion between fiber mats: **a** without epoxy components and **b** with epoxy components in the fiber cores. Specimens are roller-pressed. Curves marked as (-1) correspond to pristine specimens, (-2) indicate specimens after 3 h of bending fatigue with almost immediate testing, (-3) indicate specimens after 3 h of bending fatigue and 24 h of rest before testing. Reprinted with permission from Lee et al. (2016c)

Table 8.5 Cohesion energy T. The table summarizes all the parameters measured in the blister test. The rows (a-1)-(a-3) and (b-1)-(b-3) correspond to the curves in Fig. 8.14, indicating fibers without and with epoxy components in their cores and varying fatigue histories

Case	a (mm)	ζ_0 (mm)	P (N)	h (mm)	E (MPa)	T (J/m^2)
(a-1)	13.73	4.17	0.087	0.09	2.725	0.153
(a-2)	10.13	3.00	0.106			0.298
(a-3)	6.86	4.97	0.067			0.127
(b-1)	6.54	5.47	0.263	0.08	2.125	2.004
(b-2)	8.63	5.02	0.242			1.987
(b-3)	3.73	3.25	0.651			16.385

together with the roller. A blister test was then used to measure the cohesion energy, i.e., the energy required for the delamination of the upper and lower layers. The experiments and the results are shown in Figs. 8.14 and 8.15. The corresponding cohesion energies T listed in Table 8.5 reveal that for the fiber mats without epoxy components, the measured cohesion energies are relatively close for fatigue histories: for the pristine specimen (a-1), that tested immediately after 3 h of bending (a-2), and that tested 24 h after 3 h of bending (a-3). However, for the self-healing specimens containing epoxy components in the fiber cores, the pattern is different. For the pristine specimen (b-1) and the specimen tested after 3 h fatigue (b-2) the cohesion energies are similar, while for the specimen tested after 3 h followed by the 24-h rest time (b-3), it is increased by a factor of 8. This is attributed to the epoxy components released from the fiber cores during bending fatigue having sufficient time to react and solidify; this process not only heals the damaged interface, but also significantly reinforces it.

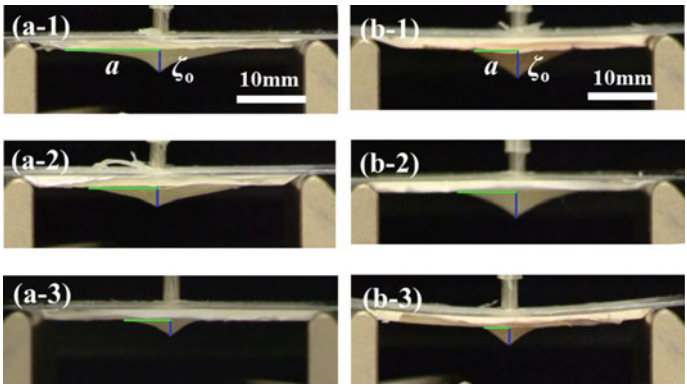

Fig. 8.15 Photographs of blister tests of specimens (a-#) without epoxy components and (b-#) with epoxy components in the fiber cores. All specimens are initially roller-pressed to the substrates. Fatigue levels (#) are as designated in Fig. 8.14. Reprinted with permission from Lee et al. (2016c)

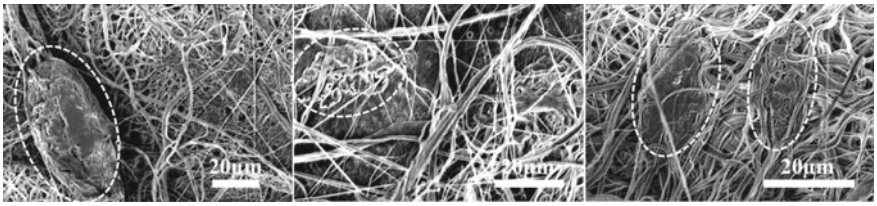

Fig. 8.16 Epoxy resin and hardener squeezed from the core-shell fibers after prolonged fatigue, blister testing, and subsequent pressing. Reprinted with permission from Lee et al. (2016c)

It should be emphasized that the self-healing fiber mats contain significant amounts of epoxy resin and hardener even after prolonged damage (bending fatigue) and subsequent blister testing, as demonstrated in Fig. 8.16, where the healing agents are squeezed from the fibers by pressing.

8.3 Double-Cantilever Beam and Bending Tests

8.3.1 Double-Cantilever Beam Test

The double-cantilever beam test introduced by Mostovoy et al. (1967) has been widely used for the evaluation of the self-healing characteristics of both microcapsule-based and vascular materials (see Fig. 8.17) (White et al. 2001; Brown et al. 2002; Kessler et al. 2003; Brown et al. 2004, 2005; Rule et al. 2005; Jones et al. 2007; Rule et al. 2007; Jin et al. 2011; Brown 2011; Hart et al. 2015; Vahedi et al. 2015). The healing agent employed in the tapered double-cantilever beam (TDCB)

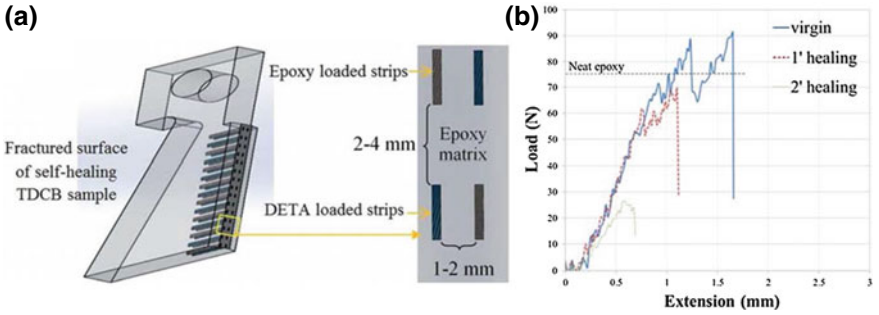

Fig. 8.17 **a** Schematic of fractured surface and spatial distribution of TDCB specimens. **b** Typical load–displacement curves for virgin and healed TDCB specimens at 50 °C. Reprinted with permission from Vahedi et al. (2015)

specimens fills an open delamination crack and cures within it, healing the crack. The load–displacement data were recorded using the delamination crack induced during the Mode I fracture test (see Fig. 6.3 in Sect. 6.2). The crack-healing efficiency is evaluated through fracture toughness tests performed on virgin and healed specimens. After the first fracture, the specimen is left to allow the crack to heal autonomously. Thus, the ratio of the fracture toughness of the healed specimen ($K_{Ic,healed}$) to that of the corresponding virgin one ($K_{Ic,virgin}$) is defined as the healing efficiency η. The crack-length-independent fracture toughness $K_{Ic} = \alpha P_c$, where α is a geometric factor determined experimentally and P_c is the critical fracture load (Irwin and Kies 1954). Thus, the quantitative healing efficiency is calculated as:

$$\eta = \frac{K_{Ic,healed}}{K_{Ic,virgin}} = \frac{P_{c,healed}}{P_{c,virgin}} \tag{8.2}$$

Similarly, the self-healing efficiencies of TDCB specimens with embedded epoxy-carrying fiber strips were investigated in Vahedi et al. (2015). The specimens, healed at room temperature demonstrated autonomous recover after the critical fracture loading during six repeated tests when neopentyl glycol diglycidyl ether (NGDGE) and diethylenetriamine (DETA) were used as the healing agents in a vascular system.

8.3.2 Bending Test

Three- and four-point bending tests are classical methods for measuring the stiffness of a material using beam-shaped specimens (Stafford and Smith 1968; Standard 1968; Standard 1970; Whitney et al. 1974; Stafford and Handley 1975). They are also suitable for testing multi-ply sandwich-like composite laminates containing relatively rigid epoxy (Papa and Corigliano 2001; Laffan et al. 2012; Li 2014). The test specimen for both methods has a uniform rectangular cross-section. In the three-

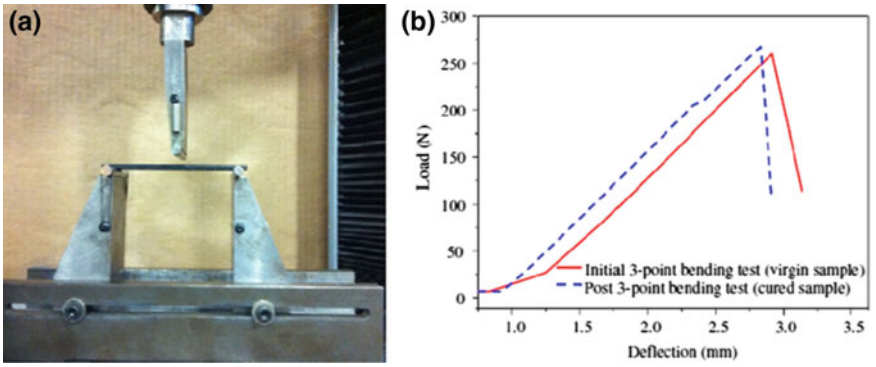

Fig. 8.18 **a** Three-point bending test setup (the span is 75 mm). **b** Comparative load–displacement curves of two typical hybrid multi-ply self-healing PMC specimens subjected to three-point bending loads. Reprinted with permission from Wu et al. (2013)

point bending test, the specimen is supported by two anvils, and a load is applied at the center between the two supports. The elastic modulus E_B is calculated using Eq. (8.3), which involves the measured yield load L and the corresponding measured deflection, δ:

$$E_B = \frac{mL^3}{4bd^3} \tag{8.3}$$

where b is the beam width, d is the beam depth, and m is the slope of the load–deflection curve corresponding to the early linear elastic region ($m = \Delta L/\Delta\delta$).

The recovery ratio η is evaluated based on the flexural strengths and the stiffness values measured in the corresponding pre- and post-damage tests, respectively (Trask and Bond 2006; Williams et al. 2007a; Wu and Yarin 2013; Fifo et al. 2014; Zanjani et al. 2015, 2017; Chen et al. 2013a):

$$\eta = \frac{E_{B,\text{healed}}}{E_{B,\text{initial}}} \tag{8.4}$$

According to Wu et al. (2013), the flexural stiffness of self-healing polymer-matrix composite (PMC) specimens decreased to 30–50% of the initial pre-damage value and then recovered to 70–100% of the initial value owing by self-healing (Fig. 8.18a). In Fifo et al. (2014) test specimens were damaged by bending but recovered their maximum stiffness almost completely, with the self-healing efficiency of approximately 97% (not shown here). Similarly, Wu et al. (2013) demonstrated the self-healing of fractured and delaminated multi-ply PMCs (see Fig. 8.18b).

8.4 Interfacial Toughening Due to NFs: Intrinsic Versus Extrinsic Toughening and Self-Healing Characterized by Impact Testing

Delamination at the ply surfaces in PMCs, as described in Sect. 6.6, can be potentially prevented by interfacial toughening. Several approaches have been proposed for this aim, including free-edge delamination-suppression designs, laminate stitching, the modification of matrix resins by incorporation with rigid or rubbery micro- or nanoparticles, fiber surface treatment, interleaving, and nanoreinforcing, as overviewed by Wu and Yarin (2013). The search for new interfacial toughening techniques with low costs, low weight penalties, and maintenance of the high specific properties of PMCs has continued with the incorporation of electrospun NFs as interfacial toughening elements. Such NFs provide promising nanoreinforcing materials for localized interfacial toughening of PMCs, in particular, because they can exhibit improved strengths and toughness compared to their MF counterparts (Zussman et al. 2006; Arinstein et al. 2007; Papkov et al. 2013). Kim and Reneker (1999) first used electrospun NFs as reinforcing elements in PMCs. Dzenis and Reneker (2001) patented delamination-resistant composites containing electrospun NFs for interfacial toughening at the ply interfaces. Wu (2003, 2009) conducted systematic studies on the interfacial toughening effect of electrospun NFs in aerospace-grade laminated PMCs. His results revealed unusual increases in the ultimate tensile strengths of such composite laminates. In addition, dynamic fracture tests based on the Hopkinson pressure bar revealed the toughening effect of electrospun NFs on the dynamic delamination toughness. Zhang et al. (2012) and Chen et al. (2013b) used electrospun NFs either as-spun or with carbonization after electrospinning, for interfacial toughening in PMCs. Recently, De Schoenmaker et al. (2013), van der Heijden et al. (2014), Daelemans et al. (2015), and Daelemans et al. (2016) employed electrospun NFs to develop damage-resistant composites toughened by NF bridging of interlaminar crossings. On the nanoscale level NFs can introduce additional energy dissipation routes in the matrix at crack initiation (intrinsic toughening; cf. Sect. 6.2), as well as span the banks of an emerging crack near its tip, thus acting as staplers or stitches (extrinsic toughening; Sects. 6.3 and Barenblatt 2014) and diminishing the crack's propensity to propagate (Fig. 8.19).

Unlike metal-based composites, which can absorb and dissipate impact energy by their inherent ductility (Norris et al. 2011c), PMCs are readily damaged by out-of-plane impacts. In particular, for fiber-reinforced polymer (FRP) composites, out-of-plane impacts can cause significant damage or reductions in mechanical performance because of the unique planar nature of FRP composites. FRP composites show high impact resistance along the fiber axis, but low resistance in the transversal direction. Nevertheless, typically no discernible evidence of damage arises on the composite surface, even after a significant mechanical degradation; this is called barely visible impact damage (BVID). Accordingly, self-repairing approaches, especially those based on vascular self-healing systems, have attracted great attention because not

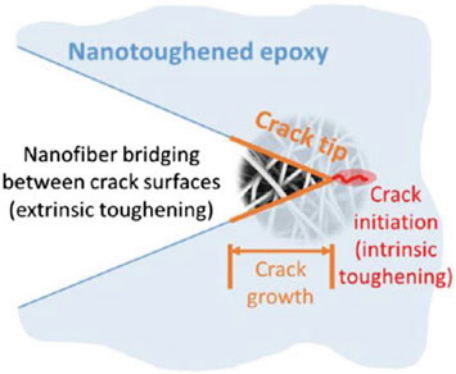

Fig. 8.19 Sketch of the intrinsic and extrinsic toughening mechanisms during crack growth and propagation by NF-incorporating composites. Reprinted with permission from Daelemans et al. (2016)

only can they autonomously repair BVID in FRP composites, but also the embedded fibers can facilitate additional mechanical reinforcement of such composites.

Dry (1996) first employed a microscopic hollow-tube-based self-healing technique to reinforce a polymeric matrix in a composite and conducted a low-velocity impact test that caused cracks throughout the composite body. The healing agents were released from the embedded hollow tubes, allowing self-repairing of the cracks. A low-velocity impact test at $\leq$10 m/s is preferable to a high-velocity impact test in the 300–2500 m/s range. This is because the low-velocity impact test can globally affect the entire composite, including cracks, whereas, under high-velocity impact only a localized penetrative crack is caused in the composite (Norris et al. 2013). Motuku et al. (1999) also conducted low-velocity impact tests on composites with embedded microtubes with the impact velocity in the 1.74–2.74 m/s range, having impact energies of 22–56 J. They parametrically studied the self-healing performance depending on the microtube type, number of tubes, spatial distribution of tubes, impact energy, and other variables.

On the other hand, Pang and Bond (2005a, b), Trask and Bond (2006), Trask et al. (2007), and Williams et al. (2007b) employed indentation tests on epoxy composites involving microscopic hollow-fiber-embedded plies. The indentation test is a pseudo-impact test similar to a low-velocity impact test, but it causes less damage to the tested specimens. First, Pang and Bond (2005a, b) performed indentation tests by applying the 1200-N compression to the composites (equivalent to impact energies of 0.5–0.6 J). The tests caused the fracture of the embedded hollow fibers, cracks, and delamination (cf. Fig. 8.20). Although many fractures in the composites were repaired by the embedded self-healing fibers, the healing efficiency was decreased from 93% to 55% (compared to the virgin flexural strength) as the aging time of the specimens increased from zero to nine weeks (Pang and Bond 2005b), which indicated that further studies were necessary to improve the effective service lifetimes of the self-healing composites. Norris et al. (2011a, b, 2012, 2013) also studied the self-healing performance of vascular networks of carbon fiber-reinforced polymer (CFRP) composites after low-velocity impact tests with 10 J impact energies.

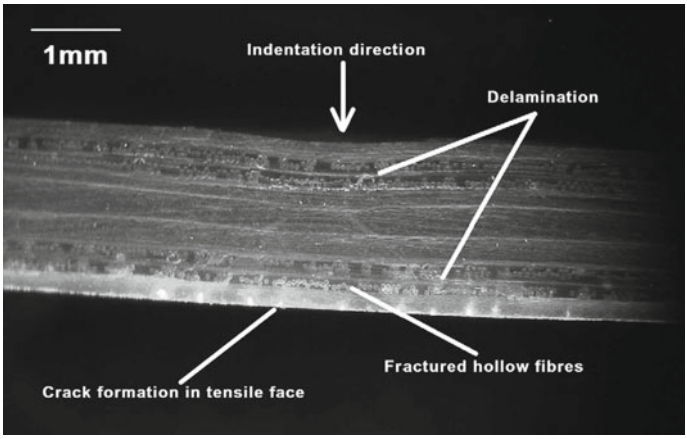

Fig. 8.20 Cross-sectional optical microscope image of the hollow-fiber-embedded composite after impact testing. Reprinted with permission from Pang and Bond (2005b)

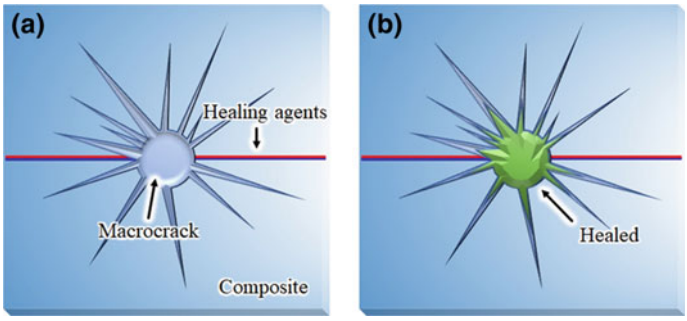

Fig. 8.21 Snapshots of a damaged macrocrack in the composite: **a** before filling and **b** after filling with self-healing agents

White et al. (2014) studied the self-healing performance for large-scale cracks in a microvascular channels at the impact energy of 6.26 J (Fig. 8.21). They showed that a macrocrack of 35 mm in diameter could be healed.

Trask and Bond (2006) studied the self-healing effect on the performance of composites, including self-healing sandwich-structured panels, after impact damage using epoxy-based two-part healing agents that were separately injected into microscopic hollow fibers. Furthermore, Trask et al. (2007) studied the self-healing effect of such fibers on CFRP composites. Both studies revealed that the flexural strengths after indentation tests with 2500 N of pseudo-impact force were significantly restored by self-healing, although the inclusion of the hollow fibers also weakened the initial strength of the composites by 14–16% (Trask and Bond 2006; Trask et al. 2007). Williams et al. (2007b) also conducted indentation tests on CFRP composites intended for aerospace applications. They conducted 1700-N or 2000-

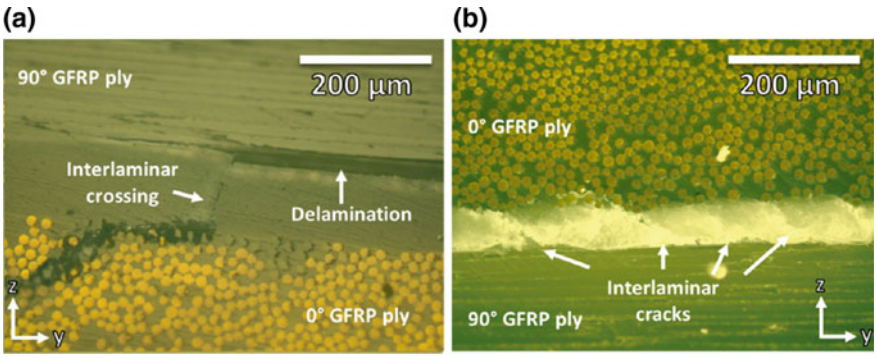

Fig. 8.22 Glass fiber-reinforced polymer (GFRP) composites. **a** The damage mechanisms resulting from the impact test reveal delamination with sporadic interlaminar crossings. **b** The additional damage mechanisms accompanying the impact test, with interlaminar cracks unrelated to delamination shown; cf. the sketch in Fig. 6.7 in Sect. 6.6. Reprinted with permission from Daelemans et al. (2016)

N pseudo-impacts on the composites. The uniformly distributed microscopic self-healing fibers in the composites did not induce weakness during the impact, whereas clusters of the fibers caused serious defects that facilitated crack propagation, including interlaminar crossing cracks. Although the interlaminar crossing fractures were healed by the embedded self-healing fibers, this study revealed that the distribution uniformity of the embedded self-healing fibers is significant in determining the crack path deviation.

In order to toughen the interlaminar structure of FRP composites, the inclusion of monolithic electrospun NFs was recently suggested and yielded decent results related to toughening against interlaminar fracture (Daelemans et al. 2016). The latter authors conducted low-velocity impact testing at the impact energy of 67 J. Their results are depicted in Figs. 8.22 and 8.23. These images show the damage mechanisms accompanying the impact testing of laminated composites and the reinforcement effects provided by electrospun NFs.

The laminates of Daelemans et al. (2016) did not include any self-healing function. However, they clearly revealed an additional potential benefit of self-healing NF mats. Because they are geometrically similar to ordinary NFs, self-healing NFs can also bridge interlaminar crossings, span crack tips, and prevent or deflect crack propagation. Moreover, the interfacial shear strength and the interlaminar fracture toughness of laminated PMCs are always degraded with aging. Therefore, self-healing NFs embedded at the ply surfaces can also diminish potential damage from the weakening of the interfacial toughness comparing to the ordinary electrospun fibers used thus far. Accordingly, self-healing core-shell vascular NF mats hold great potential for the interfacial toughening of PMCs.

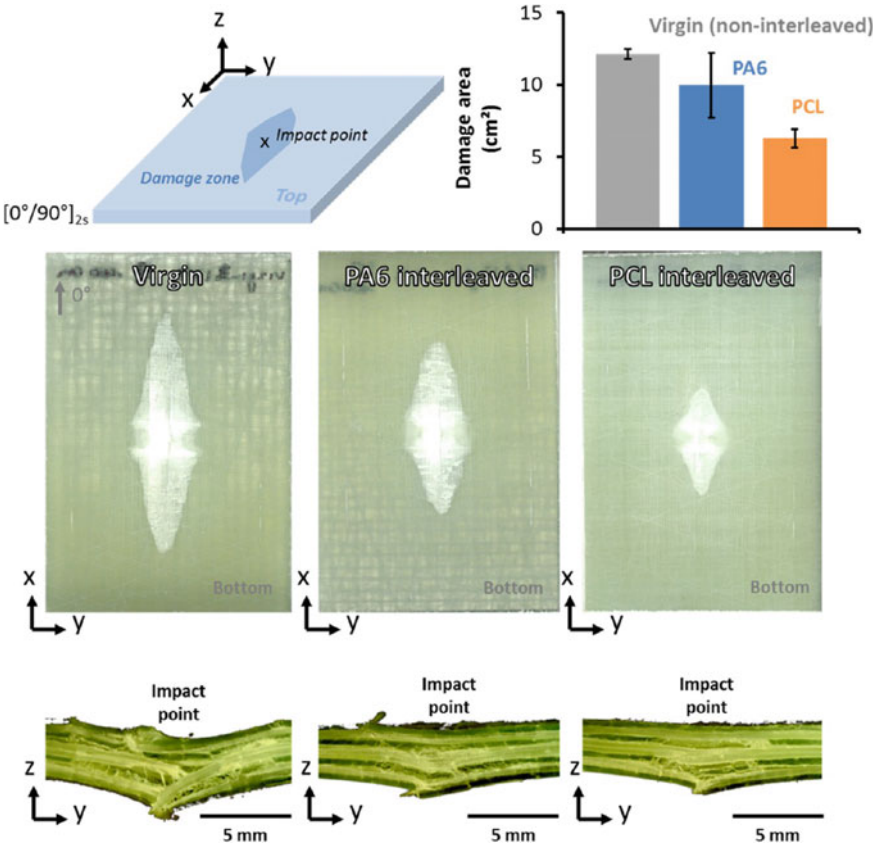

Fig. 8.23 Damage decrease because of the presence of polycaprolactone (PCL) NFs interleaved in composite laminates after impact testing. The damage area is decreased up to 50% for PCL-interleaved laminates (middle row, top view); bulging and the internal damage are also diminished (bottom row, side view). Reprinted with permission from Daelemans et al. (2016)

8.5 Cumulative Results on Mechanical Recovery of Self-Healing Vascular Materials

The results of multiple studies on the mechanical recovery of self-healing vascular materials after damage are summarized in Table 8.6. Over the last 17 years, different self-healing composites based on vascular systems using hollow fibers, tubing, channels left by pulled-out wires, core-shell NFs, etc., have been fabricated and their healing efficiencies have been evaluated. Various mechanical tests, including tensile testing, bending tests, compression testing, blister testing, double-cantilever beam tests, and impact testing have been employed to analyze these composites. In most of these studies, two-part epoxies have been used as the healing agent; the fracture toughness, flexural strength, crack propagation speed, and adhesion or cohe-

sion energy provided by these materials have been used as measures of successful self-healing.

Table 8.6 Mechanical recovery of self-healing vascular materials

Vascular type	Healing agents	Damage and mechanical test	Healing evaluation	Healing efficiency	Year	References
Hollow glass fiber	Two-part epoxy	Impact, compression tests	Compression strength	N/A	2001	Bleay et al. (2001)
Hollow glass fiber	Two-part epoxy	Indentation, four-point bending test	Flexural strength	97%	2005	Pang and Bond (2005a)
Hollow glass fiber	Two-part epoxy	Indentation, four-point bending test	Flexural strength	93%	2005	Pang and Bond (2005b)
Hollow glass fiber	Two-part epoxy	Indentation, three-point bending test	Flexural strength	87%	2006, 2007	Trask and Bond (2006), Trask et al. (2007)
Hollow glass fiber	Two-part epoxy	Impact, four-point bending test	Flexural strength	97%	2007	Williams et al. (2007b)
Polyvinyl chloride (PVC) tubing	Two-part epoxy	Four-point bending test	Flexural strength	~100%	2007	Williams et al. (2007a)
Direct write method	DCPD-Grubbs' catalyst	Four-point bending test	Fracture toughness	33–70% (7 cycles)	2007	Toohey et al. (2007)
Molding	Two-part epoxy	Impact test	Impact energy	65%	2007	Hayes et al. (2007)
Silicone tubing	Two-part epoxy	Impact, edgewise compression tests	Skin compressive strength	115%	2008	Williams et al. (2008)

(continued)

Table 8.6 (continued)

Vascular type	Healing agents	Damage and mechanical test	Healing evaluation	Healing efficiency	Year	References
Hollow glass fiber	Two-part epoxy	Impact, four-point bending test	Flexural strength	95%	2009	Williams et al. (2009)
Direct write method	DCPD-Grubbs' catalyst	Four-point bending test	Fracture toughness	38% (7 cycles)	2009	Toohey et al. (2009b)
Direct write assembly	Two-part epoxy	Four-point bending test	Fracture toughness	89% (23 cycles)	2009	Toohey et al. (2009a)
Direct write assembly	Two-part epoxy	Four-point bending test	Fracture toughness	~50% (30 cycles)	2009	Hansen et al. (2009)
Direct write assembly	Two-part epoxy	Mode I fracture test	Fracture toughness	30 ~ 86% (13 cycles)	2010	Hamilton et al. (2010)
Wire (removed)	Two-part epoxy	Impact, compression test	Compression strength	99%	2011	Norris et al. 2011c)
Wire (removed)	Two-part epoxy	Impact, compression test	Compression strength	~100%	2011	Norris et al. 2011a)
Wire (removed)	Two-part epoxy	Mode I/II fracture test	Fracture toughness	260%/180%	2011	Norris et al. 2011b)
Wire (removed)	Two-part epoxy	Impact, four-point bending, edgewise compression tests	Fracture toughness	39%	2013	Chen et al. (2013a)
Casting	Shape memory polymer fiber (SMPF)	Tensile test	Fracture toughness	~100% (7 cycles)	2013	Li et al. (2013)

(continued)

Table 8.6 (continued)

Vascular type	Healing agents	Damage and mechanical test	Healing evaluation	Healing efficiency	Year	References
Hollow glass fiber	Two-part epoxy	Impact test	Impact energy	87%	2014	Zainuddin et al. (2014)
Hollow glass fiber	Two-part epoxy	Impact, three-point bending test	Flexural strength	178%	2014	Kling and Czigany (2014)
Vaporization of sacrificial components	Two-part epoxy	Tensile, acoustic emissions test	Fracture toughness, acoustic emission	98%	2014	Coppola et al. (2014)
Vaporization of sacrificial components	Two-part epoxy	Mode I fracture test	Fracture toughness	125%	2014	Patrick et al. (2014)
Cell (channel) casting	Shape-conforming dynamic gel	Impact test	Impact energy	62%	2014	White et al. (2014)
Casting	Thermo-plastic healing agent	Three-point bending test	Fracture toughness	>50% (10 cycles)	2015	Zhang and Li (2015)
Co-electrospinning	PDMS	Tensile test	Young's modulus	125–140% (4 cycles)	2015	Lee et al. (2015)
Co-electrospinning	PDMS	Blister test	Adhesion energy	110%	2015	An et al. (2015)
Tri-axial electrospinning	DCPD	Three-point bending test	Fracture toughness	96%	2015	Zanjani et al. (2015)
Coaxial solution blowing	Two-part epoxy	Blister test	Adhesion energy	318%	2016	Lee et al. (2016c)
Coaxial solution blowing	Two-part epoxy	Tensile test	Crack propagation	N/A	2016	Lee et al. (2016b)

(continued)

Table 8.6 (continued)

Vascular type	Healing agents	Damage and mechanical test	Healing evaluation	Healing efficiency	Year	References
Coaxial solution blowing	Two-part epoxy	Tensile test	Young's modulus	171%	2016	Lee et al. (2016a)
Tri-axial electrospinning	Two-part epoxy	Three-point bending, tensile, acoustic emission test	Fracture toughness, acoustic emission, clustering patterns	>86–89% (4–9 cycles)	2017	Zanjani et al. (2017)
Co-electrospinning	PDMS	Tensile test	Crack propagation speed	11% (delay)	2017	Lee et al. (2017a)
Microchannel	PDMS	Tensile test	Crack propagation	N/A	2017	Lee et al. (2017b)

8.6 Self-Healing of Three-Dimensional Materials

The mechanical behavior of three-dimensional self-healing materials, as described in Sect. 4.7, was studied in Lee et al. (2018). The 3D PDMS block specimens with sizes of 15 mm × 7 mm × 20 mm (w × d×l, see Fig. 8.24d) were completely cut into two parts by a razor blade and then re-attached manually. Then, the specimens were left for 2 days under atmospheric conditions without any further treatment. In 2 days, the specimens were analyzed by tensile testing under stretching normal to the cut to evaluate the cohesion energy that emerged by self-healing during the 2 days (Fig. 8.24). Two pins (d = 3.15 mm) were placed through the punched holes in the middles of the upper and lower bodies of a given specimen. Each pin was attached to a plate, which was held by the upper and lower grips of the Instron 5942 system with a 100-N load cell. As the tensile machine stretched the specimen, the force required to disconnect the self-healed scar in the specimen was recorded with the corresponding extension. This force, essentially, the adhesion force, was measured for all specimens with and without embedded self-healing core-shell fibers. If the self-healing fibers worked properly at the cut interface (i.e., released the DMS resin monomer and curing agent stored in the fiber cores in sufficient amounts), a non-zero adhesion force (and thus adhesion energy) is measured in the test.

To observe the inner structures of the 3D blocks with the embedded fibers after cutting, a cross-sectional SEM image of the 3D block is obtained by focused ion

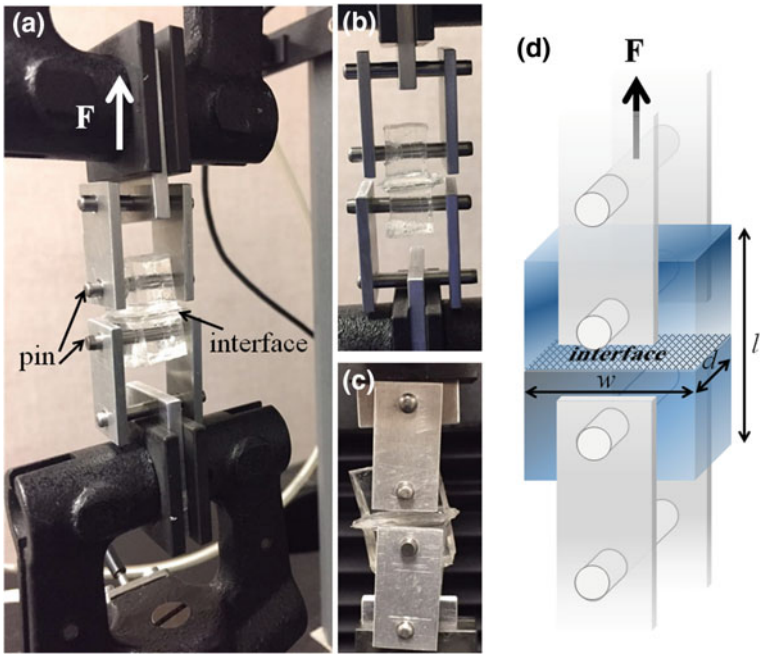

Fig. 8.24 **a** Setup used to measure interfacial adhesion at the self-healed surface. **b** Side view. **c** Front view. **d** Schematic. Reprinted with permission from Lee et al. (2018)

beam (FIB) milling, as shown in Fig. 8.25a. Although it seems that the ends of the embedded fibers are damaged (melted) by the high thermal energy involved in the FIB process, traces of the embedded fibers are clearly visible. The reinforcing fibers embedded in the composite material were also observed along the fracture surface in the literature; cf. Molnar et al. (2014). If a matrix material is brittle, individual fibers can be seen at the fracture surface. However, at the clean-cut surfaces of elastic matrix materials, as in the present case, only dots indicating the fibers are visible in the SEM image (cf. Fig. 8.25a). On the other hand, the embedded fibers and epoxy drops released by the mechanical damage are clearly seen in the optical microscope images (Fig. 8.25b, c).

Tensile tests for specimens of each kind are repeated thrice to evaluate repeatability. The weakest specimen was not used in further measurements: the results reported here are obtained for the two stronger specimens. The complete measured load–extension curves are shown in Fig. 8.26a. The areas under the curves yield the work of detaching the healed halves of the specimens from each other. Under the assumption that viscous losses during the stretching process, as well as the elastic energy stored in the specimen by the rupture moment, are negligibly small, this calculated work implies the cohesion energy. The interfacial area is $15\,\text{mm} \times 7\,\text{mm} = 1.05 \times 10^{-4}\text{m}^2$. Using this value and the measured detachment work, the cohesion energy values displayed in Fig. 8.26b are obtained. It is

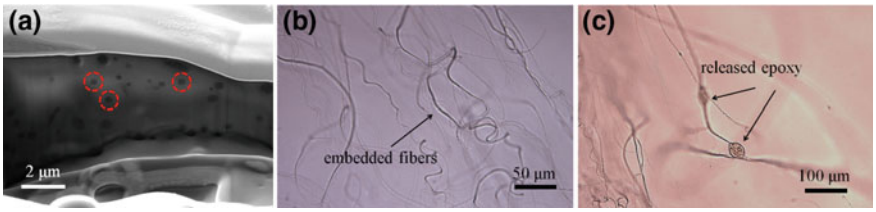

Fig. 8.25 **a** Interior SEM image of the FIB-treated 3D block specimen. Several cut edges of the embedded fibers with self-healing materials are encircled by dashed red circles. Magnification: 22600 × . **b** The optical microscope image of the undamaged embedded fibers. Magnification: 200 × . **c** The optical microscope images of the released epoxy in 3D block specimen after mechanical damage. Magnification: 100 × . Reprinted with permission from Lee et al. (2018)

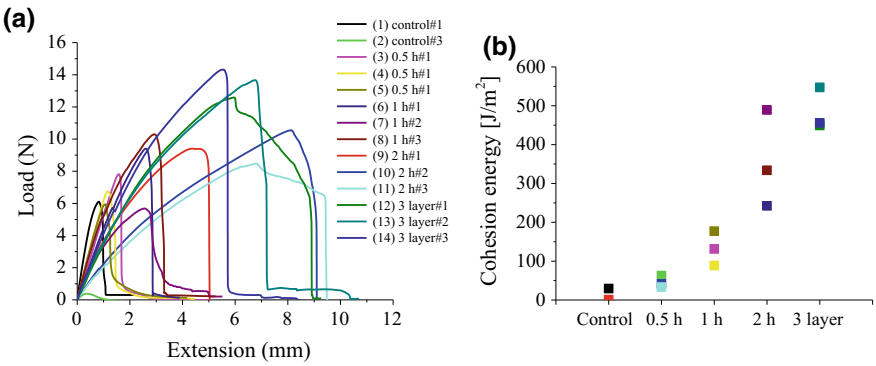

Fig. 8.26 **a** Load–extension curve. **b** Cohesion energies. In both panels the following data is presented: Control: a composite specimen embedded with the ordinary non-self-healing fibers; a composite specimen with the embedded self-healing fibers deposited for 0.5, 1, and 2 h; a three-layer composite specimen with the embedded self-healing fibers with total deposition time of 1.5 h. Each layer was deposited for 0.5 h upon a partially cured PDMS bath after 6 h of curing time. In panel (**a**), - # is the case number. In panels **a** and **b**, identical colors correspond to the same set of data. Reprinted with permission from Lee et al. (2018)

noteworthy that the case with three layers of the embedded self-healing fibers (cf. Sect. 4.7.1 in Sect. 4.7) reveals the highest cohesion energy. This means that not only the number of the embedded fibers, but also the distribution of the fibers in the bulk affect the healing efficiency. Compared to the ordinary specimens with 2 h of fiber deposition, the three-layer specimen may even have fewer fibers because of its shorter deposition time of 1.5 h, despite being more effective from a self-healing perspective because of its better fiber distribution. In addition, the cohesion energies on the order of 100 J/m^2 in Fig. 8.26b are much higher than that of approximately 16 J/m^2 measured for the nanotextured self-healing composites (cf. Table 8.5) or that of approximately 0.4 J/m^2 measured for the self-healing NF mats (cf. Table 8.2 and Fig. 8.9).

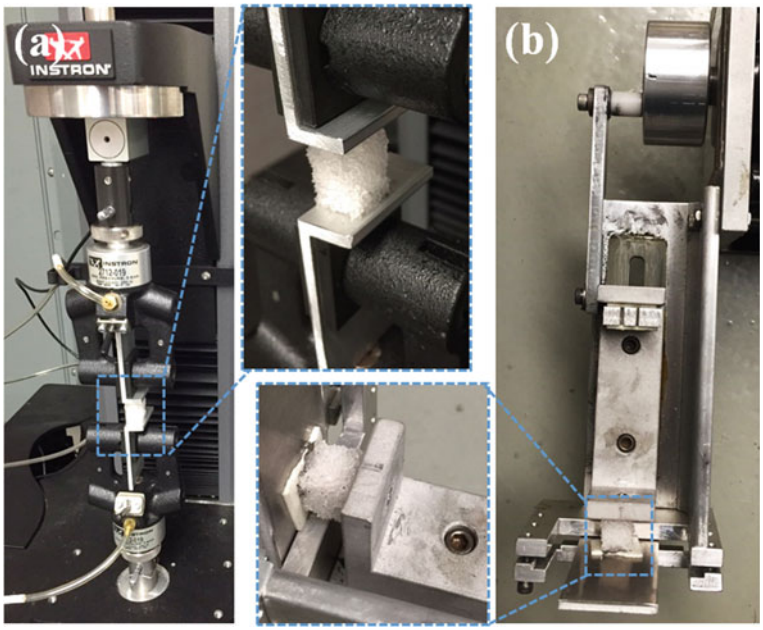

Fig. 8.27 **a** Setup for compression test. **b** Cyclic compression setup. Reprinted with permission from Lee et al. (2018)

In addition, three different types of the three-dimensional self-healing sponges of pure PDMS, PDMS–PAN, and PDMS–PRC, as described in Sect. 4.7.2 in Sect. 4.7, were cut into specimens with dimensions of 10 mm × 10 mm × 15 mm (w × d× h) and then subjected to compression testing to characterize their the self-healing ability (see Fig. 8.27). The strain–stress curves for the compression tests are obtained with up to 60% compression at the compression rate of 10 mm/min using an Instron 5942 machine (Fig. 8.27a). For the fatigue tests, similar specimens are cyclically compressed 3600 times to the strain of $\varepsilon = 60\%$ at the frequency of $f = 1$ Hz (Fig. 8.27b). In addition to the cyclic compression fatigue, the cyclic shear fatigue testing of the PDMS–PRC sponge is conducted 3600 times at the frequency of $f = 1$ Hz using the shear fatigue setup shown in Fig. 8.28. The top and bottom surfaces of the sponge specimen are held by the top and bottom plates, respectively, while the top plate moved in reciprocating motion resulting in the maximum shear strain of $\gamma \sim 50\%$. This caused a moderate shear fatigue to the sponge specimen in 1 h.

The internal sponge structure is shown in Fig. 4.34 in Sect. 4.7. The pure PDMS sponge and PAN/PRC fiber-reinforced PDMS sponges are compressed to the compressive strain of 60%. The corresponding stress–strain curves are shown in Fig. 8.29a. The presences of PAN and PRC fibers embedded in the PDMS matrices weaken the composites. The stress–strain curves in compression are measured using

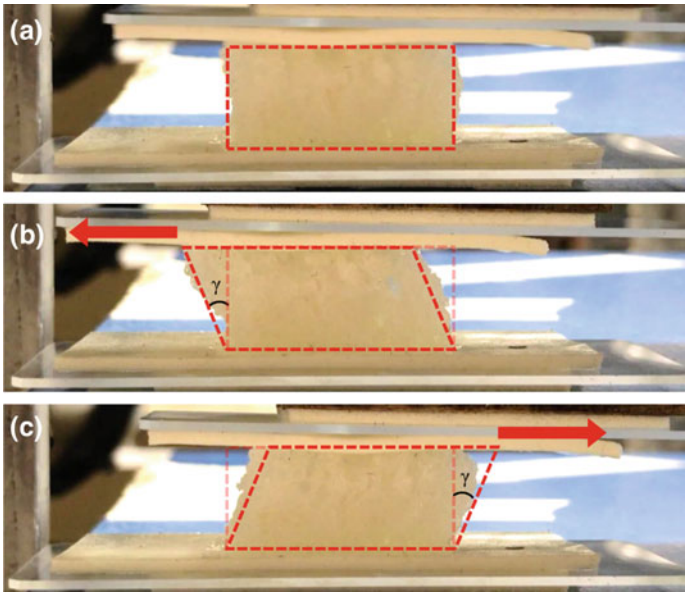

Fig. 8.28 Setup used for cyclic shearing fatigue test

(i) a pristine with no preceding fatigue, (ii) an identical specimen after the repeated compressive fatigue testing for 1 h, or (iii) using the specimens left for 2 days after fatigue testing. As shown in Fig. 8.29b, the rubber-like pure PDMS matrix material partially recovers its mechanical properties after a certain level of damage in the compressive fatigue test without the interference of self-healing NFs. The σ/σ_0 value of 42.4% is measured at the compressive strain $\varepsilon = 60.5\%$ in Fig. 8.29e, where σ is the compressive stress revealed by the damaged and "restored" material, and σ_0 is the stress from the undamaged specimen. The PDMS–PAN sponge also partially recovers its mechanical properties (the ratio σ/σ_0 is increased from 80.4 to 86.5% at the strain $\varepsilon = 60.5\%$; cf. Fig. 8.29e). On the other hand, the PDMS–PRC sponge containing self-healing NFs shows the greatest recovery of mechanical properties, with the ratio σ/σ_0 increasing from 90.5 to 106.4% at the strain $\varepsilon = 60.5\%$, even surpassing its original properties, as shown in Fig. 8.29e.

The mechanical behavior of sponge specimens in compression was also tested after they underwent the preceding cyclic shearing fatigue. As shown in Fig. 8.29f, the PDMS–PRC sponge specimens show the highest recovery of the mechanical properties in compression, despite damage from the preceding cyclic shearing fatigue test. Namely, the ratio σ/σ_0 is increased from 96.8 to 105.5% at the strain $\varepsilon = 60.5\%$.

In other three-dimensional self-healing bulky materials described in the literature (Toohey et al. 2007; Fang et al. 2013), the vascular structures containing healing agents were formed using hollow tubing or sacrificial fibers (e.g., glass fibers), fugitive inks, and other methods (cf. Sects. 1.1 and 1.4). The healing efficiencies in these studies were 70–80% based on the recovery of mechanical properties in tensile

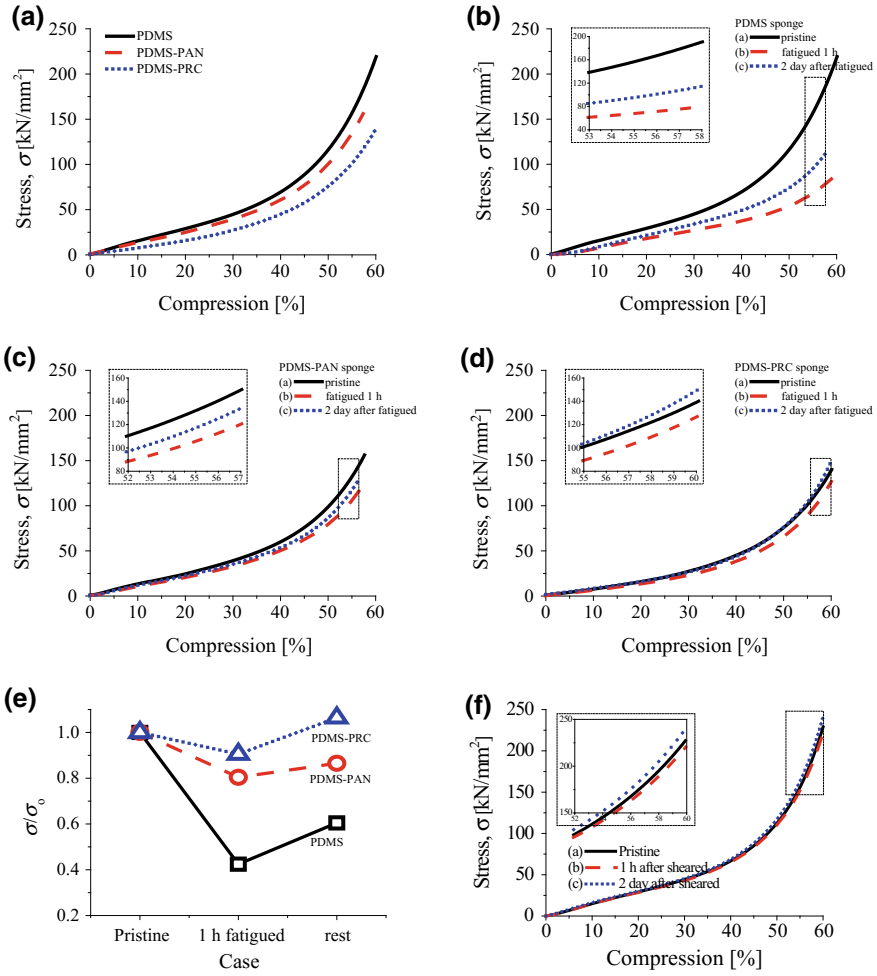

Fig. 8.29 Compression testing. **a** Pristine sponges. **b** Pure PDMS sponge (10.87 mm × 10.63 mm × 16.18 mm). **c** PDMS–PAN sponge (10.11 mm × 10.27 mm × 16.57 mm) without self-healing materials. **d** PDMS–PRC sponge (10.06 mm × 9.60 mm × 15.08 mm), with self-healing materials. **e** Compressive stress (σ) measured in damaged material versus the compressive stress (σ_0) in the same undamaged material, at the compressive strain $\varepsilon = 60.5\%$. (f) Stress–strain curves in compression of specimens after shearing fatigue compared to the pristine specimen. Reprinted with permission from Lee et al. (2018)

or bending tests. In comparison, Fig. 8.29e reveals approximately 85–100% recovery observed for the self-healing nanotextured sponges in compression testing after cyclic compressive fatigue testing; Fig. 8.29f demonstrates nearly 100% recovery after a cyclic shearing text.

References

An S, Liou M, Song KY, Jo HS, Lee MW, Al-Deyab SS, Yarin AL, Yoon SS (2015) Highly flexible transparent self-healing composite based on electrospun core–shell nanofibers produced by coaxial electrospinning for anti-corrosion and electrical insulation. Nanoscale 7:17778–17785

Arinstein A, Burman M, Gendelman O, Zussman E (2007) Effect of supramolecular structure on polymer nanofibre elasticity. Nat Nanotechnology 2:59–62

Ballarin FM, Blackledge TA, Davis NLC, Frontini PM, Abraham GA, Wong S-C (2013) Effect of topology on the adhesive forces between electrospun polymer fibers using a T-peel test. Polym Eng Sci 53:2219–2227

Barenblatt GI (2014) Flow, deformation and fracture. Cambridge Univ. Press, Cambridge

Bleay SM, Loader CB, Hawyes VJ, Humberstone L, Curtis PT (2001) A smart repair system for polymer matrix composites. Compos A 32:1767–1776

Brown EN (2011) Use of the tapered double-cantilever beam geometry for fracture toughness measurements and its application to the quantification of self-healing. JStA 46:167–186

Brown EN, Sottos NR, White SR (2002) Fracture testing of a self-healing polymer composite. ExM 42:372–379

Brown EN, White SR, Sottos NR (2004) Microcapsule induced toughening in a self-healing polymer composite. J Mater Sci 39:1703–1710

Brown EN, White SR, Sottos NR (2005) Retardation and repair of fatigue cracks in a microcapsule toughened epoxy composite – Part I: manual infiltration. Compos Sci Technol 65:2466–2473

Chen C, Peters K, Li Y (2013a) Self-healing sandwich structures incorporating an interfacial layer with vascular network. SMaS 22:025031

Chen Q, Zhao Y, Zhou Z, Rahman A, Wu X-F, Wu W, Xu T, Fong H (2013b) Fabrication and mechanical properties of hybrid multi-scale epoxy composites reinforced with conventional carbon fiber fabrics surface attached with electrospun carbon nanofiber mats. Compos B 44:1–7

Coppola AM, Thakre PR, Sottos NR, White SR (2014) Tensile properties and damage evolution in vascular 3D woven glass/epoxy composites. Compos A 59:9–17

Daelemans L, van der Heijden S, De Baere I, Rahier H, Van Paepegem W, De Clerck K (2015) Nanofibre bridging as a toughening mechanism in carbon/epoxy composite laminates interleaved with electrospun polyamide nanofibrous veils. Compos Sci Technol 117:244–256

Daelemans L, van der Heijden S, De Baere I, Rahier H, Van Paepegem W, De Clerck K (2016) Damage-resistant composites using electrospun nanofibers: a multiscale analysis of the toughening mechanisms. ACS Appl Mater Interfaces 8:11806–11818

Derjaguin BV, Muller VM, Toporov YP (1975) Effect of contact deformations on the adhesion of particles. J Colloid Interface Sci 53:314–326

De Schoenmaker B, Van der Heijden S, De Baere I, Van Paepegem W, De Clerck K (2013) Effect of electrospun polyamide 6 nanofibres on the mechanical properties of a glass fibre/epoxy composite. Polym Testing 32:1495–1501

Dry C (1996) Procedures developed for self-repair of polymer matrix composite materials. Compos Struct 35:263–269

Dzenis YA, Reneker DH (2001) Delamination resistant composites prepared by small diameter fiber reinforcement at ply interfaces. U.S. Patent 6265333

Fang Y, Wang C-F, Zhang Z-H, Shao H, Chen S (2013) Robust self-healing hydrogels assisted by cross-linked nanofiber networks. Scientific Reports 3:2811

Fifo O, Ryan K, Basu B (2014) Glass fibre polyester composite with in vivo vascular channel for use in self-healing. SMaS 23:095017
Hamilton AR, Sottos NR, White SR (2011) Pressurized vascular systems for self-healing materials. J R Soc Interface 2011:1–9
Hansen CJ, Wu W, Toohey KS, Sottos NR, White SR, Lewis JA (2009) Self-healing materials with interpenetrating microvascular networks. Adv Mater 21:4143–4147
Hart KR, Sottos NR, White SR (2015) Repeatable self-healing of an epoxy matrix using imidazole initiated polymerization. Polymer 67:174–184
Hayes SA, Zhang W, Branthwaite M, Jones FR (2007) Self-healing of damage in fibre-reinforced polymer-matrix composites. J R Soc Interface 4:381–387
Hutchinson JW, Suo Z (1992) Mixed mode cracking in layered materials. Adv Appl Mech 29:63–191
Irwin GR, Kies JA (1954) Critical energy rate analysis of fracture strength. American Welding Society Journal 33:193–198
Jin H, Miller GM, Sottos NR, White SR (2011) Fracture and fatigue response of a self-healing epoxy adhesive. Polymer 52:1628–1634
Jones AS, Rule JD, Moore JS, Sottos NR, White SR (2007) Life extension of self-healing polymers with rapidly growing fatigue cracks. J R Soc Interface 4:395–403
Kessler MR, Sottos NR, White SR (2003) Self-healing structural composite materials. Compos A 34:743–753
Kim JS, Reneker DH (1999) Mechanical properties of composites using ultrafine electrospun fibers. Polym Compos 20:124–131
Kling S, Czigany T (2014) Damage detection and self-repair in hollow glass fiber fabric-reinforced epoxy composites via fiber filling. Compos Sci Technol 99:82–88
Laffan MJ, Pinho ST, Robinson P, McMillan AJ (2012) Translaminar fracture toughness testing of composites: a review. Polym Testing 31:481–489
Lee MW, An S, Jo HS, Yoon SS, Yarin AL (2015) Self-healing nanofiber-reinforced polymer composites: 2. Delamination/debonding, and adhesive and cohesive properties. ACS Appl Mater Interfaces 7:19555–19561
Lee MW, An S, Kim YI, Yoon SS, Yarin AL (2018) Self-healing three-dimensional bulk materials based on core-shell nanofibers. Chem Eng J 334:1093–1100
Lee MW, Sett S, An S, Yoon SS, Yarin AL (2017a) Self-healing nano-textured vascular-like materials: Mode I crack propagation. ACS Appl Mater Interfaces 9:27223–27231
Lee MW, Sett S, Yoon SS, Yarin AL (2016a) Self-healing of nanofiber-based composites in the course of stretching. Polymer 103:180–188
Lee MW, Sett S, Yoon SS, Yarin AL (2016b) Fatigue of self-healing nanofiber-based composites: static test and subcritical crack propagation. ACS Appl Mater Interfaces 8:18462–18470
Lee MW, Yoon SS, Yarin AL (2016c) Solution-blown core–shell self-healing nano- and microfibers. ACS Appl Mater Interfaces 8:4955–4962
Lee MW, Yoon SS, Yarin AL (2017b) Release of self-healing agents in a material: What happens next? ACS Appl Mater Interfaces 9:17449–17455
Li AAW (2014) An experimental investigation on the three-point bending behavior of composite laminate. IOP Conf Ser Mater Sci Eng 62:012016
Li G, Ajisafe O, Meng H (2013) Effect of strain hardening of shape memory polymer fibers on healing efficiency of thermosetting polymer composites. Polymer 54:920–928
Malyshev BM, Salganik RL (1965) The strength of adhesive joints using the theory of cracks. Int J Fract Mech 1:114–128
Molnar K, Kostakova E, Meszaros L (2014) The effect of needleless electrospun nanofibrous interleaves on mechanical properties of carbon fabrics/epoxy laminates. Express Polym Lett 8:62–72
Mostovoy S, Crosley PB, Ripling EJ (1967) Use of crack-line-loaded specimens for measuring planestrain fracture toughness. J Mater 2:661–681
Motuku M, Vaidya UK, Janowski GM (1999) Parametric studies on self-repairing approaches for resin infused composites subjected to low velocity impact. Smart Mater Struct 8:623–638

Na H, Chen P, Wan K-T, Wong S-C, Li Q, Ma Z (2012) Measurement of adhesion work of electrospun polymer membrane by shaft-loaded blister test. Langmuir 28:6677–6683
Najem JF, Wong S-C, Ji G (2014) Shear adhesion strength of aligned electrospun nanofibers. Langmuir 30:10410–10418
Norris CJ, Bond IP, Trask RS (2011a) The role of embedded bioinspired vasculature on damage formation in self-healing carbon fibre reinforced composites. Compos A 42:639–648
Norris CJ, Bond IP, Trask RS (2011b) Interactions between propagating cracks and bioinspired self-healing vascules embedded in glass fibre reinforced composites. Compos Sci Technol 71:847–853
Norris CJ, Bond IP, Trask RS (2013) Healing of low-velocity impact damage in vascularized composites. Compos A 44:78–85
Norris CJ, Meadway GJ, O'Sullivan MJ, Bond IP, Trask RS (2011c) Self-healing fibre reinforced composites via a bioinspired vasculature. Adv Funct Mater 21:3624–3633
Norris CJ, White JAP, McCombe G, Chatterjee P, Bond IP, Trask RS (2012) Autonomous stimulus triggered self-healing in smart structural composites. Smart Mater Struct 21:094027
Obreimoff JW (1930) The splitting strength of mica. Proc R Soc A 127:290–297
Pang JWC, Bond IP (2005a) 'Bleeding composites'—damage detection and self-repair using a biomimetic approach. Compos A 36:183–188
Pang JWC, Bond IP (2005b) A hollow fibre reinforced polymer composite encompassing self-healing and enhanced damage visibility. Compos Sci Technol 65:1791–1799
Papa E, Corigliano A (2001) Mechanical behaviour of a syntactic foam/glass fibre composite sandwich: experimental results. Struct Eng Mech 12:169–188
Papkov D, Zou Y, Andalib MN, Goponenko A, Cheng SZ, Dzenis YA (2013) Simultaneously strong and tough ultrafine continuous nanofibers. ACS Nano 7:3324–3331
Patrick JF, Hart KR, Krull BP, Diesendruck CE, Moore JS, White SR, Sottos NR (2014) Continuous self-healing life cycle in vascularized structural composites. Adv Mater 26:4302–4308
Rule JD, Brown EN, Sottos NR, White SR, Moore JS (2005) Wax-protected catalyst microspheres for efficient self-healing materials. Adv Mater 17:205–208
Rule JD, Sottos NR, White SR (2007) Effect of microcapsule size on the performance of self-healing polymers. Polymer 48:3520–3529
Sett S, Lee MW, Weith M, Pourdeyhimi B, Yarin AL (2015) Biodegradable and biocompatible soy protein/polymer/adhesive sticky nano-textured interfacial membranes for prevention of Esca fungi invasion into pruning cuts and wounds of vines. J Mater Chem B 3:2147–2162
Stafford GD, Handley RW (1975) Transverse bend testing of denture base polymers. J Dent 3:251–255
Stafford GD, Smith DC (1968) Some studies of the properties of denture base polymers. Br Dent J 125:337–342
Standard Test Method for Flexural Properties of Unreinforced and Reinforced Plastics and Electrical Insulating Materials by Four-Point Bending (1968) D6272: American Society for Testing and Materials
Standard Methods of Test for Flexural Properties of Plastics (1970) ASTM: D790-71: American Society for Testing and Materials
Toohey KS, Hansen CJ, Lewis JA, White SR, Sottos NR (2009a) Delivery of two-part self-healing chemistry via microvascular networks. Adv Mater 19:1399–1405
Toohey KS, Sottos NR, Lewis JA, Moore JS, White SR (2007) Self-healing materials with microvascular networks. Nat Mater 6:581–585
Toohey KS, Sottos NR, White SR (2009b) Characterization of microvascular-based self-healing coatings. ExM 49:707–717
Trask RS, Bond IP (2006) Biomimetic self-healing of advanced composite structures using hollow glass fibres. SMaS 15:704–710
Trask RS, Williams GJ, Bond IP (2007) Bioinspired self-healing of advanced composite structures using hollow glass fibres. J R Soc Interface 4:363–371

Vahedi V, Pasbakhsh P, Piao CS, Seng CE (2015) A facile method for preparation of self-healing epoxy composites: using electrospun nanofibers as microchannels. J Mater Chem A 3:16005–16012

van der Heijden S, Daelemans L, De Schoenmaker B, De Baere I, Rahier H, Van Paepegem W, De Clerck K (2014) Interlaminar toughening of resin transfer moulded glass fibre epoxy laminates by polycaprolactone electrospun nanofibers. Compos Sci Technol 104:66–73

Wan K-T, Mai Y-W (1995) Fracture mechanics of a shaft-loaded blister of thin flexible membrane on rigid substrate. Int J Fract 74:181–197

White SR, Moore JS, Sottos NR, Krull BP, Cruz WAS, Gergely RCR (2014) Restoration of large damage volumes in polymers. Science 344:620–623

White SR, Sottos NR, Geubelle PH, Moore JS, Kessler MR, Sriram SR, Brown EN, Viswanathan S (2001) Autonomic healing of polymer composites. Nature 409:794–797

Whitney J, Browning C, Mair A (1974) Analysis of the flexure test for laminated composite materials. ASTM International, West Conshohocken, PA

Williams HR, Trask RS, Bond IP (2007a) Self-healing composite sandwich structures. SMaS 16:1198–1207

Williams G, Trask R, Bond I (2007b) A self-healing carbon fibre reinforced polymer for aerospace applications. Compos A 38:1525–1532

Williams HR, Trask RS, Bond IP (2008) Self-healing sandwich panels: Restoration of compressive strength after impact. Compos Sci Technol 68:3171–3177

Williams GJ, Bond IP, Trask RS (2009) Compression after impact assessment of self-healing CFRP. Compos A 40:1399–1406

Wong S-C, Na H, Chen P (2013) Measurement of adhesion energy of electrospun polymer membranes using a shaft-loaded blister test. 13th Int Conf Fract, 1–7

Wu X-F (2003) Fracture of advanced polymer composites with nanofiber-reinforced interfaces. Ph.D. Thesis. University of Nebraska-Lincoln: Lincoln, Nebraska, USA

Wu X-F (2009) Fracture of advanced composites with nanofiber reinforced interfaces. VDM, Saarbrucken

Wu X-F, Rahman A, Zhou Z, Pelot DD, Sinha-Ray S, Chen B, Payne S, Yarin AL (2013) Electrospinning core-shell nanofibers for interfacial toughening and self-healing of carbon-fiber/epoxy composites. J Appl Polym Sci 129:1383–1393

Wu X-F, Yarin AL (2013) Recent progress in interfacial toughening and damage self-healing of polymer composites based on electrospun and solution-blown nanofibers: an overview. J Appl Polym Sci 129:2225–2237

Zainuddin S, Arefin T, Fahim A, Hosur MV, Tyson JD, Kumar A, Trovillion J, Jeelani S (2014) Recovery and improvement in low-velocity impact properties of e-glass/epoxy composites through novel self-healing technique. Compos Struct 108:277–286

Zanjani JSM, Okan BS, Letofsky-Papst I, Menceloglu Y, Yildiz M (2015) Repeated self-healing of nano and micro scale cracks in epoxy based composites by tri-axial electrospun fibers including different healing agents. RSC Adv 5:73133–73145

Zanjani JSM, Okan BS, Yilmaz C, Menceloglu Y, Yildiz M (2017) Monitoring the interface and bulk self-healing capability of triaxial electrospun fibers in glass fiber reinforced epoxy composites. Compos A 99:221–232

Zhang J, Yang T, Lin T, Wang CH (2012) Phase morphology of nanofibre interlayers: critical factor for toughening carbon/epoxy composites. Compos Sci Technol 72:256–262

Zhang P, Li G (2015) Healing-on-demand composites based on polymer artificial muscle. Polymer 64:29–38

Zussman E, Burman M, Yarin AL, Khalfin B, Cohen Y (2006) Tensile deformation of electrospun Nylon 6,6 nanofibers. J Polym Sci, Part B- Polymer Physics 44:1482–1489

Part IV
Self-Healing Nanotextured Materials for Corrosion Protection

Chapter 9
Capsule-Based Self-Healing Approaches for Corrosion Protection

This chapter begins with a brief discussion of the fundamental electrochemical aspects of corrosion cracking (Sect. 9.1). Section 9.2 discusses the capsule-based extrinsic self-healing approach. The discussion is divided between healing agent-embedded capsules and the corrosion inhibitor-embedded capsules. Their self-healing performances for corrosion protection are discussed in detail in Sects. 9.3 and 9.4, respectively.

9.1 Electrochemical Fundamentals of Corrosion Cracking of Metals

Corrosion is an umbrella term encompassing different undesirable oxidation-reduction (redox) reactions occurring on metallic surfaces in contact with water, which contains ions and is thus an electrolyte. Corrosion can also happen on glass and polymer (elastomer) surfaces, but for metals it is a dominant, undesirable, and dangerous phenomenon, with potentially severe and even catastrophic consequences for many loaded structures. The severity of corrosion-related problems arises from two main points. First, corrosion creates new cracks, even in the absence of loading, which accelerate mechanical damage to loaded materials (cf. Chap. 6). Second, mechanical stresses facilitate crack growth, destroy the protective oxide at the surface, expose new metal surfaces to aggressive electrolytes, and thus further accelerate corrosion damage. A similar interplay between corrosion and the appearance and growth of fatigue cracks in vibrating constructions also accelerates fatigue. Accordingly, the terms of stress corrosion cracking (SCC) and corrosion fatigue are used (Perez 2004; Landolt 2007; Ohtsuka et al. 2018). The fracture toughness K_{Ic}, which is the material characteristic describing resistance to Mode I cracking (cf. Sect. 6.2), is decreased by corrosion to a value $K_{Ic,SCC}$, which is lower than K_{Ic}. Thus, the fracture condition corresponding to the beginning of catastrophic crack growth, $K_I > K_{Ic,SCC}$, is

A. L. Yarin et al., *Self-Healing Nanotextured Vascular Engineering Materials*, Advanced Structured Materials 105, https://doi.org/10.1007/978-3-030-05267-6_9

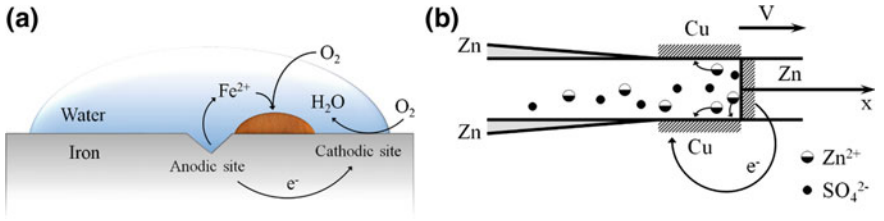

Fig. 9.1 Electrochemical mechanisms of metal corrosion. **a** Rusting of metallic iron in contact with water. **b** Galvanic corrosion of zinc (Zn) in contact with copper (Cu) and electrolyte (aqueous solution of sulfuric acid, H_2SO_4)

more easily fulfilled, and the cracking threshold is further diminished by continuous corrosion (Cherepanov 1979).

One corrosion mechanism of the rusting of metallic iron in contact with water serves as an example (cf. Fig. 9.1). In real materials, different impurities are present at the iron surface. Here, the impurity is an inclusion of another metal, which is nobler than iron according to the galvanic series. Therefore, iron and the impurity form a galvanic cell.

Ions of iron, being a less noble material, are transferred to water under the action of the electromotive force (emf) of the galvanic cell. In the solvated state, these ions are oxidized by atmospheric oxygen dissolved in water to form an insoluble hydrated oxide (red-brownish rust, $Fe_2O_3 \bullet xH_2O$), which is deposited on the iron surface (see Fig. 9.1a). Accordingly, the impurity is the cathode and iron is the anode of the galvanic cell (cf. Fig. 9.1a). The corresponding redox reactions can be written as reduction and oxidation half-reactions, respectively:

$$\text{at the cathode}: \quad O_{2(\text{gas})} + 4H^{+}_{(\text{aqueous})} + 4e^{-} \rightarrow 2H_2O_{(\text{liquid})} \tag{9.1}$$

$$\text{at the anode}: \quad Fe_{(\text{solid})} \rightarrow Fe^{2+}_{(\text{aqueous})} + 2e^{-} \tag{9.2}$$

The overall reaction for such a galvanic cell reads:

$$2Fe_{(\text{solid})} + O_{2(\text{gas})} + 4H^{+}_{(\text{aqueous})} \rightarrow 2Fe^{2+}_{(\text{aqueous})} + 2H_2O_{(\text{liquid})} \tag{9.3}$$

The corresponding emf sustains the electric current through the bulk of iron, thus delivering electrons to the cathode (see Fig. 9.1a).

In addition, the reactions responsible for rust formation proceed as:

$$4Fe^{2+}_{(\text{aqueous})} + O_2 \rightarrow 4Fe^{3+} + 2O^{2-} \tag{9.4}$$

accompanied by the following multistep acid–base reactions:

$$Fe^{2+}_{(\text{aqueous})} + 2H_2O \rightarrow Fe(OH)_2 + 2H^{+} \tag{9.5}$$

$$Fe^{3+}_{(aqueous)} + 3H_2O \rightarrow Fe(OH)_3 + 3H^+ \tag{9.6}$$

Then, the following dehydration equilibria occur, resulting in rust deposition:

$$Fe(OH)_2 \rightarrow FeO + H_2O \tag{9.7}$$

$$Fe(OH)_3 \rightarrow FeO(OH) + H_2O \tag{9.8}$$

$$2FeO(OH) \rightarrow Fe_2O_3 + H_2O \tag{9.9}$$

Reaction (9.2) is accelerated in low-pH acidic environments. Modern industry provides acidic environments, including acidic rain. The combustion of fuels yields combustion products containing sulfur dioxide and nitric oxides. These are released to the atmosphere and converted into sulfuric acid and nitric acid. Sulfur dioxide in air is oxidized according to the following reaction with the hydroxyl radical:

$$SO_2 + OH^- \rightarrow HOSO_2^- \tag{9.10}$$

which is accompanied by the next reaction step, leading to the formation of sulfur trioxide:

$$HOSO_2^- + O_2 \rightarrow HO_2^- + SO_3 \tag{9.11}$$

In the presence of atmospheric water, sulfur trioxide is rapidly converted to sulfuric acid:

$$SO_{3(gas)} + H_2O_{(liquid)} \rightarrow H_2SO_{4(aqueous)} \tag{9.12}$$

Thus, an aqueous solution of sulfuric acid is delivered to metallic structures on the ground in the form of acidic rains.

The formation of galvanic cells causing corrosion can occur by other mechanisms. Construction metals typically comprise different metal alloys, which have crevices at their joins. As such a crevice can contain an electrolyte, here an aqueous solution of sulfuric acid delivered as acid rain, the two neighboring metals thus form a galvanic cell (see Fig. 9.1b). For a zinc layer in a copper body, as in Fig. 9.1b, protons migrate in the electrolyte toward the copper cathode and are reduced there, forming hydrogen molecules (ultimately, hydrogen bubbles) by the following reduction half-reaction:

$$\text{at the cathode}: \quad 2H^+ + 2e^- \rightarrow H_2 \tag{9.13}$$

The electrons are supplied to the cathode by the electric current through the metal body. The current is sustained by the emf of the cell. The electrons are formed at the zinc anode. Zinc dissolves in sulfuric acid much more than copper, because the latter

in a nobler metal. Therefore, zinc ions Zn^{2+} are formed, leaving their electrons at the anode, and then transported by the emf into the electrolyte. This process corresponds to the following oxidation half-reaction:

$$\text{at the anode}: \quad Zn_{(\text{solid})} \rightarrow Zn^{2+}_{(\text{aqueous})} + 2e^{-} \tag{9.14}$$

In the electrolyte, the metal ions react with sulfate ions (SO_4^{2-}). The overall reaction corresponding to this galvanic element is:

$$Zn + H_2SO_4 \rightarrow ZnSO_4 + H_2 \tag{9.15}$$

In addition, the same amount of zinc ions is discharged at the copper cathode, thereby anodizing the copper surface (cf. Fig. 9.1b). However, the main outcome of the processes described above is in the propagation of the crevice toward the right at the velocity V, as depicted in Fig. 9.1b, which is determined by the rate of the cathodic electrochemical reaction, i.e., by the Frumkin–Butler–Volmer kinetics (Bard and Faulkner 2001; Antropov 2001).

In both cases depicted in Fig. 9.1a and b and considered in detail in this chapter, galvanic corrosion causes the growth of crevices in the metal body, which weaken the material and thus form proto-cracks. The latter facilitate both SCC and corrosion fatigue when the material is loaded, because these mechanisms diminish the threshold value of the fracture toughness $K_{Ic,SCC}$.

9.2 Healing Agent-Embedded Capsule-Based Self-Healing

The difference between intrinsic and extrinsic corrosion protection is described in Sect. 1.2. Capsule-based methods used for the development of coatings for corrosion protection provide extrinsic corrosion protection, because they involve no rearrangement of chemical bonds by external stimuli.

Although some improvements have been developed for capsule-based self-healing, the microcapsules in current use are still fabricated by the urea–formaldehyde (UF) polycondensation method of Brown et al. (2003). However, different types of healing agents are encased within these capsules. Suryanarayana et al. (2008) studied the anticorrosion effect of linseed oil (LO) encapsulated within UF microcapsules with sizes of 5–100 μm (cf. Table 1.1 in Sect. 1.3). The presence of LO was confirmed by Fourier-transform infrared spectroscopy (FTIR; cf. Sect. 5.2) and differential scanning calorimetry (DSC). A corrosion test was conducted by encasing the microcapsules within an epoxy matrix that was deposited on a steel substrate; the epoxy was scratched and the scratched specimen was exposed to a salt-sprayed atmosphere. It was observed that the scratched epoxy layer with the embedded microcapsules completely prevented the corrosion of the underlying metal because the released LO filled the cracks and formed a layer protecting it from

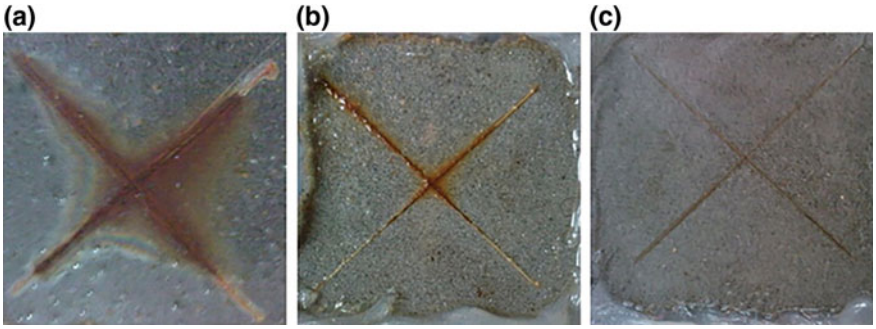

Fig. 9.2 Corrosion test images of scratched specimens **a** without capsules, **b** with microscale capsules, and **c** with nanoscale capsules. Reprinted with permission from Boura et al. (2012)

moisture and oxygen. Meanwhile, specimens in which the epoxy layer contained no LO-filled microcapsules were rusted by oxidation. Other drying oils can be also used as healing agents. Drying oils such as LO and tung oil (TO) are preferable to self-healing coatings with dicyclopentadiene (DCPD)-filled microcapsules because the former do not require a catalyst (Samadzadeh et al. 2011). Recently, neem oils have been introduced as healing agents (Chaudhari et al. 2013; Marathe et al. 2015), and showed great promise as eco-friendly renewable self-healing materials.

Boura et al. (2012) decreased the size of the LO-containing UF capsules to <1 μm using ultrasonication, which facilitated the formation of fine LO droplets during the UF polymerization process (cf. Table 1.1 in Sect. 1.3). Compared to microscale capsules, these submicrometer-sized capsules exhibit improved anticorrosion performance during corrosion tests (Fig. 9.2).

Finely dispersed capsules had increased probabilities of forming contacts with the cracks formed, as the specific surface-area-to-volume ratio (S/V) of the smaller capsules was increased. A similar S/V effect was also observed for hollow-fiber-based self-healing (cf. Chap. 10). Recently, Lang and Zhou (2017) reported the improvement of the size-uniformity of LO-filled microcapsules as well as their distribution in an epoxy matrix. This was achieved by either adding polyvinyl alcohol (PVA) stabilizers of different molecular weight (M_w), or by varying the stirring rate during the fabrication process. The average size of the UF microcapsules decreased from 138 to 48 μm as the M_w of the PVA stabilizer was increased from 31 to 130 kDa (cf. Table 1.1 in Sect. 1.3). In addition, the average microcapsule size decreased from 130 to 76 μm as the stirring rate was increased from 600 to 900 rpm.

9.3 Modified Healing Agents and Microcapsules

Siloxane- and silyl-ester-based healing agents have also been proposed for encapsulation within UF microcapsules by Cho et al. (2009) and García et al. (2011),

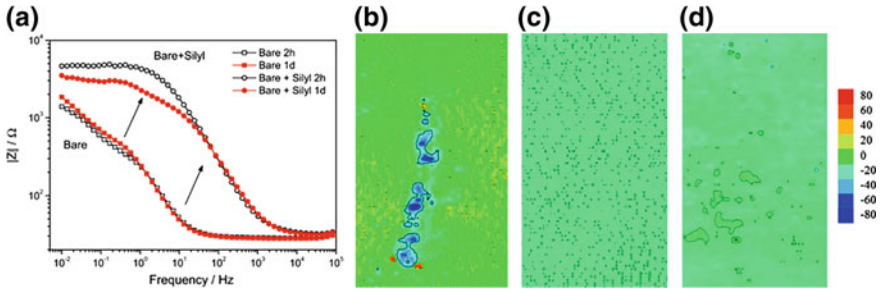

Fig. 9.3 **a** Impedance as function of frequency for bare and microcapsule-embedding self-healing composites after 1 and 2 days of exposure to 0.05 M NaCl solution. **b** Current density maps of intentionally damaged self-healing composite after **b** 1, **c** 24, and **d** 48 h of exposure to 0.05 M NaCl solution. Composites were deposited on aluminum substrates. Reprinted with permission from García et al. (2011)

respectively. Siloxane-based healing agents have been actively used in nanoscale hollow-fiber-based self-healing materials because of their chemical stability during fabrication (cf. Chap. 10). Cho et al. (2009) introduced a dual-capsule-based self-healing system involving microcapsules of two types. The first type were 60-μm UF microcapsules with encapsulated siloxane-based healing agent, while the second type were 90-μm polyurethane (PU) microcapsules containing dimethyl dineodecanoate tin (DMDNT) as a catalyst (cf. Table 1.1 in Sect. 1.3). After embedding in an epoxy matrix, these microcapsules formed a self-healing composite that could be coated on steel substrates. The thus-coated and scratched specimens were immersed in salt water for corrosion testing, which revealed suitable anticorrosion performance by the system based on electrochemical measurements.

Silyl esters possess good reactivity with both water and metal, which allows these materials to form adhered-to-metal barriers that can prevent corrosive media from reaching the underlying metal. Similar to the case of oil-based healing agents, silyl esters do not require catalysts or crosslinkers for polymerization (or solidification) because, in their case, barrier formation is based on a hydrolysis process. García et al. (2011) fabricated an epoxy-matrix composite, wherein silyl-ester-filled 100-μm UF microcapsules were embedded in the epoxy (cf. Table 1.1 in Sect. 1.3). The anticorrosion performance of the composite was evaluated by electrochemical impedance spectroscopy (EIS) and the scanning vibrating electrode technique (SVET) (Fig. 9.3). The impedance and current density measurement results obtained from the microcapsule-embedding composite confirmed its exhibited satisfactory anticorrosion performance compared to that of the bare specimens.

Healing agents that can form anti-corrosion barriers without catalysts or other materials (e.g., LO, TO, and siloxane-, and silyl-ester-based healing agents) are called catalyst-free one-part self-healing agents. Among the most attractive catalyst-free one-part healing agents are water-friendly compounds containing the isocyanate functional group (cf. Sect. 2.3), which facilitates both reaction with water and the formation of anti-corrosion shields (Binder 2013). However, the water-friendly

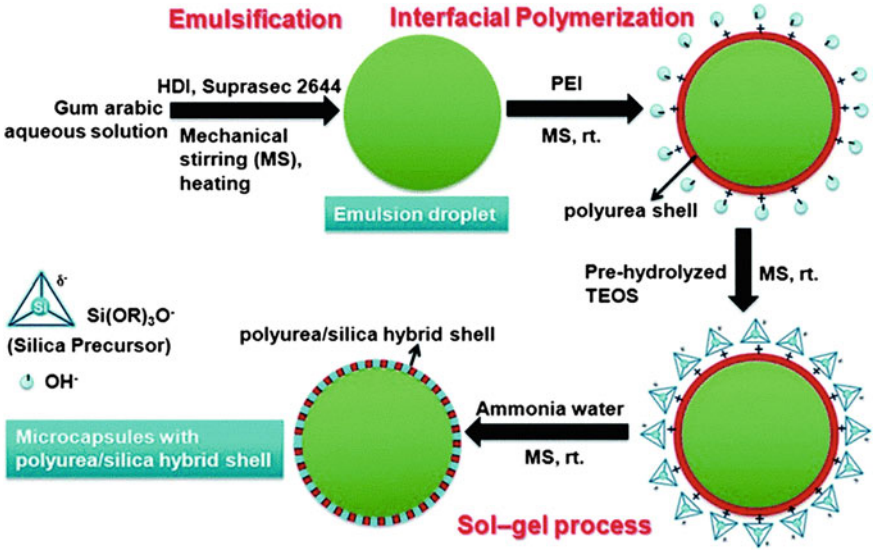

Fig. 9.4 Schematic of the fabricating process for polyurea/silica hybrid self-healing microcapsules. HDI: hexamethylene diisocyanate; PEI: polyethyleneimine; TEOS: tetraethyl orthosilicate. Reprinted with permission from Wu et al. (2014)

properties of the isocyanate group can cause issues in shell polymers because of its high reactivity, according to Ulla et al. (2016). Several researchers have attempted to overcome this problem (Yang et al. 2008; Huang and Yang 2011; Wu et al. 2014). For instance, Wu et al. (2014) fabricated polyurea/silica hybrid microcapsules for encasing isocyanate-based healing agents by combining interfacial polymerization and in situ sol-gel process (Fig. 9.4). The thus-fabricated hybrid microcapsules had sizes of 57–328 μm, which could be controlled by varying the agitation rate during fabrication (cf. Table 1.1 in Sect. 1.3). The hybrid structure of the microcapsules not only allowed successful encapsulation of the isocyanate-based healing agent but also improved the thermal and chemical properties of the microcapsules. Therefore, during corrosion testing, wherein the specimens were immersed in a 10 wt% NaCl solution for 48 h, the hybrid-microcapsule-embedding epoxy completely prevented rusting of the substrate. More recently, Sun et al. (2015) fabricated 88-μm double-layered polyurea microcapsules by a similar interfacial polymerization method (cf. Table 1.1 in Sect. 1.3). Without using silica, they successfully encased an isocyanate-based healing agent within microcapsules with shells as thick as 8 μm by using a triethylenetetramine solution.

The chemical stability of catalyst-free one-part self-healing agents and the feasibility of using self-healing materials based on them on the industrial scale have also been studied. To improve the healing capabilities of these agents, heat and light sources have primarily been employed to provide stimuli (Ghosh and Urban 2009; Klukovich et al. 2011; Ling et al. 2012; Song et al. 2013; Kiskan and Yagci 2014).

Because of their obvious environmental and economic advantages, self-healing composites using ultraviolet (UV) light or solar light as a stimulus have also been studied. To fabricate such photoresponsive self-healing composites, Gao et al. (2015) introduced photoabsorbing UF/TiO_2 hybrid self-healing microcapsules containing an epoxy-based healing agent. Using the Pickering emulsion polymerization method, Stiller et al. (2004), Chen et al. (2007), and Chevalier and Bolzinger (2013) embedded nanoscale TiO_2 particles within microcapsule shells. The size of the microcapsules was 87–520 μm, controlled by varying the mechanical stirring speed from 500 to 1500 rpm before polymerization (cf. Table 1.1 in Sect. 1.3). The presence of TiO_2 particles enabled the microcapsules to absorb UV light with the wavelength of 330 nm. The photocatalytic effect triggered by the photoabsorbing TiO_2 particles accelerated the solidification (or healing) of the epoxy-based healing agent. Furthermore, multicycle healing was achieved using this photoresponsive self-healing system, as confirmed by corrosion tests.

In addition to the polyurea-based microcapsules described above, other similar microcapsules have been synthesized. He et al. (2017) reported a method for fabrication of polyvinyl alcohol (PVA)-based microcapsules. The shells of these microcapsules also had a polyurea layer. However, the outmost layers were formed from PVA. The hydrolyzed PVA layer yielded significant improvements over polyurea-based microcapsules, namely, a more robust fabrication process, greater stiffness and water resistance, and improved compatibility between the microcapsules and the epoxy matrix. Microcapsules with the size of 96 μm were embedded in the epoxy matrix at the concentration of 15 wt% (cf. Table 1.1 in Sect. 1.3). Corrosion tests were performed by coating steel with the self-healing composite, scratching the coating, and immersing the steel specimen in a 10 wt% NaCl solution (Fig. 9.5). The epoxy layer completely protected the steel from corrosion, because of the healing agent released from the damaged microcapsules.

9.4 Corrosion Inhibitor-Embedded Capsule-Based Self-Healing

Using corrosion inhibitors without encapsulation in some type of microstructure has several disadvantages. For instance, it can cause the degradation or inconsistency of the surrounding coating materials, as well as an increase in the deactivation rate of the embedded inhibitors (Voevodin et al. 2001; Garcia-Heras et al. 2004). In addition, chromates, the most frequently used corrosion inhibitors, were banned in 2007 by the Environmental Protection Agency (EPA) owing to their carcinogenicity. To avoid these drawbacks, corrosion inhibitors are now usually encapsulated. Generally, the size of corrosion-inhibitor-containing capsules is much smaller than that of healing-agent-containing ones (cf. Sect. 1.3). On the one hand, a small amount of the inhibitor is necessary for inhibitor-embedded systems because self-healing (or corrosion protection) by the inhibitor is related to a chemical reaction. On the

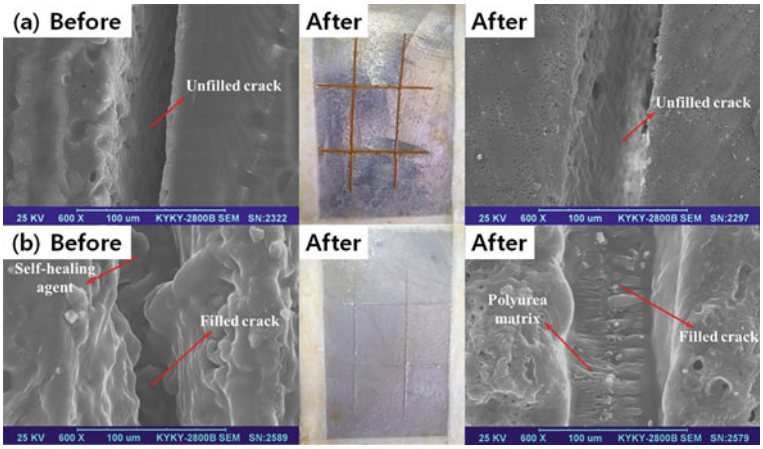

Fig. 9.5 Photographs and SEM images of scratched specimens **a** without and **b** with microcapsules after immersion in salt solution. Reprinted with permission from He et al. (2017)

other hand, many capsules containing the healing agent are needed to physically fill the damaged area within the specimen in question, in order to block the passage of external corrosive components (i.e., oxygen, water, and electrolytes; cf. Sect. 9.1). Note that most studies on inhibitor-based self-healing have focused on the effects of changes in pH on the corroded area, attributable to the redox reactions between the underlying metal and corrosive materials (cf. Sect. 9.1).

To produce corrosion-inhibitor-containing nanocapsules, Zheludkevich et al. (2007) used 70-nm silica nanoparticles to fabricate multilayered nanocapsules in a layer-by-layer manner, with the corrosion inhibitor layer being entrapped between the polyelectrolyte multilayers. These polyelectrolyte multilayers, sensitive to minor pH changes, allowed the controlled release of the entrapped inhibitors, because corrosion causes pH changes near the damaged areas. The polyelectrolyte multilayers were composed of polyethyleneimine (PEI) and polystyrene sulfonate (PSS), while benzotriazole was used as the corrosion inhibitor. The layer-by-layer deposition process yielded nanocapsules of 100 nm in size (cf. Table 9.1). Zheludkevich et al. (2007) then coated the nanocapsule-embedded polymeric matrix onto an aluminum substrate and evaluated its anticorrosive performance through EIS and SVET measurements. The nanocapsule-embedded composite completely prevented corrosion, owing to the released inhibitor, which reduced the corrosion rate by preventing the cathodic reduction of oxygen (cf. Sect. 9.1).

Choi et al. (2012) reported a method for fabricating of 400–450-nm nanocapsules in a layer-by-layer manner by sequential emulsion polymerization (cf. Table 9.1). They used 100-nm latex particles as the cores for the nanocapsules. Triethanolamine (TEA), used as the corrosion inhibitor, was encapsulated by an outermost polystyrene (PS) shell. The presence of TEA within the nanocapsules was confirmed by thermogravimetric analysis (TGA; cf.

Table 9.1 Corrosion protection through self-healing based on corrosion-inhibitor-containing capsules. PS-polystyrene, PANI-polyaniline, PDADMAC-poly(diallyl dimethyl ammonium chloride)

Fabrication method	Shell material	Composite structure	Capsule diameter (nm)	Corrosion inhibitor	References
Layer-by-layer deposition	PEI/PSS	Sol-gel matrix	70–100 (OD)	Benzotriazole	Zheludkevich et al. (2007)
Sequential emulsion polymerization	PS	Polymeric matrix	400–450 (OD)	Triethanolamine	Choi et al. (2012)
Multi-stage emulsion polymerization	PS	Polymeric matrix	300–600 (OD)	Ethanolamine/5-Amino-1-pentanol/Diethanolamine/Triethanolamine/Propylamine/Dipropylamine	Choi et al. (2013)
Direct encapsulation	PDADMAC	Epoxy matrix	100 (OD)	2-mercaptobenzothiazole	Plawecka et al. (2014)
Polymerization	PANI	Polymeric matrix	<1000 (OD)	3-Nitrosalicylic acid	Vimalanandan et al. (2013)
In situ emulsion polymerization	UF	Epoxy matrix	70–200 (OD)	2-mercaptobenzothiazole	Siva and Sathiyanarayanan (2015)

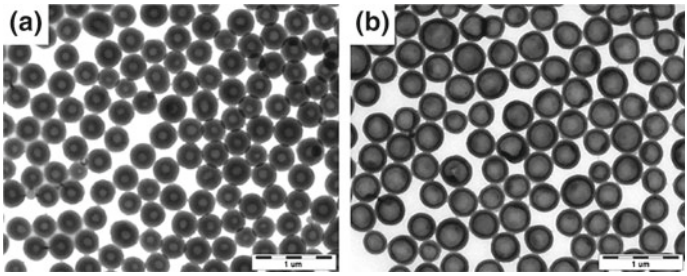

Fig. 9.6 Transmission electron microscopy (TEM) images of self-healing nanocapsules **a** without and **b** with corrosion inhibitor. Reprinted with permission from Choi et al. (2012)

Sect. 5.3) and gas chromatography–mass spectrometry (GC-MS). Encapsulating the inhibitor within the PS nanocapsules increased their size from 350 to 450 nm (Fig. 9.6). During corrosion testing in a NaCl solution, pH changes (regardless of acidity or basicity) over the damaged area of the self-healing coating triggered the release of the inhibitor into the microgaps between the PS shell and the surrounding polymeric matrix by osmotic swelling. Thus, the corrosion rate of the damaged steel substrate was reduced significantly. Choi et al. (2013) also studied the effects of different types of amine-based corrosion inhibitors on the anticorrosive performances of coatings. Both the encapsulation process and the osmotic swelling process were improved when an inhibitor with greater water solubility was used. In particular, linearly structured and highly water-soluble amines exhibited faster release rate than did the other inhibitors.

Recently, 2-mercaptobenzothiazole (MBT) has also attracted significant attention as a corrosion inhibitor when encased in multilayered nanocapsules because it is a very efficient anticorrosion agent, especially for aluminum alloys. Plawecka et al. (2014) fabricated 100-nm MBT-containing poly(diallyl dimethyl ammonium chloride) (PDADMAC) nanocapsules (cf. Table 9.1). Unlike the previously discussed studies, they did not use a core supporter, such as silica or latex nanoparticles but instead employed a direct encapsulation method. Localized EIS and SVET measurements revealed that these pH-responsive nanocapsules efficiently inhibited corrosion even for small surface defects.

In addition to pH-responsive capsule-based self-healing materials, other self-healing materials have been reported. Vimalanandan et al. (2013) introduced a redox-responsive capsule-based approach wherein a conducting polymer of polyaniline (PANI) and 3-nitrosalicylic acid (3-NisA) were used as the shell material and the core corrosion inhibitor, respectively (cf. Table 9.1). The conducting polymer allowed the release of the inhibitor in response to changes in the electrochemical potential at the onset of corrosion. In other words, the corrosion rate was significantly diminished not only because of the active anions stored within the capsules, which would depend on the corrosion process, but also because of the release of the inhibitor at the metal–polymer interface. To overcome the unsuitability of using conducting polymers as sensors for electrochemical potential changes, Vimalanandan et al. (2013) decorated the capsules with gold nanoparticles (Fig. 9.7). They then investigated the

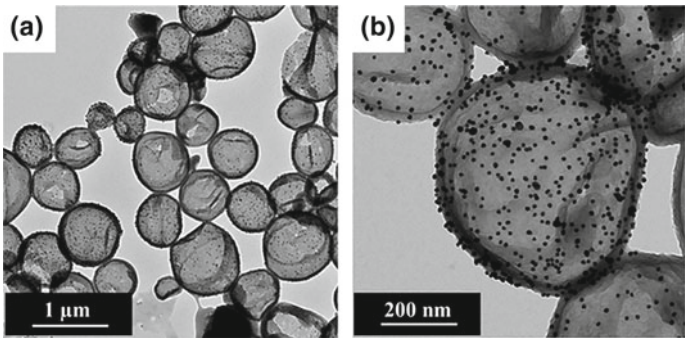

Fig. 9.7 TEM images of redox-responsive PANI capsules decorated with gold nanoparticles. Reprinted with permission from Vimalanandan et al. (2013)

changes in the electrochemical potential using a scanning Kelvin probe (Stratmann 1987; Stratmann and Streckel 1990; Stratmann et al. 1996; Fürbeth and Stratmann 2001; Frankel et al. 2007; Umeda et al. 2016).

A combined method involving the mixing of a healing agent and a corrosion inhibitor as the core materials has also been proposed. Siva and Sathiyanarayanan (2015) reported 70–200-nm self-healing capsules encapsulating LO (cf. Sect. 1.3) and MBT as the core materials (cf. Table 9.1). It should be emphasized that the fabricated capsules were neither pH-responsive nor redox-responsive because their shells were composed of UF (cf. Sect. 1.3). The presence of the corrosion inhibitor not only allowed for the fabrication of nanoscale capsules despite the use of a healing agent, but also resulted in an improved anticorrosion performance, as determined by EIS and SVET measurements.

References

Antropov LI (2001) Theoretical electrochemistry. Honolulu University Press of the Pacific, Honolulu

Bard AJ, Faulkner LR (2001) Electrochemical methods fundamentals and applications. John Wiley & Sons, New York

Binder WH (2013) Self-healing polymers: from principles to applications. John Wiley & Sons, New York

Boura SH, Peikari M, Ashrafi A, Samadzadeh M (2012) Self-healing ability and adhesion strength of capsule embedded coatings—Micro and nano sized capsules containing linseed oil. Prog Org Coat 75:292–300

Brown EN, Kessler MR, Sottos NR, White SR (2003) In situ poly (urea-formaldehyde) microencapsulation of dicyclopentadiene. J Microencapsul 20:719–730

Chaudhari AB, Tatiya PD, Hedaoo PK, Kulkarni RD, Gite VV (2013) Polyurethane prepared from neem oil polyesteramides for self-healing anticorrosive coatings. Ind Eng Chem Res 52:10189–10197

Chen T, Colver PJ, Bon SAF (2007) Organic–inorganic hybrid hollow spheres prepared from TiO_2-stabilized Pickering emulsion polymerization. Adv Mater 19:2286–2289
Cherepanov GP (1979) Mechanics of brittle fracture. McGraw Hill, New York
Chevalier Y, Bolzinger M-A (2013) Emulsions stabilized with solid nanoparticles: Pickering emulsions. Colloids Surf A 439:23–34
Cho SH, White SR, Braun PV (2009) Self-healing polymer coatings. Adv Mater 21:645–649
Choi H, Kim KY, Park JM (2013) Encapsulation of aliphatic amines into nanoparticles for self-healing corrosion protection of steel sheets. Prog Org Coat 76:1316–1324
Choi H, Song YK, Kim KY, Park JM (2012) Encapsulation of triethanolamine as organic corrosion inhibitor into nanoparticles and its active corrosion protection for steel sheets. Surf Coat Technol 206:2354–2362
Frankel GS, Stratmann M, Rohwerder M, Michalik A, Maier B, Dora J, Wicinski M (2007) Potential control under thin aqueous layers using a Kelvin probe. Corros Sci 49:2021–2036
Fürbeth W, Stratmann M (2001) The delamination of polymeric coatings from electrogalvanised steel–a mechanistic approach: Part 1: delamination from a defect with intact zinc layer. Corros Sci 43:207–227
Gao L, He J, Hu J, Wang C (2015) Photoresponsive self-healing polymer composite with photoabsorbing hybrid microcapsules. ACS Appl Mater Interfaces 7:25546–25552
García SJ, Fischer HR, White PA, Mardel J, González-García Y, Mol AJMC, Hughes AE (2011) Self-healing anticorrosive organic coating based on an encapsulated water reactive silyl ester: synthesis and proof of concept. Prog Org Coat 70:142–149
Garcia-Heras M, Jimenez-Morales A, Casal B, Galvan JC, Radzki SS, Villegas MA (2004) Preparation and electrochemical study of cerium–silica sol–gel thin films. J Alloys Compd 380:219–224
Ghosh B, Urban MW (2009) Self-repairing oxetane-substituted chitosan polyurethane networks. Science 323:1458–1460
He Z, Jiang S, Li Q, Wang J, Zhao Y, Kang M (2017) Facile and cost-effective synthesis of isocyanate microcapsules via polyvinyl alcohol-mediated interfacial polymerization and their application in self-healing materials. Compos Sci Technol 138:15–23
Huang M, Yang J (2011) Facile microencapsulation of HDI for self-healing anticorrosion coatings. J Mater Chem 21:11123–11130
Kiskan B, Yagci Y (2014) Self-healing of poly (propylene oxide)-polybenzoxazine thermosets by photoinduced coumarine dimerization. J Polym Sci Part A-Polym Chem 52:2911–2918
Klukovich HM, Kean ZS, Iacono ST, Craig SL (2011) Mechanically induced scission and subsequent thermal remending of perfluorocyclobutane polymers. J Am Chem Soc 133:17882–17888
Landolt D (2007) Corrosion and surface chemistry of metals. CRC Press (EPFL Press), Boca Raton
Lang S, Zhou Q (2017) Synthesis and characterization of poly (urea-formaldehyde) microcapsules containing linseed oil for self-healing coating development. Prog Org Coat 105:99–110
Ling J, Rong MZ, Zhang MQ (2012) Photo-stimulated self-healing polyurethane containing dihydroxyl coumarin derivatives. Polymer 53:2691–2698
Marathe R, Tatiya P, Chaudhari A, Lee J, Mahulikar P, Sohn D, Gite V (2015) Neem acetylated polyester polyol—Renewable source based smart PU coatings containing quinoline (corrosion inhibitor) encapsulated polyurea microcapsules for enhance anticorrosive property. Ind Crops Prod 77:239–250
Ohtsuka T, Nishikata A, Sakairi M, Fushimi K (2018) Electrochemistry for corrosion fundamentals. Springer, Singapore
Perez N (2004) Electrochemistry and corrosion science. Kluwer Academic Publishers, New York
Plawecka M, Snihirova D, Martins B, Szczepanowicz K, Warszynski P, Montemor MF (2014) Self healing ability of inhibitor-containing nanocapsules loaded in epoxy coatings applied on aluminium 5083 and galvanneal substrates. Electrochim Acta 140:282–293
Samadzadeh M, Boura SH, Peikari M, Ashrafi A, Kasiriha M (2011) Tung oil: an autonomous repairing agent for self-healing epoxy coatings. Prog Org Coat 70:383–387
Siva T, Sathiyanarayanan S (2015) Self healing coatings containing dual active agent loaded urea formaldehyde (UF) microcapsules. Prog Org Coat 82:57–67

Song Y-K, Jo Y-H, Lim Y-J, Cho S-Y, Yu H-C, Ryu B-C, Lee S-I, Chung C-M (2013) Sunlight-induced self-healing of a microcapsule-type protective coating. ACS Appl Mater Interfaces 5:1378–13784

Stiller S, Gers-Barlag H, Lergenmueller M, Pflücker F, Schulz J, Wittern KP, Daniels R (2004) Investigation of the stability in emulsions stabilized with different surface modified titanium dioxides. Colloids Surf A 232:261–267

Stratmann M (1987) The investigation of the corrosion properties of metals, covered with adsorbed electrolyte layers—a new experimental technique. Corros Sci 27:869–872

Stratmann M, Leng A, Fürbeth W, Streckel H, Gehmecker HG, Groβe-Brinkhaus K-H (1996) The scanning Kelvin probe; a new technique for the in situ analysis of the delamination of organic coatings. Prog Org Coat 27:261–267

Stratmann M, Streckel H (1990) On the atmospheric corrosion of metals which are covered with thin electrolyte layers—I. Verification of the experimental technique. Corros Sci 30:681–696

Sun D, An J, Wu G, Yang J (2015) Double-layered reactive microcapsules with excellent thermal and non-polar solvent resistance for self-healing coatings. J Mater Chem A 3:4435–4444

Suryanarayana CV, Rao KC, Kumar D (2008) Preparation and characterization of microcapsules containing linseed oil and its use in self-healing coatings. Prog Org Coat 63:72–78

Ullah H, Azizli KAM, Man ZB, Ismail MBC, Khan MI (2016) The potential of microencapsulated self-healing materials for microcracks recovery in self-healing composite systems: a review. Polym Rev 56:429–485

Umeda J, Nakanishi N, Kondoh K, Imai H (2016) Surface potential analysis on initial galvanic corrosion of Ti/Mg-Al dissimilar material. Mater Chem Phys 179:5–9

Vimalanandan A, Lv LP, Tran TH, Landfester K, Crespy D, Rohwerder M (2013) Redox-responsive self-healing for corrosion protection. Adv Mater 25:6980–6984

Voevodin NN, Grebasch NT, Soto WS, Arnold FE, Donley MS (2001) Potentiodynamic evaluation of sol–gel coatings with inorganic inhibitors. Surf Coat Technol 140:24–28

Wu G, An J, Sun D, Tang X, Xiang Y, Yang J (2014) Robust microcapsules with polyurea/silica hybrid shell for one-part self-healing anticorrosion coatings. J Mater Chem A 2:11614–11620

Yang J, Keller MW, Moore JS, White SR, Sottos NR (2008) Microencapsulation of isocyanates for self-healing polymers. Macromol 41:9650–9655

Zheludkevich ML, Shchukin DG, Yasakau KA, Möhwald H, Ferreira MGS (2007) Anticorrosion coatings with self-healing effect based on nanocontainers impregnated with corrosion inhibitor. Chem Mater 19:402–411

Chapter 10
Fiber-Based Self-Healing Approaches for Corrosion Protection

In this chapter in Sects. 10.1 and 10.2, corrosion protection provided by co-electrospun and emulsion-spun nanofibers (NFs), respectively, is discussed. These NFs are embedded in protective coatings, forming composite materials that are deposited on steel substrates. Upon scratching, these coatings are capable of self-healing, thus protecting the underlying metal from exposure to corrosive environments, as demonstrated by several types of corrosion testing.

10.1 Corrosion Protection Provided by Coatings with Embedded Core-Shell NFs Formed by Co-Electrospinning

Although emulsion electrospinning is among the simplest methods for fabricating core-shell NFs (cf. Sect. 4.3), the process has a significant drawback compared with co-electrospinning in its rate of core formation. The disordered formation of droplets of curing agent in the emulsion as well as the difficulties associated with material selection can interrupt the electrospinning process. Therefore, An et al. (2015) employed co-electrospinning (see Sect. 4.2) to form mats with interwoven NFs containing either resin monomer or curing agent in the cores. They prepared composites using miniscule amounts of the embedded NFs. These composites exhibited outstanding corrosion protection during corrosion tests.

Figure 10.1 illustrates the results of the corrosion test with the pristine polydimethylsiloxane (PDMS) and the self-healing core-shell NF-embedded composite (in PDMS matrix), both deposited on steel substrates. In the core-shell fibers, dimethyl siloxane (DMS) resin monomer or curing agent were in the cores, and polyacrylonitrile (PAN) was used as the shells (cf. Sects. 2.2 and 4.2). All coatings are scratched deeply with crossed lines in X shapes using a razor blade. After scratching, the specimens are left for 48 h. Then, an acetic acid solution is poured onto them.

A. L. Yarin et al., *Self-Healing Nanotextured Vascular Engineering Materials*, Advanced Structured Materials 105, https://doi.org/10.1007/978-3-030-05267-6_10

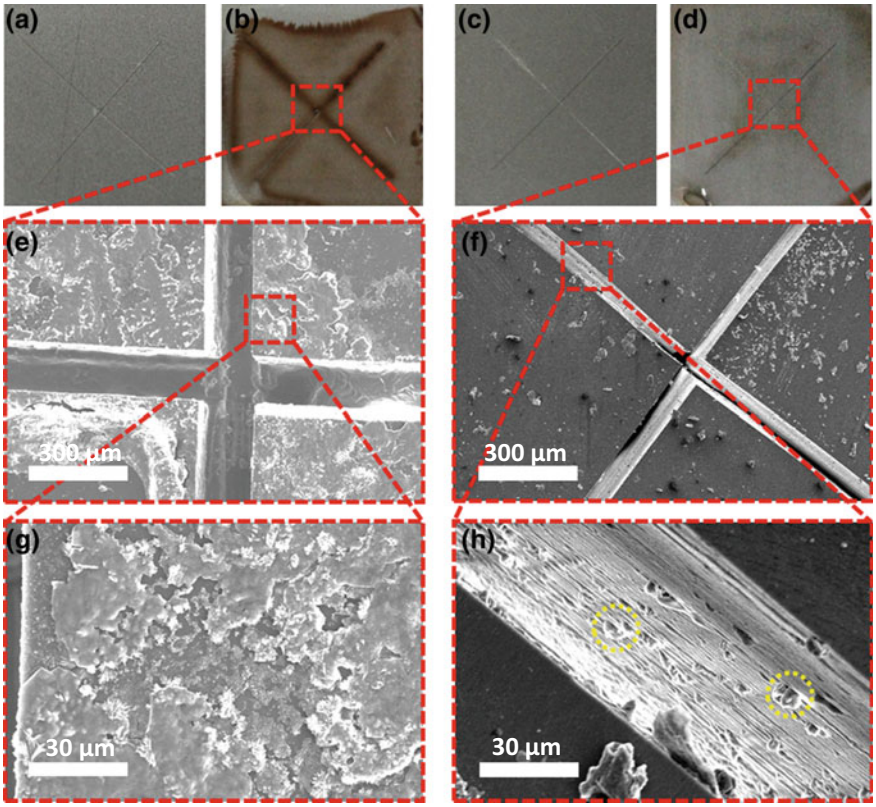

Fig. 10.1 Corrosion test images evaluating RC–PAN (resin or curing agent in the cores, PAN shells) NFs in composite layers on steel substrates. Corrosion test images of (**a**, **b**) deposition time $t_{dep} = 0$ min (scratched metal with pristine PDMS coating), (**c**, **d**) $t_{dep} = 5$ min (scratched metal with NF-composite coating). Specimens shown as time passed: (**a**, **c**) 0 min and (**b**, **d**) 60 min. SEM images of the tested specimens: (**e**, **g**) $t_{dep} = 0$ min and (**f**, **h**) $t_{dep} = 5$ min. Reprinted with permission from An et al. (2015)

Unlike the pristine PDMS case, where significant corrosion occurs (Fig. 10.1b, e and g), the self-healing composite exhibits perfect anticorrosive performance, or rust prevention (Fig. 10.1d, f and h), after the coatings were damaged. Clots, as indicated by yellow dashed circles in Fig. 10.1h, are formed by the polymerization of the released resin monomer in the presence of the released curing agent, which is also evident in the SEM images of the composite in Fig. 10.2.

The results of the tests used to characterize the protective performance of the self-healing composites of Figs. 10.1 and 10.2 are shown in Figs. 10.3 and 10.4. The pristine PDMS and self-healing composites are prepared on steel substrates with different deposition times; all specimens were identically scratched, as depicted in Fig. 10.3a. After 48 h, open bottom cylinders are placed on the specimens with no gaps between the specimen support and the cylinder openings. The cylinders are

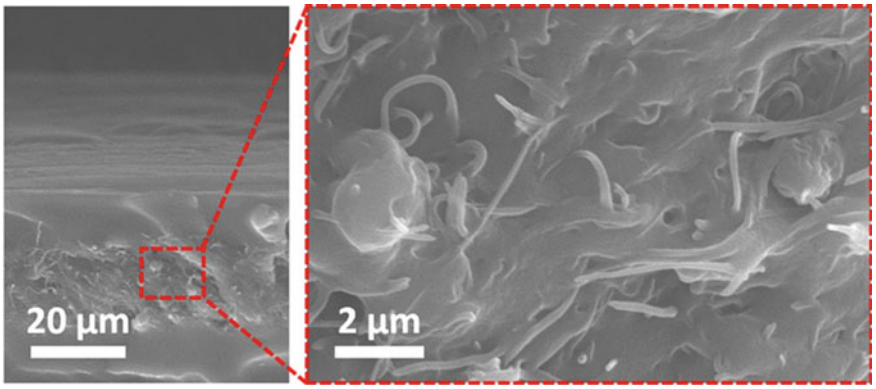

Fig. 10.2 Cross-sectional SEM images of cut composite film with healing agent release visible (NF deposition time $t_{dep} = 120$ min). Reprinted with permission from An et al. (2015)

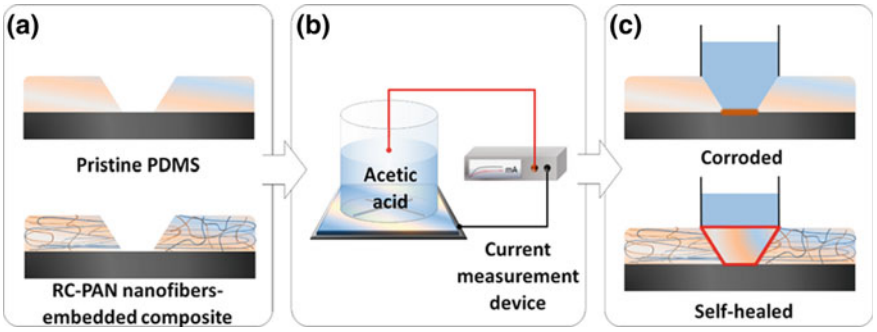

Fig. 10.3 Electrochemical test. **a** Scratched composite films on steel substrates. **b** Schematic of the electrochemical test setup. **c** The tested specimens. Reprinted with permission from An et al. (2015)

filled with acetic acid (Fig. 10.3b). Electric wires from a current-measuring device are directly connected to the electrolyte and the base of the steel substrate. As depicted in Fig. 10.3c, the self-healed specimen forms a protective layer between the steel and the electrolyte. However, the pristine PDMS does not offer this protection, as confirmed through the electrochemical testing and plotted in Fig. 10.4. The pristine PDMS ($t_{dep} = 0$ min) yields an electric current of 10–25 mA, indicating the exposure of the base steel substrate to the electrolyte because of the absence of self-healing in the damaged layer. On the other hand, perfect electrical insulation, demonstrated by the current of ~0 mA, is observed with the damaged and healed self-healing composites with $t_{dep} \geq 30$ min. A non-zero current was detected for $t_{dep} = 5$ and 10 min (not shown). This indicates that $t_{dep} \leq 10$ min is insufficient to create an intact anticorrosive coating containing such NFs, and that $t_{dep} \geq 30$ min is required to fabricate a coating with anticorrosive and electrically insulating properties.

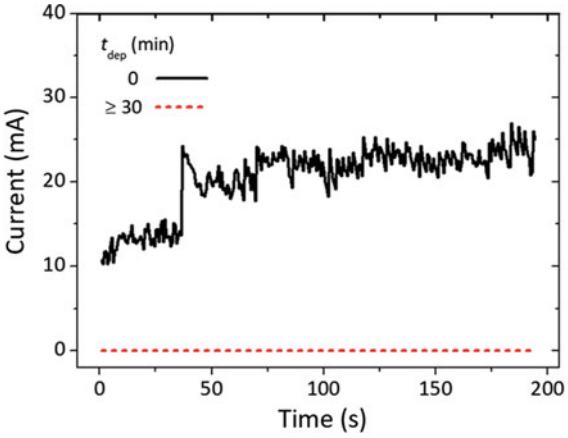

Fig. 10.4 Results of electrochemical test with RC-PAN NF-embedded composite film with different deposition times t_{dep} on steel substrates (the electric current $I \rightarrow 0$ mA for $t_{dep} \geq 30$ min, for which all straight lines are overlaid, indicating complete electrical insulation achieved with the self-healed materials). Reprinted with permission from An et al. (2015)

Park and Braun (2010) fabricated bead-on-the-string NFs using co-electrospinning (cf. Sect. 4.2) with the healing agents (resin monomer and curing agent) encapsulated primarily within capsule-like beads with outer diameter of 2–10 μm. A coating containing these fibers was deposited on cold-rolled steel sheet specimens. To examine the anticorrosion performance of the NF-embedded coating, they pre-notched cracks on the specimen coatings and let them heal for 24 h. Then, they immersed the specimens in salt water for hundreds of hours and analyzed the formation of rust. Significant corrosion had occurred in the control specimen with no self-healing coating. On the other hand, no corrosion was observed in the NF-containing specimen, as the damaged cracks were healed successfully, which protected the underlying metal substrate from the salt water.

10.2 Corrosion Protection Provided by Coatings with Embedded Core-Shell NFs Formed by Emulsion Spinning

Lee et al. (2014a) used the dual-emulsion electrospinning method to simultaneously encapsulate a siloxane-based resin and its curing agent as healing agents within the NF cores (cf. Sect. 4.3). The NF shell was PAN; the self-healing NFs were embedded in a PDMS matrix. The surfaces of steel specimens are coated with the self-healing NF mat. The coatings are then cut with X-shaped scratches (see Fig. 10.5) with a paper knife. The bare steel specimens used as controls are also scratched with X marks. The performance of the self-healing mat is evaluated by the corrosion testing in either 4 wt% NaCl solution (modeling sea water) or acetic acid. The scratched specimens (both coated and unprotected) are submerged into the corrosive media.

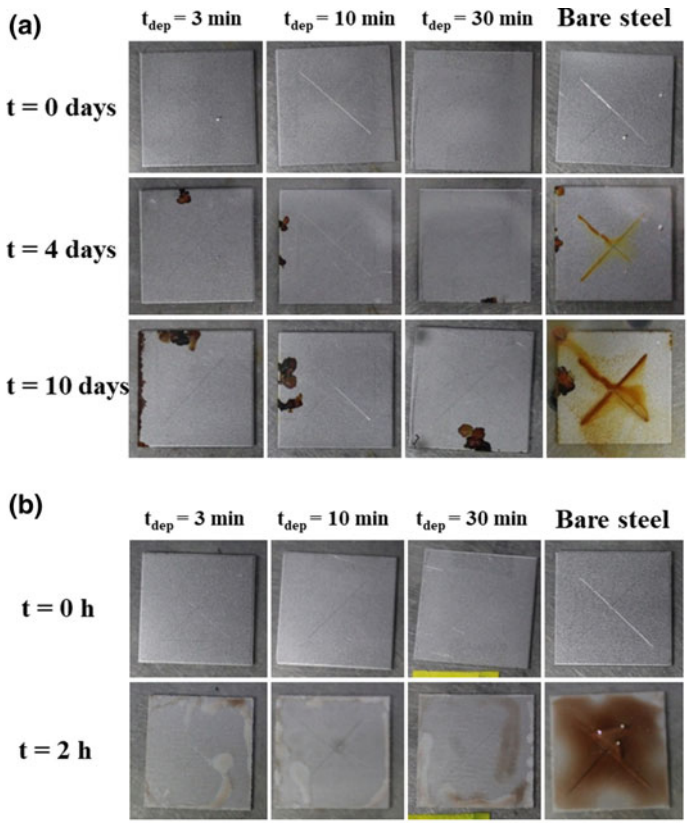

Fig. 10.5 Corrosion testing in **a** NaCl 4 wt% aqueous solution; **b** acetic acid. Reprinted with permission from Lee et al. (2014a)

Figure 10.5a shows the results of the corrosion test in the 4 wt% NaCl solution. In this case the corrosion time scale is a few days. Meanwhile, Fig. 10.5b shows the results of the corrosion tests in acetic acid with the corrosion time scale of a few hours. After the damaged specimens are immersed in the corrosive solutions, the corrosion processes are monitored. The self-healing mats used herein are fabricated with the deposition times of $t_{dep} = 3$, 10, and 30 min. As is seen in Fig. 10.5, none of the self-healing specimens are corroded near the X- shaped cuts; see the photographs in the first three columns of the figure. The corrosion observed near the edges of the substrate arises from the imperfection of the protective mat at the specimen edges. The damaged X-shaped regions show no corrosion, indicating the rapid self-healing provided by the NF mat. All three mats with different deposition times (i.e., $t_{dep} = 3$, 10, and 30 min) completely prevent corrosion. This indicates that exceedingly thick coatings with such self-healing NFs may be unnecessary to protect the steel surface;

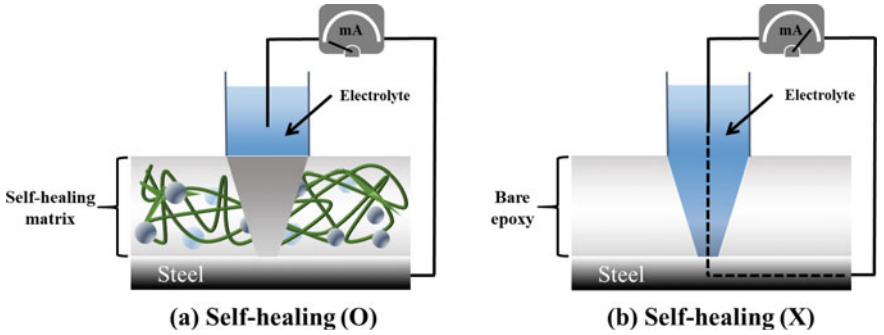

Fig. 10.6 Schematic of electrochemical test. **a** Steel protected by self-healing epoxy coating (with embedded NFs containing curing agent in the cores, and embedded microdroplets with resin monomer). **b** Steel without self-healing coating, the control case. This experiment is an electrochemical analog of SVET. Reprinted with permission from Lee et al. (2014b)

a thin core-shell self-healing mat with $t_{dep} = 3$ min is sufficient for protecting the steel surface from corrosion.

Lee et al. (2014b) employed a slightly different approach to fabricate self-healing core-shell NF-embedded composites. They formed a hybrid epoxy-matrix composite with embedded core-shell NFs with curing agent in the fiber cores and DMS resin monomer in microdroplets embedded in the epoxy matrix (cf. Sect. 4.3). To analyze the corrosion protection provided by such a self-healing composite, they performed electrochemical tests. They placed scratched metal substrates with and without the self-healing coatings in salt water or acetic acid and measured the electric currents across the substrates.

To test the self-healing performance of such a hybrid composite, an electrochemical device depicted in Fig. 10.6 is used; it is an electrochemical analog of the scanning vibrating electrode technique (SVET).

The self-healing composite coatings are prepared on stainless steel substrates. The substrate and coating are in contact with an electrolyte layer and thus included in the electric circuit; cf. Fig. 10.6. However, for an intact coating, no electric current should pass through the circuit, because the coating is an insulator. Once a cut is introduced to the coating, the stainless steel at the bottom is exposed to the electrolyte and an electric current passes through the circuit. Simultaneously, the resin monomer and curing agent liquids are released from the fractured droplets and NF cores embedded in the damaged area of the composite. Once the resin and curing agent come in contact, the resin crosslinks and solidifies (see Sect. 2.2), which manifests the self-healing of the coating and stops the current again.

The coatings are cut by a razor and left for a 48 h resting time to allow crosslinking and polymerization of the resin and curing agent. Then the electric current is measured, as described above in conjunction with Fig. 10.6. Figure 10.7 shows the measured electric current versus time. For the non-self-healing coatings (i.e., epoxy matrix with only resin droplets being embedded), an electric current of approxi-

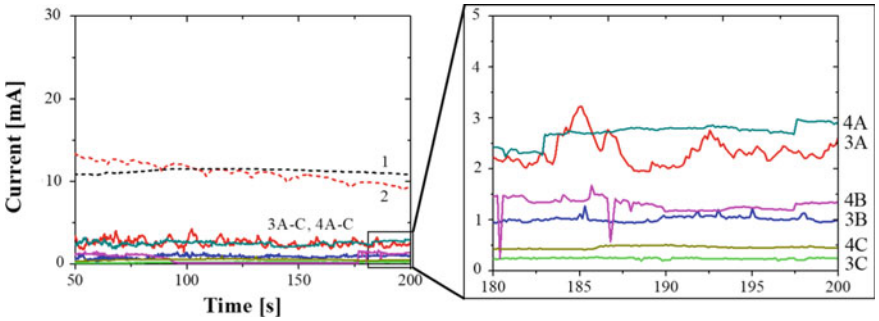

Fig. 10.7 Electric current. 1: Epoxy (non-self-healing). 2: Resin–epoxy (5 wt%) (no self-healing). 3A: curing agent NF mat with $t_{dep} = 3$ min, matrix-5. 3B: curing agent NF mat with $t_{dep} = 3$ min, matrix-10, 3C: curing agent NF mat with $t_{dep} = 3$ min, matrix-20. 4A: curing agent NF mat with $t_{dep} = 10$ min, matrix-5. 4B: curing agent NF mat with $t_{dep} = 10$ min, matrix-10. 4C: curing agent NF mat with $t_{dep} = 10$ min, matrix-20. The epoxy matrices containing 5, 10, and 20 wt% resin emulsion with respect to the weight of epoxy are denoted as matrix-5, -10 and -20, respectively. Time is counted from the moment when measurements are started. Reprinted with permission from Lee et al. (2014b)

mately 10 mA is measured for 200 s. This clearly shows that these coatings have not self-healed, as expected. On the other hand, the self-healing coatings (i.e., epoxy matrices-5, -10, and -20 with the embedded NFs deposited for $t_{dep} = 3$ and 10 min, in addition to the embedded microdroplets containing resin monomer) show electric currents below 2.5 mA (comparable to the noise level) demonstrating insulating properties. This means that these coatings undergo self-healing, which occurs with the coatings containing fibers deposited either for $t_{dep} = 3$ or 10 min, indicating that the deposition time does not significantly affect self-healing performance. This means that long deposition times for curing agent-containing NFs are not necessary, which is favorable from a manufacturing perspective. The signals below the noise level also do not allow a reliable distinction of the effects of the resin contents (i.e., the matrix-5 versus matrix-20 cases), but imply that larger resin contents relative to the amount of curing agent are preferable to maximize the self-healing performance.

References

An S, Liou M, Song KY, Jo HS, Lee MW, Al-Deyab SS, Yarin AL, Yoon SS (2015) Highly flexible transparent self-healing composite based on electrospun core–shell nanofibers produced by coaxial electrospinning for anti-corrosion and electrical insulation. Nanoscale 7:17778–17785

Lee MW, An S, Lee C, Liou M, Yarin AL, Yoon SS (2014a) Self-healing transparent core–shell nanofiber coatings for anti-corrosive protection. J Mater Chem A 2:7045–7053

Lee MW, An S, Lee C, Liou M, Yarin AL, Yoon SS (2014b) Hybrid self-healing matrix using core–shell nanofibers and capsuleless microdroplets. ACS Appl Mater Interfaces 6:10461–10468

Park JH, Braun PV (2010) Coaxial electrospinning of self-healing coatings. Adv Mater 22:496–499

Chapter 11
Concluding Remarks and Future Perspectives

11.1 Advantages and Disadvantages of Self-Healing Engineering Materials and Future Research Directions

Mimicking natural vascular systems in engineering materials is achievable by using core-shell nanofibers (NFs) whose cores are filled with self-healing agents (e.g., resin monomer and curing agent, or epoxy and hardener). This is beneficial for the following reasons: (i) uniformly distributed versus localized healing elements (as in the case of microcapsules containing healing agents), and (ii) nanoscale instead of microscale healing elements (as in the case of microcapsules). Nanoscale healing elements can fit ply areas in layered composites and avoid weakening the surrounding matrix. Another benefit of NF-based self-healing systems is that the dispersion of additional components required for self-healing reactions in the surrounding matrix is unnecessary. Specifically, a self-healing system should use two types of interwoven NFs with two complementary healing agents present within their cores, namely, a resin and its curing agent or an epoxy and its hardener. When released from the damaged core-shell nanofibers, these components react with each other to form polymerized, solidified stitches that connect the crack banks. The stiffness and self-cohesion of the damaged material can thus be restored. However, the prevention of delamination and the recovery of adhesion to surfaces of different compositions remain issues to be resolved that require additional future research efforts.

In fabrication, it has been demonstrated that the solution blowing of core-shell NFs encapsulating healing agents is a much more effective process than either co-electrospinning or emulsion spinning. However, although the solution blowing of various polymers and biopolymers has already been demonstrated on the industrial scale using commercially available equipment, it remains to be employed for fabricating core-shell NFs containing healing agents. Only after solution blowing of self-healing NFs can be achieved will self-healing engineering materials find widespread use in engineering practice. Electrospun and solution-blown fibers are usually randomly oriented and deposited unevenly on surfaces. Moreover, it remains non-trivial

A. L. Yarin et al., *Self-Healing Nanotextured Vascular Engineering Materials*, Advanced Structured Materials 105, https://doi.org/10.1007/978-3-030-05267-6_11

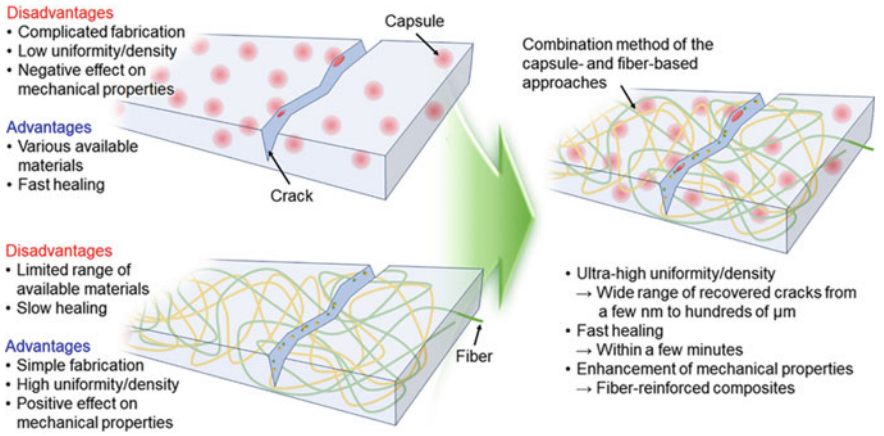

Fig. 11.1 Schematics for capsule-based, fiber-based, and hybrid self-healing approaches and the corresponding advantages and disadvantages of each method. Reprinted with permission from An et al. (2018b)

to ensure the continuous and uniform encapsulation of healing agents within core-shell NFs when using these techniques. This is an additional obstacle to the industrial fabrication of self-healing materials while maintaining high production quality. The development of three-dimensional self-healing nanotextured vascular materials has only begun recently and should attract wider attention in the future.

Although numerous self-healing materials have already been developed, it remains unclear whether the methods proposed for fabricating these materials are economically feasible and industrially scalable. Capsule-based self-healing methods have several disadvantages, such as low uniformity of the dispersed capsules and complicated fabrication processes (Fig. 11.1). To overcome these drawbacks, several fiber-based self-healing approaches have been introduced recently: the method of solution blowing has already been performed at the industrial scale, as mentioned above. Nevertheless, the range of materials that can be used as the shells for encasing the core materials in these core-shell NFs remains limited. On the other hand, capsule-based methods allow the use of a wider range of materials, despite their other limitations.

Several additional goals must be pursued in future studies. First, it would be highly desirable to be able to consistently (in all cases on demand) decrease the outer diameters of the shells from the microscale to the nanoscale, in order to enhance the self-healing performance by increasing the specific surface-area-to-volume ratio (S/V). Second, the development of core materials with shorter healing times of a few hours or less is essential. The core and shell materials currently available for the fiber-based approach to self-healing possess healing times on the order of hours in the best cases. Third, fabrication processes for self-healing composites that are industrially scalable and economically viable must be developed to allow greater use

of self-healing techniques in the aeronautical and automotive industries. The recent development of multi-nozzle coating systems and roll-to-roll devices for the fabrication of NFs is encouraging and should help in addressing the scalability challenge.

Simultaneously, hybrid methods incorporating both capsule- and fiber-based approaches (see Fig. 11.1) should be developed further to maximize the advantages of both approaches. For example, self-healing composites using both rapidly healing capsules and miniscule self-healing core-shell NFs could be used for damage recovery of a wide range of cracks of many length scales, from a few nanometers in size (by the NFs) to hundreds or thousands of nanometers wide (by the capsules). In addition, such a hybrid approach would not exhibit the limitations related to slow healing, because of the use of the capsules, or low uniformity, because of the presence of NFs. Finally, adding corrosion inhibitors or using pH- and redox-responsive polymers could lead to additional improvements in the self-healing performance, particularly in the field of corrosion protection.

The interfacial toughening of composite laminates, for the aeronautical and automotive industries as a measure of protection against impact damage and fatigue cracking, will be important. Accordingly, nanotextured self-healing interleaved structures aiming the interfacial toughening will be sought. Proliferation of soft robotics and actuators, as well as products based on them, requires innovative flexible self-healing composites, which can withstand multiple operation cycles without growth of fatigue cracks (An et al. 2018a, Kang et al. 2019). A remedy to the electrodes and solid electrolyte interphase of Li-ion batteries, which crack because of cyclic loads during charging and discharging can probably be sought in the form of embedded self-healing elements (Jin et al. 2017).

References

An S, Kang DJ, Yarin AL (2018a) A blister-like soft nano-textured thermo-pneumatic actuator as an artificial muscle. Nanoscale 10:16591–16600

An S, Lee MW, Yarin AL, Yoon SS (2018b) A review on corrosion-protective extrinsic self-healing: Comparison of microcapsule-based systems and those based on core-shell vascular networks. Chem Eng J 344:206–220

Jin Y, Li S, Kushima A, Zheng X, Sun Y, Xie J, Sun J, Xue W, Zhou G, Wu J, Shi F, Zhang R, Zhu Z, So K, Cui Y, Li J (2017) Self-healing SEI enables full-cell cycling of a silicon-majority anode with a coulombic efficiency exceeding 99.9%. Energy Environ Sci 10:580–592

Kang DJ, An S, Yarin AL, Anand S (2019) Programmable soft robotics based on nano-textured thermo-responsive actuators. Nanoscale 11: 2065–2070

Index

A. L. Yarin et al., *Self-Healing Nanotextured Vascular Engineering Materials*, Advanced Structured Materials 105, https://doi.org/10.1007/978-3-030-05267-6

D